Springer Theses
Recognizing Outstanding Ph.D. Research

Ismail Adeniran

Modelling the Short QT Syndrome Gene Mutations

And Their Role in Cardiac Arrhythmogenesis

Springer

Springer Theses

Recognizing Outstanding Ph.D. Research

For further volumes:
http://www.springer.com/series/8790

Aims and Scope

The series "Springer Theses" brings together a selection of the very best Ph.D. theses from around the world and across the physical sciences. Nominated and endorsed by two recognized specialists, each published volume has been selected for its scientific excellence and the high impact of its contents for the pertinent field of research. For greater accessibility to non-specialists, the published versions include an extended introduction, as well as a foreword by the student's supervisor explaining the special relevance of the work for the field. As a whole, the series will provide a valuable resource both for newcomers to the research fields described, and for other scientists seeking detailed background information on special questions. Finally, it provides an accredited documentation of the valuable contributions made by today's younger generation of scientists.

Theses are accepted into the series by invited nomination only and must fulfill all of the following criteria

- They must be written in good English.
- The topic should fall within the confines of Chemistry, Physics, Earth Sciences, Engineering and related interdisciplinary fields such as Materials, Nanoscience, Chemical Engineering, Complex Systems and Biophysics.
- The work reported in the thesis must represent a significant scientific advance.
- If the thesis includes previously published material, permission to reproduce this must be gained from the respective copyright holder.
- They must have been examined and passed during the 12 months prior to nomination.
- Each thesis should include a foreword by the supervisor outlining the significance of its content.
- The theses should have a clearly defined structure including an introduction accessible to scientists not expert in that particular field.

Ismail Adeniran

Modelling the Short QT Syndrome Gene Mutations

And Their Role in Cardiac Arrhythmogenesis

Doctoral Thesis accepted by
the University of Manchester, UK

Springer

Author
Dr. Ismail Adeniran
Biological Physics Group
School of Physics and Astronomy
University of Manchester
Manchester
UK

Supervisor
Prof. Henggui Zhang
Biological Physics Group
School of Physics and Astronomy
University of Manchester
Manchester
UK

ISSN 2190-5053 ISSN 2190-5061 (electronic)
ISBN 978-3-319-07199-2 ISBN 978-3-319-07200-5 (eBook)
DOI 10.1007/978-3-319-07200-5
Springer Cham Heidelberg New York Dordrecht London

Library of Congress Control Number: 2014940518

Printed on acid-free paper

Springer is part of Springer Science+Business Media (www.springer.com)

To my mother, for her continued patience and support and my father, Lateef Ajani Adeniran, who passed away from heart disease in 1996

Supervisor's Foreword

The QT interval of the electrocardiogram (ECG) corresponds to the period from the initiation of ventricular depolarisation to the completion of ventricular repolarisation. Under normal conditions, the QT interval is in a range between 360 and 440 ms. Too long or too short, a QT interval is associated with an increased risk of abnormal cardiac electrical activity, predisposing to sudden cardiac death.

Recently, a distinct, genetic syndrome involving abnormally short QT intervals (SQTS) has been identified. Patients with SQTS typically exhibit QT intervals <320 ms and have high incidence of ventricular and atrial arrhythmias and sudden death.

The mechanisms by which the SQTS results in an increased risk of arrhythmia and sudden death are not yet fully understood. In the absence of phenotypically accurate experimental models of SQTS variants, computer modelling offers the only available way of investigating how genetic forms of the SQTS lead to initiation and maintenance of atrial and ventricular arrhythmias at the tissue level. It provides the best available means of bridging understanding between molecular and clinical electrophysiology.

In this thesis, Dr. Adeniran presented details of the development of multiphysics models of the human ventricles as well as simulation results of how some of the SQTS genetic variants affecting potassium channels cause impaired cardiac electrical activity, leading to increased susceptibility to cardiac arrhythmias. The thesis presented an excellent exemplar of systems biology by which a causative link between molecular mutations and changes to heart functions can be established. The presented results provide mechanistic insight into how the SQTS influences ventricular risk. This is of value in helping optimise treatments for SQTS patients or those with disorders involving ventricular repolarisation.

The multiscale ventricular models developed and used in this thesis provide a powerful foundation for further investigation of the cellular and molecular basis of cardiac functions.

Manchester, April 2014 Prof. Henggui Zhang

Abstract

The recently identified genetic short QT syndrome is characterised by abbreviated QT intervals on the electrocardiogram, an increased risk of atrial and ventricular arrhythmias, and an increased risk of sudden death. Although the short QT syndrome has been suggested to provide a paradigm for increasing understanding of the role of potassium channels in ventricular fibrillation, the basis for arrhythmogenesis in the short QT syndrome is incompletely understood. There are no animal models that accurately reproduce a short QT phenotype, and whilst in vitro electrophysiology of short QT mutant channels provides a route to greater understanding of the effects of short QT mutants on action potential repolarisation, on its own, this approach is insufficient to explain how arrhythmias arise and are maintained at the tissue level. Consequently, this thesis is concerned with the use of the viable alternative; in silico (computational) modelling to elucidate how the short QT syndrome facilitates the genesis and maintenance of ventricular arrhythmias and its effects on ventricular contraction. Using extant biophysical data on changes induced by the short QT mutations and data from BHF-funded in vitro electrophysiology, three novel mathematical models of the first three variants of the short QT syndrome were developed; a Markov chain model for *short QT variant 1*, a Markov chain model for *short QT variant 2* and a Hodgkin-Huxley model for *short QT variant 3*. These models were incorporated into single cell and anatomically detailed tissue and organ computer models to elucidate how these variants lead to ventricular arrhythmias. The developed short QT models were then incorporated into electromechanically coupled single cell and tissue models to investigate the effects of the short QT mutants on ventricular contraction. It was found that each short QT variant uniquely increased the transmural dispersion of action potential duration across the ventricular wall, increased the temporal window of tissue vulnerability to premature excitation stimulus, leading to increased susceptibility to re-entrant arrhythmia.

Acknowledgments

I would like to thank my supervisors, Prof. Henggui Zhang and Prof. Jules Hancox for their supervision and support, without which this thesis would not have been possible. I am grateful for all the time and enthusiasm they have invested in this project, and the guidance and education they have imparted to me in cardiac electrophysiology.

Finally, I would also like to thank all the members of the Biological Physics group at the University of Manchester for providing a stimulating and inspiring environment.

Contents

Chapter 1
Introduction to Ion Channels and the Cardiac Action Potential

Every cell in the body contains ion channels. These ion channels are proteins embedded in the cell membrane and regulate the electrical signaling of each cell via egress and ingress of various intracellular and extracellular ions (predominantly Na^+, K^+, Ca^{2+} and Cl^-). Defects to the genes encoding ion channel proteins result in the impairment of the functional properties of the ion channels. These ion channel defects lead to diseases (channelopathies) which can be life threatening [1–7]. Examples of such diseases are the short QT syndrome (SQTS) where a patient shows an abnormally short QT interval on the electrocardiogram (ECG) [8, 9] and the long QT syndrome (LQTS) where a patient presents with an abnormally long QT interval on the ECG [10–12]. These usually result in arrhythmia, which is an improper rhythm in the beating of the heart.

Arrhythmias are one of the leading causes of death in the world. They are caused by several factors including mutations to ion channels [13], ischaemia with coronary occlusion [14, 15], adverse reactions to therapeutic drugs targeting ion channel mutations [16] and steroids abuse by athletes [17]. In order to better understand the SQTS, which is the subject of this thesis, this chapter gives an overview of ion channels, particularly those with mutations that are associated with arrhythmia. This chapter will review their role in generating the cardiac action potential and the functional consequences of mutations to these channels.

1.1 The Cardiac Action Potential

The rhythmic and systematic contraction of cardiac myocytes in the heart is initiated by electrical events called action potentials (APs). An AP is an electrical impulse that reflects the time course of changes in the membrane potential of cardiac myocytes due to an elaborate sequence of openings and closings of the ion channels and electrogenic transporters within the myocyte cell membrane [18–20]. There are five phases of the cardiac action potential [19, 21, 22] (Fig. 1.1). Phase 0 is the depolarisation of the cell where the membrane potential is rapidly brought from a negative to a positive potential, while Phase 1 corresponds to the end of this

I. Adeniran, *Modelling the Short QT Syndrome Gene Mutations*,
Springer Theses, DOI: 10.1007/978-3-319-07200-5_1,

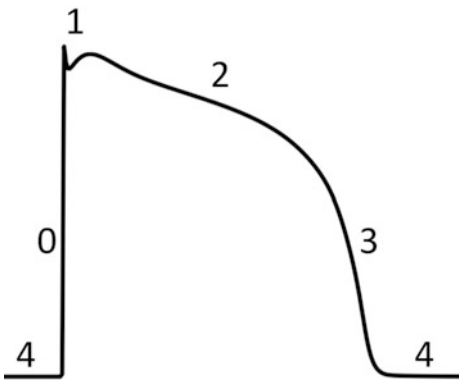

Fig. 1.1 Schematic diagram showing phases of the cardiac action potential. Phase 0: Upstroke. Phase 1: Early/ Partial repolarisation. Phase 2: the plateau. Phase 3: Repolarisation. Phase 4: Resting period

upstroke. In some cell types, a partial repolarisation occurs (in which the membrane potential is brought from a positive to a more negative potential), resulting in a notch between phases 0 and 2. The membrane potential can be repolarised to about 0 mV and even more negative potentials.

A plateau phase (phase 2) follows this partial repolarisation, which ends with a final repolarisation phase (phase 3). Phase 4 is the return of the membrane potential to a stable resting potential in atrial and ventricular cells. In spontaneously active cells such as those from the sinoatrial node (SAN; the heart's primary pacemaker), phase 4 is a slow depolarisation that eventually causes spontaneous activity [19, 21, 22].

1.2 Morphology of the Action Potential in Different Parts of the Heart

The SAN—located at the junction of the superior vena cava and the right atrium—is responsible for the initiation of the heart's spontaneous activity (Fig. 1.2) [18, 19, 23, 24]. Electrical activity from the SAN spreads to surrounding atrial tissue via gap junctions which couple cardiac cells electrotonically [18, 19, 23, 24]. It then spreads to the atrioventricular node (AVN) from which it excites the His Bundle Purkinje system, which in turn conducts the electrical activity to the ventricular myocardium (Fig. 1.2) [18, 19, 23, 24].

The cells in the different regions of the heart can be grouped into slow and fast response cells based on the rate of depolarisation during the upstroke of the AP (phase 0) [19, 24]. This difference in grouping is caused by the inward current that is predominantly responsible for depolarisation; Ca^{2+} for slow response cells and Na^{+} for fast response cells. The SAN and AVN cells are slow response cells while the atria, His Bundle, Purkinje and ventricular myocardial cells are fast response cells.

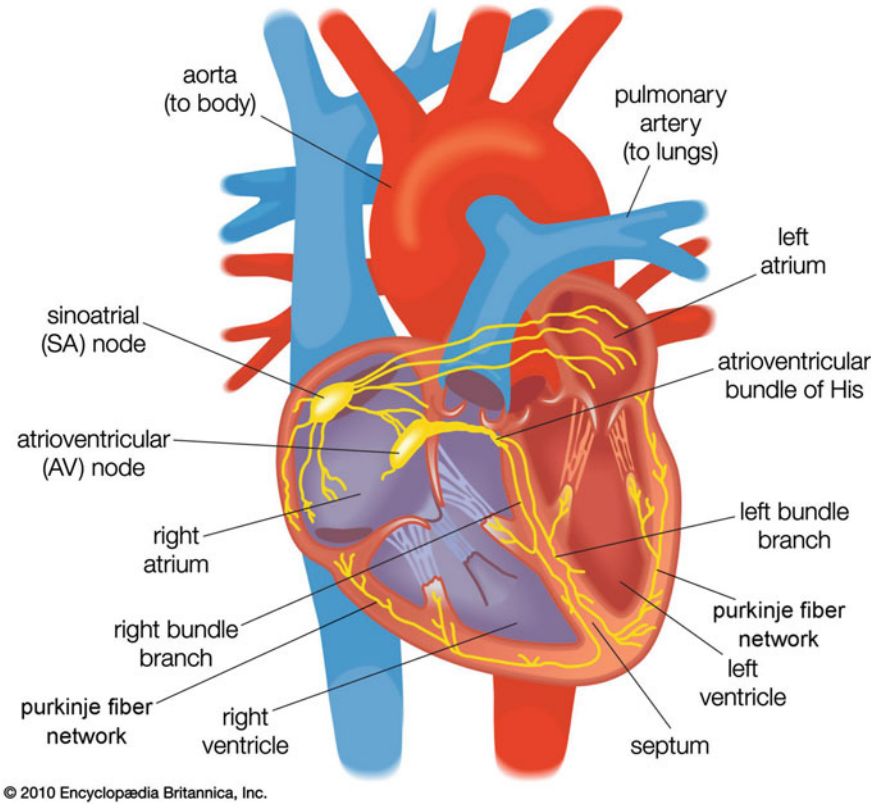

Fig. 1.2 Electrical conduction in the heart in healthy individuals is controlled by pacemaker cells in the sinoatrial node. Electrical impulses are conducted from the sinoatrial node to the atrioventricular node and bundle of His, through the bundle branches, and into the ventricles [28]

1.2.1 Sinoatrial Node

The SAN contains slow response cells with a low upstroke velocity of about 1 - 10 V/s [24, 25] in mammalian cells. Upstroke velocity is approximately 5 V/s in human [26, 27]. It is characterised by a slowly rising diastolic depolarisation in phase 4 of the AP leading to spontaneous activity (Fig. 1.3). Its diastolic potential ranges from −60 to −50 mV. SAN cells located peripherally have more negative diastolic potentials due to their electrical coupling with atrial cells (atrial cells have more negative resting potentials than the SAN). SAN cells have a diameter of about 5–10 μm, an action potential duration (APD) range of 100–200 ms and a propagation velocity that is less than 0.05 m/s [24, 25].

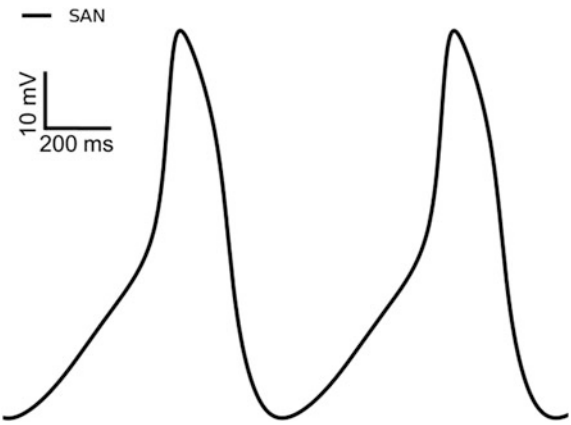

Fig. 1.3 Action potential from a human sinoatrial node. Modified from Aslanidi et al. [31]

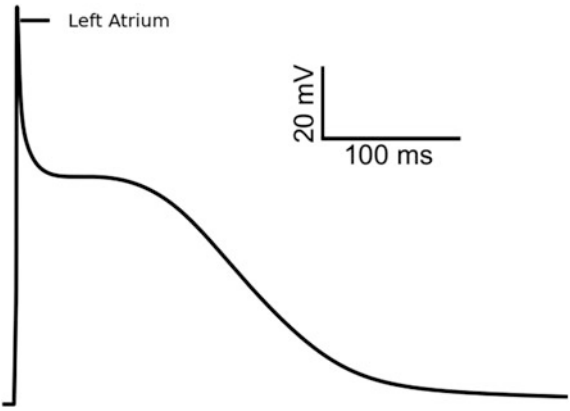

Fig. 1.4 Action potential in normal human atrium. Modified from Courtemanche et al. [32]

1.2.2 Atria

Atrial cells have a resting potential of about −80 mV and unlike the SAN, this resting potential is stable with no spontaneous activity (Fig. 1.4) [23, 24, 27]. In mammalian hearts, the APD is between 100 and 300 ms and is different in different regions of the atria [19, 24]. It is shorter in the left atrium than in the right atrium [29, 30]. There is a sharp upstroke with a velocity of 100–200 V/s [24, 25, 27] in mammalian hearts followed by a plateau phase. The cells return to the resting potential but there is no clear demarcation between the plateau (phase 2) and a final repolarisation phase (phase 3). Atrial cells have a diameter of about 10–15 μm and a propagation velocity between 0.3–0.4 m/s [19, 24, 25].

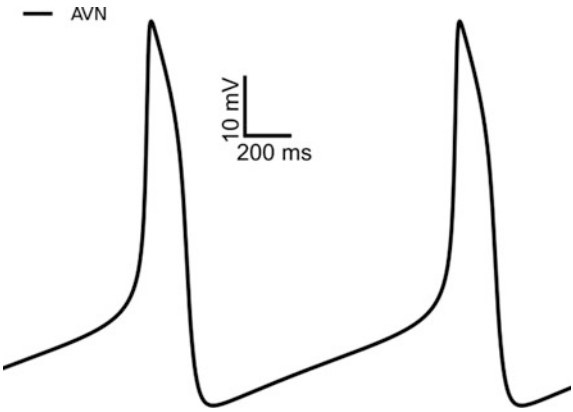

Fig. 1.5 Action potential in normal atrioventricular node. Modified from [33]

1.2.3 Atrioventricular Node

The atrioventricular node (AVN) lies at the bottom of the right atrium near the partition that divides the atria [24]. AVN cells have a diameter of about 5-10 μm and a resting potential of −60 to −70 mV [19, 24, 25]. Like the SAN, it has spontaneous activity but delays cardiac conduction from the atria to the ventricles, allowing the atria to contract and empty their contents first before relaying impulses to the His bundle [19, 24]. Its rate of depolarisation is about 5–15 V/s with an action potential that propagates at about 0.1 m/s and a duration of 100–300 ms [19, 24, 25] in mammalian cells. An example AP is shown in Fig. 1.5.

1.2.4 His Bundle Purkinje System

The His bundle (also known as the AV bundle of His) proceeds from the AVN and penetrates the tissue separating the atria and ventricles. It penetrates the ventricles and divides into left and right bundle branches (also known as AV bundle branches), which end in a network of Purkinje fibres. This network of Purkinje fibres serves as the source of electrical activity to the ventricular myocardium as they form the only contact with the walls. The His bundle Purkinje system is the fast conduction pathway of the heart, propagating impulses rapidly towards the apex of the ventricles, ensuring their near uniform activation [19, 24, 25].

The cells have a diameter of 100 μm [25], a resting potential of −90 to −95 mV [19, 24, 25] and a fast upstroke of about 500–700 V/s [25]. The APD is about 319 ± 23 ms in human hearts [35] depending on the frequency of stimulation. The AP has propagation velocity of 2 to 5 m/s [19, 24, 25] and usually has all the phases of the action potential shown in Fig. 1.1 (phase 1: the notch may sometimes be absent). Purkinje fibre cells also show slow diastolic depolarisation, which is not as marked as

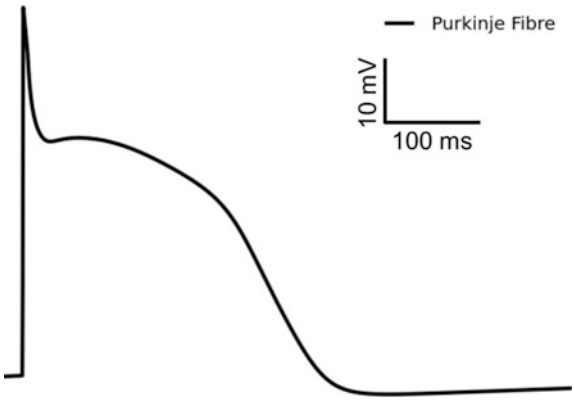

Fig. 1.6 Action potential in normal human Purkinje fibre cell. Modified from [34]

in SAN cells. At low frequencies, this may lead to spontaneous activity if not previously activated by normal sinus activity via electrotonic interactions with neighbouring cells [19, 24]. An example AP is shown in Fig. 1.6.

1.2.5 Ventricle

Ventricular myocardial cells show different characteristics in different regions of the ventricles. The APD is shorter in the right ventricle than in the left ventricle and also has a more markedly pronounced notch (phase 1 repolarisation) [19, 24]. Transmurally, the ventricular myocardium has three cell types; the endocardium (ENDO), the mid-myocardium (MCELL) and the epicardium (EPI) [19, 24, 36, 37]. The ENDO cell is the innermost layer while the EPI cell is the outermost layer. The MCELL has the longest APD (comparable to the purkinje fibre cells). Generally, the APD of the EPI cell is shorter than that of the ENDO cell across all species but there is some experimental data showing the opposite in human ventricular cells [37]. The EPI cell has a pronounced phase 1 repolarisation, as does the MCELL, which results in a pronounced notch, giving the AP a spike-dome appearance. In comparison, there is less phase 1 repolarisation in the ENDO cell and consequently a less pronounced notch [19, 24].

Ventricular myocardial cells have a diameter of 10–20 μm [24, 25], a resting potential of about −80 to −90 mV and an upstroke velocity of 100–200 V/s [24, 25] in mammalian cells. The AP propagates at about 0.3–1.0 m/s [19, 24, 25] and spreads from the endocardium near the apex to the epicardial wall at the base (Fig. 1.7).

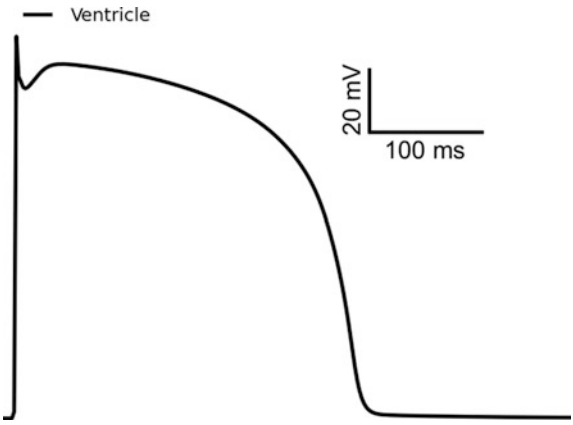

Fig. 1.7 *Left* ventricular epicardial action potential in a normal human ventricle. Modified from [38]

1.3 Ionic Basis of Resting and Action Potential

1.3.1 The Uniformly Polarised Cell

The cell membrane is electrically equivalent to a capacitor because it consists of a lipid bilayer that separates the intracellular medium from the extracellular medium (Fig. 1.8). The lipid bilayer has a capacitance of about 1 μF/cm^2, is non-conducting and acts as a dielectric. It also contains proteins, some of which behave as ion permeation pathways through which ions enter or exit the cell membrane. The cell membrane is thus not a perfect isolator and can be regarded as a "leaky" capacitor. The electrical equivalent of the cell membrane is then a capacitor in parallel with a resistor (ion permeation pathways) (Figs. 1.9 and 1.10).

When current passes through the membrane (I_m), some of it goes into charging the capacitor (I_c) while the rest (I_{ion}) flows through the resistive pathway (Fig. 1.10). I_c will cause a change in the amount of charge being separated and consequently, a change in the membrane potential. This change in potential will in turn cause an equivalent change in current. The total membrane current (I_m) can then be written as:

$$\begin{aligned} I_m &= I_c + I_{ion} \\ Q &= C_m V_m \\ I_c &= \frac{dQ}{dt} \\ I_m &= \frac{dQ}{dt} + I_{ion} \\ I_m &= C_m \frac{dV_m}{dt} + I_{ion} \end{aligned} \tag{1}$$

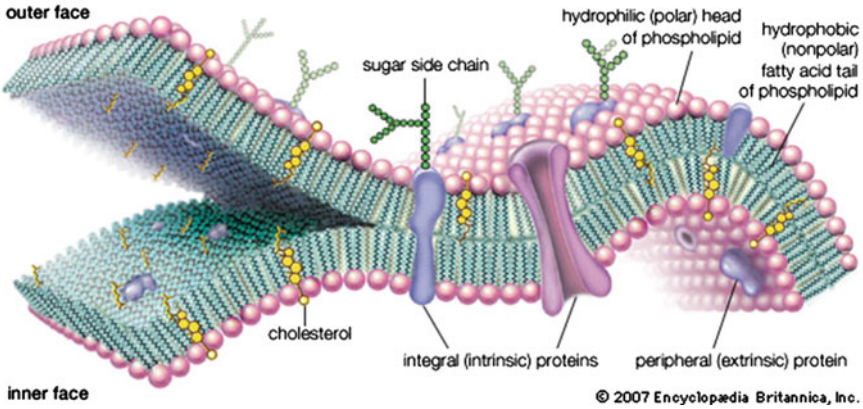

Fig. 1.8 Intrinsic proteins penetrate and bind tightly to the lipid bilayer, which is made up largely of phospholipids and cholesterol and which typically is between 4 and 10 nm (nm; 1 nm = 10^{-9} m) in thickness. Extrinsic proteins are loosely bound to the hydrophilic (polar) surfaces, which face the watery medium both inside and outside the cell. Some intrinsic proteins present sugar side chains on the cell's outer surface [39]

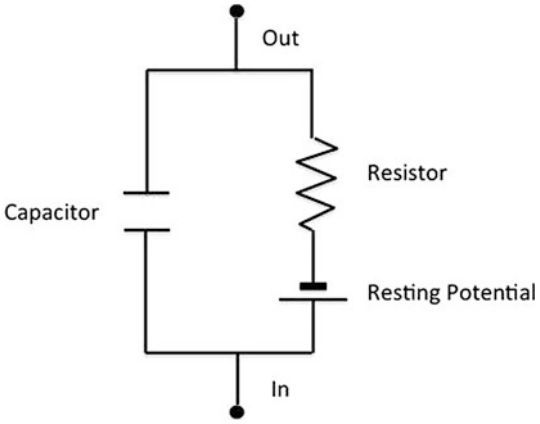

Fig. 1.9 Electrical equivalent of the cell membrane

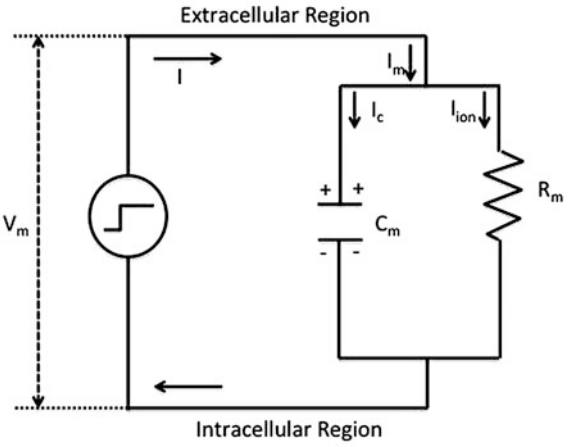

Fig. 1.10 Passive membrane electrical circuit. V_m is the transmembrane potential, I_m is the total membrane current, I_{ion} is the ionic current, I_c is capacitative current, C_m is the membrane capacitance and R_m is the membrane resistance

where Q is the charge in coloumb, C_m is the capacitance in farads and V_m is the membrane potential in volts.

1.3.2 Electrical Equivalent Circuit of a Cell

The cell membrane contains many ion channels, each of which contribute to the net ionic current I_{ion}. The ion channels would then be represented as variable resistors in parallel (variable resistors because the channel opening and hence resistance may not be constant) [18–20, 24]. For each ion, there is a concentration gradient across the cell membrane, which can be represented as a battery (electromotive force). Therefore, each ion channel is a variable resistor in series with a battery (Figs. 1.9 and 1.10). The ionic current flowing through each ion channel can then be represented mathematically using a modification of Ohm's law, which takes the ion concentration gradient into account:

$$I_{ion} = G_{ion}(V_m - E_{ion}) \tag{2}$$

where I_{ion} is the ionic current, G_{ion} is the inverse of the resistance (conductance of the channel), E_{ion} is the equilibrium potential of the ion and V_m has the same meaning as in Eq. (1). The equilibrium potential of the ion is the potential at which no net transport of the ion occurs. At this potential, the free energy due to the concentration gradient is equal and exactly opposite to the potential gradient (see Sect. 1.3.3).

According to standard convention, the direction of current flow is generally considered to be the direction of flow of the positive charges. Positive current flow is described as positive charges leaving the cell across the cell membrane, e.g., K^+ ions leaving the cell is outward current and Na^+ entering the cell is inward current. The membrane potential (V_m) is computed as the intracellular potential relative to the extracellular potential (V_i - V_e) and at the normal resting potential, V_m is negative [18, 19, 23, 24]. A change to the potential that makes it more negative is referred to as *hyperpolarisation* while a change that makes it less negative (or, equivalently, more positive) is referred to as *depolarisation*. Following a depolarisation, the return of the membrane to its resting potential is known as *repolarisation*.

1.3.3 Equilibrium Potential

As an analogy to a cell, let us assume there are two compartments, A and B separated by a membrane that is selectively permeable to one ion (for the sake of discussion, K^+; Fig. 1.11). Let compartment A be the intracellular region and B the extracellular region. If K^+ has a higher intracellular concentration compared to its

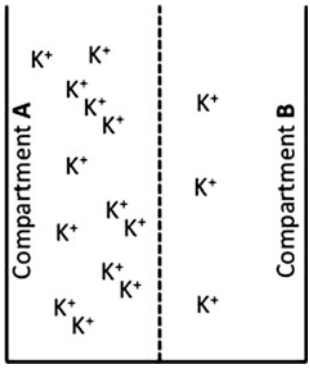

Fig. 1.11 Compartment with unequal concentrations of K^+ across a semipermeable membrane. Due to the concentration gradient, a net K^+ ion flux will occur setting up a potential difference across the membrane. Net K^+ ion flux will cease once the transmembrane potential equals the equilibrium potential of K^+

extracellular concentration (as it does in a cell), it would flow from compartment A to compartment B due to its concentration gradient. This will leave compartment A negatively charged, counteracting further efflux of K^+ ions.

Simultaneously, the efflux of K^+ ions will set up an electric potential and as more K^+ ions leave compartment A, the potential difference increases, also counteracting further K^+ efflux. The potential at which the gradient in electric potential exactly equals the opposite K^+ concentration gradient is the equilibrium potential of the ion. At the equilibrium potential, the system is in equilibrium and the net K^+ (ion) flux is zero.

The equilibrium potential for an ion, E_{ion} is determined by the Nernst equation [40] developed by the German scientist, Walther Herman Nernst:

$$E_{ion} = \frac{RT}{zF} \ln\left(\frac{[C]_o}{[C]_i}\right) \tag{3}$$

where E_{ion} is equilibrium potential (as in Eq. 2), z is the valence of the ion, R is the universal gas constant, T is the temperature in degrees Kelvin, F is Faraday's constant, $[C]_o$ is the concentration of the ion outside the cell and $[C]_i$ is the concentration of the ion outside the cell.

1.4 Properties of Ion Channels

The movement of ions across the cell membrane via ion channels leads to the generation of action potentials. To understand the contribution of each ion channel to cardiac AP electrogenesis, it is necessary to understand the two basic characteristics of ion channels: ion permeation and gating [20]. Ion permeation refers to the selectivity of the channel for a particular ion while gating refers to the kinetics of opening and closing of the channel. Also of importance are the molecular structure of the channel and the density of the channel in the cell membrane.

In general, ion transport processes as well as the opening and closing of ion channels are functions of membrane potential. They can, however, be modulated by other processes such as agonists in the extracellular medium, binding of intracellular or membrane-bound ligands and mechanical forces [20, 22, 24]. These modulatory processes confer time dependence on the response of the channels, i.e., a conformational change of the channels is not instantaneous but takes time. To account for the effect of these modulatory processes, an additional kinetic factor (gating factor) is incorporated into the ionic current formulation given in Eq. (2). It is fractional; hence, it ranges from 0 and 1 and represents the fraction of channels that are open. The current for an ion X (I_X) can then be written as:

$$I_X = \bar{G}_X K_X (V_m - E_X) \tag{4}$$

where $\bar{G}_X$ is the maximal conductance of the channel, K_X is the kinetic factor representing the fraction of channels in the open state, V_m is transmembrane voltage and E_X is the equilibrium potential for the ion.

1.4.1 Ion Permeation

When the kinetic factor (K_X) from Eq. (4) has a value of 1, all the channels are open and the equation is referred to as the fully activated current-voltage (I–V) relation. If the I–V relation behaves like an ohmic conductor, then the current is a linear function of the membrane potential. In general, however, the I–V relation for ion channels is nonlinear with the channels said to show rectification [20, 24]. This is because they pass current inward or outward. If the channel passes current outwards more easily, it is called an outward rectifier otherwise it is an inward rectifier. With increasing depolarisation, the slope of an outwardly rectifying current increases whilst it decreases for an inwardly rectifying current.

1.4.2 Gating

Ion channels may be classified into different types according to the mechanism of gating (opening and closing): voltage-dependent, ligand-dependent and mechanosensitive [20, 22, 24]. Voltage-dependent gated channels are the most abundant. Their conductance changes in response to a change in membrane potential. Most of the channels open in response to depolarisation and inactivate (if the channel shows inactivation) with further maintained depolarisation. A crude definition of inactivation is a ‘temporary’ blockade of the ion channel, which renders it non-conducting. To recover from inactivation, the channels need to close/deactivate at hyperpolarised potentials before they can be activated again. These channels can also inactivate directly from a closed state. Thus, these channels have two methods

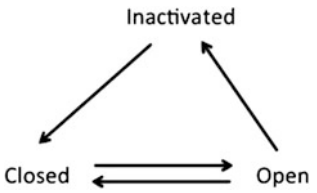

Fig. 1.12 Example state diagram for a channel showing activation and inactivation. This channel can inactivate only from an open state and can close either from an open or inactivated state

of closure: (1) closure from an open state and (2) closure from an inactivated state. Figure 1.12 shows a simple kinetic scheme for possible transitions between states.

In ligand-dependent gated channels, channel opening depends on the binding of a ligand to a receptor site. For example, the inward-rectifying acetylcholine-activated K^+ channel ($I_{K,Ach}$), which is the best studied of these types of channels. Acetylcholine binds to the M-2 muscarinic receptor, which eventually leads to a release of Gβγ subunit along a G-protein signaling pathway that activates $I_{K,Ach}$ [20, 22, 24]. Another ligand-gated channel is the ATP-sensitive K^+ channel ($I_{K,ATP}$). Its open probability is proportional to the ratio of the concentration of intracellular adenosine diphosphate (ADP) to adenosine triphosphate (ATP) ([ADP]/[ATP]). $I_{K,ATP}$ therefore couples the metabolic state of the cell to the shape of the action potential [20, 22, 24].

The mechano-sensitive (stretch-activated) channels (see Sect. 1.8) convert a physical input such as stretch into an electric signal by changing channel conductance. For example, if the heart experiences mechanical deformation at an appropriate time during the cardiac cycle (for example from a golf ball or base-ball impact on the chest), it is feasible that ventricular fibrillation may result [20, 22, 24].

1.5 Sodium Channels

The influx of Na^+ depolarises the cell causing a rapid upstroke of the AP (phase 0). The AP thus generated propagates through the heart. With depolarisation to between −60 and 10 mV, the Na^+ current (I_{Na}) magnitude increases but positive to 10 mV, it decreases [19, 20, 22, 24]. The current reverses at about 50 mV. I_{Na} has properties of activation and inactivation. It activates at about -60 mV and recovers from inactivation very quickly (1–10 ms). This recovery rate increases with hyperpolarisation. Na^+ channels are abundant in the atria, ventricles and the His Bundle Purkinje system. I_{Na} is also present in some cells from the SAN and AVN but plays little or no active role in central nodal cells due either/both to its absence or the low diastolic potential in these cells, which cause it to be inactivated [19, 20, 22, 24]. I_{Na} can contribute to cellular activity in peripheral nodal cells [41–43].

The gene encoding the major subunit of cardiac fast Na^+ channels is SCN5A [44]. Associated with mutations and defects of the channel are the congenital

forms of the Long QT Syndrome (LQTS) [44, 45], the Brugada syndrome [46], the primary cardiac conduction system disease (PCCP) [47, 48] and dilated cardiomyopathy [49]. Variant 3 of the LQTS involves gain of function mutations that lead to a small but persistent Na^+ current contributing to the plateau phase of the action potential because of slow or incomplete inactivation of the channel [50, 51]. Brugada syndrome involves loss of function mutations, which reduces the Na^+ current density and consequently shortens the APD [52–54]. Resulting clinical syndromes include AV block [54], atria standstill [55] and sinus node dysfunction [46]. The mechanisms that link Na^+ channel dysfunction to dilated cardiomyopathy are not well understood [56].

1.6 Calcium Channels

There are two types of Calcium (Ca^{2+}) channels: L-type (low threshold type) and T-type (transient type) calcium channels [22, 57]. They differ in their electrophysiological and pharmacological characteristics. Their densities also vary in different parts of the heart. Mutations to the calcium channel result in disorders such as Timothy syndrome (a combination of hypoglycaemia, LQTS, cognitive abnormalities, immune deficiency and syndactyly [58]) and a sudden death syndrome that combines the Brugada syndrome with a short QT interval [59].

1.6.1 L-Type Calcium Channel

The L-type Ca^{2+} current ($I_{Ca,L}$) is found in all cardiac cell types and is responsible for the generation of the action potential upstroke (phase 0) in SAN and AVN cells [22, 24, 57]. It activates rapidly upon depolarisation (but not as quickly as the sodium channel current, I_{Na}). In other cells, it contributes to the plateau phase and is responsible for the spike and dome appearance of the action potential. It also regulates excitation-contraction coupling by inducing Ca^{2+} release from the sarcoplasmic reticulum (SR). It has three modes of operation [24, 57]. Mode 1 is characterised by bursts of short repetitive openings and closures, with long closures between bursts [24, 57]. Mode two is characterised by longer opening times and occurs in the presence of dihydropyridine agonists or following β–reception stimulation [24, 57]. Mode 3 corresponds to the inactivated state of the channel and has either no openings or opens infrequently [24, 57].

The L-type Ca^{2+} channel shows two types of inactivation process: voltage-dependent inactivation and calcium-induced inactivation, which is dependent on the intracellular Ca^{2+} concentration $[Ca^{2+}]_i$ [24, 57]. Ca^{2+}-induced inactivation enhances the amplitude of $[Ca^{2+}]_i$, which in turn increases the rate of inactivation. This then limits further Ca^{2+} influx thereby preventing Ca^{2+} overload of the cell.

Recovery from inactivation is also both voltage-dependent and dependent on $[Ca^{2+}]_i$ [57].

The channel shows a high selectivity for Ca^{2+} but a very low selectivity for K^+ [60–62]. Despite the low selectivity of K^+ by the channel, K^+ can still contribute a substantial amount of current through this channel. This is due to higher intracellular concentration of K^+ compared to Ca^{2+}. This also explains the lower reversal potential of $I_{Ca,L}$ compared to the theoretical equilibrium potential of Ca^{2+} ions [57].

1.6.2 T-Type Calcium Channel

T-type calcium channel current ($I_{Ca,T}$) is found in the SAN, AVN, atrial and Purkinje cells [22, 24, 57]. Its threshold of activation is about −70 to −50 mV (lower than that for $I_{Ca,L}$). Like $I_{Ca,L}$, it activates rapidly upon depolarisation (but not as quickly as I_{Na}) and it also shows faster inactivation than $I_{Ca,L}$. It therefore contributes only to early phases of the action potential. It is also thought to play a role in late pacemaker depolarisation [63, 64].

1.7 Potassium Channels

Potassium (K^+) channels can be functionally subdivided into voltage-dependent (or voltage-activated) K^+ channels (channels responsible for I_{to}, I_{Kr}, I_{Ks}, I_{Kur}) and the inward-rectifying K^+ channels (channels responsible for I_{K1}, $I_{K,ATP}$, $I_{K,ACh}$). $I_{K,ATP}$ and $I_{K,ACh}$ are ligand- gated or ligand-activated K^+ channel currents [19, 20, 22, 24, 57]. Under normal physiological conditions, K^+ channels play an important role in shaping the action potential, particularly the voltage-gated channels. This is because the cell membrane resting potential is greater than the equilibrium potential of K^+ ions resulting in a net outward current, which serves to repolarise the cell membrane during an AP or (in the case of I_{K1}) help maintain a stable resting potential.

1.7.1 Voltage-Dependent K^+ Channels

Table 1.1 shows the voltage-gated K^+ currents in the heart and some of their properties. The main channels are: the transient outward K^+ currents (fast and slow), the rapid (I_{Kr}), slow (I_{Ks}) and ultra-rapid (I_{Kur})-delayed rectifier outward K^+ currents. These currents play a significant role in the morphology of the action potential [19, 20, 22, 24, 57].

Table 1.1 Voltage-gated K^+ currents/channels in the human heart

Current	Activation	Inactivation	Tissue
$I_{to,f}$	Fast	Fast	Atrium, Ventricle, Purkinje fibres, SAN
$I_{to,s}$	Slow	Slow	Atrium, Ventricle, SAN
I_{Kr}	Moderate	Fast	Atrium, Ventricle, Purkinje fibres, SAN
I_{Ks}	Very slow	None	Atrium, Ventricle, Purkinje fibres, SAN
I_{Kur}	Fast	None	Atrium

1.7.1.1 The Transient Outward Current (I_{to})

There are two types of transient outward current. I_{to} (also known as I_{to1}) is a K^+ current while the second type, I_{to2} is a Ca^{2+}-activated Cl^- current [22, 24, 57]. I_{to1} has both fast $I_{to,f}$ and slow $I_{to,s}$ components with the fast component being the primary subtype expressed in the human atrium. Both components are expressed in the human ventricle. Henceforth, any reference to I_{to} is a reference to I_{to1}. I_{to} is found in all cell types including the SAN and AVN. Its major contribution is to phase 1 (early repolarisation phase) of the action potential [19, 20, 22, 24, 57].

Different parts of the heart show different expression of I_{to}. Thus, I_{to} shows a greater density in the right ventricle than the left ventricle [22, 24, 57, 65, 66]. Hence, the notch in phase 1 is more pronounced in the right ventricle [65–67]. There is also a difference in the transmural expression of I_{to} across the ventricular myocardium; it has a greater density in the mid-myocardial cells than either the endodcardial or epicardial cells [22, 24, 57].

Activation of I_{to} occurs by depolarisation and is a fast process [68]. Inactivation and recovery from inactivation are also fast with recovery from inactivation being sensitive to voltage [68]. The greater the hyperpolarisation, the faster is the recovery from inactivation.

1.7.1.2 The Slowly-Activated Delayed Outward Rectifier Current (I_{Ks})

In the human heart, I_{Ks} has been found in all cell types including the atrial and ventricular cells [22, 24, 57]. It is differentially expressed across the ventricular wall with the lowest density being in the mid-myocardial cells [69–72]. Its density in the epicardial and endocardial cells far exceeds its density in the mid-myocardial cells [22, 24, 57]. It thus contributes to the transmural dispersion of the action potential duration (APD) across the ventricular wall. It shows activation but no inactivation and is important for regulating the APD. Activation is slow but deactivation is (comparatively) fast [70, 71, 73, 74]. It contributes to phase 3 of the AP where it serves to repolarise the cell back to its resting potential following a depolarisation. The channel is very selective to K^+ ions (although less so than I_{Kr}) and is largely carried by K^+ ions [70, 71, 73, 74]. The fully-activated current-voltage relation approaches linearity [70, 71, 73, 74].

1.7.1.3 The Rapidly-Activated Delayed Outward Rectifier Current (I_{Kr})

In the human heart, I_{Kr} has been found in all cell types including the atrial and ventricular cells [22, 24, 57]. It is differentially expressed across the ventricular wall with the highest density of its pore-forming transcript being in the epicardial cells [75]. Its transcript density in epicardial cells exceeds that in the mid-myocardium by approximately 60 % [75]. It thus contributes to the transmural dispersion of the APD across the ventricular wall. It shows slow activation but fast and profound inactivation and is important for regulating the action potential duration [76–79]. Activation is moderately fast but deactivation is slow. It contributes to phase 3 of the AP where it serves to repolarise the cell back to its resting potential following a depolarisation. The channel is very selective to K^+ ions (more so than I_{Ks} but less than I_{K1}) and is largely carried by K^+ ions.

1.7.1.4 The Ultrarapidly-Activated Delayed Outward Rectifier Current (I_{Kur})

In the human heart, I_{Kur} is found in atrial cells but not in the ventricles [80–82] and contributes to the shorter APD in the atria, SAN and AVN cells [22, 24, 57]. It shows fast activation (faster than I_{Kr} and I_{Ks}) and little inactivation [22, 24, 57]. Its fully-activated I–V relation shows outward rectification. Its recovery from inactivation is slow, and at high stimulation rates, its density is reduced [24].

1.7.2 Inward Rectifier Potassium Channels

1.7.2.1 The Inward Rectifier K^+ Current (I_{K1})

I_{K1} is absent in the SAN but highly expressed in ventricular and purkinje cells but less so in atrial cells [22, 24, 57]. In the atria, it is still sufficiently expressed to produce a stable resting potential [22, 24, 57]. The channel is able to carry a substantial amount of current at negative potentials but little outward current at potentials more positive than ~ -40 mV. It also shows strong inward rectification with a region of negative slope, allowing it to contribute to the maintenance of a stable resting potential (protection form pacemaker activity) without generating excessive repolarising current during the plateau phase or phases 0 and 1. The channel thus plays an important role during the plateau phase and in the final repolarisation portion of phase 3 [22, 24, 57]. Of all the K^+ channels, it has the highest selectivity for K^+ ions [24, 57].

1.7.2.2 Acetylcholine-Activated K^+ Channel ($I_{K,Ach}$)

$I_{K,Ach}$ is highly expressed in the SAN, AVN and atria cells but has low expression in the ventricle [22, 24, 57]. Its activation by acetylcholine results in a weakly inward-rectifying K^+ current (inward rectification is weaker than that for I_{K1}) that hyperpolarises the cell and shortens the APD. It is activated when acetylcholine binds to the M2 muscarinic receptor, which is coupled to the K^+ channel via the guanine nucleotide binding protein (G protein) [22, 24, 57]. It deactivates on depolarisation but incompletely.

1.7.2.3 ATP-Senstitve K^+ Channel ($I_{K,ATP}$)

$I_{K,ATP}$ is expressed abundantly in all regions of the heart including ventricular, atrial, SAN and AVN cells [22, 24, 57]. It is activated according to the intracellular ratio of ADP to ATP, i.e., [ADP]:[ATP]. This ratio is increased during ischaemia by energy depletion. It consequently protects the heart by shortening the APD, reducing excitability and moving the membrane potential closer to the K^+ equilibrium potential. Channels for $I_{K,ATP}$ are very selective for K^+ ions [22, 24, 57].

1.8 Stretch-Activated Channels

A sequence of electrical excitation waves propagating in the heart trigger its mechanical contraction. This is known as excitation-contraction coupling [25, 57]. In response to changes in volume load or contractile function, the heart is able to regulate its cellular electrical activity [83–86]. This is commonly referred to as mechano-electric feedback [85, 87–89]. The stretch-related electrical activities that are regulated include prolongation [90–92] or shortening [93–96] of the AP, changes in AP morphology such as diastolic depolarisation [97, 98], premature excitation [95, 98, 99] and after-depolarisation [89, 95, 100]. These changes occur via the activation of stretch-activated channels (SACs). Additionally, stretch induces a rise in the amplitude of the intracellular Ca^{2+} concentration [91, 101–106]; a change that is related to contractile force in the heart.

1.9 Cardiac Muscle Contraction

1.9.1 Cardiac Muscle Fibre

Cardiac muscle just like skeletal and smooth muscles is composed of fibres, which in turn are composed of successively smaller subunits. The typical organisation of muscle fibres is shown in Fig. 1.13. The cell membrane of the muscle fibres is

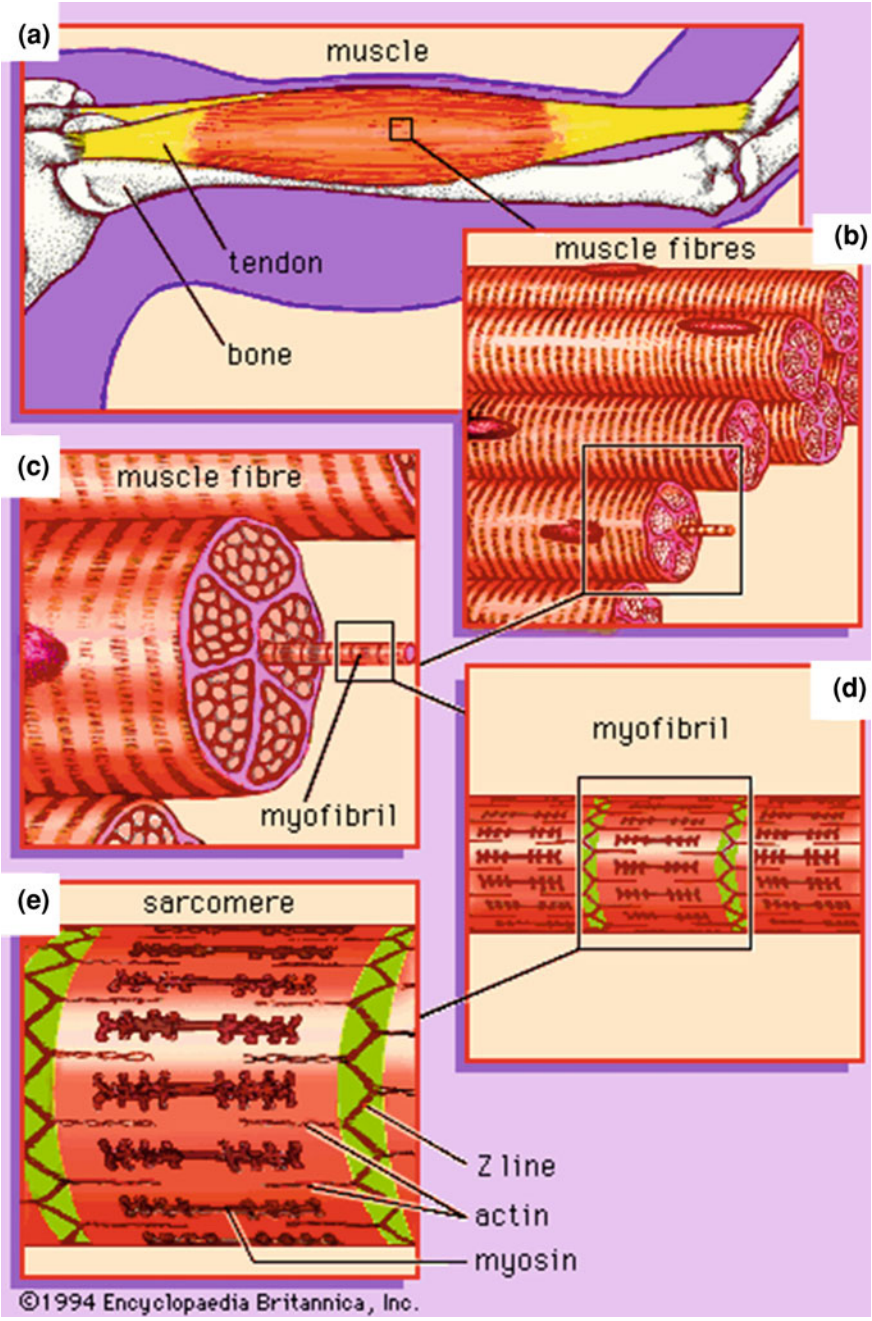
(a)
muscle
tendon
bone
muscle fibres
(b)
(c)
muscle fibre
myofibril
(d)
myofibril
(e)
sarcomere
Z line
actin
myosin
©1994 Encyclopaedia Britannica, Inc.

◀ **Fig. 1.13** The structure of striated muscle Striated muscle tissue, such as the tissue of the human heart and biceps muscle, consists of long, fine fibres (**a**, **b**), each of which is in effect a bundle of finer myofibrils (**c**, **d**). Within each myofibril are filaments of the proteins myosin and actin (**e**); these filaments slide past one another as the muscle contracts and expands. On each myofibril, regularly occurring dark bands, called Z lines, can be seen where actin and myosin filaments overlap. The region between two Z lines is called a sarcomere; sarcomeres can be considered the primary structural and functional unit of muscle tissue [108]

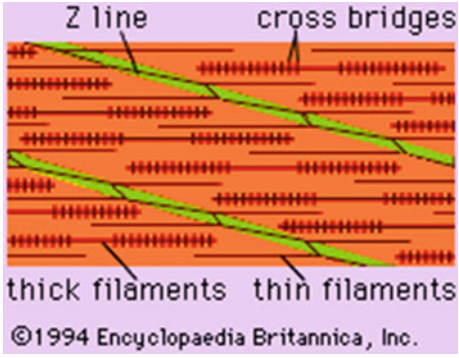

Fig. 1.14 The arrangement of the myofilaments in obliquely striated muscle [109]

called the sarcolemma. It consists of two parts; an inner plasma membrane (sometimes called the true membrane) and an outer membrane made up of numerous thin collagen fibrils [19, 57, 107].

1.9.1.1 Myofibrils; Actin and Myosin Filaments

Each muscle fibre (Fig. 1.13b) consists of thousands of myofibrils clustered in groups (Fig. 1.13c). Each myofibril in turn consists of thousands of thick myosin and thin actin filaments lying adjacent to each other (Fig. 1.13d, e); these are responsible for muscle contraction. The ends of the actin filaments are embedded in a structure called the Z-line or Z-disc (Fig. 1.13e) from which the actin filaments extend in both directions, interlocking with the myosin filaments. The part of the myofibril that lies between two Z-lines is called the sarcomere.

Projecting from the sides of the myosin filaments are cross-bridges (Fig. 1.14). It is the interaction between the crossbridges and the actin filaments that causes contraction [19, 25, 107]. The Z-disc or Z-line traverses the myofibril crosswise and also traverses crosswise from myofibril to myofibril and in doing so, attaches each myofibril to the other, hence, the clustered groups of myofibrils seen in Fig. 1.13b, c. The oblique traversal of the Z-line across the muscle fibre results in light and dark bands, which gives cardiac and skeletal muscle a striated appearance [19, 25, 107] (Fig. 1.14).

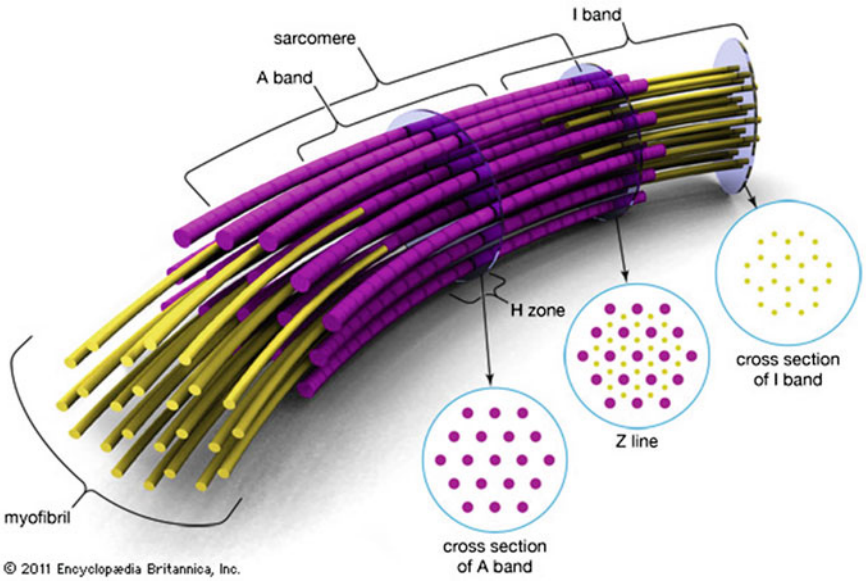

Fig. 1.15 A cross section of a muscle fibre [110]

Figure 1.13e shows that the actin and myosin filaments overlap and interlock. This gives rise to light and dark bands on the myofibril just as the Z-line results in light and dark bands across the muscle fibre. The light bands contain only actin filaments and due to being isotropic to polarised light are called *I bands* [19, 25, 107] (Fig. 1.15). The dark bands are called *A bands* because they are anisotropic to polarised light [19, 25, 107]. They consist of myosin filaments and the ends where the actin filaments overlap the myosin filaments. The *H zone* is the portion of the *A band* where the actin and myosin filaments do not overlap [19, 25, 107].

Figure 1.16 shows a myofibril in a relaxed and contracted state. On contraction, the sarcomere length (the portion between two successive Z-lines) is approximately 2μm [25, 107]. At this length, the thin actin filaments are drawn much closer than shown in the bottom figure of Fig. 1.16. The maximum contractile force is also generated at this length [25, 107].

1.9.1.2 Sarcoplasm, Transverse Tubule and Sarcoplasmic Reticulum and the General Mechanism of Contraction

The intracellular space between the thousands of myofibrils making up a muscle fibre is filled with the fluid called sarcoplasm; it consists of large amounts of potassium, magnesium, phosphate and protein enzymes [19, 25, 107]. Mitochondria, which align themselves parallel to the fibre are also present in abundant

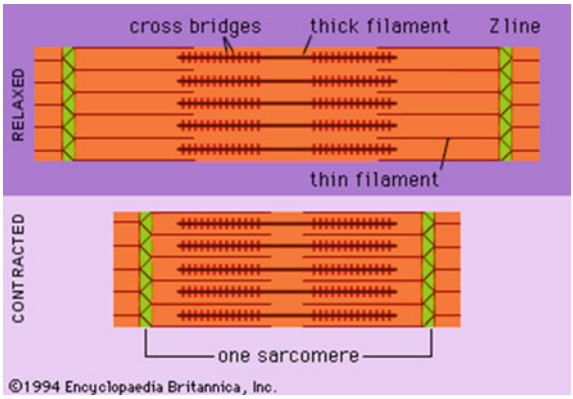

Fig. 1.16 Myofibril in relaxed and contracted states. The thin filaments (actin) in a relaxed non-contracted state (*top*) slide and overlap the thick myosin filaments (*bottom*) pulling the Z-lines towards each other. The thin actin filaments are able to completely overlap the thick myosin filaments [111]

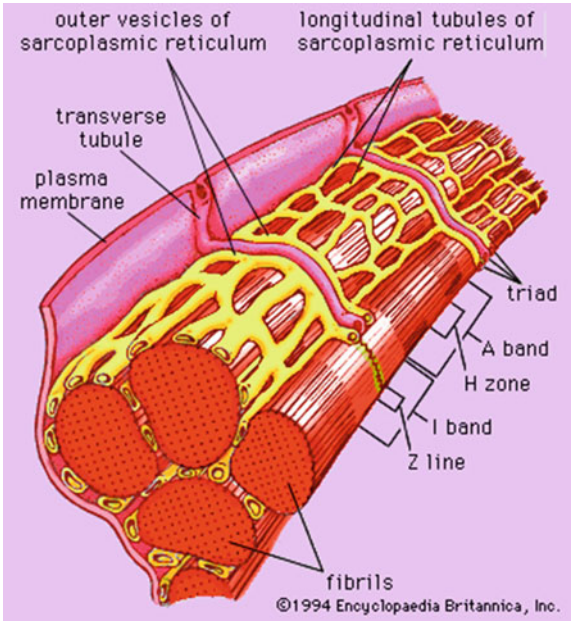

Fig. 1.17 Ultrastructure of a group of myofibrils, showing the sarcoplasmic reticulum and transverse tubules, which constitute the two membrane systems within a muscle fibre [112]

amounts. These serve the purpose of providing energy for the contracting myofibrils via the formation of adenosine triphosphate (ATP) [19, 25, 107].

The transverse tubule (T-tubule) originates from the cell membrane and traverses across the myofibrils from one side all the way across to the other [19, 25, 107] (Fig. 1.17). From its starting point at the cell membrane, it is open to the same extracellular fluid as the cell membrane, implying that the T-tubule is an extension of the cell membrane [19, 25, 107]. Thus an action potential spreading over a muscle fibre membrane causes potential changes that also spread through

the T-tubule to the interior of the muscle fibre. The resulting electrical excitation is what initiates muscle contraction [19, 25, 107].

The sarcoplasmic reticulum is shown in yellow in Fig. 1.17. It completely covers the surface of the myofibrils. It contains an excess of calcium ions. When the action potentials from the cell membrane reach the T-tubules, it causes the opening of the calcium ion channels of the sarcoplasmic reticulum terminals, which touch the T-tubules. The spread of electrical excitation consequently activates nearby calcium channels of the other parts of the sarcoplasmic reticulum. The T-tubules themselves contain calcium ions, which are also released into the sarcoplasm [19, 25, 107]. Calcium ions thus flow out of the sarcoplasmic reticulum into the sarcoplasm, diffuse into the myofibrils and catalyse the reactions that cause the sliding of the actin and myosin filaments along one another and cause muscle contraction [19, 25, 107].

As long as calcium ions remain in high concentration in the sarcoplasm, muscle contraction persists. However, pumps in the walls of the sarcoplasmic reticulum pump calcium ions back into it and in addition, calsequestrin, which is a protein in the sarcoplasmic reticulum also binds to some of the calcium ions. The end of phase 3 of the action potential (plateau phase) is approximately when the flow of calcium ions into the sarcoplasm ceases and is rapidly pumped back into the sarcoplasmic reticulum and the extracellular fluid space of the T-tubules. These mechanisms ensure that muscle contraction terminates and only restarts at the commencement of a new action potential.

1.9.2 Molecular Mechanism of Contraction

1.9.2.1 Myosin Filament

The thick myosin filament consists of multiple myosin molecules. Each myosin molecule (Fig. 1.18) consists of two heavy chains and four light chains. The two heavy chains wrap around each other in a double helix called the tail or rod. The end of each heavy chain is folded into a globular structure called a head. Thus, the myosin molecule consists of two heads. Each head contains two light chains making up the four aforementioned light chains [19, 25, 107].

The collection of multiples of the myosin molecules forms the myosin filament shown in the middle of Fig. 1.18. The heads of the myosin molecules protrude from the body of the myosin filament via rope-like arms. The arms together with the protruding heads are called cross-bridges [19, 25, 107]. The arms impart the flexibility that allows the heads to be extended far away from the body of the myosin filament or drawn closer to it. The point where the arm attaches to the head also allows movement of the head enabling it to participate in the contraction process [19, 25, 107].

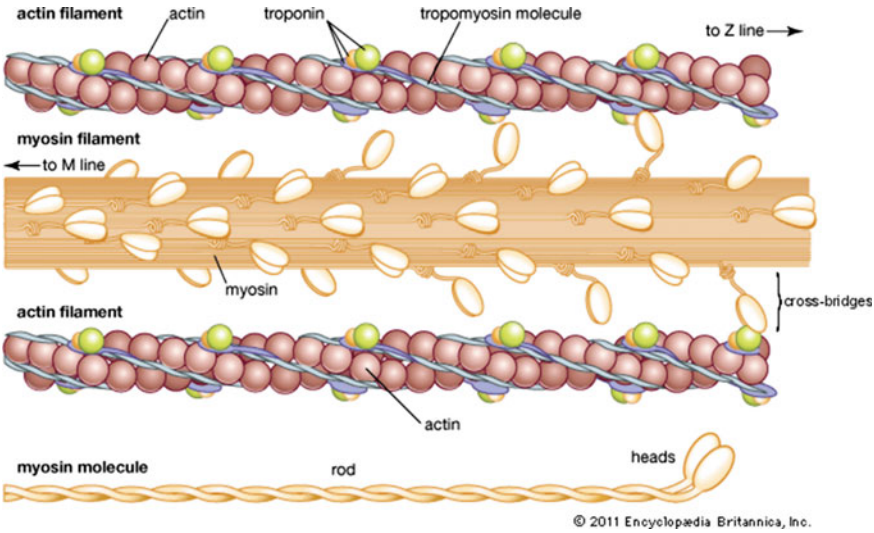

Fig. 1.18 The structure of actin and myosin filaments [113]

1.9.2.2 Actin Filament

Figure 1.18 shows the myosin filament interacting on both sides with two actin filaments. The actin filament consists of three protein components: actin, tropomyosin and troponin [19, 25, 107]. The actin protein molecule consists of other proteins that enable it to carry one molecule of adenosine diphosphate (ADP), which are believed to be the sites on the actin filament with which the cross-bridges on the myosin filament interact to cause contraction [19, 25, 107]. These ADP sites are staggered across the actin filament.

The tropomyosin constituent (shown in blue in Fig. 1.18) of the actin filament wraps around the actin protein constituent. It covers the active ADP sites of the actin filament in the resting state, so that interaction between the actin and myosin filaments cannot occur, consequently hindering contraction [19, 25, 107].

Attached at intermittent intervals to the tropomyosin protein is troponin, which itself is a complex of three loosely bound protein subunits; Troponin I which binds strongly with actin, Troponin T with a high affinity for tropomyosin and Troponin C which binds strongly with calcium ions [19, 25, 107]. The troponin complex attaches tropomyosin to actin and its strong binding with calcium ions initiates the contraction process [19, 25, 107].

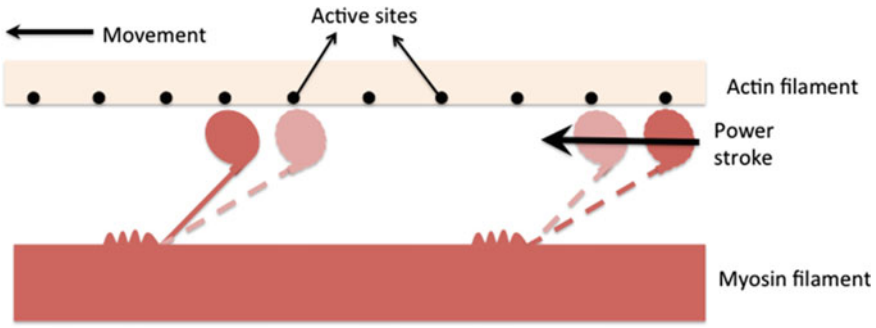

Fig. 1.19 "Walk-along" mechanism for muscle contraction

1.9.2.3 Cross-Bridge Cycling or The "Walk-Along" Theory of Contraction

In the presence of the troponin-tropomyosin complex, contraction is inhibited because the tropomyosin protein covers the active ADP sites on the actin filament. The role of the calcium ions is to remove the inhibitory effect of the troponin-tropomyosin complex [25, 107]. It is believed that the binding of troponin C with calcium ions makes the troponin complex undergo a conformational change which drags the tropomyosin deeper into the recesses between the actin strands, thus uncovering the active ADP sites [25, 107]. Once uncovered, the actin filament binds strongly with the cross-bridges on the myosin filament permitting contraction to proceed.

The precise mechanism by which the binding of the actin filament with the myosin filament leads to contraction is still a subject of much research but a hypothesis with considerable evidence is "cross-bridge cycling" or the "walk-along" or "ratchet" theory of contraction [25, 107]. This idea is depicted in Fig. 1.19 with two myosin heads attaching to and disengaging from the active ADP sites of an actin filament. It is postulated that when a myosin head attaches to an active site, profound changes in the intermolecular forces between the myosin head and its arm occur (i.e., within the cross-bridge). These forces cause the myosin head to incline towards the active site, attach to it and with the force of inclination, to drag the actin filament forwards. This tilt of the head is known as the *power stroke*. Once complete, the myosin head unfastens from the active site and extends back to its original angle, whence it attaches again to the next active site farther down the actin filament and drags that forward with another power stroke. As this cycle continues, the ends of two successive actin filaments are moved towards the center of the myosin filament. The cross-bridges are thought to work independently of one another in carrying out this power stroke cycle implying that the greater the number of cross-bridges attached to the actin filament active sites, the greater, theoretically, the force of contraction [25, 107].

1.9.2.4 The Source of Energy for Contraction: ATP

Muscle contraction requires energy and ATP is the source of this energy. When contraction occurs, ATP is broken down into ADP and phosphate ions. The greater the amount of work carried out by the muscle, the greater the amount of ATP that is broken down. This phenomenon is known as the Fenn Effect [107, 114, 115].

The process involved in obtaining the energy for contraction is thought to be as follows:

1. An additional characteristic of the myosin head is that it acts as an ATPase enzyme, which breaks down ATP into ADP and a phosphate ion. It does this prior to the commencement of contraction when the cross-bridges bind to ATP. The ADP and phosphate ion are left on the myosin head, which extends towards the active site on the actin filament but does not yet bind to it [25, 107].
2. When calcium ions are released into the sarcoplasm from the sarcoplasmic reticulum and the T-tubules, the troponin-tropomyosin complex binds to the calcium ions leaving the active sites on the actin filament uncovered. This allows the myosin head to attach to the active site [25, 107].
3. The energy stored from the break down of ATP in step 1 is then used by the head of the bound cross-bridge to generate the power stroke that allows the myosin head to move the actin filament towards the center of the myosin filament [25, 107] (see Sect. 1.9.2.3).
4. Once the myosin head tilts and drags the actin filament forward, the ADP and phosphate ion are released from it. Another ATP molecule then attaches to the now empty ADP site. This ATP binding causes the detachment of the myosin head from the actin filament [25, 107].

Steps 1–4 are then repeated again and again until the Z-line is pulled up against the ends of the myosin filament or until the load on the muscle becomes too great for further pulling to occur [25, 107].

References

1. Lehnart SE, Ackerman MJ, Benson DW Jr, Brugada R, Clancy CE, Donahue JK et al (2007) Inherited arrhythmias: a National Heart, Lung, and Blood Institute and Office of Rare Diseases workshop consensus report about the diagnosis, phenotyping, molecular mechanisms, and therapeutic approaches for primary cardiomyopathies of gene mutations affecting ion channel function. Circulation 116(20):2325–2345
2. London B, Michalec M, Mehdi H, Zhu X, Kerchner L, Sanyal S et al (2007) Mutation in glycerol-3-phosphate dehydrogenase 1 like gene (GPD1-L) decreases cardiac Na + current and causes inherited arrhythmias. Circulation 116(20):2260–2268
3. Skinner JR, Chung S-K, Montgomery D, McCulley CH, Crawford J, French J et al (2005) Near-miss SIDS due to Brugada syndrome. Arch Dis Child 90(5):528–529
4. Arnestad M, Crotti L, Rognum TO, Insolia R, Pedrazzini M, Ferrandi C et al (2007) Prevalence of long-QT syndrome gene variants in sudden infant death syndrome. Circulation 115(3):361–367

5. Gaita F, Giustetto C, Bianchi F, Wolpert C, Schimpf R, Riccardi R et al (2003) Short QT syndrome: a familial cause of sudden death. Circulation 108(8):965–970
6. Wu Y, MacMillan LB, McNeill RB, Colbran RJ, Anderson ME (1999) CaM kinase augments cardiac L-type Ca2 + current: a cellular mechanism for long Q-T arrhythmias. Am J Physiol 276(6 Pt 2):H2168–H2178
7. Lahat H, Pras E, Olender T, Avidan N, Ben-Asher E, Man O et al (2001) A missense mutation in a highly conserved region of CASQ2 is associated with autosomal recessive catecholamine-induced polymorphic ventricular tachycardia in Bedouin families from Israel. Am J Hum Genet 69(6):1378–1384
8. Hancox JC, McPate MJ, Harchi A, Duncan RS, Dempsey CE, Witchel HJ et al (2011) The short QT syndrome. In: Tripathi ON, Ravens U, Sanguinetti MC (eds) Heart rate and rhythm [Internet]. Springer, Heidelberg, pp 431–49. Available from: http://www.springerlink.com/content/m8l86l8n3h81w43m/
9. Anttonen O, Junttila J, Giustetto C, Gaita F, Linna E, Karsikas M et al (2009) T-Wave morphology in short QT syndrome. Ann Noninvasive Electrocardiol 14(3):262–267
10. Kramer DB, Zimetbaum PJ (2011) Long-QT syndrome. Cardiol Rev 19(5):217–225
11. Zareba W, Cygankiewicz I (2008) Long QT syndrome and short QT syndrome. Prog Cardiovasc Dis 51(3):264–278
12. Modell SM, Lehmann MH (2006) The long QT syndrome family of cardiac ion channelopathies: a HuGE review. Genet Med 8(3):143–155
13. Giudicessi JR, Ackerman MJ (2012) Potassium-channel mutations and cardiac arrhythmias|[mdash]|diagnosis and therapy. Nature Reviews Cardiology Available from: http://www.nature.com/nrcardio/journal/vaop/ncurrent/full/nrcardio.2012.3.html
14. Ghuran AV, Camm AJ (2001) Ischaemic heart disease presenting as arrhythmias. Br Med Bull 59(1):193–210
15. Sedlis SP (1992) Mechanisms of ventricular arrhythmias in acute ischemia and reperfusion. Cardiovasc Clin 22(1):3–18
16. Roden DM (2001) Pharmacogenetics and Drug-Induced Arrhythmias. Cardiovasc Res 50(2):224–231
17. Kindermann W (2006) Cardiovascular side effects of anabolic-androgenic steroids. Herz 31(6):566–573
18. Plonsey R, Barr RC (2007) Bioelectricity: a quantitative approach. 3rd ed. Springer, New York
19. Katz A (2010) Physiology of the heart. Fifth. Lippincott Williams & Wilkins, Philadelphia
20. Hille B (2001) Ion channels of excitable membranes. 3rd ed. Sinauer Associates, New York
21. Hoffmann B, Cranefield P (1960) Electrophysiology of the heart. McGraw-Hill, New York
22. Grant AO (2009) Cardiac ion channels. Circ Arrhythm Electrophysiol 2(2):185–194
23. Jalife J, Delmar M, Anumonwo J, Berenfeld O, Kalifa J (2009) Basic cardiac electrophysiology for the clinician. 2nd ed. Wiley-Blackwell, Oxford
24. Carmeliet E, Vereecke J (2002) Cardiac cellular electrophysiology. 1st ed. Springer, New York
25. Bonow RO, Mann DL, Zipes DP, Libby P (2011) Braunwald's heart disease: a textbook of cardiovascular medicine, 2-volume set: expert consult premium edition—enhanced online features and print, 9e (Heart Disease (Braunwald). 9th ed. Saunders
26. Verkerk AO, Wilders R, van Borren MMGJ, Peters RJG, Broekhuis E, Lam K et al (2007) Pacemaker current (I(f)) in the human sinoatrial node. Eur Heart J 28(20):2472–2478
27. Boyett MR, Tellez JO, Dobrzynski H (2009) Chap 12: The sinoatrial node: its complex structure and unique ion channel gene program. In: Zipes DP, Jalife J (eds) Cardiac electrophysiology: from cell to bedside. 5th ed. Philadelphia, Saunders, Elsevier Science, pp 127–38
28. Heart: electrical impulses from pacemaker, Art, from Encyclopædia Britannica Online, accessed March 2, 2012, http://www.britannica.com/EBchecked/media/64469/Electrical-conduction-in-the-heart-in-healthy-individuals-is-controlled

29. Li D, Zhang L, Kneller J, Nattel S (2001) Potential ionic mechanism for repolarization differences between canine right and left atrium. Circ Res 88(11):1168–1175
30. Ramirez RJ, Nattel S, Courtemanche M (2000) Mathematical analysis of canine atrial action potentials: rate, regional factors, and electrical remodeling. Am J Physiol Heart Circ Physiol 279(4):H1767–H1785
31. Aslanidi OV, Colman MA, Stott J, Dobrzynski H, Boyett MR, Holden AV et al (2011) 3D virtual human atria: a computational platform for studying clinical atrial fibrillation. Prog Biophys Mol Biol 107(1):156–168
32. Courtemanche M, Ramirez RJ, Nattel S (1998) Ionic mechanisms underlying human atrial action potential properties: insights from a mathematical model. Am J Physiol 275(1 Pt 2):H301–H321
33. Inada S, Hancox JC, Zhang H, Boyett MR (2009) One-dimensional mathematical model of the atrioventricular node including atrio-nodal, nodal, and nodal-his cells. Biophys J 97(8):2117–2127
34. Stewart P, Aslanidi OV, Noble D, Noble PJ, Boyett MR, Zhang H (2009) Mathematical models of the electrical action potential of Purkinje fibre cells. Philos Transact A Math Phys Eng Sci 367(1896):2225–2255
35. Lee F-Y, Wei J, Wang J-J, Liu H, Shih T, Lin C-I (2004) Electromechanical properties of Purkinje fiber strands isolated from human ventricular endocardium. J Heart Lung Transplant 23(6):737–744
36. Antzelevitch C (2010) M cells in the human heart. Circ Res 106(5):815–817
37. Drouin E, Charpentier F, Gauthier C, Laurent K, Le Marec H (1995) Electrophysiologic characteristics of cells spanning the left ventricular wall of human heart: evidence for presence of M cells. J Am Coll Cardiol 26(1):185–192
38. ten Tusscher KHWJ, Panfilov AV (2006) Alternans and spiral breakup in a human ventricular tissue model. Am J Physiol Heart Circ Physiol 291(3):H1088–H1100
39. Molecular view of the cell membrane, Art, from Encyclopædia Britannica Online, accessed March 2, 2012, http://www.britannica.com/EBchecked/media/45550/Intrinsic-proteins-penetrate-and-bind-tightly-to-the-lipid-bilayer
40. Nernst W (1888) Zur Kinetik der in Lösung befindlichen Körper. Z Phys Chem 2:613–37
41. Lei M, Zhang H, Grace AA, Huang CL-H (2007) SCN5A and sinoatrial node pacemaker function. Cardiovasc Res 74(3):356–365
42. Lei M, Huang CL-H, Zhang Y (2008) Genetic Na + channelopathies and sinus node dysfunction. Prog Biophys Mol Biol 98(2–3):171–178
43. Kodama I, Nikmaram MR, Boyett MR, Suzuki R, Honjo H, Owen JM (1997) Regional differences in the role of the Ca2 + and Na + currents in pacemaker activity in the sinoatrial node. Am J Physiol Heart Circ Physiol 272(6):H2793–H2806
44. Schwartz PJ, Priori SG, Locati EH, Napolitano C, Cantù F, Towbin JA et al (1995) Long QT syndrome patients with mutations of the SCN5A and HERG genes have differential responses to Na + channel blockade and to increases in heart rate. Implications Gene-specific Ther Circulation 92(12):3381–3386
45. Witchel HJ, Hancox JC (2000) Familial and acquired long qt syndrome and the cardiac rapid delayed rectifier potassium current. Clin Exp Pharmacol Physiol 27(10):753–766
46. Meregalli PG, Wilde AAM, Tan HL (2005) Pathophysiological mechanisms of Brugada syndrome: depolarization disorder, repolarization disorder, or More? Cardiovasc Res 67(3):367–378
47. Smits JPP, Veldkamp MW, Wilde AAM (2005) Mechanisms of inherited cardiac conduction disease. Europace 7(2):122–137
48. Schott JJ, Alshinawi C, Kyndt F, Probst V, Hoorntje TM, Hulsbeek M et al (1999) Cardiac conduction defects associate with mutations in SCN5A. Nat Genet 23(1):20–21
49. Clancy CE, Kass RS (2005) Inherited and acquired vulnerability to ventricular arrhythmias: cardiac Na + and K + channels. Physiol Rev 85(1):33–47
50. Kass RS, Moss AJ (2003) Long QT syndrome: novel insights into the mechanisms of cardiac arrhythmias. J Clin Invest 112(6):810–815

51. Dumaine R, Wang Q, Keating MT, Hartmann HA, Schwartz PJ, Brown AM et al (1996) Multiple mechanisms of Na + channel–linked long-QT syndrome. Circ Res 78(5):916–924
52. Antzelevitch C (2006) Brugada syndrome. Pacing Clin Electrophysiol 29(10):1130–1159
53. Chen P-S, Priori SG (2008) The Brugada syndrome. J Am Coll Cardiol 51(12):1176–1180
54. Vorobiof G, Kroening D, Hall B, Brugada R, Huang D (2008) Brugada syndrome with marked conduction disease: dual implications of a SCN5A mutation. Pacing Clin Electrophysiol 31(5):630–634
55. Takehara N, Makita N, Kawabe J, Sato N, Kawamura Y, Kitabatake A et al (2004) A cardiac sodium channel mutation identified in Brugada syndrome associated with atrial standstill. J Intern Med 255(1):137–142
56. McNair WP, Ku L, Taylor MRG, Fain PR, Dao D, Wolfel E et al (2004) SCN5A mutation associated with dilated cardiomyopathy, conduction disorder, and arrhythmia. Circulation 110(15):2163–2167
57. Bers D (2001) Excitation-contraction coupling and cardiac contractile force. 2nd ed. Springer, New York
58. Splawski I, Timothy KW, Decher N, Kumar P, Sachse FB, Beggs AH, et al (2005) Severe arrhythmia disorder caused by cardiac L-type calcium channel mutations. Proc Natl Acad Sci USA 102(23):8089–8096; discussion 8086–8088
59. Antzelevitch C, Pollevick GD, Cordeiro JM, Casis O, Sanguinetti MC, Aizawa Y et al (2007) Loss-of-function mutations in the cardiac calcium channel underlie a new clinical entity characterized by ST-segment elevation, short QT intervals, and sudden cardiac death. Circulation 115(4):442–449
60. Varadi G, Strobeck M, Koch S, Caglioti L, Zucchi C, Palyi G (1999) Molecular elements of ion permeation and selectivity within calcium channels. Crit Rev Biochem Mol Biol 34(3):181–214
61. Yang J, Elllnor PT, Sather WA, Zhang J-F, Tsien RW (1993) Molecular determinants of Ca2 + selectivity and ion permeation in L-type Ca2 + channels., Published online: 11 November 1993; | doi:10.1038/366158a0. 366(6451):158–61
62. Sather WA, McCleskey EW (2003) Permeation and selectivity in calcium channels. Annu Rev Physiol 65:133–159
63. Hagiwara N, Irisawa H, Kameyama M (1988) Contribution of two types of calcium currents to the pacemaker potentials of rabbit sino-atrial node cells. J Physiol (Lond.) 395:233–253
64. Zhou Z, Lipsius SL (1994) T-type calcium current in latent pacemaker cells isolated from cat right atrium. J Mol Cell Cardiol 26(9):1211–1219
65. Volders PGA, Sipido KR, Carmeliet E, Spätjens RLHMG, Wellens HJJ, Vos MA (1999) Repolarizing K + Currents ITO1 and IKs are larger in right than left canine ventricular Midmyocardium. Circulation 99(2):206–210
66. Diego JMD, Cordeiro JM, Goodrow RJ, Fish JM, Zygmunt AC, Pérez GJ et al (2002) Ionic and Cellular Basis for the Predominance of the Brugada Syndrome Phenotype in Males. Circulation 106(15):2004–2011
67. Verkerk AO, Wilders R, Schulze-Bahr E, Beekman L, Bhuiyan ZA, Bertrand J et al (2005) Role of sequence variations in the human ether-a-go-go-related gene (HERG, KCNH2) in the Brugada syndrome. Cardiovasc Res 68(3):441–453
68. Patel SP, Campbell DL (2005) Transient outward potassium current, “Ito”, phenotypes in the mammalian left ventricle: underlying molecular, cellular and biophysical mechanisms. J Physiol (Lond) 569(Pt 1):7–39
69. Zeng J, Laurita KR, Rosenbaum DS, Rudy Y (1995) Two components of the delayed rectifier K + current in ventricular myocytes of the guinea pig type. Theoretical formulation and their role in repolarization. Circ Res 77(1):140–152
70. Viswanathan PC, Shaw RM, Rudy Y (1999) Effects of IKr and IKs heterogeneity on action potential duration and its rate dependence: a simulation study. Circulation 99(18):2466–2474
71. Silva J, Rudy Y (2005) Subunit interaction determines IKs participation in cardiac repolarization and repolarization reserve. Circulation 112(10):1384–1391

72. Rudy Y, Silva JR (2006) Computational biology in the study of cardiac ion channels and cell electrophysiology. Q Rev Biophys 39(1):57–116
73. Osteen JD, Sampson KJ, Kass RS (2010) The cardiac IKs channel, complex indeed. Proc Natl Acad Sci USA 107(44):18751–18752
74. Jiang M, Xu X, Wang Y, Toyoda F, Liu X-S, Zhang M et al (2009) Dynamic partnership between KCNQ1 and KCNE1 and influence on cardiac IKs current amplitude by KCNE2. J Biol Chem 284(24):16452–16462
75. Szabó G, Szentandrássy N, Bíró T, Tóth BI, Czifra G, Magyar J et al (2005) Asymmetrical distribution of ion channels in canine and human left-ventricular wall: epicardium versus midmyocardium. Pflugers Arch 450(5):307–316
76. Hancox JC, Levi AJ, Witchel HJ (1998) Time course and voltage dependence of expressed HERG current compared with native "rapid" delayed rectifier K current during the cardiac ventricular action potential. Pflugers Arch 436(6):843–853
77. Hancox JC, Witchel HJ, Varghese A (1998) Alteration of HERG current profile during the cardiac ventricular action potential, following a pore mutation. Biochem Biophys Res Commun 253(3):719–724
78. Kiehn J, Lacerda AE, Brown AM (1999) Pathways of HERG inactivation. Am J Physiol 277(1 Pt 2):H199–H210
79. McPate MJ, Duncan RS, Milnes JT, Witchel HJ, Hancox JC (2005) The N588 K-HERG K + channel mutation in the "short QT syndrome": mechanism of gain-in-function determined at 37 degrees C. Biochem Biophys Res Commun 334(2):441–449
80. Feng J, Wible B, Li GR, Wang Z, Nattel S (1997) Antisense oligodeoxynucleotides directed against Kv1.5 mRNA specifically inhibit ultrarapid delayed rectifier K + current in cultured adult human atrial myocytes. Circ Res 80(4):572–579
81. Wang Z, Fermini B, Nattel S (1993) Sustained depolarization-induced outward current in human atrial myocytes. Evidence for a novel delayed rectifier K + current similar to Kv1.5 cloned channel currents. Circ Res 73(6):1061–1076
82. Amos GJ, Wettwer E, Metzger F, Li Q, Himmel HM, Ravens U (1996) Differences between outward currents of human atrial and subepicardial ventricular myocytes. J Physiol (Lond) 491(Pt 1):31–50
83. Franz MR (1996) Mechano-electrical feedback in ventricular myocardium. Cardiovasc Res 32(1):15–24
84. Lab MJ (1982) Contraction-excitation feedback in myocardium. Physiological basis and clinical relevance. Circ Res 50(6):757–766
85. Lab MJ (1996) Mechanoelectric feedback (transduction) in heart: concepts and implications. Cardiovasc Res 32(1):3–14
86. Youm JB, Han J, Kim N, Zhang Y-H, Kim E, Leem CH et al (2005) Role of stretch-activated channels in the heart: action potential and Ca2 + transients—mechanosensitivity in cells and tissues—NCBI Bookshelf. In: Kamkin A, Kiseleva I (eds) Academia, Moscow. [cited 2012 Sep 15]. Available from: http://www.ncbi.nlm.nih.gov/books/NBK7490/
87. Kohl P, Ravens U (2003) Cardiac mechano-electric feedback: past, present, and prospect. Prog Biophys Mol Biol 82(1–3):3–9
88. Kohl P, Sachs F (2001) Mechanoelectric feedback in cardiac cells. Phil Trans R Soc Lond A 359(1783):1173–1185
89. Hansen DE (1993) Mechanoelectrical feedback effects of altering preload, afterload, and ventricular shortening. Am J Physiol 264(2 Pt 2):H423–H432
90. Belus A, White E (2003) Streptomycin and intracellular calcium modulate the response of single guinea-pig ventricular myocytes to axial stretch. J Physiol (Lond) 546(Pt 2):501–509
91. Tavi P, Han C, Weckström M (1998) Mechanisms of stretch-induced changes in [Ca2 +]i in rat atrial myocytes: role of increased troponin C affinity and stretch-activated ion channels. Circ Res 83(11):1165–1177
92. Zeng T, Bett GC, Sachs F (2000) Stretch-activated whole cell currents in adult rat cardiac myocytes. Am J Physiol Heart Circ Physiol 278(2):H548–H557

93. Calkins H, el-Atassi R, Kalbfleisch S, Langberg J, Morady F (1992) Effects of an acute increase in atrial pressure on atrial refractoriness in humans. Pacing Clin Electrophysiol 15(11 Pt 1):1674–1680
94. Dean JW, Lab MJ (1989) Effect of changes in load on monophasic action potential and segment length of pig heart in situ. Cardiovasc Res 23(10):887–896
95. Franz MR, Burkhoff D, Yue DT, Sagawa K (1989) Mechanically induced action potential changes and arrhythmia in isolated and in situ canine hearts. Cardiovasc Res 23(3):213–223
96. Taggart P (1996) Mechano-electric feedback in the human heart. Cardiovasc Res 32(1):38–43
97. Boland J, Troquet J (1980) Intracellular action potential changes induced in both ventricles of the rat by an acute right ventricular pressure overload. Cardiovasc Res 14(12):735–740
98. Franz MR, Cima R, Wang D, Profitt D, Kurz R (1992) Electrophysiological effects of myocardial stretch and mechanical determinants of stretch-activated arrhythmias. Circulation 86(3):968–978
99. Stacy GP Jr, Jobe RL, Taylor LK, Hansen DE (1992) Stretch-induced depolarizations as a trigger of arrhythmias in isolated canine left ventricles. Am J Physiol 263(2 Pt 2):H613–H621
100. Lab MJ (1978) Mechanically dependent changes in action potentials recorded from the intact frog ventricle. Circ Res 42(4):519–528
101. Alvarez BV, Pérez NG, Ennis IL, Camilión de Hurtado MC, Cingolani HE (1999) Mechanisms underlying the increase in force and Ca(2 +) transient that follow stretch of cardiac muscle: a possible explanation of the Anrep effect. Circ Res 85(8):716–722
102. Gannier F, White E, Lacampagne A, Garnier D, Le Guennec JY (1994) Streptomycin reverses a large stretch induced increases in [Ca2 +]i in isolated guinea pig ventricular myocytes. Cardiovasc Res 28(8):1193–1198
103. Gannier F, White E (1996) Garnier, Le Guennec JY. A possible mechanism for large stretch-induced increase in [Ca2 +]i in isolated guinea-pig ventricular myocytes. Cardiovasc Res 32(1):158–167
104. Kentish JC, Wrzosek A (1998) Changes in force and cytosolic Ca2 + concentration after length changes in isolated rat ventricular trabeculae. J Physiol (Lond) 506(Pt 2):431–444
105. Le Guennec JY, White E, Gannier F, Argibay JA, Garnier D (1991) Stretch-induced increase of resting intracellular calcium concentration in single guinea-pig ventricular myocytes. Exp Physiol 76(6):975–978
106. White E, Le Guennec JY, Nigretto JM, Gannier F, Argibay JA, Garnier D (1993) The effects of increasing cell length on auxotonic contractions; membrane potential and intracellular calcium transients in single guinea-pig ventricular myocytes. Exp Physiol 78(1):65–78
107. PhD JEH (2010) Guyton and hall textbook of medical physiology: with STUDENT CONSULT Online Access, 12e. 12th ed. Saunders
108. Striated muscle: structure, Art, from Encyclopaedia Britannica Online, accessed February 27, 2012,http://www.britannica.com/EBchecked/media/46939/The-structure-of-striated-muscle-Striated-muscle-tissue-such-as
109. Myofilament: obliquely striated muscle, Art, from Encyclopædia Britannica Online, accessed February 27, 2012,http://www.britannica.com/EBchecked/media/2570/The-arrangement-of-the-myofilaments-in-obliquely-striated-muscle
110. Muscle fibre, Art, from Encyclopædia Britannica Online, accessed February 27, 2012,http://www.britannica.com/EBchecked/media/156378/A-cross-section-of-a-muscle-fibre
111. Myofilament: striated muscle, Art, from Encyclopædia Britannica Online, accessed February 27, 2012,http://www.britannica.com/EBchecked/media/2565/The-arrangement-of-the-myofilaments-in-a-striated-muscle
112. Transverse tubule: ultrastructure of myofibrils, Art, from Encyclopædia Britannica Online, accessed February 27, 2012,http://www.britannica.com/EBchecked/media/2568/Ultrastructure-of-a-group-of-myofibrils-showing-the-sarcoplasmic-reticulum

113. Muscle: actin and myosin, Art, from Encyclopædia Britannica Online, accessed February 27, 2012,http://www.britannica.com/EBchecked/media/46641/The-structure-of-actin-and-myosin-filaments
114. Brandt PW, Orentlicher M (1972) Muscle Energetics and the Fenn Effect. Biophys J 12(5):512–527
115. Podolsky RJ, Nolan AC (1973) Muscle contraction transients, Cross-bridge kinetics, and the fenn effect. Cold Spring Harb Symp Quant Biol 1(37):661–668

Chapter 2
Potassium Channels Implicated in the Short QT Syndrome

The work presented in this thesis centres on the in silico investigation of arrhythmia substrates in an inherited cardiac condition: the short QT syndrome (SQTS). Chapter 3 provides detailed background information on this syndrome (which consequently will be discussed only briefly here). The three variants of the SQTS examined in this thesis—SQT1, SQT2 and SQT3—involve gene mutations that affect proteins forming different potassium channels [1–6]. SQT1 affects the *hERG* channel, which is responsible for the rapid-delayed outward rectifier potassium current (I_{Kr}) [7–9], SQT2 affects the *KCNQ1* gene, which encodes the α-subunit of channels mediating slow-delayed outward rectifier potassium channel (I_{Ks}) [10]. SQT3 affects *KCNJ2*, which encodes the Kir2.1 protein that contributes to inwardly-rectifying potassium channel current (I_{K1}) [11]. Building upon the brief descriptions of these channels in Chap. 1, this chapter gives a detailed consideration of their structure and characteristics.

2.1 Rectification

In Sect. 1.3, it was established that the lipid bilayer of the cell membrane can be thought of as a capacitor that separates charges in the intracellular and extracellular regions. The charges separated are the ions in intracellular/extracellular fluid that can flow across the membrane through ion channels, when these are in a conducting state. The ion channels are thus resistors. Simple resistors follow Ohm's law:

$$V = IR \tag{2.1}$$

where V is the voltage (membrane potential), I is the current and R is the resistance. To describe the biophysical properties of ion channels during voltage clamp experiments, the conductance of the channels (inverse of resistance) is normally employed. If an ion channel has a linear current-voltage (I–V) relationship, i.e., the slope (conductance) is linear, the channel is said to show 'ohmic' behaviour (Fig. 2.1).

I. Adeniran, *Modelling the Short QT Syndrome Gene Mutations*,
Springer Theses, DOI: 10.1007/978-3-319-07200-5_2,

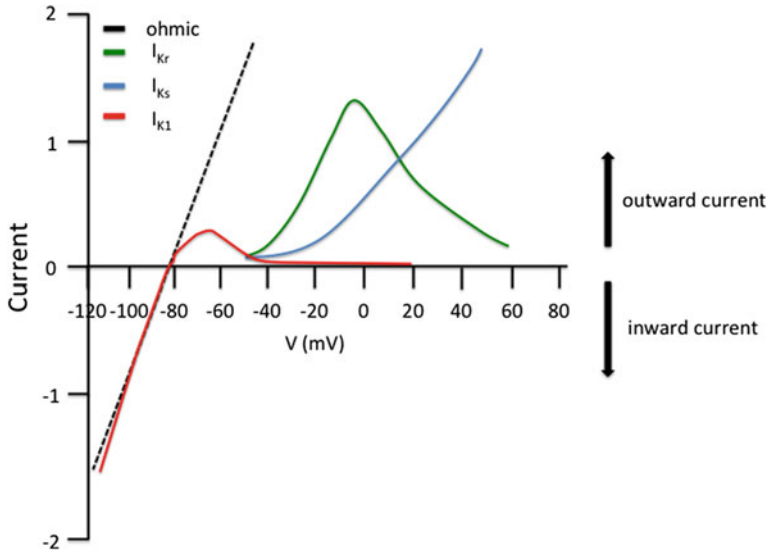

Fig. 2.1 Schematic representation of the I–V relationship for an ohmic channel and channels showing rectification. The black dashed line represents an ohmic channel with a linear I–V relationship. The green line shows the I–V relationship for I_{Kr}, which shows outward rectification. The blue line represents the I–V relationship for I_{Ks}, which also shows outward rectification and the red line represents I_{K1}, which is an inwardly rectifying current because it passes current preferentially in the inward direction. Note that currents are not drawn to scale

When the I–V relationship of the channel is nonlinear, i.e., channel conductance changes with voltage, the channel is said to show voltage-dependent rectification (Fig. 2.1). In this event, the channel passes current preferentially in one direction over another. For example, Fig. 2.1 shows a schematic representation of the I–V relationships for four channels: an ohmic channel, hERG/I_{Kr} (outward rectifier), KCNQ1-KCNE1/I_{Ks} (outward rectifier) and KCNJ2/I_{K1} (inward rectifier). hERG/I_{Kr} and KCNQ1-KCNE1/I_{Ks} pass current preferentially in the outward direction while KCNJ2/I_{K1} passes current preferentially in the inward direction over the outward direction.

2.2 The hERG/I_{Kr} Potassium Channel

The significance of the hERG/I_{Kr} channel for normal human cardiac electrical activity was discovered when inherited gene mutations to hERG resulted in long QT syndrome (LQTS) [12–14]; a cardiac repolarization disorder. In the LQTS, patients have a lengthened QT interval on the ECG and become susceptible to the potentially fatal arrhythmia *torsades de pointes* [15–17]. hERG is also now known to be responsible for pharmacologically induced (“acquired”) Long QT syndrome

[16, 18–20]. This is due to structural features of the channel that have been established to render it particularly susceptible to pharmacological blockade [15, 16, 21, 22]. The consideration of hERG here focuses on its electrophysiological properties and for detailed consideration of the basis of its pharmacological promiscuity the reader is referred to [15, 16, 21, 22]. Some antihistamines and antibiotics have also been known to cause arrhythmia and sudden death through blockade of the hERG/I_{Kr} channel [23].

hERG/I_{Kr} is expressed in several tissue and cell types including cardiac [13], neurons, neuroendocrine glands [24, 25], smooth muscle [26] and tumour cells [27, 28]. Its expression is greatest in cardiac cells and this is the region that has received the greatest research focus and from which its properties and function are best understood. Heterologous expression studies have shown that hERG encodes the α-subunit of the I_{Kr} channel [13, 14, 29–31].

2.2.1 *hERG/I_{Kr} Potassium Channel Gating*

hERG/I_{Kr} plays a significant role in cardiac action potential repolarization; it is the channel that is largely responsible for the early and middle stages of ventricular action potential repolarization (phase 3; Fig. 1.1) after which I_{K1} (being responsible for terminal repolarization) takes over, bringing the membrane potential back to its normal resting value (phase 4; Fig. 1.1) [13, 14]. It is characterised by slow activation but fast and profound voltage-dependent inactivation [14, 29, 32–35]. Its inactivation (a non-conducting state) is considerably faster than its activation.

Figure 2.2 shows characteristic features of I_{hERG}. With depolarisation to more positive membrane potentials, outward I_{hERG} is elicited, which increases rapidly and then plateaus for the duration of the pulse. A step repolarization of the membrane potential (to a negative potential) results in a resurgent increase in I_{hERG} (tail current); this increase in I_{hERG} is despite the decrease in the driving force for K^+ out of the cell membrane. This is due to the rapid recovery of I_{hERG} from inactivation [13, 14, 33]. Eventually, via channel deactivation, I_{hERG} decreases bi-exponentially [36].

Further insight can be gleaned from the current-voltage (I–V) relation of I_{hERG}/I_{Kr} (Fig. 2.3). At the membrane resting potential (~ -80 mV), hERG/I_{Kr} channels are closed and in that state conduct no current. As the membrane is depolarised to more positive membrane potentials greater than ~ -60 mV, the channels get activated (open) and conduct current (Fig. 2.3); K^+ ions flow out of the cell across the cell membrane according to their electrochemical gradient. At the same time, the channel begins to inactivate. As hERG/I_{Kr} inactivation with progressive depolarisation is faster than its activation, channel inactivation with increasing depolarisation eventually overtakes channel activation resulting in the channel entering the non-conducting, inactivated state. This gives the current-voltage relationship a region of negative slope (Fig. 2.3). This helps to prolong phase 2 of the action potential. Eventually, the channel begins to deactivate (close) and also

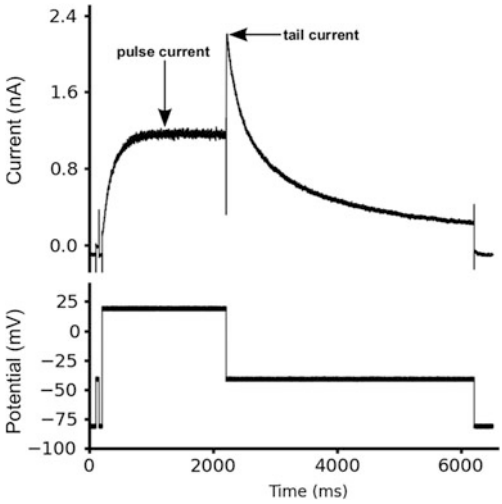

Fig. 2.2 Representative current trace for hERG elicited by a standard voltage protocol from a hERG-expressing Chinese Hamster Ovary (CHO) cell (recording made at 37 °C). Outward I_{hERG}/I_{Kr} current is elicited when the membrane potential is stepped to 20 mV from a holding potential of −80 mV. On stepping the membrane potential to −40 mV, I_{hERG}/I_{Kr} (tail current) of greater amplitude than that seen at the 20 mV are produced. Modified from [35]

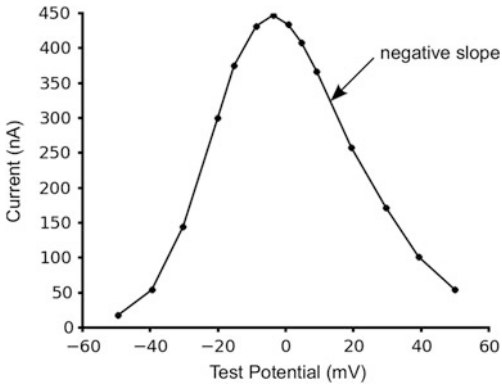

Fig. 2.3 Current-voltage (I–V) relationship for I_{hERG}/I_{Kr} (recorded in Xenopus oocytes). Depolarisation activates I_{hERG}/I_{Kr} causing an increase in outward current. At around 0 mV, I_{hERG}/I_{Kr} reaches a maximum then declines in amplitude with further depolarisation (negative slope region). Modified from [13]

begins to recover from inactivation. However, recovery from inactivation for hERG/I_{Kr} is faster than deactivation, thus allowing the channel to again conduct current, which repolarises the cell membrane (phase 3 of the action potential), returning it to its resting state (phase 4).

2.2.2 *hERG/I_{Kr} Channel Structure*

The hERG/I_{Kr} K^+ channel is a comprised of a protein tetramer consisting of four identical α-subunits [29, 37–39]. Each subunit contains six α-helical transmembrane domains (S1–S6). Functionally, each α-subunit can be divided into two parts: a voltage-sensing region and a pore-forming K^+-selective filter (Fig. 2.4). Segments S1–S4 form the transmembrane potential sensor region with S4 in particular having

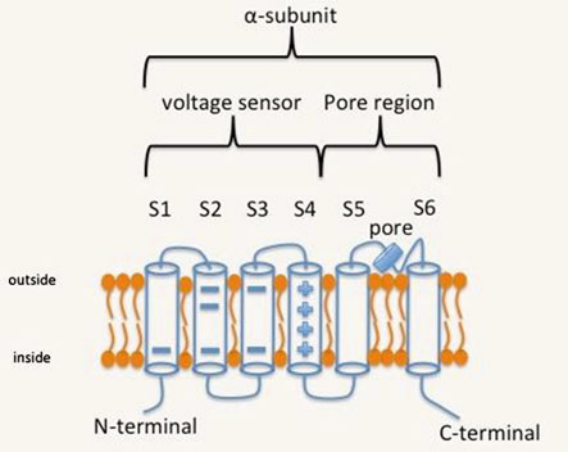

Fig. 2.4 Schematic diagram showing a representative hERG/I_{Kr} α-subunit. hERG channels consist of four identical α-subunits. Each subunit contains six transmembrane segments S1–S6. S4 has positively charged amino acids and acts as the main voltage sensor for transmembrane potential changes. The blue cylinder indicates the pore of the P-loop that acts as a K^+ selectivity filter by blocking or unblocking the pore. Intracellularly, the α-subunit has N and C termini

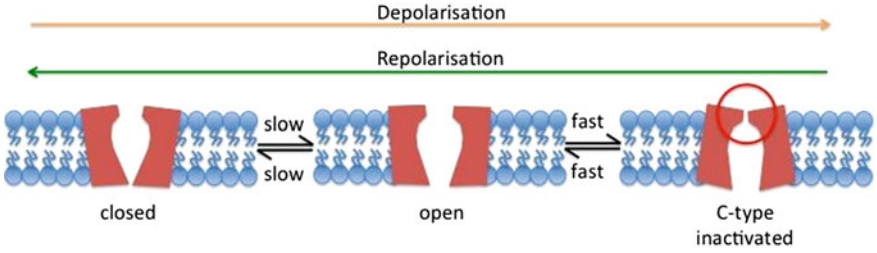

Fig. 2.5 Membrane depolarisation to voltages more positive than ~ -60 mV activates (opens) the channel slowly. With greater depolarisation, the channel rapidly inactivates (it undergoes C-type inactivation—a slight constriction of the K^+ selectivity filter). Repolarization reverses the whole process

positive charges, which allow it to react to a change in membrane potential by moving its position [40–43]. Voltage-sensor movement leads to conformational changes that open, inactivate or close the channel (Fig. 2.5). Segments S5–S6 form the ion permeation pathway and consist of the P-loop (S5) that penetrates the membrane and creates a pore through which ions enter or leave. Together, these traits confer voltage dependence and ion selectivity on the channel [40–43].

Below the P-loop is a water-filled cavity that is lined by S6 α-helices. In a conducting (open) state, i.e., in response to membrane depolarisation, all four S6 α-helices are spread out allowing the passage of K^+ ions. They crisscross in the closed state, forming a narrow cleft that blocks entry of K^+ ions [41]. hERG also

has a pair of intracellular termini (an N terminus and a C terminus), which contribute to its function. The N-terminus is responsible for channel deactivation following membrane depolarisation while mutations to the C-terminus affect trafficking and disrupt the processing of hERG channels [44, 45].

Voltage-gated K^+ channels can inactivate via two different mechanisms: rapid 'N-type' inactivation (also known as "ball and chain" type) and slow 'C-type' inactivation. N-type inactivation occurs when a ball-like structure (an intracellular protein segment) anchored to the channel's N-terminus blocks the channel pore [33] whereas 'C-type' inactivation has been suggested to occur via a slight narrowing of the K^+-selectivity filter [46] at the extracellular mouth. Deletion of the N-terminus removes 'N-type' inactivation but has no significant effect on hERG inactivation [33, 47] suggesting that hERG inactivates via 'C-type' inactivation. This was confirmed by removing 'C-type' inactivation via the Ser 631 Val mutation [48], which resulted in the elimination hERG inactivation. In addition, application of extracellular tetraethylammonium (TEA) blockade but not intracellular TEA blockade has been shown to slow inactivation suggesting that the process involves changes towards the channel exterior [49].

In addition to the four α-subunits, hERG also interacts with a β–subunit, MiRP1 (minK-related protein 1) in heterologous expression systems. The expression of MiRP1 in atrial or ventricular tissue is quite low but it is highly expressed in Purkinje fibres and the atrial pacemaking cells [50, 51]. The effect of this co-expression of the hERG α-subunit and MiRP1 is to reduce the trafficking of the channel to the cell membrane surface, reduce channel conductance and to increase channel deactivation [52]. As MiRP1 expression is low outside of the conduction system [53], it has been suggested that it may not function as hERG β–subunit in other regions and comparison of hERG with and without MiRP1 has shown that when hERG is heterologously expressed in mammalian instead of amphibian cells (*Xenopus* oocytes), it adequately recapitulates I_{Kr} [54]. Also, MiRP1 can co-assemble with a variety of other cardiac ion channels [53, 55], and so may exhibit broad interactions rather than being specific for hERG.

hERG is heteromeric and consists of two isoforms: hERG 1a (the major isoform) and hERG 1b, which differ by a truncated N-terminus in the latter. This heteromeric form of hERG (hERG 1a/1b) has recently been proposed to recapitulate native I_{Kr} more accurately than hERG 1a expressed alone [56, 57].

2.3 The KCNQ1-KCNE1/I_{Ks} Potassium Channel

Similar to the hERG/I_{Kr} potassium channel, the KCNQ1 potassium channel also plays a significant role in cardiac repolarization. The KCNQ1 α-subunit co-expresses with the KCNE1 β–subunit (minK) [40, 58, 59], the result of which is a protein complex that is responsible for the slow-delayed rectifier potassium channel I_{Ks}, which is partially responsible for action potential repolarization (phase 3) along with hERG/I_{Kr} [40, 58, 59]. In the event of an impairment to I_{Kr},

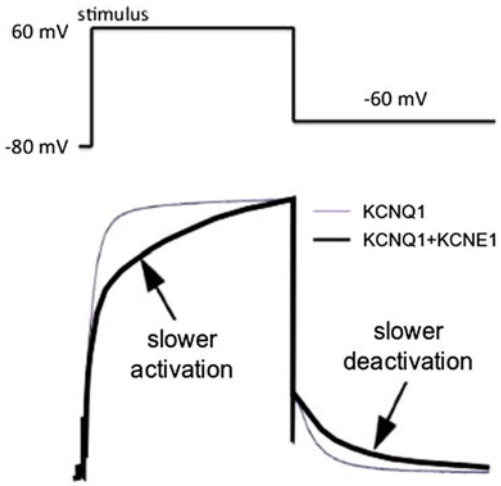

Fig. 2.6 Representative superimposed current traces for KCNQ1 (*purple*) and KCNQ1 + KCNE1 (black) elicited by a standard voltage protocol from KCNQ1-expressing oocytes (recording made at 36 °C). The *left arrow* shows the slower activation of KCNQ1 when co-expressed with KCNE1 when the membrane potential is stepped to 60 mV from a holding potential of −80 mV. On stepping the membrane potential to −60 mV, KCNQ1-KCNE1/I_{Ks} (tail current) deactivates more slowly than KCNQ1 (*right arrow*). Modified from [78]

e.g., channel block or gene mutation, I_{Ks} is a key component of repolarization reserve [40, 60, 61]. A *loss-of-function* mutation to the channel results in the first variant of the long QT syndrome LQTS1 [62–64].

In the ventricular wall, KCNQ1-KCNE1/I_{Ks} is heterogeneously distributed with its expression being very low in the mid-myocardial cells [60, 65–67]. Consequently, mid-myocardial cells have the longest APD and repolarise later than epicardial and endocardial cells. This leads to a transmural dispersion of repolarization across the ventricular wall [68–70] (meaning repolarization occurs at different rates in the different cell types that make up the wall of the myocardium), which is a substrate for re-entry. Re-entry is the continuous (usually several cycles) re-excitation of a cardiac tissue region by a single electrical signal and it usually results in arrhythmias.

In addition to being expressed in cardiac tissue, the *KCNQ1* protein is also expressed in epithelial tissue of different organs: stomach, cochlea, lungs, intestine and kidney. Its function in these tissue types is the transport of salt and water [65]. In humans, impairment to *KCNQ1* expression in epithelial tissue has been known to cause deafness [65, 71, 72], while in knockout mice, it causes deafness, balance problems and morphological abnormalities in the gastrointestinal tract and inner ear [65, 73, 74].

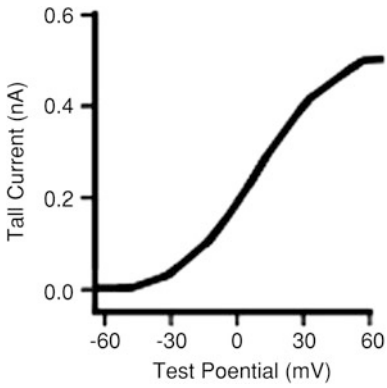

Fig. 2.7 I–V relationship of I_{Ks} tail current (recording in HEK 293 cells at 36 °C) measured from peak tail current to complete deactivation. Depolarisation activates KCNQ1-KCNE1/I_{Ks} causing an increase in outward current. Modified from [79]

2.3.1 KCNQ1-KCNE1/I_{Ks} Potassium Channel Gating

Similar to hERG, KCNQ1 is a voltage-gated channel, though its kinetic properties differ considerably from those of hERG (Fig. 2.8). Depolarisation activates (opens) KCNQ1 channels but very slowly. Upon further depolarisation, a fraction of the open channels inactivates [40, 60, 75–77] (Fig. 2.6). The channel is also characterised by slow deactivation kinetics [40, 60, 75–77]. Recovery from inactivation, however, is faster than deactivation and is seen as a hook on the current trace during the repolarization (Fig. 2.6). On co-expression with KCNE1, thus reproducing I_{Ks}, the current is enhanced (Fig. 2.6) because KCNE1 increases the single channel conductance causing a positive shift in voltage activation threshold, i.e., KCNE1 slows activation (Fig. 2.6) considerably and inactivation is completely eliminated [28, 60, 76]. Figure 2.7 shows the tail current I–V relationship for KCNQ1-KCNE1/I_{Ks} measured from peak tail current to complete deactivation.

2.3.2 KCNQ1-KCNE1/I_{Ks} Channel Structure

Structurally, KCNQ1 is a voltage-gated potassium channel like hERG described in Sect. 2.2.2 above. It consists of four identical subunits, each of which is comprised of six α-helical transmembrane domains (S1–S6). Segments S1–S4 form the voltage sensor while segments S5 and S6 form the ion permeation pathway with a pore loop and K^+ selectivity filter [58, 59, 65, 80] (Fig. 2.8). Each α-subunit also has intracellular 'N' and 'C' terminals. A major difference from hERG is KCNQ1's co-assembly with KCNE1 β–subunit, which together encode the human I_{Ks}. A representation of the KCNQ1-KCNE1 structure is shown in Fig. 2.8. The effect of the KCNE1 subunit is to stabilise the open state of the channel by altering the interaction between the pore loop, the K^+ selectivity filter and the S5/S6

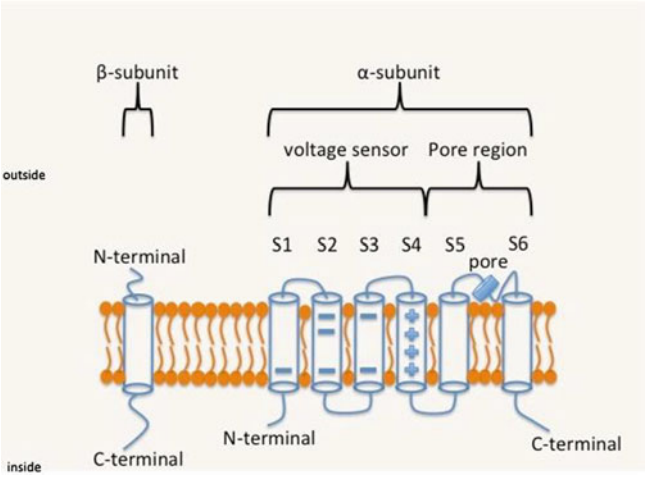

Fig. 2.8 A structural representation of the α and 0-subunits KCNQ1-KCNE1/I_{Ks}. KCNQ1 channels consist of four identical α-subunits. Each subunit contains six transmembrane segments S1−S6. S4 has positively charged amino acids and acts as the main voltage sensor for transmembrane potential changes. The blue cylinder indicates the pore of the P-loop that acts as a K^+ selectivity filter by blocking or unblocking the pore. KCNQ1 has intracellular N and C termini

segment [81]. However, the stoichiometry of KCNQ1:KCNE1 is still a matter of debate because there is no extant crystal structure for KCNQ1 with or without KCNE1 [82, 83]. Stoichiometries of 4:4 [84], 4:2 [85] and other forms [77, 83] have been proposed. A recent review can be found in [83].

2.4 The KCNJ2/I_{K1} Potassium Channel

The KCNJ2-encoded Kir2.1 protein belongs to the family of inwardly rectifying potassium (Kir) channels [86, 87]. Specifically, it belongs to the Kir2.x channel family. It is expressed in skeletal muscle, blood vessels, neurons and richly in cardiac tissue, where it is expressed in Purkinje fibres, atrial and ventricular tissues [87–92]. This family of channels allows K^+ to flow more easily into the cell than out of it. They therefore, preferentially pass current in the inward direction over the outward direction. A schematic representation of the I–V relation for I_{K1} is shown in Fig. 2.1 (red line) and an experimentally observed I–V relation is shown in Fig. 2.9.

Unlike voltage-gated K^+ channels such as I_{Kr} and I_{Ks}, the behaviour of Kir channels depends not only on the membrane potential but also predominantly on the electrochemical gradient of K^+ in the cell, i.e., the difference between the membrane potential and the K^+ reversal potential (E_K). They therefore have greater K^+ conductance at potentials negative to E_K and pass comparatively little current at depolarised membrane potentials, i.e., potentials positive to E_K (see red

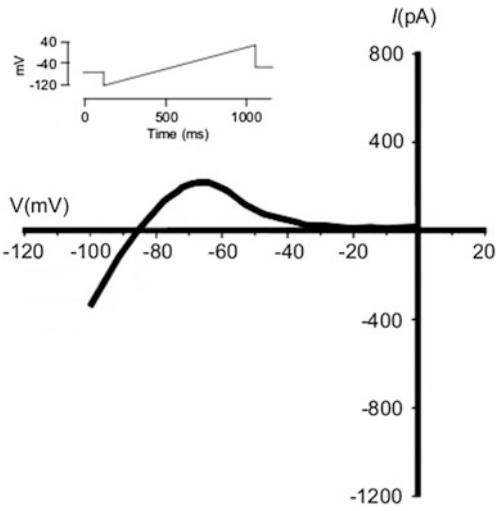

Fig. 2.9 Current-voltage (I-V) relations of the KCNJ2-encoded Kir2.1 channel expressed in HEK cells elicited by the ascending voltage ramp command shown inset. Modified from [93]

line in Figs. 2.1 and 2.9) [86–88, 94–97]. As membrane depolarisation increases further, the outward I_{K1} current decreases due to its inward rectification.

These characteristics make myocardial cells expressing I_{K1} have resting potentials close to E_K whereas cells without I_{K1} or those with an insignificant expression of I_{K1} have depolarised resting potentials and tend to show spontaneous activity, e.g., the SAN [98]. This is because with little I_{K1} present, the cells have high membrane resistances at negative voltages and so small changes in current can produce substantial changes in voltage (i.e. membrane potential is more 'labile' in the absence of I_{K1}). Consequently, in cardiac cells, I_{K1} plays a role in stabilizing the resting potential of the cell and in the duration of the action potential [86–88, 94–97]. As I_{K1} channels pass little outward current at depolarised potentials, there is little K^+ efflux through I_{K1} channels during phase 2 (the plateau phase) of the ventricular action potential [99] (Fig. 2.10b); therefore, the rectification property of I_{K1} channels also serves to maintain membrane depolarisation, thereby facilitating prolonged action potential duration. When phase 3 repolarization commences (via I_{Kr} and $I_{Ks)}$ and the membrane becomes more and more hyperpolarised, relatively large outward I_{K1} current is generated. This serves to accelerate terminal repolarization [100–103]. Figure 2.10b shows the I–V relationship of I_{K1} and relates it to the action potential, which is drawn sideways to give a better indication of the current amplitude at different phases of the action potential.

2.4.1 Kir2.1/I_{K1} Potassium Channel Gating

The inward rectification of I_{K1} and Kir2.x channels is due to blockade of outward K^+ movement through the channel pore by intracellular Mg^{2+} ions and polyamines

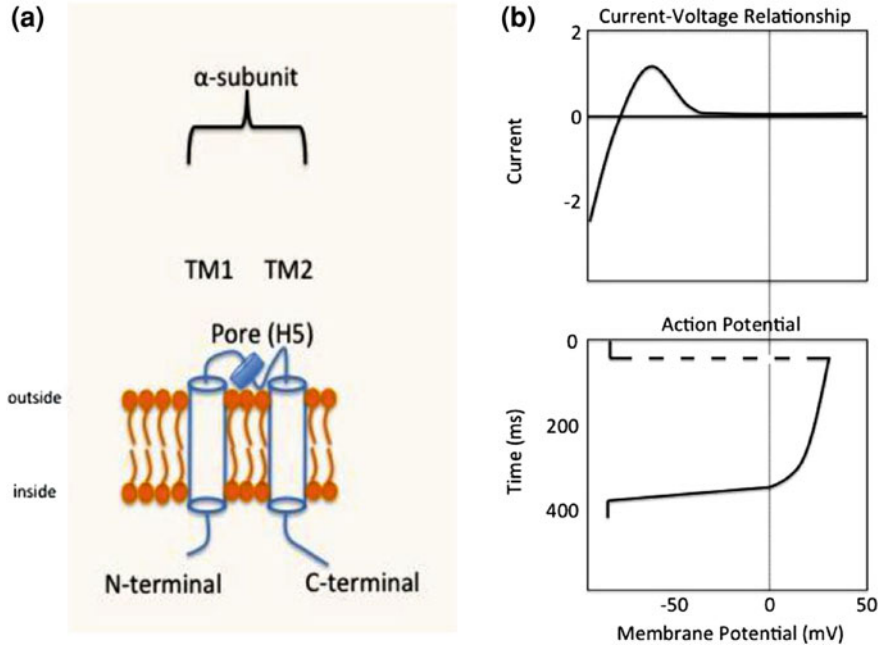

Fig. 2.10 A: structure of the Kir2.1/KCNJ2/I_{K1} channel. Each of its four α-subunits consists of two transmembrane segments (TM1 and TM2), a pore-forming loop (H5) and intracellular N and C terminals. B: I_{K1} current-voltage relationship related to the membrane action potential. The action potential is drawn sideways to give a better understanding of the contribution of I_{K1} during the action potential. The reader should focus on the repolarization phase and resting potential (the *non-dashed* parts of the action potential

[87, 97, 104–107]. At depolarised membrane potentials, the Mg^{2+} ions and polyamines such as spermine and spermidine, which are present in sub-micromolar quantities within the cell, reduce outward K^+ current. On hyperpolarisation, the Mg^{2+} ions and polyamines unblock the pore, thereby leading to increased current. This inward current first increases time-independently due to the unblocking of Mg^{2+} ions and then increases time-dependently due to unblocking of the polyamines. The unblocking of the Mg^{2+} ions is fast while the polyamine unblocking is slow [87, 108].

2.4.2 KCNJ2/I_{K1} Channel Structure

Functional Kir2.x channels (similarly to hERG/I_{Kr} and KCNQ1/I_{Ks}) also have four α-subunits but each subunit consists of only two transmembrane segments, TM1 and TM2 (Fig. 2.10a), which are highly homologous to the S5 and S6 domains of the K^+ channels discussed previously [87, 109, 110]. These two segments are

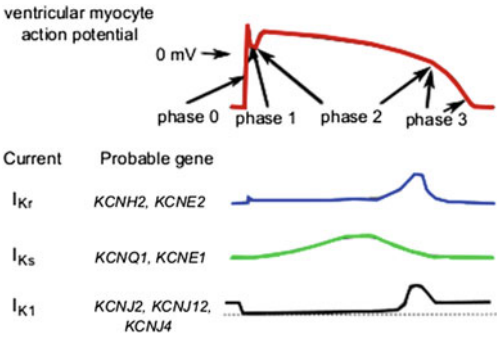

Fig. 2.11 A schematic diagram of the current profiles of I_{Kr}, I_{Ks} and I_{K1} ionic currents during a ventricular action potential. Also shown are the major gene candidates responsible for these currents. Modified from [111]

linked by the extracellular pore-forming loop or P-loop (H5), which acts as the K^+ selectivity filter. The intracellular 'N' and 'C' termini are also present. Unlike hERG/I_{Kr} and KCNQ1/I_{Ks}, there is no voltage sensor region or S4 segment; hence the channel is not truly voltage-gated in a traditional sense, with voltage-dependence instead occurring through voltage-dependent channel block/unblock by Mg^{2+} and polyamines (as described above).

2.5 Current Profiles During an Action Potential

Figure 2.11 shows a schematic diagram of the current profiles of each potassium channel currents discussed in this chapter during a ventricular action potential. I_{Kr} contributes during most of phase 3 repolarization, I_{K1} contributes later in phase 3 than I_{Kr} while I_{Ks} contributes earlier during phase 3 and some part of phase 2.

References

1. Hancox JC, McPate MJ, Harchi A, Duncan RS, Dempsey CE, Witchel HJ, et al (2011) The short QT syndrome. In: Tripathi ON, Ravens U, Sanguinetti MC (eds). Heart rate and rhythm [Internet]. Springer, Berlin pp 431–49. http://www.springerlink.com/content/m8l86l8n3h81w43m/
2. Cross B, Homoud M, Link M, Foote C, Garlitski A, Weinstock J et al (2011) The short QT syndrome. J Intervent Card Electrophysiol 31(1):25–31
3. Schimpf R, Wolpert C, Gaita F, Giustetto C, Borggrefe M (2005) Short QT syndrome. Cardiovasc Res 67(3):357–366
4. McPate MJ, Witchel HJ, Hancox JC (2006) Short QT syndrome. Future Cardiol 2(3):293–301
5. Maury P, Extramiana F, Sbragia P, Giustetto C, Schimpf R, Duparc A et al (2008) Short QT syndrome. Update on a recent entity. Arch Cardiovasc Dis 101(11–12):779–786
6. Lu LX, Zhou W, Zhang X, Cao Q, Yu K, Zhu C (2006) Short QT syndrome: a case report and review of literature. Resuscitation 71(1):115–121

7. Brugada R, Hong K, Dumaine R, Cordeiro J, Gaita F, Borggrefe M et al (2004) Sudden death associated with short-QT syndrome linked to mutations in HERG. Circulation 109(1):30–35
8. Hong K, Bjerregaard P, Gussak I, Brugada R (2005) Short QT syndrome and atrial fibrillation caused by mutation in KCNH2. J Cardiovasc Electrophysiol 16(4):394–396
9. Sun Y, Quan X-Q, Fromme S, Cox RH, Zhang P, Zhang L et al (2011) A novel mutation in the KCNH2 gene associated with short QT syndrome. J Mol Cell Cardiol 50(3):433–441
10. Bellocq C, van Ginneken ACG, Bezzina CR, Alders M, Escande D, Mannens MMAM et al (2004) Mutation in the KCNQ1 gene leading to the short QT-interval syndrome. Circulation 109(20):2394–2397
11. Priori SG, Pandit SV, Rivolta I, Berenfeld O, Ronchetti E, Dhamoon A et al (2005) A novel form of short QT syndrome (SQT3) is caused by a mutation in the KCNJ2 gene. Circ Res 96(7):800–807
12. Curran ME, Splawski I, Timothy KW, Vincent GM, Green ED, Keating MT (1995) A molecular basis for cardiac arrhythmia: HERG mutations cause long QT syndrome. Cell 80(5):795–803
13. Sanguinetti MC, Jiang C, Curran ME, Keating MT (1995) A mechanistic link between an inherited and an acquired cardiac arrhythmia: HERG encodes the IKr potassium channel. Cell 81(2):299–307
14. Trudeau MC, Warmke JW, Ganetzky B, Robertson GA (1995) HERG, a human inward rectifier in the voltage-gated potassium channel family. Science 269(5220):92–95
15. Kramer DB, Zimetbaum PJ (2011) Long-QT syndrome. Cardiol Rev 19(5):217–225
16. Kallergis EM, Goudis CA, Simantirakis EN, Kochiadakis GE, Vardas PE (2012) Mechanisms, risk factors, and management of acquired long QT syndrome: a comprehensive review. Sci World J 2012:212178
17. Roden DM, Lazzara R, Rosen M, Schwartz PJ, Towbin J, Vincent GM (1996) Multiple mechanisms in the long-QT syndrome. Current knowledge, gaps, and future directions. The SADS foundation task force on LQTS. Circulation 94(8):1996–2012
18. Dennis A, Wang L, Wan X, Ficker E (2007) hERG channel trafficking: novel targets in drug-induced long QT syndrome. Biochem Soc Trans 35(Pt 5):1060–1063
19. Wehrens XHT, Vos MA, Doevendans PA, Wellens HJJ (2002) Novel insights in the congenital long QT syndrome. Ann Intern Med 137(12):981–992
20. Camm AJ, Janse MJ, Roden DM, Rosen MR, Cinca J, Cobbe SM (2000) Congenital and acquired long QT syndrome. Eur Heart J 21(15):1232–1237
21. Sanguinetti MC, Mitcheson JS (2005) Predicting drug-hERG channel interactions that cause acquired long QT syndrome. Trends Pharmacol Sci 26(3):119–124
22. Mitcheson JS, Chen J, Lin M, Culberson C, Sanguinetti MC (2000) A structural basis for drug-induced long QT syndrome. Proc Natl Acad Sci USA 97(22):12329–12333
23. Haverkamp W, Breithardt G, Camm AJ, Janse MJ, Rosen MR, Antzelevitch C et al (2000) The potential for QT prolongation and proarrhythmia by non-antiarrhythmic drugs: clinical and regulatory implications. Report on a policy conference of the European Society of Cardiology. Eur Heart J 21(15):1216–1231
24. Warmke JW, Ganetzky B (1994) A family of potassium channel genes related to eag in Drosophila and mammals. Proc Natl Acad Sci USA 91(8):3438–3442
25. Shen XZ, Wu J, Lin JJ (2008) HERG and arrhythmia. Adv Cardiovasc Dis 29:436–440
26. Farrelly AM, Ro S, Callaghan BP, Khoyi MA, Fleming N, Horowitz B et al (2003) Expression and function of KCNH2 (HERG) in the human jejunum. Am J Physiol Gastrointest Liver Physiol 284(6):G883–G895
27. Chiesa N, Rosati B, Arcangeli A, Olivotto M, Wanke E (1997) A novel role for HERG K^+ channels: spike-frequency adaptation. J Physiol (Lond) 501(Pt 2):313–318
28. Smith GAM, Tsui H-W, Newell EW, Jiang X, Zhu X-P, Tsui FWL et al (2002) Functional up-regulation of HERG K^+ channels in neoplastic hematopoietic cells. J Biol Chem 277(21):18528–18534

29. Tristani-Firouzi M, Sanguinetti MC (2003) Structural determinants and biophysical properties of HERG and KCNQ1 channel gating. J Mol Cell Cardiol 35(1):27–35
30. Mitcheson JS, Sanguinetti MC (1999) Biophysical properties and molecular basis of cardiac rapid and slow delayed rectifier potassium channels. Cell Physiol Biochem 9(4–5):201–216
31. Sanguinetti MC, Tristani-Firouzi M (2006) hERG potassium channels and cardiac arrhythmia. Nature 440(7083):463–469
32. McPate MJ, Duncan RS, Milnes JT, Witchel HJ, Hancox JC (2005) The N588 K-HERG K^+ channel mutation in the short QT syndrome: mechanism of gain-in-function determined at 37 °C. Biochem Biophys Res Commun 334(2):441–449
33. Spector PS, Curran ME, Zou A, Keating MT, Sanguinetti MC (1996) Fast inactivation causes rectification of the IKr channel. J Gen Physiol 107(5):611–619
34. Hancox JC, McPate MJ, El Harchi A, Zhang YH (2008) The hERG potassium channel and hERG screening for drug-induced torsades de pointes. Pharmacol Ther 119(2):118–132
35. McPate MJ, Duncan RS, Hancox JC, Witchel HJ (2008) Pharmacology of the short QT syndrome N588 K-hERG K^+ channel mutation: differential impact on selected class I and class III antiarrhythmic drugs. Br J Pharmacol 155(6):957–966
36. Zhou Z, Gong Q, Ye B, Fan Z, Makielski JC, Robertson GA et al (1998) Properties of HERG channels stably expressed in HEK 293 cells studied at physiological temperature. Biophys J 74(1):230–241
37. Stuhmer W, Conti F, Stocker M, Pongs O, Heinemann SH (1991) Gating currents of inactivating and non-inactivating potassium channels expressed in Xenopus oocytes. Pflugers Arch 418(4):423–429
38. Stefani E, Toro L, Perozo E, Bezanilla F (1994) Gating of Shaker K^+ channels: I Ionic and gating currents. Biophys J 66(4):996–1010
39. Bezanilla F, Perozo E, Stefani E (1994) Gating of Shaker K^+ channels: II. The components of gating currents and a model of channel activation. Biophys J 66(4):1011–1021
40. Rudy Y, Silva JR (2006) Computational biology in the study of cardiac ion channels and cell electrophysiology. Q Rev Biophys 39(1):57–116
41. Doyle DA, Morais Cabral J, Pfuetzner RA, Kuo A, Gulbis JM, Cohen SL, et al (1998) The structure of the potassium channel: molecular basis of K^+ conduction and selectivity. Science 280(5360):69–77
42. Long SB, Campbell EB, Mackinnon R (2005) Voltage sensor of Kv1.2: structural basis of electromechanical coupling. Science 309(5736):903–908
43. Jiang Y, Lee A, Chen J, Cadene M, Chait BT, MacKinnon R (2002) The open pore conformation of potassium channels. Nature 417(6888):523–526
44. Akhavan A, Atanasiu R, Noguchi T, Han W, Holder N, Shrier A (2005) Identification of the cyclic-nucleotide-binding domain as a conserved determinant of ion-channel cell-surface localization. J Cell Sci 118(Pt 13):2803–2812
45. Zhou P, Babcock J, Liu L, Li M, Gao Z (2011) Activation of human ether-a-go-go related gene (hERG) potassium channels by small molecules. Acta Pharmacol Sin 32(6):781–788
46. Baukrowitz T, Yellen G (1995) Modulation of K^+ current by frequency and external $[K^+]$: a tale of two inactivation mechanisms. Neuron 15(4):951–960
47. Smith PL, Baukrowitz T, Yellen G (1996) The inward rectification mechanism of the HERG cardiac potassium channel. Nature 379(6568):833–836
48. Fan JS, Jiang M, Dun W, McDonald TV, Tseng GN (1999) Effects of outer mouth mutations on hERG channel function: a comparison with similar mutations in the Shaker channel. Biophys J 76(6):3128–3140
49. Smith PL, Yellen G (2002) Fast and slow voltage sensor movements in HERG potassium channels. J Gen Physiol 119(3):275–293
50. Pourrier M, Zicha S, Ehrlich J, Han W, Nattel S (2003) Canine ventricular KCNE2 expression resides predominantly in Purkinje fibers. Circ Res 93(3):189–191
51. Lundquist AL, Manderfield LJ, Vanoye CG, Rogers CS, Donahue BS, Chang PA et al (2005) Expression of multiple KCNE genes in human heart may enable variable modulation of I(Ks). J Mol Cell Cardiol 38(2):277–287

52. Abbott GW, Sesti F, Splawski I, Buck ME, Lehmann MH, Timothy KW et al (1999) MiRP1 forms IKr potassium channels with HERG and is associated with cardiac arrhythmia. Cell 97(2):175–187
53. Yu H, Wu J, Potapova I, Wymore RT, Holmes B, Zuckerman J et al (2001) MinK-related peptide 1: a beta subunit for the HCN ion channel subunit family enhances expression and speeds activation. Circ Res 88(12):E84–E87
54. Weerapura M, Nattel S, Chartier D, Caballero R, Hébert TE (2002) A comparison of currents carried by HERG, with and without coexpression of MiRP1, and the native rapid delayed rectifier current. Is MiRP1 the missing link? J Physiol (Lond) 540(Pt 1):15–27
55. Zhang M, Jiang M, Tseng GN (2001) MinK-related peptide 1 associates with Kv4.2 and modulates its gating function: potential role as beta subunit of cardiac transient outward channel? Circ Res 88(10):1012–1019
56. Jones EMC, Roti Roti EC, Wang J, Delfosse SA, Robertson GA (2004) Cardiac IKr channels minimally comprise hERG 1a and 1b subunits. J Biol Chem 279(43):44690–44694
57. Sale H, Wang J, O'Hara TJ, Tester DJ, Phartiyal P, He J-Q et al (2008) Physiological properties of hERG 1a/1b heteromeric currents and a hERG 1b-specific mutation associated with Long-QT syndrome. Circ Res 103(7):e81–e95
58. Barhanin J, Lesage F, Guillemare E, Fink M, Lazdunski M, Romey G (1996) K(V)LQT1 and lsK (minK) proteins associate to form the I(Ks) cardiac potassium current. Nature 384(6604):78–80
59. Sanguinetti MC, Curran ME, Zou A, Shen J, Spector PS, Atkinson DL et al (1996) Coassembly of K(V)LQT1 and minK (IsK) proteins to form cardiac I(Ks) potassium channel. Nature 384(6604):80–83
60. Silva J, Rudy Y (2005) Subunit interaction determines IKs participation in cardiac repolarization and repolarization reserve. Circulation 112(10):1384–1391
61. Jost N, Virág L, Bitay M, Takács J, Lengyel C, Biliczki P et al (2005) Restricting excessive cardiac action potential and QT prolongation: a vital role for IKs in human ventricular muscle. Circulation 112(10):1392–1399
62. Mikuni I, Torres CG, Bienengraeber MW, Kwok W-M (2011) Partial restoration of the long QT syndrome associated KCNQ1 A341 V mutant by the KCNE1 β-subunit. Biochim Biophys Acta 1810(12):1285–1293
63. Moric-Janiszewska E, Głogowska-Ligus J, Paul-Samojedny M, Smolik S, Woźniak M, Markiewicz-Łoskot G et al (2011) Expression of genes KCNQ1 and HERG encoding potassium ion channels Ikr, Iks in long QT syndrome. Kardiol Pol. 69(5):423–429
64. Eldstrom J, Xu H, Werry D, Kang C, Loewen ME, Degenhardt A et al (2010) Mechanistic basis for LQT1 caused by S3 mutations in the KCNQ1 subunit of IKs. J Gen Physiol 135(5):433–448
65. Jespersen T, Grunnet M, Olesen S-P (2005) The KCNQ1 potassium channel: from gene to physiological function. Physiol (Bethesda) 20:408–416
66. Akar FG, Yan G-X, Antzelevitch C, Rosenbaum DS (2002) Unique topographical distribution of M cells underlies reentrant mechanism of torsade de pointes in the long-QT syndrome. Circulation 105(10):1247–1253
67. Antzelevitch C, Dumaine R (2002) Electrical heterogeneity in the heart: physiological, pharmacological and clinical implications. In: Page E, Fozzard H, Solaro J (eds). Handbook of physiology, section 2: the cardiovascular system, Volume I: The Heart. Oxford University Press, New York, pp 654–92
68. Viswanathan PC, Shaw RM, Rudy Y (1999) Effects of IKr and IKs heterogeneity on action potential duration and its rate dependence: a simulation study. Circulation 99(18):2466–2474
69. Di Diego JM, Belardinelli L, Antzelevitch C (2003) Cisapride-induced transmural dispersion of repolarization and torsade de pointes in the canine left ventricular wedge preparation during epicardial stimulation. Circulation 108(8):1027–1033
70. Xue J, Chen Y, Han X, Gao W (2010) Electrocardiographic morphology changes with different type of repolarization dispersions. J Electrocardiol 43(6):553–559

71. Jervell A, Lange-Nielsen F (1957) Congenital deaf-mutism, functional heart disease with prolongation of the Q-T interval and sudden death. Am Heart J 54(1):59–68
72. Neyroud N, Tesson F, Denjoy I, Leibovici M, Donger C, Barhanin J et al (1997) A novel mutation in the potassium channel gene KVLQT1 causes the Jervell and Lange-Nielsen cardioauditory syndrome. Nat Genet 15(2):186–189
73. Casimiro MC, Knollmann BC, Ebert SN, Vary JC Jr, Greene AE, Franz MR et al (2001) Targeted disruption of the Kcnq1 gene produces a mouse model of Jervell and Lange-Nielsen Syndrome. Proc Natl Acad Sci USA 98(5):2526–2531
74. Lee MP, Ravenel JD, Hu RJ, Lustig LR, Tomaselli G, Berger RD et al (2000) Targeted disruption of the Kvlqt1 gene causes deafness and gastric hyperplasia in mice. J Clin Invest 106(12):1447–1455
75. Pusch M (1998) Increase of the single-channel conductance of KvLQT1 potassium channels induced by the association with minK. Pflugers Arch 437(1):172–174
76. Splawski I, Tristani-Firouzi M, Lehmann MH, Sanguinetti MC, Keating MT (1997) Mutations in the hminK gene cause long QT syndrome and suppress IKs function. Nat Genet 17(3):338–340
77. Wang W, Xia J, Kass RS (1998) MinK-KvLQT1 fusion proteins, evidence for multiple stoichiometries of the assembled IsK channel. J Biol Chem 273(51):34069–34074
78. Jiang M, Xu X, Wang Y, Toyoda F, Liu X-S, Zhang M et al (2009) Dynamic partnership between KCNQ1 and KCNE1 and influence on cardiac IKs current amplitude by KCNE2. J Biol Chem 284(24):16452–16462
79. Dong M-Q, Lau C-P, Gao Z, Tseng G-N, Li G-R (2006) Characterization of recombinant human cardiac KCNQ1/KCNE1 channels (I (Ks)) stably expressed in HEK 293 cells. J Memb Biol 210(3):183–192
80. Wang Q, Curran ME, Splawski I, Burn TC, Millholland JM, VanRaay TJ et al (1996) Positional cloning of a novel potassium channel gene: KVLQT1 mutations cause cardiac arrhythmias. Nat Genet 12(1):17–23
81. Seebohm G, Sanguinetti MC, Pusch M (2003) Tight coupling of rubidium conductance and inactivation in human KCNQ1 potassium channels. J Physiol (Lond) 552(Pt 2):369–378
82. Osteen JD, Sampson KJ, Kass RS (2010) The cardiac IKs channel, complex indeed. Proc Natl Acad Sci USA 107(44):18751–18752
83. Wang M, Kass R (2012) Stoichiometry of the slow I(Ks) potassium channel in human embryonic stem cell-derived myocytes. Pediatr Cardiol 33(6):938–942
84. Nakajo K, Ulbrich MH, Kubo Y, Isacoff EY (2010) Stoichiometry of the KCNQ1—KCNE1 ion channel complex. Proc Natl Acad Sci USA 107(44):18862–18867
85. Morin TJ, Kobertz WR (2008) Counting membrane-embedded KCNE beta-subunits in functioning K^+ channel complexes. Proc Natl Acad Sci USA 105(5):1478–1482
86. Sakmann B, Trube G (1984) Conductance properties of single inwardly rectifying potassium channels in ventricular cells from guinea pig heart. J Physiol 347:641–657
87. Hibino H, Inanobe A, Furutani K, Murakami S, Findlay I, Kurachi Y (2010) Inwardly rectifying potassium channels: their structure, function, and physiological roles. Physiol Rev 90(1):291–366
88. Noble D (1965) Electrical properties of cardiac muscle attributable to inward going (anomalous) rectification. J Cell Comp Physiol 66(S2):127–135
89. Beeler GW Jr, Reuter H (1970) Voltage clamp experiments on ventricular myocarial fibres. J Physiol (Lond) 207(1):165–190
90. Kurachi Y (1985) Voltage-dependent activation of the inward-rectifier potassium channel in the ventricular cell membrane of guinea-pig heart. J Physiol (Lond) 366:365–85
91. McAllister RE, Noble D (1966) The time and voltage dependence of the slow outward current in cardiac Purkinje fibres. J Physiol (Lond) 186(3):632–662
92. Rougier O, Vassort G, Stämpfli R (1968) Voltage clamp experiments on frog atrial heart muscle fibres with the sucrose gap technique. Pflugers Arch Gesamte Physiol Menschen Tiere 301(2):91–108

93. Dhamoon AS, Pandit SV, Sarmast F, Parisian KR, Guha P, Li Y et al (2004) Unique Kir2.x properties determine regional and species differences in the cardiac inward rectifier K^+ current. Circ Res 94(10):1332–1339
94. Hagiwara S, Takahashi K (1974) The anomalous rectification and cation selectivity of the membrane of a starfish egg cell. J Membr Biol 18(1):61–80
95. Miyazaki SI, Takahashi K, Tsuda K, Yoshii M (1974) Analysis of non-linearity observed in the current-voltage relation of the tunicate embryo. J Physiol (Lond) 238(1):55–77
96. Sakmann B, Trube G (1984) Voltage-dependent inactivation of inward-rectifying single-channel currents in the guinea-pig heart cell membrane. J Physiol (Lond) 347:659–83
97. Dhamoon AS, Jalife J (2005) The inward rectifier current (IK1) controls cardiac excitability and is involved in arrhythmogenesis. Heart Rhythm 2(3):316–324
98. Schram G, Pourrier M, Melnyk P, Nattel S (2002) Differential distribution of cardiac ion channel expression as a basis for regional specialization in electrical function. Circ Res 90(9):939–950
99. Nichols CG, Makhina EN, Pearson WL, Sha Q, Lopatin AN (1996) Inward rectification and implications for cardiac excitability. Circ Res 78(1):1–7
100. Miake J, Marbán E, Nuss HB (2003) Functional role of inward rectifier current in heart probed by Kir2.1 overexpression and dominant-negative suppression. J Clin Invest 111(10):1529–1536
101. Nerbonne JM, Kass RS (2005) Molecular physiology of cardiac repolarization. Physiol Rev 85(4):1205–1253
102. Lopatin AN, Nichols CG (2001) Inward rectifiers in the heart: an update on I(K1). J Mol Cell Cardiol 33(4):625–638
103. Nichols CG, Lopatin AN (1997) Inward rectifier potassium channels. Annu Rev Physiol 59:171–191
104. Lopatin AN, Makhina EN, Nichols CG (1994) Potassium channel block by cytoplasmic polyamines as the mechanism of intrinsic rectification. Nature 372(6504):366–369
105. Matsuda H, Saigusa A, Irisawa H (1987) Ohmic conductance through the inwardly rectifying K channel and blocking by internal Mg2+. Nature 325(7000):156–159
106. Vandenberg CA (1987) Inward rectification of a potassium channel in cardiac ventricular cells depends on internal magnesium ions. Proc Natl Acad Sci USA 84(8):2560–2564
107. Yamada M, Kurachi Y (1995) Spermine gates inward-rectifying muscarinic but not ATP-sensitive K^+ channels in rabbit atrial myocytes. Intracellular substance-mediated mechanism of inward rectification. J Biol Chem 270(16):9289–9294
108. Lopatin AN, Makhina EN, Nichols CG (1995) The mechanism of inward rectification of potassium channels: long-pore plugging by cytoplasmic polyamines. J Gen Physiol 106(5):923–955
109. Glowatzki E, Fakler G, Brändle U, Rexhausen U, Zenner HP, Ruppersberg JP et al (1995) Subunit-dependent assembly of inward-rectifier K^+ channels. Proc Biol Sci 261(1361):251–261
110. Yang J, Jan YN, Jan LY (1995) Determination of the subunit stoichiometry of an inwardly rectifying potassium channel. Neuron 15(6):1441–1447
111. James AF, Choisy SCM, Hancox JC (2007) Recent advances in understanding sex differences in cardiac repolarization. Prog Biophys Mol Biol 94(3):265–319

Chapter 3
The Short QT Syndrome

3.1 Introduction

The Long QT Syndrome (LQTS) is well-established as a distinct pathological, clinical entity [1–4] as is its association with increased susceptibility to the polymorphic ventricular arrhythmia *torsade de pointes* [5–7]. It has a congenital form and an acquired form. The congenital form is due to genetic channelopathies while the acquired form occurs as a result of ion channel-blocking effects of cardiac-related or non-cardiac drugs [5, 8–10]. It is characterised by an abnormally long QT interval on the ECG; rate-corrected QT (QT_C) of >440–460 ms.

In contrast to LQTS, there are circumstances in which the QT interval can become abnormally short and in some instances, this is associated with an increased arrhythmia risk [11–14]. It is now established that QT interval shortening can either be 'acquired' or associated with cardiac ion channel gene defects [12–17]. Acquired QT interval shortening can be caused by several chemical agents, for example, exposure to glycosides increases intracellular Na^+ and Ca^{2+}, which increase outward Na–Ca exchange current during the phase 2 (plateau phase) of the action potential [18] leading to a shortening of the action potential. Clinically, this can be observed as digitalis-induced QT interval shortening in some patients [19–21]. Another acquired form of QT interval shortening is that associated with anabolic steroid use [22–24] and its abuse by bodybuilders and strength athletes [23, 25]. In that instance, it is possible that androgen associated modulation of ion channels involved in ventricular repolarization may account for the observed QT interval shortening seen in some strength athletes who abuse androgenic steroids [23, 25].

SQTS associated with ion channel gene defects is a relatively new clinical entity when compared to the LQTS. In 2000, SQTS was first recognised as a distinct clinical syndrome by Gussak et al. [12] who identified three members of

Portions of this chapter appear in [70].

I. Adeniran, *Modelling the Short QT Syndrome Gene Mutations*,
Springer Theses, DOI: 10.1007/978-3-319-07200-5_3,

the same family with $QT_C < 300$ ms. The youngest presented with syncope and paroxysmal atrial fibrillation (AF). A patient from an unrelated family underwent sudden death [12]. Thereafter, six members from two different families were identified with QT_C intervals of 300 ms or less, shortened atrial and ventricular refractory periods and easily induced ventricular tachyarrhythmias [26]. The SQTS is characterised by an abnormally short QT interval on the ECG with QT_C intervals that are typically less than 320 ms [27–30]), tall and peaked T-waves and a wider than normal T_{peak}-T_{end} duration (Fig. 3.1), patients usually have structurally normal hearts and have shortened atrial and ventricular refractory periods, poor heart rate-adaptation, and exhibit increased susceptibility to atrial and ventricular arrhythmia and sudden death [26, 31–34].

To date, five different forms of the SQTS have been identified: SQT1 to SQT5. A mutation to the KCNH2 (*hERG*) gene responsible for the SQT1 variant was the first to be identified in 2004 [35, 36], followed by a mutation for KCNQ1 responsible for the SQT2 variant [37, 38]. The SQT3 variant is due to a mutation in the *KCNJ2* gene [39]. SQT4 and SQT5 are the most recently identified variants and are due to mutations to the CACNB2b and CACNA1C genes [40]. These mutations (SQT4 and SQT5) are linked to a mixed short QT/Brugada syndrome phenotype because in addition to shortening the QT interval, ST-segment elevation on the ECG is observed [40]. Figure 3.2 shows a schematic of the current profiles for the channels involving the *KCNH2*-, *KCNQ1*-, *KCNJ2*- and *CACNB2b* + *CACNA1C*-encoded subunits.

3.2 SQT1 and KCNH2

Mutations to the KCNH2 [41] gene are responsible for the first variant of the SQTS. The first and main of these was discovered during the genetic screening of two unrelated families, members of which exhibited the same hERG mutation. Both families manifested distinct substitutions at nucleotide 1764 of KCNH2. In one family, there was a C → G substitution while the other displayed a C → A substitution. Both substitutions led to a common amino-acid substitution in the KCNH2 product of the hERG K^+ channel (Kv11.1), which was an asparagine to lysine exchange (N588K) at position 588 in the hERG channel protein [35]. Another independent study identified a third family with the same asparagine to lysine N588K amino-acid substitution [36]. Affected individuals displayed shortened rate corrected QT (QT_C) intervals (225–240 ms over the normal heart range), shortened atrial and ventricular refractory periods, atrial fibrillation (AF), easily induced ventricular fibrillation (VF) during programmed electrical stimulation, syncope and sudden death [35].

As noted in Chap. 2, fast and profound voltage-dependent inactivation causes the current elicited in membrane depolarisation to decline at voltages positive to about 0 mV [2, 3, 43, 44] (and see Fig. 2.3). This kinetic property limits the amount of current produced early during the AP [45–47]. I_{hERG}/I_{Kr} reaches a

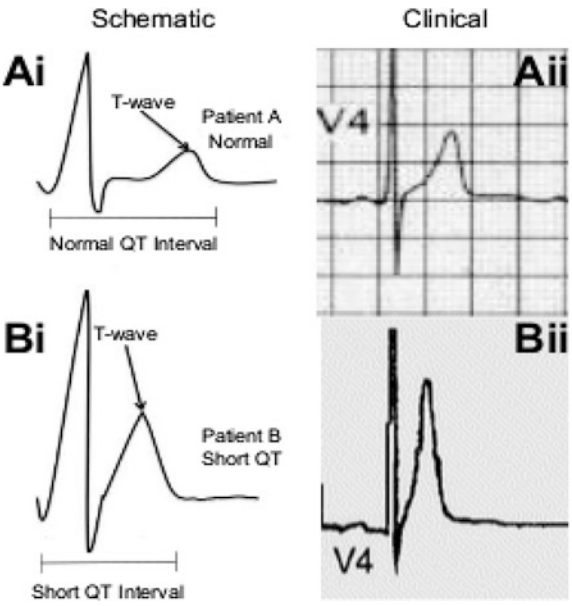

Fig. 3.1 Schematic representation (**ai**, **bi**) and example clinical ECG (**aii**, **bii**) of a normal and an SQTS patient. Patient A shows a normal QT interval on the ECG (**ai**, **aii**). Patient B has short QT syndrome (SQTS) and displays a shorter QT interval on the ECG including a taller and peaked T-wave (**aii**, **bii**). Modified from [30]

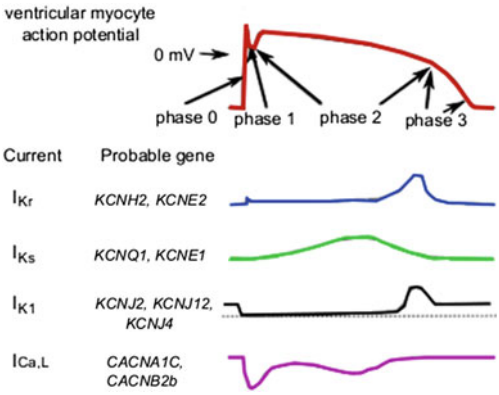

Fig. 3.2 A schematic diagram of the current profiles of I_{Kr}, I_{Ks} and I_{K1} and $I_{Ca,L}$ ionic currents during a ventricular action potential. Also shown are the major gene candidates responsible for these currents. Modified from [42]

maximum towards phase 3 of the ventricular AP. The S5 Pore (S5P) linker in which residue N588 resides plays a part in conferring inactivation to the channel [48–50], as do conformational changes in the mouth of the channel [44, 51–53].

In SQT1, the N588K-hERG mutation attenuates inactivation of the channel (seen as non-rectification of the current on the I–V curve in Fig. 3.3), leading to excessive current being generated earlier during the ventricular AP (more precisely during the plateau phase), thereby shortening the AP [35, 54, 55]. AP clamp measurements conducted at 37 °C have shown that this enhances hERG current early during atrial, ventricular and purkinje APs [56]. This is consistent with shortened APD, QT interval and increased incidence of AF in SQT1 patients [35, 36]. Figure 3.3 shows

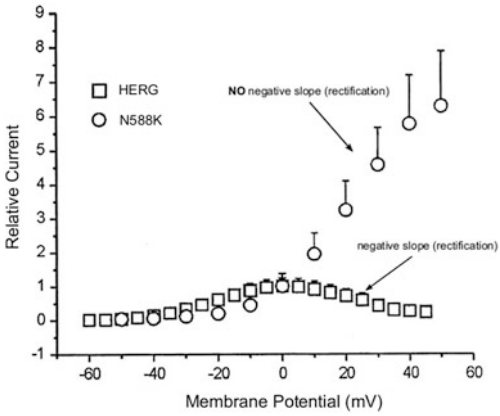

Fig. 3.3 Current-Voltage (I–V) relationships for hERG and N588K-hERG. The N588K-hERG mutation attenuates the rectification of hERG. Modified from [35]

the excessive current generated by the N588K-hERG mutation on the I–V relation while Fig. 3.4 shows a schematic representation of APD shortening by the mutation.

The initial study performed by Brugada et al. [35] suggested that the N588K mutation might eliminate entirely inactivation of the channel with the I–V relation showing no rectification [35] (Fig. 3.3). However, subsequent detailed kinetic studies conducted at both ambient [55] and physiological [54] temperatures show that inactivation is not eliminated by the N588K mutation but is attenuated and shifted to more positive voltages by ~+60–90 mV. Accompanying this is a modest increase in Na^+/K^+ permeability ratio [54, 55].

Recently, a second mutation in the KCNH2 gene was discovered in a 34-year old man [57]. It involved a single base pair G → A substitution, which resulted in an amino-acid substitution of histidine for arginine at codon 1135 (R1135H) in the hERG channel protein [57]. The R1135H mutation alters hERG gating kinetics by significantly attenuating deactivation resulting in a gain-of-function in the I_{Kr} channel [57].

A third mutation in the KCNH2 gene was also very recently discovered in a Chinese family [58]. It involved a single base pair C → T substitution at nucleotide 1853 (C1853T) of the KCNH2 gene, which resulted in an amino-acid substitution (threonine to isoleucine exchange) at position 618 (T618I) in the hERG channel protein [58]. The T618I mutation alters hERG gating kinetics by attenuating inactivation and increasing the rate of recovery from inactivation [58].

3.3 SQT2 and KCNQ1

Mutations to the KCNQ1 gene are responsible for variant 2 of the short QT syndrome (SQT2) [37, 38]. The first clinical case of SQT2 was that of a 70-year-old male who was resuscitated from VF [37]. He had a short QT_C interval of

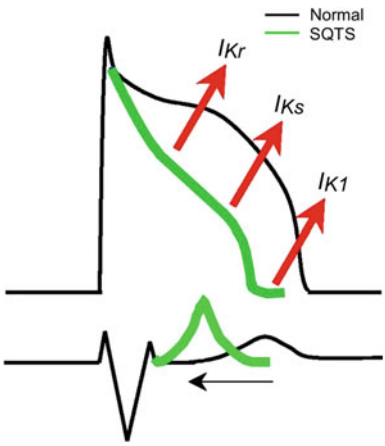

Fig. 3.4 A schematic representation of the effect of the gain-of-function mutations of the I_{Kr} channel (SQT1), I_{Ks} channel (SQT2) and I_{K1} channel (SQT3) on the normal action potential. The mutations shorten the action potential (*green*) and the QT interval. Modified from [59]

302 ms. Genetic screening revealed no abnormalities to *KCNH2*, *KCNE2* or *KCNE1* but showed a G919 → C base transition, which resulted in an amino acid substitution (V307L) in the pore helix of the KCNQ1 channel protein [37]. The mutation was found to shift negatively the voltage dependence of activation of the mutant KCNQ1 channels [37] and to accelerate the time course of current activation in comparison to wild type (WT) channels [37] (Fig. 3.5). When these changes were incorporated into a human ventricular single cell model, the AP and QT intervals were shortened [37]. Subsequent detailed cell and tissue simulations involving the SQT2 mutation also showed marked ERP shortening and significant effects on the transmural distribution of the AP across the ventricular wall [60].

The second clinical case of SQT2 was found in a baby girl who had bradycardia and irregular heart rhythm in utero, which persisted after she was born (in 38 weeks) [38]. Her ECG showed no P or F wave and had a QT interval of 280 ms [38]. Genetic screening revealed a G → A substitution on codon 421 of the *KCNQ1* gene, which resulted in an amino acid substitution (V141M) in the S1 domain of the KCNQ1 channel protein. The mutation was de novo as it was not present in her parents [38]. In a human ventricular cell model, the mutation shortened the AP while it arrested spontaneous activity in a rabbit SAN cell model [38]. Both mutations have recently been suggested to result in a marked negative shift of the voltage dependence of I_{Ks} channels and to a strong deceleration of current deactivation [61].

3.4 SQT3 and KCNJ2

In 2005, during a routine clinical examination, a 5-year-old child showed a QTc interval of 315 ms and a tall, narrow and peaked T-wave on the ECG [39]. Her father, who had a history of pre-syncopal events and palpitations also had a QTc

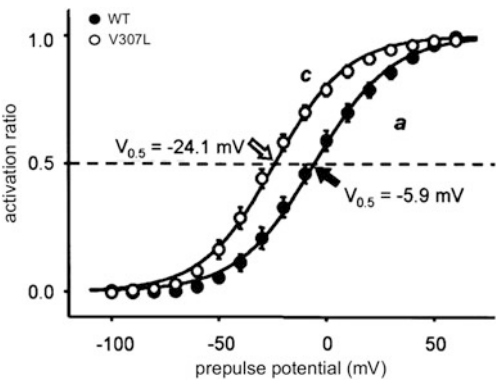

Fig. 3.5 Tail current I–V relation for WT and V307L (recorded in COS-7 cells). The half-activation voltage ($V_{0.5}$) for V307L is more negative compared to WT implying that the V307L mutation accelerates channel activation. Modified from [37]

interval of 320 ms and similar ECG T-wave characteristics [39]. Her mother exhibited a normal ECG [39]. On genetic analysis, a single base pair substitution (G514A) in KCNJ2 was discovered in both the child and her father. This led to an aspartate to asparagine (D → N; D172N) amino acid substitution in codon 172 of the Kir 2.1 K^+ channel protein [39]. This case gave rise to the "SQT3" variant of the SQTS.

The D172N residue lies in the ion conduction pathway of Kir 2.1 where it binds to polyamines and Mg^{2+} ions [62]. This binding is responsible for the inward rectification of the current, which the D172N mutation impairs giving rise to an increased outward current and a modest rightward voltage-shift of the peak outward current [39, 62, 63] (Fig. 3.6). The proband—the 5-year-old child—had a heterozygote mutation, i.e., a co-expression of WT and D172N channels which, when replicated in vitro, resulted in an outward current that is intermediate between WT and pure D172N expressed alone [39, 63] (Fig. 3.6).

In an AP model, the kinetic changes due to the Kir 2.1 D172N mutation led to AP shortening and steeper AP duration restitution [39]. The ECG T-wave characteristics of the mutation seen in the proband were also replicated using 1D tissue [39]. Results from in vitro action potential voltage clamp experiments have also shown that the heterozygote mutation possessed by the proband leads to increased I_{K1} during terminal repolarization of ventricular action potentials [63]; these experiments also showed that the mutation has the potential to affect the contribution of I_{K1} to atrial repolarization [63].

Very recently, a second heterozygous mutation in the KCNJ2 gene was discovered in an 8-year old girl [64]. It involved a single base pair C → T substitution at nucleotide 902 (c.902T > A) of the *KCNJ2* gene, which resulted in an amino-acid substitution (methionine to lysine exchange) at position 301 (M301K) in the Kir2.1 K^+ channel [64]. The M301K mutation impaired inward rectification and consequently resulted in larger outward currents compared to WT [64].

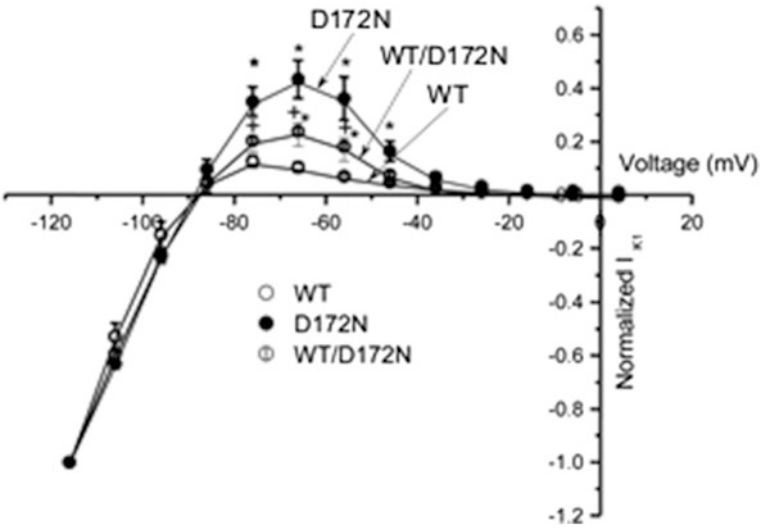

Fig. 3.6 I-V relationship (recorded in CHO cells) for WT, WT/D172N (heterozygous mutant) and D172N (homozygote) mutant showing the increased outward current by the mutations compared to WT. Modified from [39]

3.5 SQT4 and SQT5

The SQT4 and SQT5 variants of the SQTS were discovered during genetic screening of patients with Brugada syndrome [40]. The classic feature of the Brugada syndrome phenotype is ST segment elevation in leads V_1–V_3 on the ECG, which descends with upward convexity into an inverted T-wave [65–67]. SQT4 and SQT5 are therefore associated with a mixed Brugada-SQT phenotype. While SQT1, SQT2 and SQT3 affect repolarising K^+ currents (Figs. 3.2 and 3.4) and involve gain-of-function mutations, SQT4 and SQT5 affect the depolarising L-type Ca^{2+} current ($I_{ca,L}$) (Fig. 3.2) and involve *loss-of-function* mutations to channel subunits. SQT4 results from a loss-of-function mutation to *CACNA1C* (which is responsible for the α_1 subunit of L-type channels) while SQT5 results from a loss-of-function mutation to *CACNB2b* (which is responsible for the β_{2b} subunit of L-type channels) [40]. Eighty-two probands with Brugada syndrome were genetically screened. Seven of these had mutations to the genes responsible for the α_1 and β_{2b} subunits of the L-type Ca^{2+} channel and of these seven, three had moderately short QT_C intervals (<360 ms).

The first patient studied was a 25-year old male with a QT_C interval of 330 ms. He presented with aborted sudden cardiac death (SCD). His brother was also symptomatic and his relatives had tall and peaked T-waves on the ECG. Genetic analysis showed that the proband had a serine → leucine substitution at position 481 (S481L) of the β_{2b} subunit due to a heterozygous C1442T change in CACNAB2b.

The second patient was a 41-year old male (from a different family to patient 1) with a QT_C interval of 300 ms. He presented with AF and his brother died suddenly at the age of 45. Genetic analysis showed that the proband had an A → G substitution (A1468G) that led to a glycine → arginine substitution at position 490 (G490R) of the CACNA1C protein. This mutation was also found in his two daughters.

The third identified case was a 48-year old male with a QT_C interval of 360 ms and a prominent ST-segment elevation on the ECG. His father had no known symptoms but his mother had undergone SCD at the age of 48. Genetic analysis showed that the proband had an alanine → valine amino acid substitution (A39V) due to a heterozygous C → T transition in position 116 of CACNA1C. Co-expression of WT and the pertinent α/β subunits for each mutant resulted in significantly reduced current through the channel. Table 3.1 summarises the currently identified SQTS variants, their associated ion channels and functional consequences.

3.6 Current Treatment of SQT Patients

Due to the risk of sudden death in SQTS, the prevailing treatment is the use of an implantable cardioverter defibrillator device (ICD; [15, 32, 68, 69]).

However, this is not an ideal, sole solution because of the possibility of an inappropriate shock by the ICD due to T-wave over-sensing (due to the pronounced tall, peaked T-waves in many SQT patients) [15, 31, 32, 68]. This risk can be lessened by ICD reprogramming [68]. ICDs do not restore the QT interval to its normal duration and are not suitable for all patients (e.g., infants). These drawbacks to ICDs make it important also to have adjunct (or alternative—for patients who refuse ICDs) pharmacological treatments that may help restore the normal QT interval duration and protect against arrhythmia [15, 32, 71, 72].

Historically, the first drug to be investigated as a pharmacological treatment for the SQTS was sotalol (a class III antiarrhythmic drug) by Brugada et al. [35]. They found that the N588K mutation reduced the blocking potency of sotalol and the QTc interval was unchanged on its administration [35]. A subsequent study investigated the effects of a number of drugs on six SQTS patients [73]. The drugs were flecainide (a class Ic antiarrhythmic drug), hydroquinidine (a class Ia agent) and sotalol and ibutilide (both class III agents). Only hydroquinidine successfully produced a significant lengthening of the QT interval and prolongation of the ERP [73]. It was also found to protect against VF. A subsequent study compared quinidine and sotalol in vitro [74]. It found that sotalol's IC_{50} for I_{hERG}/I_{Kr} current was raised 20-fold by the N588K mutation but only by 5-fold for quinidine. The IC_{50} is the concentration of a drug that produces a half-maximal effect [75]. In SQT1 patients, quinidine—which was less affected in vitro by the N588K mutation than was sotalol—restored the heart rate adaption of the QT interval towards normal [74].

Table 3.1 Known SQTS ion channel gene mutations and their functional consequences

SQT variant	Gene/gene product	Channel (subunit)	Mutation (amino acid change)	Principal alterations to channel function/activity
SQT1	KCNH2 (hERG)	I_{Kr} (α [pore-forming] subunit)	N588K	Reduced inactivation
			R1135H	Delayed deactivation
			T618I	Reduced inactivation
SQT2	KCNQ1 (KCNQ1/KvLQT1)	I_{Ks} (α subunit)	V307L	Enhanced/accelerated activation
			V141M	Constitutively open/shifted activation and delayed deactivation
SQT3	KCNJ2 (Kir 2.1)	I_{K1}	D172N	Preferential increase in outward current
			M301K	Preferential increase in outward current
SQT4	CACNA1C ($Ca_v1.2$)	$I_{Ca,L}$ (α subunit)	A39V	Reduced trafficking/current
			G490R	Reduced current
SQT5	CACNB2b (β_{2b} subunit)	$I_{Ca,L}$ ((β_{2b} subunit)	S481L	Reduced current

Modified from [70]

In 2006, McPate et al. [76] reported effects of the N588K hERG mutation on the I_{hERG} blocking potency of disopyramide (which, like quinidine, is a class Ia antiarrhythmic agent) and the high affinity class III inhibitor E-4031. For disopyramide, they found that its I_{hERG} blocking potency was comparatively little affected by the N588K mutation, i.e., its IC_{50} was 1.5-fold that of WT-hERG compared to 3.5-fold that for quinidine. For E-4031, its I_{hERG} blocking potency was changed significantly (it had a >11-fold change in IC_{50}). Subsequently, disopyramide was used in a pilot study involving two SQT1 patients [77] and was found to extend the QT interval, rate dependence and ventricular ERP. Mizobuchi et al. have also reported beneficial effects of disopyramide in an SQTS patient of unknown genotype [78].

In a subsequent study [79], McPate et al. identified amiodarone and propafenone as effective N588K-hERG inhibitors. This study was in vitro and the efficacy of amiodarone on SQT1 in vivo is currently unknown although it has been found to be beneficial in an SQT patient of unknown genotype [16]. Propafenone on the other hand has been reported to prevent AF in an SQT1 patient but without affecting the QT interval [36].

Compared to SQT1, there is very little available on the in vitro pharmacology of SQT2—SQT5. Lerche et al. [80] showed that the V307L-KCNQ1 mutation reduced the KCNQ1/I_{Ks} blocking potency of chromanol 293B. Recently, El Harchi et al. [81] identified mefloquine as an effective pharmacological inhibitor of recombinant I_{Ks} channels incorporating the V307L-KCNQ1 mutation. These

findings are relevant to SQT2, though neither compound has been tested on patients in vivo.

Chloroquine has recently been reported to be an effective inhibitor of the D172N-KCNJ2 SQT3 mutation [63, 82] in vitro, but its efficacy in SQT3 patients is as yet unknown.

In a study involving the long-term prognosis of a large cohort of SQT patients [83], hydroquinidine was found to be effective in preventing the induction of ventricular arrhythmias with patients receiving hydroquinidine having no arrhythmic events [83]. Nevertheless, due to the scarcity of data on the in vitro pharmacology of SQT2-SQT5, in silico characterisation provides an alternative means to characterise and quantify the effects of drugs targeting these mutations.

References

1. Dumaine R, Wang Q, Keating MT, Hartmann HA, Schwartz PJ, Brown AM et al (1996) Multiple mechanisms of Na^+ channel–linked long-QT syndrome. Circ Res 78(5):916–924
2. Sanguinetti MC, Jiang C, Curran ME, Keating MT (1995) A mechanistic link between an inherited and an acquired cardiac arrhythmia: HERG encodes the IKr potassium channel. Cell 81(2):299–307
3. Trudeau MC, Warmke JW, Ganetzky B, Robertson GA (1995) HERG, a human inward rectifier in the voltage-gated potassium channel family. Science 269(5220):92–95
4. Sanguinetti MC, Curran ME, Spector PS, Keating MT (1996) Spectrum of HERG K^+ -channel dysfunction in an inherited cardiac arrhythmia. Proc Natl Acad Sci USA 93(5):2208–2212
5. Camm AJ, Janse MJ, Roden DM, Rosen MR, Cinca J, Cobbe SM (2000) Congenital and acquired long QT syndrome. Eur Heart J 21(15):1232–1237
6. Roden DM (1997) A practical approach to torsade de pointes. Clin Cardiol 20(3):285–290
7. Janeira LF (1995) Torsades de pointes and long QT syndromes. Am Fam Physician 52(5):1447–1453
8. Kramer DB, Zimetbaum PJ (2011) Long-QT syndrome. Cardiol Rev 19(5):217–225
9. Sanguinetti MC, Mitcheson JS (2005) Predicting drug-hERG channel interactions that cause acquired long QT syndrome. Trends Pharmacol Sci 26(3):119–124
10. Mitcheson JS, Chen J, Lin M, Culberson C, Sanguinetti MC (2000) A structural basis for drug-induced long QT syndrome. Proc Natl Acad Sci USA 97(22):12329–12333
11. Anttonen O, Junttila MJ, Rissanen H, Reunanen A, Viitasalo M, Huikuri HV (2007) Prevalence and prognostic significance of short QT interval in a middle-aged Finnish population. Circulation 116(7):714–720
12. Gussak I, Brugada P, Brugada J, Wright RS, Kopecky SL, Chaitman BR et al (2000) Idiopathic short QT interval: a new clinical syndrome? Cardiology 94(2):99–102
13. Gussak I, Brugada P, Brugada J, Antzelevitch C, Osbakken M, Bjerregaard P (2002) ECG phenomenon of idiopathic and paradoxical short QT intervals. Card Electrophysiol Rev 6(1–2):49–53
14. Makarov LM, Chuprova SN, Kiseleva II (2004) QT interval shortening in families with history of sudden death at young age. Kardiologiia 44(2):51–56
15. Maury P, Extramiana F, Sbragia P, Giustetto C, Schimpf R, Duparc A et al (2008) Short QT syndrome. update on a recent entity. Arch Cardiovasc Dis 101(11–12):779–786
16. Lu LX, Zhou W, Zhang X, Cao Q, Yu K, Zhu C (2006) Short QT syndrome: a case report and review of literature. Resuscitation 71(1):115–121

17. Garberoglio L, Giustetto C, Wolpert C, Gaita F (2007) Is acquired short QT due to digitalis intoxication responsible for malignant ventricular arrhythmias? J Electrocardiol 40(1):43–46
18. Levi AJ (1993) A role for sodium/calcium exchange in the action potential shortening caused by strophanthidin in guinea pig ventricular myocytes. Cardiovasc Res 27(3):471–481
19. Cheng TO (2004) Digitalis administration: an underappreciated but common cause of short QT interval. Circulation. 2004 Mar 9;109(9):e152; author reply e152
20. Hachimi-Idrissi S, Corne L, Maes V, Ramet J (1996) Gitaloxin poisoning in a child. Intensive Care Med 22(12):1442–1444
21. Jowett NI (2002) Foxglove poisoning. Hosp Med 63(12):758–759
22. Bidoggia H, Maciel JP, Capalozza N, Mosca S, Blaksley EJ, Valverde E et al (2000) Sex differences on the electrocardiographic pattern of cardiac repolarization: possible role of testosterone. Am Heart J 140(4):678–683
23. Bigi MAB, Aslani A, Aslani A (2009) Short QT interval: a novel predictor of androgen abuse in strength trained athletes. Ann Noninvasive Electrocardiol 14(1):35–39
24. Charbit B, Christin-Maître S, Démolis J-L, Soustre E, Young J, Funck-Brentano C (2009) Effects of testosterone on ventricular repolarization in hypogonadic men. Am J Cardiol 103(6):887–890
25. Hancox JC, Choisy SC, James AF (2009) Short QT interval linked to androgen misuse: wider significance and possible basis. Ann Noninvasive Electrocardiol 14(3):311–312
26. Gaita F, Giustetto C, Bianchi F, Wolpert C, Schimpf R, Riccardi R et al (2003) Short QT Syndrome: a familial cause of sudden death. Circulation 108(8):965–970
27. Cross B, Homoud M, Link M, Foote C, Garlitski A, Weinstock J et al (2011) The short QT syndrome. J Intervent Card Electrophysiol 31(1):25–31
28. Gollob MH, Redpath CJ, Roberts JD (2011) The short QT syndrome: proposed diagnostic criteria. J Am Coll Cardiol 57(7):802–812
29. Couderc J-P, Lopes CM (2010) Short and long QT syndromes: does QT length really matter? J Electrocardiol 43(5):396–399
30. Patel U, Pavri BB (2009) Short QT syndrome: a review. Cardiol Rev. 17(6):300–303
31. Anttonen O, Junttila J, Giustetto C, Gaita F, Linna E, Karsikas M et al (2009) T-Wave morphology in short QT syndrome. Ann Noninvasive Electrocardiol 14(3):262–267
32. Schimpf R, Wolpert C, Gaita F, Giustetto C, Borggrefe M (2005) Short QT syndrome. Cardiovasc Res 67(3):357–366
33. McPate MJ, Witchel HJ, Hancox JC (2006) Short QT syndrome. Future Cardiol 2(3):293–301
34. Giustetto C, Di Monte F, Wolpert C, Borggrefe M, Schimpf R, Sbragia P et al (2006) Short QT syndrome: clinical findings and diagnostic-therapeutic implications. Eur Heart J 27(20):2440–2447
35. Brugada R, Hong K, Dumaine R, Cordeiro J, Gaita F, Borggrefe M et al (2004) Sudden death associated with short-QT syndrome linked to mutations in HERG. Circulation 109(1):30–35
36. Hong K, Bjerregaard P, Gussak I, Brugada R (2005) Short QT syndrome and atrial fibrillation caused by mutation in KCNH2. J Cardiovasc Electrophysiol 16(4):394–396
37. Bellocq C, van Ginneken ACG, Bezzina CR, Alders M, Escande D, Mannens MMAM et al (2004) Mutation in the KCNQ1 gene leading to the short QT-interval syndrome. Circulation 109(20):2394–2397
38. Hong K, Piper DR, Diaz-Valdecantos A, Brugada J, Oliva A, Burashnikov E et al (2005) De novo KCNQ1 mutation responsible for atrial fibrillation and short QT syndrome in utero. Cardiovasc Res 68(3):433–440
39. Priori SG, Pandit SV, Rivolta I, Berenfeld O, Ronchetti E, Dhamoon A et al (2005) A novel form of short QT syndrome (SQT3) is caused by a mutation in the KCNJ2 gene. Circ Res 96(7):800–807
40. Antzelevitch C, Pollevick GD, Cordeiro JM, Casis O, Sanguinetti MC, Aizawa Y et al (2007) Loss-of-function mutations in the cardiac calcium channel underlie a new clinical entity characterized by ST-segment elevation, short QT intervals, and sudden cardiac death. Circulation 115(4):442–449

41. Warmke JW, Ganetzky B (1994) A family of potassium channel genes related to eag in Drosophila and mammals. Proc Natl Acad Sci USA 91(8):3438–3442
42. James AF, Choisy SCM, Hancox JC (2007) Recent advances in understanding sex differences in cardiac repolarization. Prog Biophys Mol Biol 94(3):265–319
43. Spector PS, Curran ME, Zou A, Keating MT, Sanguinetti MC (1996) Fast inactivation causes rectification of the IKr channel. J Gen Physiol 107(5):611–619
44. Smith PL, Baukrowitz T, Yellen G (1996) The inward rectification mechanism of the HERG cardiac potassium channel. Nature 379(6568):833–836
45. Hancox JC, Levi AJ, Witchel HJ (1998) Time course and voltage dependence of expressed HERG current compared with native rapid delayed rectifier K current during the cardiac ventricular action potential. Pflugers Arch 436(6):843–853
46. Hancox JC, Witchel HJ, Varghese A (1998) Alteration of HERG current profile during the cardiac ventricular action potential, following a pore mutation. Biochem Biophys Res Commun 253(3):719–724
47. Zhou Z, Gong Q, Ye B, Fan Z, Makielski JC, Robertson GA et al (1998) Properties of HERG channels stably expressed in HEK 293 cells studied at physiological temperature. Biophys J 74(1):230–241
48. Liu J, Zhang M, Jiang M, Tseng G-N (2002) Structural and functional role of the extracellular s5-p linker in the HERG potassium channel. J Gen Physiol 120(5):723–737
49. Jiang M, Zhang M, Maslennikov IV, Liu J, Wu D-M, Korolkova YV et al (2005) Dynamic conformational changes of extracellular S5-P linkers in the hERG channel. J Physiol (Lond) 569(Pt 1):75–89
50. Clarke CE, Hill AP, Zhao J, Kondo M, Subbiah RN, Campbell TJ et al (2006) Effect of S5P alpha-helix charge mutants on inactivation of hERG K^+ channels. J Physiol (Lond) 573(Pt 2):291–304
51. Sanguinetti MC, Tristani-Firouzi M (2006) hERG potassium channels and cardiac arrhythmia. Nature 440(7083):463–469
52. Hancox JC, McPate MJ, El Harchi A, Zhang YH (2008) The hERG potassium channel and hERG screening for drug-induced torsades de pointes. Pharmacol Ther 119(2):118–132
53. Schönherr R, Heinemann SH (1996) Molecular determinants for activation and inactivation of HERG, a human inward rectifier potassium channel. J Physiol (Lond) 493(Pt 3):635–642
54. McPate MJ, Duncan RS, Milnes JT, Witchel HJ, Hancox JC (2005) The N588K-HERG K^+ channel mutation in the short QT syndrome: mechanism of gain-in-function determined at 37 °C. Biochem Biophys Res Commun 334(2):441–449
55. Cordeiro JM, Brugada R, Wu YS, Hong K, Dumaine R (2005) Modulation of I(Kr) inactivation by mutation N588K in KCNH2: a link to arrhythmogenesis in short QT syndrome. Cardiovasc Res 67(3):498–509
56. McPate MJ, Zhang H, Adeniran I, Cordeiro JM, Witchel HJ, Hancox JC (2009) Comparative effects of the short QT N588K mutation at 37 °C on hERG K^+ channel current during ventricular, Purkinje fibre and atrial action potentials: an action potential clamp study. J Physiol Pharmacol 60(1):23–41
57. Itoh H, Sakaguchi T, Ashihara T, Ding W-G, Nagaoka I, Oka Y et al (2009) A novel KCNH2 mutation as a modifier for short QT interval. Int J Cardiol 137(1):83–85
58. Sun Y, Quan X-Q, Fromme S, Cox RH, Zhang P, Zhang L et al (2011) A novel mutation in the KCNH2 gene associated with short QT syndrome. J Mol Cell Cardiol 50(3):433–441
59. Brugada R, Hong K, Cordeiro JM, Dumaine R (2005) Short QT syndrome. CMAJ 173(11):1349–1354
60. Zhang H, Kharche S, Holden AV, Hancox JC (2008) Repolarization and vulnerability to re-entry in the human heart with short QT syndrome arising from KCNQ1 mutation–a simulation study. Prog Biophys Mol Biol 96(1–3):112–131
61. Restier L, Cheng L, Sanguinetti MC (2008) Mechanisms by which atrial fibrillation-associated mutations in the S1 domain of KCNQ1 slow deactivation of IKs channels. J Physiol (Lond) 586(Pt 17):4179–4191

62. Abrams CJ, Davies NW, Shelton PA, Stanfield PR (1996) The role of a single aspartate residue in ionic selectivity and block of a murine inward rectifier K^+ channel Kir2.1. J Physiol (Lond) 493(Pt 3):643–9
63. El Harchi A, McPate MJ, Zhang Y hong, Zhang H, Hancox JC (2009) Action potential clamp and chloroquine sensitivity of mutant Kir2.1 channels responsible for variant 3 short QT syndrome. J Mol Cell Cardiol 47(5):743–7
64. Hattori T, Makiyama T, Akao M, Ehara E, Ohno S, Iguchi M, et al (2012) A novel gain-of-function KCNJ2 mutation associated with short QT syndrome impairs inward rectification of Kir2.1 currents. Cardiovasc Res [Internet]. 2011 Dec 8. http://www.ncbi.nlm.nih.gov/pubmed/22155372
65. Antzelevitch C (2006) Brugada syndrome. Pacing Clin Electrophysiol 29(10):1130–1159
66. Chen P-S, Priori SG (2008) The Brugada syndrome. J Am Coll Cardiol 51(12):1176–1180
67. Martini B, Nava A, Thiene G, Buja GF, Canciani B, Scognamiglio R et al (1989) Ventricular fibrillation without apparent heart disease: description of six cases. Am Heart J 118(6):1203–1209
68. Schimpf R, Wolpert C, Bianchi F, Giustetto C, Gaita F, Bauersfeld U et al (2003) Congenital short QT syndrome and implantable cardioverter defibrillator treatment: inherent risk for inappropriate shock delivery. J Cardiovasc Electrophysiol 14(12):1273–1277
69. Schimpf R, Bauersfeld U, Gaita F, Wolpert C (2005) Short QT syndrome: successful prevention of sudden cardiac death in an adolescent by implantable cardioverter-defibrillator treatment for primary prophylaxis. Heart Rhythm 2(4):416–417
70. Hancox JC, McPate MJ, Harchi A, Duncan RS, Dempsey CE, Witchel HJ, et al (2011) The Short QT Syndrome. In: Tripathi ON, Ravens U, Sanguinetti MC, editors. Heart Rate Rhythm [Internet]. Berlin, Heidelberg. pp 431–49. http://www.springerlink.com/content/m8l86l8n3h81w43m/
71. Bjerregaard P, Jahangir A, Gussak I (2006) Targeted therapy for short QT syndrome. Expert Opin Ther Targets 10(3):393–400
72. Duncan RS, McPate MJ, Ridley JM, Gao Z, James AF, Leishman DJ et al (2007) Inhibition of the HERG potassium channel by the tricyclic antidepressant doxepin. Biochem Pharmacol 74(3):425–437
73. Gaita F, Giustetto C, Bianchi F, Schimpf R, Haissaguerre M, Calò L et al (2004) Short QT syndrome: pharmacological treatment. J Am Coll Cardiol 43(8):1494–1499
74. Wolpert C, Schimpf R, Giustetto C, Antzelevitch C, Cordeiro J, Dumaine R et al (2005) Further insights into the effect of quinidine in short QT syndrome caused by a mutation in HERG. J Cardiovasc Electrophysiol 16(1):54–58
75. Sebaugh JL (2011) Guidelines for accurate EC50/IC50 estimation. Pharm Stat 10(2):128–134
76. McPate MJ, Duncan RS, Witchel HJ, Hancox JC (2006) Disopyramide is an effective inhibitor of mutant HERG K^+ channels involved in variant 1 short QT syndrome. J Mol Cell Cardiol 41(3):563–566
77. Schimpf R, Veltmann C, Giustetto C, Gaita F, Borggrefe M, Wolpert C (2007) In vivo effects of mutant HERG K^+ channel inhibition by disopyramide in patients with a short QT-1 syndrome: a pilot study. J Cardiovasc Electrophysiol 18(11):1157–1160
78. Mizobuchi M, Enjoji Y, Yamamoto R, Ono T, Funatsu A, Kambayashi D et al (2008) Nifekalant and disopyramide in a patient with short QT syndrome: evaluation of pharmacological effects and electrophysiological properties. Pacing Clin Electrophysiol 31(9):1229–1232
79. McPate MJ, Duncan RS, Hancox JC, Witchel HJ (2008) Pharmacology of the short QT syndrome N588K-hERG K^+ channel mutation: differential impact on selected class I and class III antiarrhythmic drugs. Br J Pharmacol 155(6):957–966
80. Lerche C, Bruhova I, Lerche H, Steinmeyer K, Wei AD, Strutz-Seebohm N et al (2007) Chromanol 293B binding in KCNQ1 (Kv7.1) channels involves electrostatic interactions with a potassium ion in the selectivity filter. Mol Pharmacol 71(6):1503–1511

81. El Harchi A, McPate MJ, Zhang YH, Zhang H, Hancox JC (2010) Action potential clamp and mefloquine sensitivity of recombinant I KS channels incorporating the V307L KCNQ1 mutation. J Physiol Pharmacol 61(2):123–131
82. Lopez-Izquierdo A, Ponce-Balbuena D, Ferrer T, Sachse FB, Tristani-Firouzi M, Sanchez-Chapula JA (2009) Chloroquine blocks a mutant Kir2.1 channel responsible for short QT syndrome and normalizes repolarization properties in silico. Cell Physiol Biochem 24(3–4):153–160
83. Giustetto C, Schimpf R, Mazzanti A, Scrocco C, Maury P, Anttonen O et al (2011) Long-term follow-up of patients with short QT syndrome. J Am Coll Cardiol 58(6):587–595

Chapter 4
Model Development

In the absence of phenotypically accurate experimental models of K^+ channel mutation linked SQTS variants (SQT1–SQT3), in silico models offer the best complementary method to in vivo and in vitro electrophysiology for investigating the functional consequences of these and other gene mutations. These models can be used for investigations at the single cell, tissue and organ levels. Importantly, explorations to determine the effect of a gene mutation can be performed from the single cell to the tissue and organ levels or in reverse; from the organ to the tissue and single cell levels. Thus, the in silico approach offers a means both of recapitulating kinetic changes to ion channel function and of exploring with specificity, the links between single gene mutations and effects at the single cell, tissue and organ levels. This chapter elucidates on the development of the in silico biophysically detailed and physiologically accurate models used to investigate the functional consequences of SQT1, SQT2 and SQT3.

4.1 Modelling Voltage-dependent Channels: Hodgkin-Huxley Versus Markov Chain Models

Alan Lloyd Hodgkin and Andrew Fielding Huxley developed the first model of cellular excitability in 1952 [1] for which they were awarded a Nobel prize. The model, which reproduced their experimental data on the currents from the Na^+ and K^+ channels of the Squid Giant Axon was based on biophysical characterisation of the conductance of these channels which generate the axon's action potential. Today, Hodgkin-Huxley (HH) models still form the basis of most ionic channel model development because estimating the parameters necessary to reproduce experimental data is relatively straight-forward with modern computational methods.

Hodgkin and Huxley's work preceded the identification of ion channel proteins or single channel current recording. They postulated that the electrical currents flowing through the cell membrane was due to freely moving gating particles

I. Adeniran, *Modelling the Short QT Syndrome Gene Mutations*,
Springer Theses, DOI: 10.1007/978-3-319-07200-5_4,

within it. Consequently, they produced equations to describe macroscopic ionic current flow, incorporating concepts of gating [1], but no identification of ion channel proteins as their work preceded this and single channel measurements. Molecularly, it is now known that proteins within the membrane form a pore through which ions flow. These pores are selectively permeable to different ions. Their permeability is mediated by several factors including sensitivity to voltage and ligand binding [2, 3].

From single channel recordings of ion channel activity, we now know that ion channels undergo rapid and stochastic transitions between conducting (open) or non-conducting (closed) states [4]. Occupancy of these states is governed by conformational changes of the underlying protein structure of these channels. With Markov chain models, these conformational changes can be represented accurately with state diagrams. Markov chain models therefore capture ion channel kinetics more precisely than HH models [5]. Their only limitation in comparison with HH models is the greater difficulty in estimating the necessary parameters from experimental data.

In this thesis, the SQT1 and SQT2 variants of the SQTS are modeled using the Markov chain model formalism while the SQT3 variant uses the Hodgkin-Huxley formalism. The reasons for using a HH model for SQT3 will be discussed below. As will be shown, the three models developed can reproduce accurately experimental data and reproduce electrophysiological behaviour.

4.1.1 The Hodgkin-Huxley Formalism

In 1952, Sir Alan Lloyd Hodgkin and Sir Andrew Fielding Huxley discovered that membrane ionic conductance was modulated by membrane potential [1]. They described a mathematical model of the cell, which was able to reproduce the action potential of a Squid Giant Axon [1]. They studied the time course of the ionic current when subjected to different voltage steps and investigated the relationship between membrane potential and membrane current. From their experiments, they were able to separate the ionic current into three components—an inward Na^+ current (I_{Na}), an outward K^+ current (I_K) and a leakage current (I_L) carried by other unspecified ions. Thus, the ionic current can be written as:

$$I_{ion} = I_{Na} + I_K + I_L \tag{4.1}$$

They described each ionic current component as a product of two factors:

1. an instantaneous function of potential and.
2. a continuous function of voltage and time.

The current and membrane potential relationship (I–V relationship) for each ion was linear and passed through the equilibrium potential of that ion. Consequently, it could be described using Ohm's law with an accounting for the equilibrium

Fig. 4.1 A state-transition diagram of a two-state model of an ion channel

potential of the particular ion. The instantaneous function of potential is thus driving force and is equivalent to the difference between the membrane potential and the equilibrium potential of the specific ion ($V_m - E_x$).

The second factor (continuous function of voltage and time) is the conductance of the ion obtained by dividing the current from that ion by the driving force: $G_x = I_x / (V_m - E_x)$. It describes a gradual change in the membrane permeability for that ion. Each current in the model can then be written as:

$$\begin{aligned} I_{Na} &= G_{Na}(V_m - E_{Na}) \\ I_K &= G_K(V_m - E_K) \\ I_L &= G_L(V_m - E_L) \end{aligned} \tag{4.2}$$

Hodgkin and Huxley proposed a gating mechanism to describe the kinetics of each ionic current. Each gating particle could be on either side of the membrane and carries with it a net charge and consequently a membrane potential, which allows it to switch position from one side of the membrane to the other. The gate or gating particle could then be in an open or closed state depending on the voltage thereby modulating the movement of ions through the membrane. A kinetic representation is shown in Fig. 4.1:

C is the closed state, O is the open state, α and β are voltage-dependent transition rate constants governing the rate of transition from one state to the other.

If N represents the fraction of gates in the open state, then following a change in membrane potential, the net rate of change in the fraction of open gates can be calculated using the state diagram in Fig. 4.1 as:

$$\frac{dN}{dt} = \alpha(1 - N) - \beta N \tag{4.3}$$

At steady state, dN/dt = 0 and the steady state fraction of open gates (N_∞) is:

$$N_\infty = \frac{\alpha}{\alpha + \beta} \tag{4.4}$$

A change in membrane potential will cause a deviation from steady state and consequently, a change in the fraction of open gates. The time it takes for the channel to return to steady state is the time constant and is given by:

$$\tau_N = \frac{1}{\alpha + \beta} \tag{4.5}$$

Taking into account the fraction of open gates, Hodgkin and Huxley represented the conductance of a channel by:

$$G_x = \overline{G}_X N \tag{4.6}$$

where $\overline{G}_X$ is the maximal conductance of the ion channel and N is the fraction of gates in the open state.

From their experiments, Hodgkin and Huxley were able to describe the properties of each ionic current using one or more gates, acting independently of each other. These gates controlled the kinetic properties of the channel and for the channel to conduct ions, all the gates must be open. They discovered that the K^+ channel could be represented using four identical, independent activation gates (n) governed by a first-order voltage-dependent process. Consequently, its conductance is given by:

$$G_K = \overline{G}_K n^4 \tag{4.7}$$

where $\overline{G}_K$ is the maximal potassium conductance. The Na^+ channel displayed activation and inactivation behavior; inactivation being the state where the channel is open but non-conducting or blocked and hence, cannot conduct current. The kinetics of the channel is represented using three independent activation gates (m) and one independent inactivation gate (h) written as:

$$G_{Na} = \overline{G}_{Na} m^3 h \tag{4.8}$$

where $\overline{G}_{Na}$ is the maximal sodium conductance, m is the fraction of open activation gates and h is the fraction of open inactivation gates.

For each channel to conduct current, all the gates must be in the open state. Depolarisation causes the Na^+ and K^+ channels' m and n gates to open. This is referred to as *activation*. The h gate of the Na^+ channel however is closed by depolarisation (referred to as *inactivation*), which would result in the closure of the whole channel as all the gates must be open for the channel to conduct current.

4.1.1.1 The Complete Hodgkin-Huxley Model

The complete Hodgkin-Huxley (HH) model can then be written as:

$$\begin{aligned} I_{Na} &= G_{Na} m^3 h (V_m - E_{Na}) \\ I_K &= G_K n^4 (V_m - E_K) \\ I_L &= G_L (V_m - E_L) \end{aligned} \tag{4.9}$$

4.1.2 Markov Chain Models

While the Hodgkin-Huxley model was forward-looking and closely reproduced macroscopic current behaviour, it suffers from the assumption of independent gating. Experiments since its conception show that this is not accurate. For example, for the Na^+ channel to inactivate, it must first be in an activated state, i.e., activation and inactivation are coupled and not independent processes [6, 7]. Aldrich et al. [8] also showed that Na^+ channels might also show inactivation that is not voltage-dependent but state-dependent.

In contrast, Markov chain models use state diagrams to express conformational changes of the ion channel protein and assume that transitions from one state to another is dependent only on the present state. Thus, they can be mapped structurally to the molecular representation of the ion channel. HH models can be considered to be a subset of Markov chain models so that any HH model can be written as a Markov chain model scheme but the converse does not apply [9, 10]. An example of a Markov chain model state diagram is shown below where S_i represent the distinct conformational states which the channel can occupy.

$$S_1 \Leftrightarrow S_2 \Leftrightarrow \ldots \Leftrightarrow S_n \tag{4.10}$$

If $P(S_i, t)$ represents the probability of the channel being in state S_i at time t and $P(S_i \rightarrow S_j)$ represent the probability of a transition from state S_i to S_j, where i,j run from 1 to n, we can write:

$$P(S_i, t) \underset{P(S_j \rightarrow S_i)}{\overset{P(S_i \rightarrow S_j)}{\longleftrightarrow}} P(S_j, t) \tag{4.11}$$

From Eq. (4.10), we can obtain an expression for the time evolution of the states of the ion channels as:

$$\frac{dP(S_i, t)}{dt} = \sum_{j=1}^{n} P(S_j, t) P(S_j \rightarrow S_i) - \sum_{j=1}^{n} P(S_i, t) P(S_i \rightarrow S_j) \tag{4.12}$$

Equation (4.12) is called *the master equation* [11, 12]. The term on the left of the minus sign is the *source* term and represents the transitions entering state S_i while the term on the right of the minus sign represents the *sink* term and represents all contributions leaving state S_i. The time evolution depends only on the present state of the system, and is defined entirely by knowledge of the set of transition probabilities (Markovian system) [13–15].

A small patch of cell membrane will contain of a large number of identical channels. Therefore, in the limit, the *master equation* can be replaced by its macroscopic interpretation. Equation (4.10) can then be replaced by:

$$S_i \underset{r_{ji}}{\overset{r_{ij}}{\Leftrightarrow}} S_j \tag{4.13}$$

where S_i and S_j are now the probabilities of the channel being in these states and r_{ij} and r_{ji} become the transition rate constants. The time rate of evolution of the occupancy of different states by the channel (Eq. 4.12) can then be rewritten as:

$$\frac{dS_i}{dt} = \sum_{j=1}^{n} S_j r_{ji} - \sum_{j=1}^{n} S_i r_{ij} \tag{4.14}$$

The rate constants, r in Eq. (4.13) can be voltage-dependent. This voltage-dependence is due to the sensitivity of the channel conformational changes to membrane potential changes. Determination or extraction of the rate constants for a Markov chain model is quite difficult and is one of its limitations.

Changes in the membrane potential set up a transmembrane electric field, which influences formal charges or induced charges (dipoles) within the protein, thus setting up energy barriers. Conformational changes of the channel protein will then only occur when the rate constants surmount these energy barriers [16, 17]. According to reaction rate theory [16, 17], the rate constants depend exponentially on the free energy barrier between two states:

$$r(V) = r_0 e^{\frac{-\Delta G(V)}{RT}} \tag{4.15}$$

where r_0 is a constant, $\Delta G(V)$ is the free energy barrier, R is the thermodynamic gas constant and T is the temperature. The free energy barrier can be expressed as:

$$\Delta G(V) = G^*(V) - G_0(V) \tag{4.16}$$

where $G^*(V)$ is the free energy of an intermediate state (activated complex) and $G_0(V)$ is the free energy of the initial state (Fig. 4.2). To make a transition from an initial state to a final state, ion channels have to overcome the free energy barrier, which is the difference in energy between $G_0(V)$ and $G^*(V)$. The smaller this free energy barrier is, the faster are the kinetics of the channel and the more ion channels that can make the transition [18].

The free energy can be expanded with a Taylor series as:

$$G_i(V) = A_i + B_i V + C_i V^2 \tag{4.17}$$

A_i, B_i and C_i describe the potential energy barriers between each conformational state of the ion channel. A_i represents the energy barrier height in the absence of an electrical field, B_i represents the energy barrier height due to interactions between isolated charges and dipoles [12, 18–21] and C_i represents total distortion

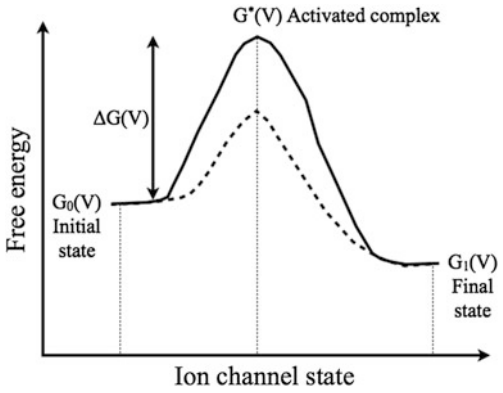

Fig. 4.2 Free energy profile of conformational changes in ion channels. The figure shows the free energy involved during the transition from one state to another. G_0 is the initial state, G^* is the intermediate state (activated complex) and G_1 is the final state. $\Delta G(V)$ is the free energy barrier which the ion channel has to overcome to make the transition from G_0 to G_1. A smaller energy barrier means faster kinetics, as more ion channels will have the required energy to make the transition. Figure modified from [18]

polarisation and pressure induced by V [12, 18–21] or mechanical restrictions on the charges by the channel protein's structure [18].

Making use of Eqs. (4.16) and (4.17), Eq. (4.15) can then be rewritten as:

$$\begin{aligned} r(V) &= r_0 e^{\frac{-[(A^* + B^*V + C^*V^2 + \cdots) - (A_0 + B_0V + C_0V^2 + \cdots)]}{RT}} \\ r(V) &= r_0 e^{\frac{-[(A + BV + CV^2 + \cdots)]}{RT}} \end{aligned} \tag{4.18}$$

In the limiting case of small transmembrane voltages, the nonlinear terms (V^2 and higher) may be insignificant and Eq. (4.18) can be simplified to:

$$r(V) = r_0 e^{\frac{-[(A + BV)]}{RT}} \tag{4.19}$$

which is the commonly used form.

4.2 Development of the SQT1 Markov Model

4.2.1 The Base I_{Kr} Markov Model

To develop a Markov model that reflected the kinetic and structural changes induced by the SQT1 mutation on hERG, an existing cardiac I_{Kr} Markov model was modified. This initial base Markov model (Fig. 4.3) was based on the hERG/

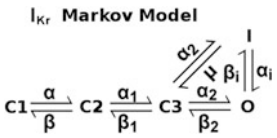

Fig. 4.3 Markov model state diagram of cardiac I_{Kr} [22–25]

I_{Kr} Markov model formulation of Kiehn et al. [22], Clancy and Rudy [23], Lu et al. [24] and Wang et al. [25]. The macroscopic current density of hERG/I_{Kr} is calculated as:

$$I_{I_{Kr}} = G_{I_{Kr}} \cdot P_{O,I_{Kr}} \cdot (V_m - E_{rev}) \tag{4.20}$$

where $P_{O,IKr}$ is the sum of all I_{Kr} channel open probabilities, V_m is the membrane potential, E_K is the potassium reversal potential and G_{IKr} is the maximum membrane conductance of I_{Kr} and is given by:

$$G_{I_{Kr}} = \sigma \cdot g_{I_{Kr}} \tag{4.21}$$

with σ being the channel density and g_{IKr} the unitary channel conductance. The state probabilities are described by first order differential equations as described in Eq. (4.14). The parameters of the model were fit to measured experimental data for activation, inactivation and deactivation [23].

The gating scheme was originally produced by the study of Kiehn et al. [22] following the study by Wang et al. [25]. The transition rates of the model were then modified (as described in Sect. 4.2.2) to account for the proper behaviour of macroscopic currents relative to data obtained at physiological temperatures and ionic concentrations from guinea pig ventricular myocytes [23].

The model consists of three closed states (C1, C2 and C3), an open state (O) and an inactivated state (I). Inactivation can occur from the open or the closed state but does so preferentially from the open state [23, 26]. The transition (α1, β1) between states C2 and C3 is voltage independent [23, 25]. The transitions from states C3 to I (C3 → I) and from C3 to O (C3 → O) are the same [22]. The model also includes dependencies on the extracellular K^+ concentration $[K^+]_{out}$; the transition between O and I as well as the maximal I_{Kr} conductance. Increasing $[K^+]_{out}$ has the effect of decreasing the transition rate between O and I.

4.2.2 The SQT1 Markov Model

The base I_{Kr} Markov model described above (Sect. 4.2.1) was modified to incorporate the experimentally observed kinetic properties of WT and N588K-mutated hERG/I_{Kr} channel. These kinetic properties include:

(1) the profound (> +60 mV) shift in the voltage dependence of inactivation of N588K-hERG that alters rectification of I_{hERG} [27–30];

(2) the substantial increase of I_{hERG} early during the ventricular action potential (AP) waveform [27–30]; and
(3) the generation of rapid, transient, outward currents in response to premature, depolarizing stimuli under 'paired stimuli' experiments [30].

To obtain the transition rates of the Markov chain model that reproduced the experimentally observed kinetic properties of WT and N588K-hERG/I_{Kr}, experimental current-voltage (I–V) relationships for WT and N588K-hERG/I_{Kr} [30] were simulated using the voltage clamp protocol in [27, 30]. In order to simulate the experimental I–V relationship, the original I_{Kr} transition rate equations were modified. First, a simulated voltage clamp as described in [30] above was set up: the membrane potential was held at −80 mV and then depolarised briefly to −40 mV (to evaluate instantaneous current), followed by 2 s depolarisations to a range of potentials from −40 mV to +60 mV (in 10 mV increments); finally, 'tail' currents were elicited by repolarisation to −40 mV for 4,000 ms. The currents at the end of the 2000 ms depolarising steps were normalised and compared to the experimental data.

To obtain a good agreement with the experimental data [27, 30], variables that modified each transition rate were introduced. The values of these variables were calculated by minimising the least squared difference between the experimental data and the simulation result. The BFGS (Broyden-Fletcher-Goldfarb-Shano) method [31] and a cubic spline interpolation algorithm [32] were used for the minimisation. The variables that produced the best fit and behaviour of macroscopic currents relative to the experimental data were selected [33]. Figure 6.2 aiii–biii (the full Markov Chain model) shows the simulated I–V relationship for both the WT and N588K mutation compared to the experimental data, which is the end pulse currents produced by the model and experimental data for both conditions The SQT1 Markov model reproduces quite closely the experimental data in both the WT and N588K mutation conditions.

The Markov chain model formulations were validated by comparing simulated results from different voltage clamp protocols—premature stimuli (Fig. 6.3biii) and AP Clamp (Fig. 6.3bi and bii)—to experimentally obtained data. To simulate the AP clamp, the same digitised ventricular AP used to generate the experimental data [30] was used to elicit the I_{hERG} in the simulation. For paired premature stimuli simulations, the protocol utilising paired ventricular AP waveform commands was applied [30]. Following an initial ventricular AP command, a second, premature AP command waveform was superimposed 100 ms before the APD_{90} (action potential duration at 90 % repolarization) of the first command. The premature stimulus was then applied in 10 ms increments for subsequent sweeps [30]. The modified model rate transition equations and parameters of the I_{Kr} Markov model for WT and N588K conditions are presented below.

$$I_{Kr} = G_{Kr} \cdot O_{Kr} \cdot (V_m - E_{Kr}) \tag{4.22}$$

G_{Kr} is the channel membrane conductance, O_{Kr} is the channel open probability, V_m is the membrane potential and E_{Kr} is the potassium reversal potential.

$$G_{Kr} = 0.0243 \times [K^+]_o^{0.59} \tag{4.23}$$

$[K^+]_o$ is the extracellular potassium concentration.

$$E_{Kr} = \frac{RT}{F} \log \frac{[K^+]_o}{[K^+]_i} \tag{4.24}$$

R is the universal gas constant, T is the temperature, F is Faraday's constant, $[K^+]_o$ and $[K^+]_i$ are the extracellular and intracellular potassium concentrations respectively.

4.2.2.1 WT

$$\alpha_1 = 2.172 \tag{4.25}$$

$$\beta_1 = 1.077 \tag{4.26}$$

$$\alpha_2 = 0.00655 \times e^{0.027735765 \times (V_m - 36)} \tag{4.27}$$

$$\beta_2 = 0.001908205 \times e^{-0.0148902 V_m} \tag{4.28}$$

$$\alpha_i = 0.04829 \times e^{-0.039984 \times (V_m + 25)} \times \left(\frac{4.5}{K_O}\right) \tag{4.29}$$

$$\beta_i = 0.2624 \times e^{0.000942 V_m} \times \left(\frac{4.5}{K_O}\right)^{0.3} \tag{4.30}$$

$$\alpha = 0.00555 \times e^{0.05547153 (V_m - 12)} \tag{4.31}$$

$$\beta = 0.002357 \times e^{-0.036588 V_m} \tag{4.32}$$

$$\mu = \frac{\alpha_i \beta_2}{\beta_i} \tag{4.33}$$

4.2.2.2 N588K

$$\alpha_1 = 2.172 \tag{4.34}$$

$$\beta_1 = 0.5385 \tag{4.35}$$

$$\alpha_2 = 0.001965 \times e^{0.05547153\times(V_m-21)} \tag{4.36}$$

$$\beta_2 = 2.260489 \times 10^{-6} \times e^{-0.0925782V_m} \tag{4.37}$$

$$\alpha_i = 0.439 \times e^{-0.02352\times(V_m+40)} \times \left(\frac{4.5}{K_O}\right) \tag{4.38}$$

$$\beta_i = 0.0164 \times e^{0.000942\times(V_m+15)} \times \left(\frac{4.5}{K_O}\right)^{0.3} \tag{4.39}$$

$$\alpha = 0.00555 \times e^{0.05547153(V_m+3)} \tag{4.40}$$

$$\beta = 0.002357 \times e^{-0.036588V_m} \tag{4.41}$$

$$\mu = \frac{\alpha_i \beta_2}{\beta_i} \tag{4.42}$$

$\alpha_1, \beta_1, \alpha_2, \beta_2, \alpha_i, \beta_i, \alpha, \beta, \mu$ are state transition rates.

4.3 Development of the SQT2 Markov Model

4.3.1 The Base I_{Ks} Markov Model

The initial base Markov chain model (Fig. 4.4) used in developing the SQT2 WT and V307L mutant Markov models was based on the I_{Ks} Markov chain model formulation of Koren et al. [34], Zagotta et al. [35] and Silva and Rudy [26]. The Markov state transition diagram, for this base model is shown in Fig. 4.4. It is developed based on experimental data at physiological temperature (37 °C) including data from human ventricular myocytes representing human I_{Ks} activation kinetics [36] and deactivation kinetics [37].

As described in Sect. 4.1.2, channel activation and inactivation are dependent. In 1994, Zagotta et al. [35, 38] suggested that channel activation also consists of dependent transitions. They proposed a model for *Shaker* K^+ channels with four subunits, each with identical activation rates. Each subunit was suggested to undergo two conformal transitions; say R1 (rest state) and R2 (intermediate state) prior to entering the activated state (A). Figure 4.5 shows one of the four subunits

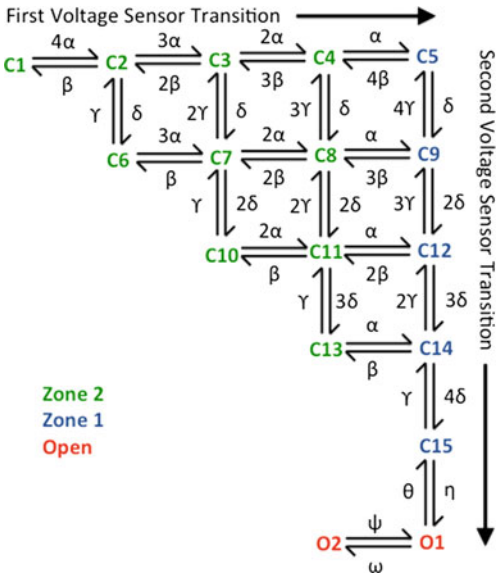

Fig. 4.4 Markov model state transition diagram of the I_{Ks} channel. There are three zones: zone 2 (*green*) consists of all closed states with voltage sensors that are yet to complete the first transition; zone 1 (*blue*) consists of the closed states where all four voltage sensors have completed the first transition; and the open zone (*red*)

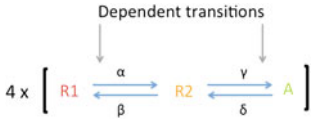

Fig. 4.5 A model of K^+ channel that undergoes two transitions before channel opening. R1 is the rest state, R2 is the intermediate state and A is the activated (open) state. Modified from [9, 26]

with the three states, R1, R2 and A. Silverman et al. [39] provided experimental data in 2003 validating Zagotta et al's two-stage voltage-sensor transition. They found that arginine residues in the voltage sensor (S4) of the *Shaker* K^+ channel interact sequentially with acidic residues in S2, thus providing a mechanism for the two-stage voltage-sensor transition.

The base I_{Ks} Markov model (Fig. 4.4) is based on this two-stage voltage sensor transition principle. It shows all the possible conformations of the channel's four subunits with a unique combination of their voltage sensor positions. It consists of 15 closed states (C_1 to C_{15}) and two open states (O_1 and O_2) [9, 26]. It contains three zones: an activated (open) zone which is encoded in red; zone 2 (green) consists of all those closed states where the voltage sensors are yet to complete the

first transition; and zone 1 (blue) consists of those closed states where the voltage sensors have made this first transition [9, 26].

Each left to right transition represents the movement of a voltage sensor from its rest state (R1) to the intermediate state (R2) while each top to bottom transition represents a voltage sensor movement from the intermediate state (R2) to the activated (A) state. For example, C_2 has three sensors in R1 and one in R2; C_8 has one voltage sensor in R1, two in R2 and one in A; C_{13} has one voltage sensor in R2 and three in A. All such combinations are represented by the 15 closed states and when all the voltage sensors are activated (C_{15}), a cooperative *voltage-independent* transition to the open state O_1 occurs before a final cooperative *voltage-dependent* transition to the open state O_2.

The first open state (O_1) models a cooperative voltage-independent transition opening to reproduce steady sate activation measurements [40] according to the work of Loussouarn et al. [41]. On application of Phosphatidylinositol-4,5-bisphosphate (PIP_2) to I_{Ks} channels on excised patches of cell membrane, they discovered that it affected their open probability markedly but had no effect on the voltage-dependent properties of the channel. Koren et al. [34] also observed this in *Shaker* K^+ channels. When the I_{Ks} channel is probed with rubidium, a second open state (O_2) responsible for two experimentally observed exponential components of deactivation is evident [42]. The macroscopic current density of I_{Ks} is calculated similar to Eqs. (4.20)–(4.21). A full description of the derivation of the initial base Markov model can be found in Silva and Rudy [26].

4.3.2 The SQT2 Markov Model

Experimental current-voltage (I–V) relationships for I_{Ks} [43] were simulated using the voltage clamp protocol in [43]. In order to simulate the experimental I–V relationship, the original I_{Ks} transition rate equations were modified. First, a simulated voltage clamp as described in [43] above was set up (Fig. 7.2aii–bii): the membrane potential was held at −80 mV and then depolarised briefly to −40 mV for 50 ms (to evaluate instantaneous current), followed by 3 s depolarisations to a range of potentials from −70 mV to +60 mV (in 10 mV increments); finally, 'tail' currents were elicited by repolarisation to −40 mV for 5 s. The currents at the end of the 3 s depolarising steps were normalised and compared to the experimental data.

To obtain a good agreement with the experimental data, variables that modified each transition rate were introduced. The values of these variables were calculated by minimising the least squared difference between the experimental data and the simulation result. The Nelder-Mead Simplex algorithm [44] was used for the minimisation. The variables that produced the best fit and behaviour of macroscopic currents relative to the experimental data were selected [33]. Figure 7.2aiii and biii show the simulated I–V relationship for both the WT and V307L mutation compared to the experimental data. The SQT2 Markov model reproduces quite

closely the experimental data in both the WT and V307L mutation conditions. The modified model rate transition equations and parameters of the I_{Ks} Markov model for WT and V30L conditions are presented below.

$$I_{Ks} = G_{Ks} \cdot O_{Ks} \cdot (V_m - E_{Ks}) \tag{4.43}$$

$$G_{Ks} = 0.779 \cdot \left(1 + \frac{0.6}{1 + \left(\frac{3.8 \cdot 10^{-5}}{[Ca^{2+}]_i} \right)^{1.4}} \right) \tag{4.44}$$

$$O_{Ks} = O_1 + O_2 \tag{4.45}$$

$$E_{Ks} = \frac{R \cdot T}{F} \cdot \log \frac{[K^+]_o + P_{Na/K} \cdot [Na^+]_i}{[K^+]_i + P_{Na/K} \cdot [Na^+]_i} \tag{4.46}$$

4.3.2.1 WT

$$\alpha = 5.56 \cdot 10^{-5} \cdot \exp\left\{ 3.61 \cdot 10^{-1} \cdot \frac{Vm \cdot F}{R \cdot T} \right\} \tag{4.47}$$

$$\beta = 8.25 \cdot 10^{-6} \cdot \exp\left\{ -9.23 \cdot 10^{-2} \cdot \frac{Vm \cdot F}{R \cdot T} \right\} \tag{4.48}$$

$$\gamma = 3.78 \cdot 10^{-4} \cdot \exp\left\{ 8.68 \cdot 10^{-1} \cdot \frac{Vm \cdot F}{R \cdot T} \right\} \tag{4.49}$$

$$\delta = 1.32 \cdot 10^{-4} \cdot \exp\left\{ -3.30 \cdot 10^{-1} \cdot \frac{Vm \cdot F}{R \cdot T} \right\} \tag{4.50}$$

$$\theta = 6.10 \cdot 10^{-4} \tag{4.51}$$

$$\eta = 1.95 \cdot 10^{-3} \cdot \exp\left\{ -4.81 \cdot 10^{-1} \cdot \frac{Vm \cdot F}{R \cdot T} \right\} \tag{4.52}$$

$$\psi = 6.25 \cdot 10^{-4} \cdot \exp\left\{ 1.27 \cdot 10^{-0} \cdot \frac{Vm \cdot F}{R \cdot T} \right\} \tag{4.53}$$

$$\omega = 3.50 \cdot 10^{-4} \cdot \exp\left\{-6.79 \cdot 10^{-1} \cdot \frac{Vm \cdot F}{R \cdot T}\right\} \tag{4.54}$$

4.3.2.2 V307L

$$\alpha = 2.52 \cdot 10^{-5} \cdot \exp\left\{3.61 \cdot 10^{-1} \cdot \frac{Vm \cdot F}{R \cdot T}\right\} \tag{4.55}$$

$$\beta = 2.51 \cdot 10^{-5} \cdot \exp\left\{-9.23 \cdot 10^{-2} \cdot \frac{Vm \cdot F}{R \cdot T}\right\} \tag{4.56}$$

$$\gamma = 1.71 \cdot 10^{-3} \cdot \exp\left\{8.68 \cdot 10^{-1} \cdot \frac{Vm \cdot F}{R \cdot T}\right\} \tag{4.57}$$

$$\delta = 6.45 \cdot 10^{-4} \cdot \exp\left\{-3.30 \cdot 10^{-1} \cdot \frac{Vm \cdot F}{R \cdot T}\right\} \tag{4.58}$$

$$\theta = 3.40 \cdot 10^{-3} \tag{4.59}$$

$$\eta = 4.75 \cdot 10^{-4} \cdot \exp\left\{-4.81 \cdot 10^{-1} \cdot \frac{Vm \cdot F}{R \cdot T}\right\} \tag{4.60}$$

$$\psi = 1.93 \cdot 10^{-3} \cdot \exp\left\{1.27 \cdot 10^{0} \cdot \frac{Vm \cdot F}{R \cdot T}\right\} \tag{4.61}$$

$$\omega = 4.52 \cdot 10^{-4} \cdot \exp\left\{-6.79 \cdot 10^{-1} \cdot \frac{Vm \cdot F}{R \cdot T}\right\} \tag{4.62}$$

where G_{Ks} is the membrane channel conductance, $[Ca^{2+}]_i$ is the intracellular calcium concentration, O_{Ks} is the channel open probability, O_1 and O_2 are the probabilities of being in these pen states respectively, E_{Ks} is the potassium reversal potential, R is the universal gas constant, T is the temperature, F is Faraday's constant, $[K^+]_o$ and $[K^+]_i$ are the extracellular and intracellular potassium concentrations respectively, $[Na^+]_o$ and $[Na^+]_i$ are the extracellular and intracellular sodium concentrations respectively, $P_{Na/K}$ is the Na^+:K^+ permeability ratio, V_m is the membrane potential and $\alpha, \beta, \gamma, \delta, \theta, \eta, \psi, \omega$ are state transition rates (see Fig. 4.4).

4.4 Development of the SQT3 Hodgkin-Huxley Model

4.4.1 The Base I_{KI} Model

The base I_{KI} model used in the formulation of the SQT3 WT, WT-D172N and D172N formulations was that of ten Tusscher et al. [45, 47]. Their formulation was based on that used in the Priebe-Beuckelmann et al. model [48]. The formulation is:

$$I_{K1} = G_{K1}\sqrt{\frac{K_o}{5.4}}x_{K1\infty}(V - E_K) \tag{4.63}$$

where E_K is the potassium reversal potential, V is the membrane potential, G_{KI} is the membrane conductance, $x_{KI\infty}$ is a rectification factor that is time-independent and a function of voltage. It describes the open probability of the channel. $\sqrt{K_o/5.4}$ represents the K_o dependence of I_{KI} and ten Tusscher et al. [45–47] assumed it to be similar to that of animal myocytes due to a lack of data on the K_o dependence of human myocytes. Fortuitously, Sakmann and Trube [49] have described this square root dependence in mammalian ventricle while Bailly et al. [50] (and others) have confirmed this in human ventricular myocytes.

This is a Hodgkin-Huxley type model and not a Markov model as was used for the SQT1 and SQT2 formulations. Yan and Ishihara [51] have developed an I_{KI} Markov model but in order to more accurately represent the quasi-instantaneous dynamics of I_{KI} (it maintains its steady state values during applied membrane potential changes), they applied a quasi-steady state approach in the development of their Markov model. The Markov model also does not represent the square root dependence of the conductance on K_o. A Hodgkin-Huxley formulation for I_{KI} was thus adopted for formulating the SQT3 models. The formulation in Eq. (4.63) assumes that the gating kinetics are sufficiently fast to be considered instantaneous.

4.4.2 The SQT3 Hodgkin-Huxley Model

The base I_{K1} model was modified to incorporate the experimentally observed kinetic properties of the WT, WT-D172N and D172N-mutant $I_{Kir,2.1}$. These kinetic properties include:

1. the marked augmentation of outward Kir2.1 current through D172N channels [52, 53]; and
2. the rightward voltage-shift of peak repolarising current during both ventricular and action potential (AP) clamp commands [52, 53].

To obtain the model parameters that reproduced the experimentally-observed kinetic properties of WT, WT-D172N and D172N Kir2.1 current ($I_{Kir,2.1}$), experimental current-voltage (I–V) relationships for WT, WT-D172N and D172N

$I_{Kir,2.1}$ were simulated using the voltage clamp protocol from El Harchi et al. [53]. Variable values for the modified model equations were obtained by minimising the least-squared difference between the experimental data and the simulation. The variables that produced the best fit and behaviour of macroscopic currents relative to the experimental data were selected (see Eqs. (4.64)–(4.72)). The minimisation was performed using the Broyden-Fletcher-Goldfarb-Shanno (BFGS) algorithm [31]. The SQT3 model reproduced quite closely the experimental data in all the three conditions.

The WT conductance was adjusted to show the same peak current density as the original ten Tusscher et al. [45–47] I_{K1} formulation current density during the I–V relation, thus maintaining the overall current densities, APD_{90} and dynamic properties of the ten Tusscher et al. human ventricular model [45–47]. Relative current proportions for WT, heterozygous (WT-D172N) and homozygous (D172N) conditions were then scaled using relative proportions of peak $I_{Kir,2.1}$ obtained previously from AP clamp experiments [53] (V_{hold} of -80 mV and E_{rev} of $\sim$ −88 to −89 mV). Peak outward D172N and WT-D172N I_{K1} was respectively $\sim$4.6-fold and $\sim$2.2-fold that for WT $I_{Kir2.1}$. The simulated AP clamp data (Fig. 8.1ci–ciii) matched closely prior experimental observations [53]. The modified model equations and parameters of I_{K1} for WT, WT-D172N and D172N conditions are presented below.

4.4.2.1 WT

$$\alpha_{K1} = \frac{0.07}{1 + e^{0.017(V - E_K - 200.2)}} \tag{4.64}$$

$$\beta_{K1} = \frac{3e^{0.0003(V - E_K + 100.2)} + e^{0.08(V - E_K - 8.7)}}{1 + e^{-0.024(V - E_K)}} \tag{4.65}$$

$$G_{K1} = 4.8\frac{nS}{pF} \tag{4.66}$$

4.4.2.2 WT-D172N

$$\alpha_{K1} = \frac{0.1}{1 + e^{0.023(V - E_K - 199.9)}} \tag{4.67}$$

$$\beta_{K1} = \frac{3e^{0.0002(V-E_K+100.4)} + e^{0.07(V-E_K-9.8)}}{1 + e^{-0.021(V-E_K)}} \tag{4.68}$$

$$G_{K1} = 6.27\frac{nS}{pF} \tag{4.69}$$

4.4.2.3 D172N

$$\alpha_{K1} = \frac{0.1}{1 + e^{0.05(V-E_K-199.9)}} \tag{4.70}$$

$$\beta_{K1} = \frac{3e^{0.0002(V-E_K+100.1)} + e^{0.08(V-E_K-10.3)}}{1 + e^{-0.006(V-E_K)}} \tag{4.71}$$

$$G_{K1} = 11.32\frac{nS}{pF} \tag{4.72}$$

References

1. Hodgkin AL, Huxley AF (1952) A quantitative description of membrane current and its application to conduction and excitation in nerve. J Physiol (Lond) 117(4):500–544
2. Hille B (2001) Ion channels of excitable membranes, 3rd edn. Sinauer Associates, Sunderland
3. Armstrong CM, Hille B (1998) Voltage-gated ion channels and electrical excitability. Neuron 20(3):371–380
4. Sakmann B, Neher E (2009) Single-channel recording, 2nd edn, 1995 2nd printing. Springer, New York
5. Cannon RC, D'Alessandro G (2006) The ion channel inverse problem: neuroinformatics meets biophysics. PLoS Comput Biol 2(8):e91
6. Armstrong CM, Bezanilla F (1977) Inactivation of the sodium channel. II. Gating current experiments. J Gen Physiol 70(5):567–590
7. Bezanilla F, Armstrong CM (1977) Inactivation of the sodium channel. I. Sodium current experiments. J Gen Physiol 70(5):549–566
8. Aldrich RW (1981) Inactivation of voltage-gated delayed potassium current in molluscan neurons. A kinetic model. Biophys J 36(3):519–532
9. Rudy Y, Silva JR (2006) Computational biology in the study of cardiac ion channels and cell electrophysiology. Q Rev Biophys 39(1):57–116
10. Fitzhugh R (1965) A kinetic model of the conductance changes in nerve membrane. J Cell Compar Physiol 66(S2):111–117
11. Colquhoun D, Hawkes AG (1981) On the stochastic properties of single ion channels. Proc R Soc Lond B Biol Sci 211(1183):205–235
12. Stevens CF (1978) Interactions between intrinsic membrane protein and electric field. An approach to studying nerve excitability. Biophys J 22(2):295–306

13. Stewart WJ (1994) Introduction to the numerical solution of Markov chains, 1st edn. Princeton University Press, Princeton
14. Meyn S, Tweedie RL (2009) Markov chains and stochastic stability, 2nd edn. Cambridge University Press, Cambridge
15. Kemeny JG, Snell JL (1960) Finite Markov chains. D. Van Nostrand, Princeton
16. Johnson FH, Eyring HJ, Stover BJ (1974) Theory of rate processes in biology and medicine. Wiley, New York
17. Eyring HJ, Lin SH, Lin SM (1980) Basic chemical kinetics. Wiley, New York
18. Destexhe A, Huguenard JR (2000) Nonlinear thermodynamic models of voltage-dependent currents. J Comput Neurosci 9(3):259–270
19. Tsien RW, Noble D (1969) A transition state theory approach to the kinetics of conductance changes in excitable membranes. J Membr Biol 1:248–273
20. Hill TL, Chen Y-D (1972) On the theory of ion transport across the nerve membrane. Biophys J 12(8):948–959
21. Andersen OS, Koeppe RE 2nd (1992) Molecular determinants of channel function. Physiol Rev 72(4 Suppl):S89–S158
22. Kiehn J, Lacerda AE, Brown AM (1999) Pathways of HERG inactivation. Am J Physiol 277(1 Pt 2):H199–H210
23. Clancy CE, Rudy Y (2001) Cellular consequences of HERG mutations in the long QT syndrome: precursors to sudden cardiac death. Cardiovasc Res 50(2):301–313
24. Lu Y, Mahaut-Smith MP, Varghese A, Huang CL, Kemp PR, Vandenberg JI (2001) Effects of premature stimulation on HERG K(+) channels. J Physiol (Lond) 537(Pt 3):843–851
25. Wang S, Liu S, Morales MJ, Strauss HC, Rasmusson RL (1997) A quantitative analysis of the activation and inactivation kinetics of HERG expressed in Xenopus oocytes. J Physiol (Lond) 502(Pt 1):45–60
26. Silva J, Rudy Y (2005) Subunit interaction determines IKs participation in cardiac repolarization and repolarization reserve. Circulation 112(10):1384–1391
27. McPate MJ, Duncan RS, Milnes JT, Witchel HJ, Hancox JC (2005) The N588K-HERG K + channel mutation in the "short QT syndrome": mechanism of gain-in-function determined at 37 °C. Biochem Biophys Res Commun 334(2):441–449
28. Brugada R, Hong K, Dumaine R, Cordeiro J, Gaita F, Borggrefe M et al (2004) Sudden death associated with short-QT syndrome linked to mutations in HERG. Circulation 109(1):30–35
29. McPate MJ, Duncan RS, Hancox JC, Witchel HJ (2008) Pharmacology of the short QT syndrome N588K-hERG K + channel mutation: differential impact on selected class I and class III antiarrhythmic drugs. Br J Pharmacol 155(6):957–966
30. McPate MJ, Zhang H, Adeniran I, Cordeiro JM, Witchel HJ, Hancox JC (2009) Comparative effects of the short QT N588K mutation at 37 °C on hERG K + channel current during ventricular, Purkinje fibre and atrial action potentials: an action potential clamp study. J Physiol Pharmacol 60(1):23–41
31. Broyden CG (1970) The convergence of a class of double-rank minimization algorithms 1. General considerations. IMA J Appl Math 6(1):76–90
32. Press WH, Teukolsky SA, Vetterling WT, Flannery BP (2007) Numerical recipes, 3rd edn. The art of scientific computing, 3rd edn. Cambridge University Press, Cambridge
33. Adeniran I, Hancox J, Zhang H (2010) Development of a biophysically detailed model of the rapid-delayed rectifier potassium channel. Comput Cardiol 37:637–640
34. Koren G, Liman ER, Logothetis DE, Nadal-Ginard B, Hess P (1990) Gating mechanism of a cloned potassium channel expressed in frog oocytes and mammalian cells. Neuron 4(1):39–51
35. Zagotta WN, Hoshi T, Aldrich RW (1994) Shaker potassium channel gating. III: evaluation of kinetic models for activation. J Gen Physiol 103(2):321–362
36. Kupershmidt S, Yang IC-H, Sutherland M, Wells KS, Yang T, Yang P et al (2002) Cardiac-enriched LIM domain protein fhl2 is required to generate I(Ks) in a heterologous system. Cardiovasc Res 56(1):93–103

37. Virág L, Iost N, Opincariu M, Szolnoky J, Szécsi J, Bogáts G et al (2001) The slow component of the delayed rectifier potassium current in undiseased human ventricular myocytes. Cardiovasc Res 49(4):790–797
38. Zagotta WN, Hoshi T, Dittman J, Aldrich RW (1994) Shaker potassium channel gating. II: transitions in the activation pathway. J Gen Physiol 103(2):279–319
39. Silverman WR, Roux B, Papazian DM (2003) Structural basis of two-stage voltage-dependent activation in K + channels. Proc Natl Acad Sci USA 100(5):2935–2940
40. Lu Z, Kamiya K, Opthof T, Yasui K, Kodama I (2001) Density and kinetics of I(Kr) and I(Ks) in guinea pig and rabbit ventricular myocytes explain different efficacy of I(Ks) blockade at high heart rate in guinea pig and rabbit: implications for arrhythmogenesis in humans. Circulation 104(8):951–956
41. Loussouarn G, Park K-H, Bellocq C, Baró I, Charpentier F, Escande D (2003) Phosphatidylinositol-4, 5-bisphosphate, PIP2, controls KCNQ1/KCNE1 voltage-gated potassium channels: a functional homology between voltage-gated and inward rectifier K + channels. EMBO J 22(20):5412–5421
42. Pusch M, Bertorello L, Conti F (2000) Gating and flickery block differentially affected by rubidium in homomeric KCNQ1 and heteromeric KCNQ1/KCNE1 potassium channels. Biophys J 78(1):211–226
43. El Harchi A, McPate MJ, Zhang YH, Zhang H, Hancox JC (2010) Action potential clamp and mefloquine sensitivity of recombinant "I KS" channels incorporating the V307L KCNQ1 mutation. J Physiol Pharmacol 61(2):123–131
44. Nelder JA, Mead R (1965) A simplex method for function minimization. Comput J 7(4):308–313
45. ten Tusscher KHWJ, Panfilov AV (2006) Alternans and spiral breakup in a human ventricular tissue model. Am J Physiol Heart Circ Physiol 291(3):H1088–H1100
46. ten Tusscher KHWJ, Noble D, Noble PJ, Panfilov AV (2004) A model for human ventricular tissue. Am J Physiol Heart Circ Physiol 286(4):H1573–H1589
47. ten Tusscher KHWJ, Panfilov AV (2006) Cell model for efficient simulation of wave propagation in human ventricular tissue under normal and pathological conditions. Phys Med Biol 51(23):6141–6156
48. Priebe L, Beuckelmann DJ (1998) Simulation study of cellular electric properties in heart failure. Circ Res 82(11):1206–1223
49. Sakmann B, Trube G (1984) Voltage-dependent inactivation of inward-rectifying single-channel currents in the guinea-pig heart cell membrane. J Physiol (Lond) 347:659–683
50. Bailly P, Mouchonière M, Bénitah JP, Camilleri L, Vassort G, Lorente P (1998) Extracellular K + dependence of inward rectification kinetics in human left ventricular cardiomyocytes. Circulation 98(24):2753–2759
51. Yan D-H, Ishihara K (2005) Two Kir2.1 channel populations with different sensitivities to Mg(2 +) and polyamine block: a model for the cardiac strong inward rectifier K(+) channel. J Physiol (Lond) 563(Pt 3):725–744
52. Priori SG, Pandit SV, Rivolta I, Berenfeld O, Ronchetti E, Dhamoon A et al (2005) A novel form of short QT syndrome (SQT3) is caused by a mutation in the KCNJ2 gene. Circ Res 96(7):800–807
53. El Harchi A, McPate MJ, Hong ZY, Zhang H, Hancox JC (2009) Action potential clamp and chloroquine sensitivity of mutant Kir2.1 channels responsible for variant 3 short QT syndrome. J Mol Cell Cardiol 47(5):743–747

Chapter 5
Methods, Experimental Protocols and Mathematical Preliminaries

5.1 Experimental Protocols

5.1.1 Action Potential Duration, Diastolic Interval and the Basic Cycle Length

Figure 5.1a illustrates schematically a number of basic measures of action potential intervals and their associated terminology. Action potential duration (APD) is the time interval between the start of membrane depolarisation (initiated by the influx of Na^+ ions (phase 0)) and the end of repolarisation (largely mediated by K^+ ion efflux; The diastolic interval (DI) is the time interval between the end of repolarisation and the next membrane depolarisation, i.e., the quiescent period preceding the subsequent APD. The basic cycle length (BCL) is the total duration consisting of the APD and DI (Fig. 5.1a). It is the duration of one heart beat and encompasses all events occurring from the commencement of one heartbeat to the next. A commonly used measure of the duration of the action potential is APD_{90}, which is the time interval between the start of membrane depolarisation and 90 % repolarisation; APD_{90} therefore reflects well ventricular repolarisation time and also its dispersion has been observed experimentally to correlate well with QT interval dispersion [1].

5.1.2 S1-S2 Protocol

The S1-S2 protocol is one of two commonly used protocols for elucidating the restitution properties of cardiac tissue [2–4]. In simulations, a BCL is chosen (e.g., 1000 ms) and the tissue model is paced at this cycle length until steady state is attained. Then, after a time delay (and utilising a variable length of the time delay, DI), a premature stimulus (S2) is applied (Fig. 5.1b). Repeatedly performing this procedure at different DIs permits the construction of an APD restitution curve, which shows the APD plotted as a function of the DI [2–4].

I. Adeniran, *Modelling the Short QT Syndrome Gene Mutations*,
Springer Theses, DOI: 10.1007/978-3-319-07200-5_5,

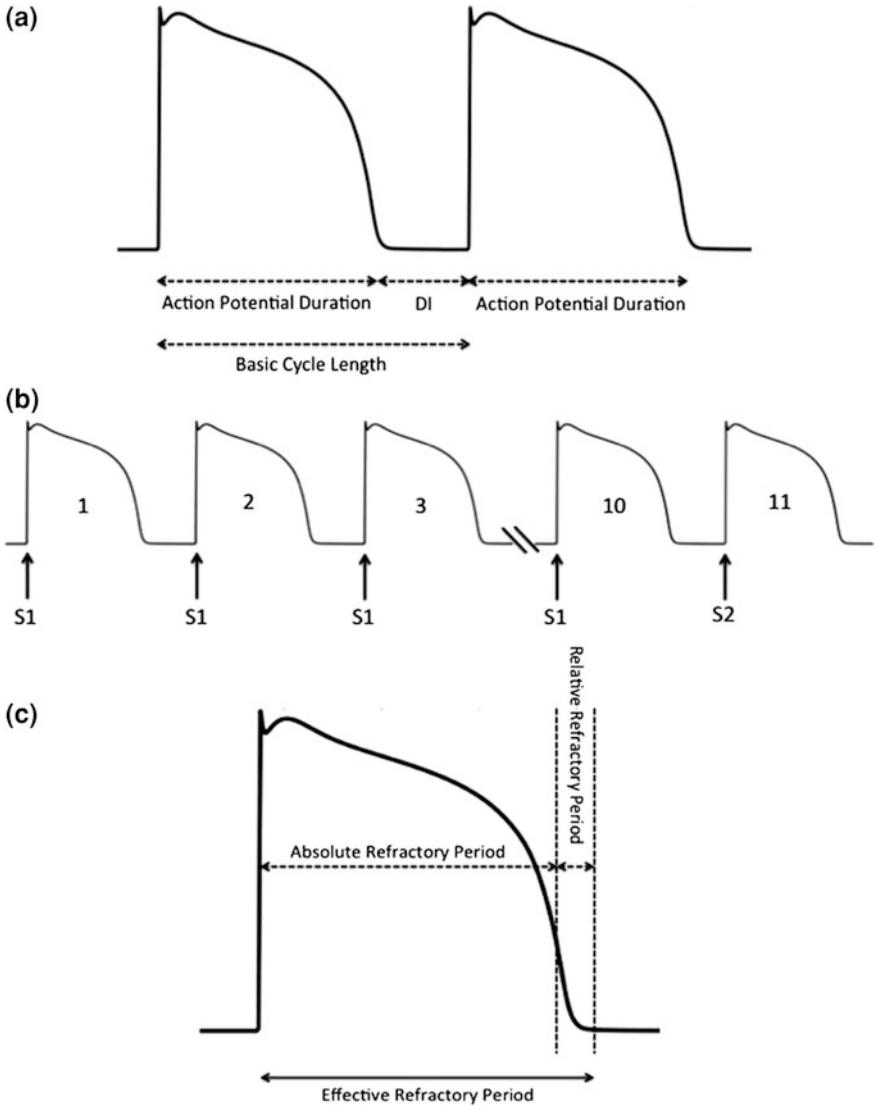

Fig. 5.1 **a** The action potential duration, diastolic interval and basic cycle length shown for an action potential. **b** A train of S1 stimuli that evoke action potentials and an S2 stimulus applied after the 10th S1 stimulus. **c** During the absolute refractory period, an action potential cannot be generated regardless of the strength of applied stimulus whereas a slowly rising action potential can be evoked during the relative refractory period. The effective refractory period is the duration that encompasses both the absolute and relative refractory periods

5.1.3 Action Potential Duration Restitution

For this study, action potential duration (APD) was defined as the action potential duration at 90 % repolarization (APD_{90}). APs were elicited with an S1-S2 protocol consisting of 10 S1 stimuli and an S2 stimulus (Fig. 5.1b). The S1 stimuli were applied at a frequency of 1 Hz and at twice the strength of the threshold value. The S2 stimulus was applied at some diastolic interval (DI) after the AP evoked by the last S1 stimulus. The Action Potential Duration Restitution (APD-R) curve was generated by decreasing the DIs and plotting the APD_{90} evoked by the S2 stimulus against the DIs. Steady-state rate dependence of the APD curve was determined by pacing single cell models at different basic cycle lengths (BCL) and plotting the APD_{90} against the BCLs.

5.1.4 Effective Refractory Period Restitution

Applying a stimulus prematurely (S2) before the cell membrane potential has recovered from a previous depolarisation (S1) could result in either an action potential that rises slowly, or in no activity at all. This period of depressed excitability is known as the refractory period.

The refractory period consists of two phases (Fig. 5.1c). The first is an absolute refractory period, during which no magnitude of S2 stimulus can evoke an action potential. The second is the relative refractory period during which only S2 stimuli exceeding the normal threshold can evoke an action potential.

At varying BCLs, the "Effective Refractory Period" (ERP) was measured as the smallest DI for which the overshoot of the AP evoked by the S2 stimulus reached 80 % of the AP evoked by the 10th S1 stimulus at each BCL. The Effective Refractory Period restitution (ERP-R) curve was generated by plotting the measured ERP against the BCLs [5].

5.2 Governing Equations, Geometries and Associated Simulation Protocols

5.2.1 Single Cell Model and AP Simulations

The SQT1-SQT3 model ionic current formulations developed in Chap. 4 were incorporated into the 2006 version of the ten Tusscher, Noble, Noble and Panfilov (TNNP) human ventricular cell model [6].

The model reproduces human ventricular cell and membrane channel properties and reproduces transmural heterogeneity of the AP [6, 7] across the ventricular wall. It has also been suggested to be well-suited to the study of re-entrant

arrhythmias in human ventricular tissue [6, 7]. In 2006, based on newly available experimental data, Xia et al. [8] updated and modified the TNNP model; their modifications were also employed in the present study.

In the single cell model, the cell membrane is modelled as a capacitor connected in parallel with variable resistances and batteries representing the different ionic channels, exchange and pump currents. Hence, the electrophysiological behaviour of a cell can be described with the following differential equation:

$$\frac{dV}{dt} = -\frac{I_{ion} + I_{stim}}{C_m} \tag{5.1}$$

where V is voltage, t is time, I_{ion} is the sum of all transmembrane ionic currents, I_{stim} is the externally applied stimulus current and C_m is the cell capacitance per unit surface area.

Equation (5.1) was integrated using the forward Euler method with a time step of 0.02 ms. The Hodgkin-Huxley-type equations for the gating variables of the various time-dependent currents in the TNNP model were integrated using the Rush and Larsen scheme [9]. The I_{Kr} Markov chain model (SQT1) was integrated with the forward Euler method. Due to the stiffness of the system of Ordinary Differential Equations (ODEs) comprising the I_{Ks} Markov chain model (SQT2), it was integrated using the 'explicit method based on the 4th order Merson's method and the first order multistage method of up to and including nine stages with stability control'. This ODE algorithm is available via the Intel Ordinary Differential Equations Solver Library [10]. The I_{K1} Hodgkin-Huxley model (SQT3) was integrated using the Rush and Larsen scheme [9].

5.2.1.1 Other I_{Kr} Models Used for Comparison

Results from the I_{Kr} Markov chain model (SQT1) were compared to three other I_{Kr} models, including (i) a reduced Markov model (r-MC); (ii) the original HH I_{Kr} formulation of the TNNP model; and (iii) the HH I_{Kr} formulation from the Luo Rudy model [11, 12]. The r-MC model was obtained by removing the transitions between the closed (C3) and inactivated (I) states in Fig. 4.3.

This comparative approach is similar to and complements recent work from Bett et al. [13] who have recently compared WT Markov and HH formulations for wild-type hERG, describing qualitative and quantitative differences that influence the predictive properties of the different models studied [13].

The TNNP I_{Kr} formulation [6, 7] is described by:

$$I_{Kr} = G_{Kr}\sqrt{\frac{Ko}{5.4}}x_{r1}x_{r2}(V - E_k) \tag{5.2}$$

where x_{r1} is an activation gating variable and x_{r2} is an inactivation gating variable. G_{kr} is the maximal conductance of I_{Kr} and is set to 0.153 nS pF^{-1} for both WT and

N588K-hERG, K_O is the extracellular K^+ concentration, $\sqrt{K_o/5.4}$ represents the K_O dependence of the current, V is the membrane potential and E_K is the K^+ reversal potential given by the Nernst equation. To enable the TNNP formulation to reproduce our N588K-hERG experimental data, the steady state value of the activation gating variable was doubled. The original formulation, without modification, served as the WT formulation.

The Luo-Rudy I_{Kr} formulation is described by:

$$I_{Kr} = G_{Kr} \cdot X_r \cdot R \cdot (V - E_{Kr}) \tag{5.3}$$

where X_r is a time-dependent activation gate and R is a time-dependent inactivation gate. G_{kr} is the maximal conductance of I_{Kr} and is modelled as $8.6 \times 10^{-3}\sqrt{K_o/5.4}$ nS pF^{-1} for both WT and N588K-hERG. V is the membrane potential and E_{Kr} is the K^+ reversal potential given by the Nernst equation. To enable the Luo-Rudy formulation to reproduce our N588K-hERG experimental data, 'R' was set to a value of 1, mimicking defective inactivation caused by the mutation. The original formulation, without modification served as the WT formulation.

5.2.2 Heterogeneous Transmural Ventricular Tissue Model

Initiation and conduction of action potentials in multicellular tissue models was modelled with the monodomain equation [14–16]:

$$C_m \frac{dV}{dt} = -(I_{ion} + I_{stim}) + \nabla \cdot (D\nabla V) \tag{5.4}$$

where D is the diffusion coefficient describing the tissue conductivity, I_{ion} is the sum of all transmembrane ionic currents, I_{stim} is the externally applied stimulus current and C_m is the cell capacitance per unit surface area.

5.2.2.1 Computation of the Diffusion Coefficient

The diffusion coefficient (D) in Eq. (5.4) is defined as [15, 17–20]:

$$D = \Lambda \Omega \Lambda^T \tag{5.5}$$

where Λ is a matrix of perpendicular unit vectors as columns (α_f in the fibre direction, α_s in the sheet direction and α_c in the cross-sheet direction). Ω is the conductivity tensor expressed in the basis formed by these three perpendicular unit vectors:

$$\begin{bmatrix} \sigma_f & 0 & 0 \\ 0 & \sigma_S & 0 \\ 0 & 0 & \sigma_c \end{bmatrix} \tag{5.6}$$

where σ_f is the conductivity in the fibre direction, σ_s is the conductivity in the sheet direction and σ_c is the conductivity in the cross-sheet direction. Therefore, an entry in D can be written as:

$$D_{ij} = \alpha_f^i \alpha_f^i \sigma_f + \alpha_s^i \alpha_s^i \sigma_s + \alpha_c^i \alpha_c^i \sigma_c \tag{5.7}$$

for $i, j = 0,1,2$.

5.2.2.2 Solving the Monodomain Equation

The operator splitting method as proposed by Qu and Garfinkel [21] was used to solve the monodomain equation representation of cardiac tissue (Eq. 4.40). Specifically, Strang splitting [18] was employed. From Eq. (5.4), two operators can be defined:

$$L_1 V = -\frac{(I_{ion} + I_{stim})}{C_m} \tag{5.8}$$

$$L_2 V = \frac{1}{C_m} \nabla.(D \nabla V) \tag{5.9}$$

These two operators define two sub-problems:

$$C_m \frac{dV}{dt} = -(I_{ion} + I_{stim}) \tag{5.10}$$

$$C_m \frac{dV}{dt} = \nabla.(D \nabla V) \tag{5.11}$$

The quasi-nonlinear Monodomain equation (Eq. 5.4) has now become a linear partial differential equation (PDE) (Eq. 5.11) and a set of nonlinear ODEs and differential-algebraic equations (DAEs) (Eq. 5.10), which is equivalent to Eq. (5.1) and therefore was solved using the methods outlined in Sect. 5.2.1. A time step using the Strang splitting algorithm [18] now proceeds as follows:

1. Solve the system of ODEs and DAEs of Eq. (5.10) for half a time step, i.e., for $t_n < t \leq t_n + \frac{1}{2}\Delta t$. The solution is denoted by $V_{0.5}^n$.
2. Solve the linear PDE (Eq. 5.11) for a full time step, i.e., for $t_n < t \leq t_{\Delta t}$ with $V(t_n) = V_{0.5}^n$. The solution is denoted by $V_{0.5}^{n+1}$.

3. Solve the system of ODEs and DAEs of Eq. (5.10) for the remaining half a time step, i.e., for $t_n + \frac{1}{2}\Delta t < t \leq t_n + \Delta t$ to obtain the approximate solution V^{n+1}at $t = t + \Delta t$.

To solve the PDE in step 2, Eq. (5.11) is discretised in time using the Crank-Nicholson scheme [22], which is a specific form of the θ-rule [22] commonly used for discretising time-dependent PDEs. Using the θ-rule, Eq. (5.11) discretised in time becomes:

$$C_m \frac{V^{n+1} - V^n}{\Delta t} = \theta(\nabla.(D\nabla V^{n+1})) + ((1-\theta)\nabla.(D\nabla V^n)) \tag{5.12}$$

The choice of $\theta = \frac{1}{2}$ gives the Crank-Nicholson scheme. It is unconditionally stable, second-order accurate and importantly, matches the accuracy of the Strang splitting scheme, which is also second order accurate.

The PDE in step 2, i.e., Equation (5.11) is discretised in space using the Finite Element Method [22–25]. It is multiplied by a test function, ϕ and integrated over the entire domain, Ω. The resulting weak formulation for Eq. (5.11) is:

$$\int_\Omega V^{n+1}\phi dx + \theta\lambda \int_\Omega D\nabla V^{n+1} \cdot \nabla\phi dx = \int_\Omega V^n \phi dx - (1-\theta)\lambda \int_\Omega D\nabla V^n.\nabla\phi dx \tag{5.13}$$

for all $\phi \epsilon$V where V is test function space. For convenience, $\lambda = \frac{\Delta t}{C^m}$.

5.2.3 1D Heterogeneous Transmural Strand

The 1D mesh used for the simulations was a 15 mm long single fibre, with 100 nodes spaced 0.15 mm apart. Each node represents a 150-μm cylindrical cell (Fig. 5.2). This total strand length of 15 mm is close to the normal range of human transmural ventricle width; ~4.0–14.0 mm [26–28]. The strand comprises 25 endocardial cells (ENDO), 35 middle cells (MCELL) and 40 epicardial cells (EPI) representing 3.75, 5.25 and 6.00 mm in the ENDO, MCELL and EPI regions respectively. The chosen proportion for each region is similar to those used in other studies [29–32].

The diffusion coefficient, '*D*' was set at 0.001 cm^2/ms giving a planar conduction velocity of 65 cm/s through the strand. This is close to the 70 cm/s velocity of conduction along the fibre direction in human myocardium [33]. At the EPI-MCELL border, there is a fivefold decrease in '*D*'. This is similar to the work of Gima and Rudy [31] who based this on the experimental of work of Yan et al. [28] who reported a sharp transition in the tissue resistance in a left ventricular wedge model. Drouin et al. [26] also reported a sharp APD transition in this region

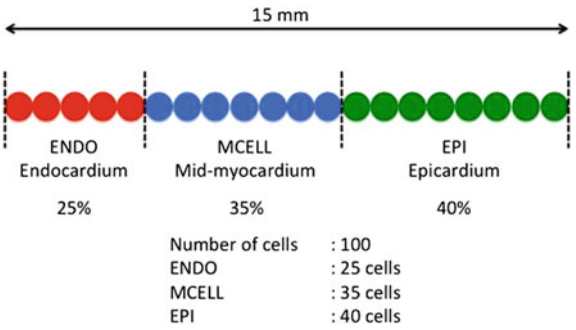

Fig. 5.2 Geometry of the 1D strand of the transmural human ventricle wall used for simulations. The strand is transmurally heterogeneous consisting of 25 endocardial cells (*red*), 35 mid-myocardial cells (*blue*) and 40 epicardial (*green*) cells making a total of 100 cells. The length of the strand is 15 mm

Fig. 5.3 Geometry of the 2D realistic human ventricle cross-section used for simulations (*left*) and the fibre orientation (*right*)

in their experimental work characterising MCELLs in the normal human heart. At the ENDO end of the strand, a supra-threshold stimulus (amplitude:-52 pA/pF, duration: 2 ms) was applied to initiate a conducting excitation wave (Fig. 5.3).

5.2.3.1 Measurement of Conduction Velocity and Conduction Velocity Restitution

The conduction velocity was calculated from nodes one-quarter and three-quarters of the way along the strand. The activation time of each point was defined to be the time at which the maximum upstroke velocity occurred.

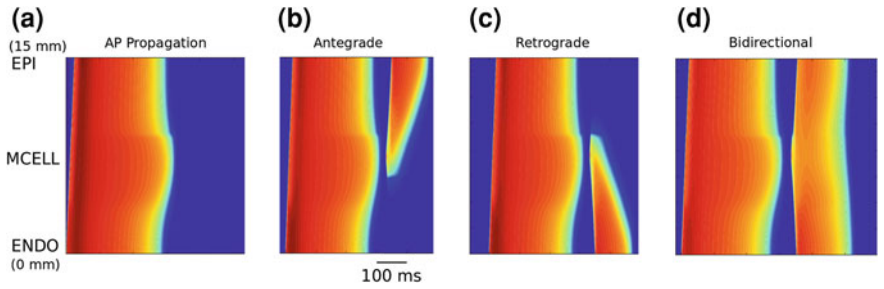

Fig. 5.4 Space-Time plot of a propagating condition wave in a 1D strand and response of the tissue to a premature test stimulus at a local part of the tissue at various time delays after a previous conditioning wave. Space runs horizontally from the ENDO end (0 mm) to the EPI end (15 mm). Time runs vertically from bottom to top. The membrane potential of 1D strand cells are mapped onto a colour spectrum ranging from *blue* (−86 mV) to *red* +50 mV) **a** Initiated conditioning excitation wave. Also, bidirectional conduction block. **b** Antegrade propagation following the application of a test stimulus after a previous conditioning excitation wave. **c** Retrograde propagation following the application of a test stimulus after a previous conditioning excitation wave. **d** Bidirectional propagation following the application of a test stimulus after a previous conditioning excitation wave

Following the application of a sequence of 10 conditioning pulses at 1 Hz, conduction velocity (CV) was measured in the 1D strand by calculating the time ΔT for the wavefront to propagate from x–Δx to $x + \Delta x$ and defining $CV = \frac{2\Delta x}{\Delta T}$. To obtain CV restitution curves, CV was plotted against varying BCLs.

5.2.3.2 Measurement of the Temporal Vulnerable window

In the 1D strand (Fig. 5.2), a conditioning excitation wave is initiated at the ENDO end by applying a stimulus (amplitude: −52 pA/pF; duration: 1 ms). This wave propagates from the ENDO end towards the EPI end (Fig. 5.4a). Following the propagating wavefront in cardiac tissue is a refractory tail. If a test stimulus is applied too late after this time period, another excitation wave that propagates in both directions along the strand will develop (bi-directional conduction, Fig. 5.4d) as the tissue surrounding this stimulus site is sufficiently recovered from the previous excitation wave. Applying this test stimulus too early after the refractory tail results in conduction block in both directions along the strand as the tissue around the test stimulus is still refractory (i.e., excited) and would not have recovered from the previous excitation wave. Between these two extremes is a time period, known as the vulnerable window (VW) during which an applied test stimulus produces a solitary wave that propagates in either the antegrade (Fig. 5.4b) or retrograde (Fig. 5.4c) direction but not in both (i.e., there is a uni-directional conduction block). In Fig. 5.4b, the solitary wave from the test stimulus propagates in the antegrade direction because the tissue in the retrograde

(backward) direction is still refractory and hence conduction in the retrograde direction is blocked. The situation is reversed in Fig. 5.4c. This unidirectional conduction block makes the tissue susceptible to re-entry [23, 34, 35]. The propagation direction depends on the region in the tissue to which the test stimulus is applied.

A sequence of 10 S1 stimuli at 1 Hz was applied at one end of the 1D transmural strand (spatial size: 0.4 mm, amplitude: −52 pA/pF, duration: 1 ms) to evoke a propagating wavefront. Following a time delay (ΔT) after the 10th S1 stimulus, a second stimulus (S2) with the same duration and amplitude as the S1 stimulus was applied to a 0.4 mm region of the strand. During the time window (T1, T2), where T1 and T2 denote the maximal and minimal value of ΔT respectively, the excitation wave evoked by the S2 stimulus propagated unidirectionally in the strand. The width (T1–T2) provides a measure of the temporal vulnerability of the tissue. This procedure was carried out for all regions across the strand.

5.2.3.3 Measurement of Tissue Excitation Threshold

The tissue excitation threshold is the minimal stimulus that evokes a propagating action potential in cardiac tissue [35]. This was measured using a standard S1-S2 protocol (Fig. 5.1b) in the 1D strand. The S1 stimulus was applied at one end of the strand with an amplitude of −52 pA/pF, spatial size of 0.4 mm and for a duration of 2 ms. The S2 stimulus was applied in the middle of the strand with the same spatial size and duration as the S1 stimulus. The tissue excitation threshold was calculated as the minimal S2 amplitude that evoked an action potential that propagated in the strand.

5.2.4 2D Human Ventricle Geometry

5.2.4.1 Idealised 2D Geometry

The idealised geometry is a simple sheet of tissue measuring 15 mm by 50 mm. It was modelled by expanding the 1D transmural strand in Fig. 5.2 (length of 15 mm in the *x*-direction) into a sheet with a width of 50 m in the *y*-direction.

5.2.4.2 Realistic 2D Geometry

The realistic geometry is a transverse cross-sectional slice taken from the middle of a 3D ventricular geometry reconstructed by DT-MRI [36] with a spatial resolution of 0.2 mm (Fig. 5.3). It was segmented into distinctive regions of ENDO (25 %), MCELL (35 %) and EPI (40 %) layers with similar contiguous

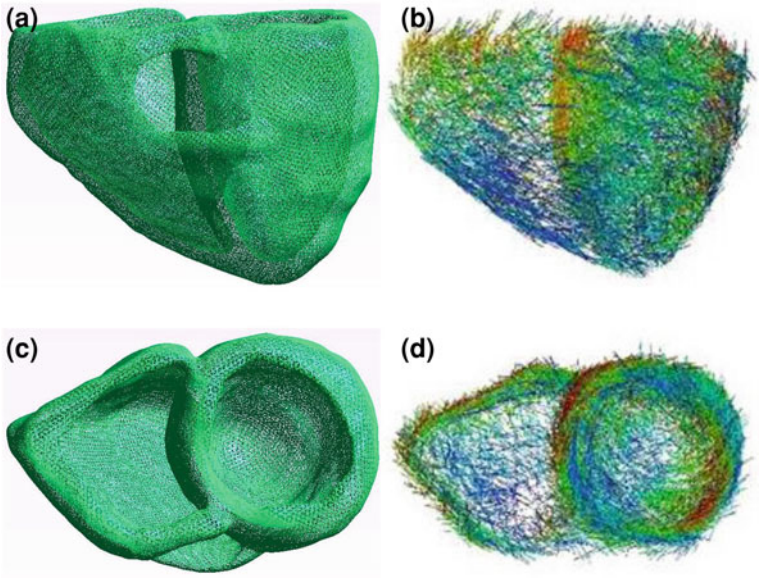

Fig. 5.5 3D human ventricle geometry reconstructed by DT-MRI and fibre orientation. **a**, **c** Anterior and cross-section view of the human left and right ventricle geometry. **b**, **d**: Fibre orientations of the geometry

proportions transmurally as the 1D strand model (Fig. 5.2). Anisotropic fibre orientations is implemented as used in the work of [36]. The intracellular conductivities in the fibre and cross-fibre directions were set to 0.3 and 0.1 mS mm^{-1} respectively.

5.2.5 3D Human Ventricle Geometry

In three-dimensions (3D), simulations were performed using an anatomical human ventricle geometry of a healthy 30 year-old male that was reconstructed via DT-MRI. Its spatial resolution is 0.2 mm with approximately 24.2 million nodes in total and includes anisotropic fibre orientation (Fig. 5.5). The tissue was segmented into distinct ENDO, MIDDLE and EPI regions in both the left and right ventricles [37] with similar contiguous proportions transmurally as the 1D strand model. The conditioning activation sites were determined empirically across the ventricular wall, and were validated by reproducing the activation sequence and the QRS complex in the measured 64-channel ECG [37] of the 30 year-old male. The intercellular conductivities in the fibre, cross-fibre and sheet directions were set to 3.0, 0.1 and 0.3 mS mm^{-1} respectively.

5.3 Other Simulation Protocols

5.3.1 Computing the Pseudo-ECG

The pseudo-ECG was computed following the method of Gima and Rudy [31]. At the extracellular space located at position (x', y', z'), a far-field unipolar potential can be computed as an integral of the spatial gradient of membrane potential at position (x, y, z) on the strand by:

$$\phi_e(x',y',z') = \frac{\alpha^2\sigma_i}{4\sigma_e}\int(-\nabla V_m).\frac{1}{r}$$
$$r = \sqrt{(x-x')^2+(y-y')^2+(z-z')^2} \tag{5.14}$$

where σ_e and σ_i are the extracellular and intracellular conductivities respectively, α is the radius of the strand, r the distance from a source point (x, y, z) to a field point (x',y',z'). The pseudo-ECG was computed as ϕ_e at a position 2.0 cm away from the epicardial end of the strand.

5.3.2 Initiation of Re-entry in 2D sheet

Re-entry was initiated by a standard S1-S2 protocol in both the idealised and realistic geometries. In the idealised 2D sheet, a plane wave was initiated at the ENDO end by an S1 stimulus. During the vulnerable window of the tissue, an S2 stimulus was applied to a local tissue area in the EPI region to evoke unidirectional propagation that can lead to re-entry.

5.3.3 Measurement of Minimal Size of S2 that Sustains Re-entry in 2D Models

On application of an S2 stimulus, unidirectional conduction of the S2-evoked excitation wave leads to formation of a pair of re-entrant excitation waves, with their counter-rotating tips that move towards each other. If the distance between both tips is sufficiently long, each will have ample space to complete its pathway, and consequently, the paired re-entrant excitation waves will be sustained. Otherwise, the two tips collide and the re-entrant excitation wave is terminated. To provide an adequate re-entrant pathway, a sufficient S2 size is required, which is dependent on the wavelength of the spiral wave. In order to evaluate the critical size of re-entrant pathway of tissue, the minimal spatial S2 length that supports the formation of re-entrant spiral waves under control and mutant conditions was estimated. This

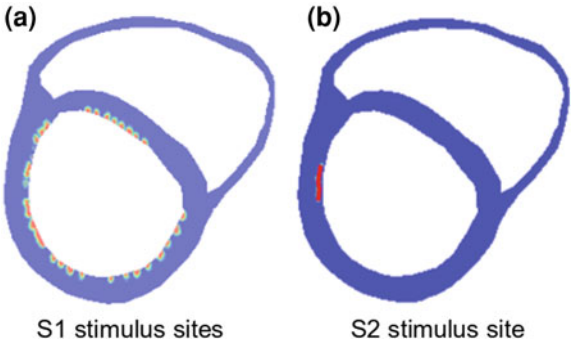

Fig. 5.6 S1-S2 stimulation sites in the 2D human ventricle cross-section. **a** S1 stimulation sites (*red*). **b** S2 stimulus site (*red*)

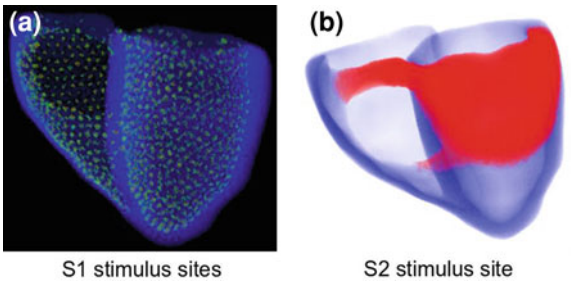

Fig. 5.7 S1-S2 stimulation sites in the 3D anatomical human ventricles. **a** S1 stimulation sites (*gold dots*). **b** S2 stimulus site (*red*)

minimal length of S2 gives an indication of the susceptibility of the tissue to re-entry, i.e., the larger the minimal length, the harder the initiation of re-entry.

5.3.4 Initiation of Re-entry in 2D Heart Cross-Section

In the 2D realistic model (cross-sectional slice), multiple stimulus sites (Fig. 5.6a) were chosen in an effort to recreate the activation pattern in a human heart observed by Durrer et al. [38]. To initiate re-entry, an S2 stimulus was applied in the endocardium of the left ventricle (see Fig. 5.6b) partly during the repolarisation phase of a conditioning wave and partly within fully recovered tissue. The S2-evoked excitation wave propagated uni-directionally, leading to the formation of re-entrant excitation wave within the transmural wall.

5.3.5 Initiation of Re-entry in the 3D Anatomical Human Ventricles

3D scroll waves were initiated by using an S1-S2 protocol. The S1 stimulus was applied to multi-stimulation sites in the endocardium of the ventricles (Fig. 5.7a).

These stimulation sites were generated to produce the activation timing sequence across the ventricles as seen experimentally. The S2 stimulus was applied over a small epicardial region consisting mainly of the left ventricle and a fraction of the right-ventricular outflow tract (Fig. 5.7b) (amplitude: -124 mV; duration: 2 ms) during the refractory tail of the S1 stimulus.

5.4 Numerical Methods

For the 1D, 2D and 3D simulations, Eq. (5.4) was solved using a Strang splitting scheme [18] and a Crank-Nicholson time-stepping scheme in the temporal direction, together with Lagrangian Q1 finite elements in the spatial direction using the deal.II adaptive finite element library [39]. The Strang splitting scheme is second-order accurate and the Crank-Nicholson time-stepping scheme is unconditionally stable and second-order accurate with respect to time [22]. The resulting computed solution is therefore second-order accurate.

The system of linear algebraic equations resulting from the discretisation of the monodomain equation was solved using the preconditioned Conjugate Gradient method with the Symmetric Successive OverRelaxation (SSOR) method as the preconditioner [40].

The TNNP single cell model was converted to CUDA/C++ via the Thrust CUDA library [41]. The cell kinetics are represented by a system of ODEs (I_{ion} in Eq. 5.4). In the 1D, 2D and 3D simulations, the collection of systems of ODEs (I_{ion}) for all the cells was solved on a Tesla C2050 "Fermi" GPU with 448 CUDA cores. The host system for the Tesla GPU is a Dell Precision T7500 with 12 Intel Xeon CPU cores at 2.80 GHz and 96 GB of memory.

References

1. Zabel M, Portnoy S, Franz MR (1995) Electrocardiographic indexes of dispersion of ventricular repolarization: an isolated heart validation study. J Am Coll Cardiol 25(3):746–752
2. Cherry EM, Fenton FH (2007) A tale of two dogs: analyzing two models of canine ventricular electrophysiology. Am J Physiol Heart Circ Physiol 292(1):43–55
3. Koller ML, Riccio ML, Gilmour RF Jr (1998) Dynamic restitution of action potential duration during electrical alternans and ventricular fibrillation. Am J Physiol 275(5 Pt 2):1635–1642
4. Surovyatkina E, Noble D, Gavaghan D, Sher A (2010) Multistability property in cardiac ionic models of mammalian and human ventricular cells. Prog Biophys Mol Biol 103(1):131–141
5. Workman AJ, Kane KA, Rankin AC (2001) The contribution of ionic currents to changes in refractoriness of human atrial myocytes associated with chronic atrial fibrillation. Cardiovasc Res 52(2):226–235
6. ten Tusscher KHWJ, Panfilov AV (2006) Alternans and spiral breakup in a human ventricular tissue model. Am J Physiol Heart Circ Physiol 291(3):1088–1100

7. ten Tusscher KHWJ, Noble D, Noble PJ, Panfilov AV (2004) A model for human ventricular tissue. Am J Physiol Heart Circ Physiol 286(4):1573–1589
8. Xia L, Zhang Y, Zhang H, Wei Q, Liu F, Crozier S (2006) Simulation of Brugada syndrome using cellular and three-dimensional whole-heart modeling approaches. Physiol Meas 27(11):1125–1142
9. Rush S, Larsen H (1978) A practical algorithm for solving dynamic membrane equations. IEEE Trans Biomed Eng 25(4):389–392
10. Kalinkin A, Gololobov S (2010) Intel ordinary differential equations solver library [Internet]. Intel; 2010. http://software.intel.com/en-us/articles/intel-ordinary-differential-equations-solver-library/
11. Zeng J, Laurita KR, Rosenbaum DS, Rudy Y (1995) Two components of the delayed rectifier K+ current in ventricular myocytes of the guinea pig type. theoretical formulation and their role in repolarization. Circ Res 77(1):140–152
12. Rudy Y, Luo CH (1993) Cellular responses to electrical stimulation: a study using a model of the ventricular cardiac action potential. Adv Exp Med Biol 346:79–90
13. Bett GCL, Zhou Q, Rasmusson RL (2011) Models of HERG gating. Biophys J 101(3):631–642
14. Clements JC, Nenonen J, Li PKJ, Horácek BM (2004) Activation dynamics in anisotropic cardiac tissue via decoupling. Ann Biomed Eng 32(7):984–990
15. Colli Franzone P, Pavarino LF, Taccardi B (2005) Simulating patterns of excitation, repolarization and action potential duration with cardiac Bidomain and Monodomain models. Math Biosci 197(1):35–66
16. Keener J, Sneyd J(2008) Mathematical physiology: II: systems physiology, 2nd edn. Springer, New York
17. Potse M, Dubé B, Richer J, Vinet A, Gulrajani RM (2006) A comparison of monodomain and bidomain reaction-diffusion models for action potential propagation in the human heart. IEEE Trans Biomed Eng 53(12 Pt 1):2425–2435
18. Sundnes J, Lines GT, Tveito A (2005) An operator splitting method for solving the bidomain equations coupled to a volume conductor model for the torso. Math Biosci 194(2):233–248
19. Whiteley JP (2007) Physiology driven adaptivity for the numerical solution of the bidomain equations. Ann Biomed Eng 35(9):1510–1520
20. Bourgault Y, Pierre C (2010) Comparing the bidomain and monodomain models in electrocardiology through convergence analysis. INSMI. 2010, hal–00545888
21. Qu Z, Garfinkel A (1999) An advanced algorithm for solving partial differential equation in cardiac conduction. IEEE Trans Biomed Eng 46(9):1166–1168
22. Burnett DS (1987) Finite element analysis: from concepts to applications, 1st edn. Addison Wesley, Reading
23. Braess D (2007) Finite elements: theory, fast solvers, and applications in solid mechanics, 3rd edn. Cambridge University Press, Cambridge
24. Brenner SC, Scott R (2008) The mathematical theory of finite element methods. Softcover Reprint of Hardcover, 3rd edn. Springer, New York
25. Hughes TJR (2000) The finite element method: linear static and dynamic finite element analysis. Dover Publications, New York
26. Drouin E, Charpentier F, Gauthier C, Laurent K, Le Marec H (1995) Electrophysiologic characteristics of cells spanning the left ventricular wall of human heart: evidence for presence of M cells. J Am Coll Cardiol 26(1):185–192
27. Feigenbaum H (1994) Echocardiolography, 5th edn. Lee and Febiger, Philadelphia
28. Yan GX, Shimizu W, Antzelevitch C (1998) Characteristics and distribution of M cells in arterially perfused canine left ventricular wedge preparations. Circulation 98(18):1921–1927
29. Zhang H, Kharche S, Holden AV, Hancox JC (2008) Repolarisation and vulnerability to re-entry in the human heart with short QT syndrome arising from KCNQ1 mutation–a simulation study. Prog Biophys Mol Biol 96(1–3):112–131
30. Weiss DL, Seemann G, Sachse FB, Dössel O (2005) Modelling of short QT syndrome in a heterogeneous model of the human ventricular wall. Europace 7(Suppl 2):105–117

31. Gima K, Rudy Y (2002) Ionic current basis of electrocardiographic waveforms: a model study. Circ Res 90(8):889–896
32. Zhang H, Hancox JC (2004) In silico study of action potential and QT interval shortening due to loss of inactivation of the cardiac rapid delayed rectifier potassium current. Biochem Biophys Res Commun 322(2):693–699
33. Taggart P, Sutton PM, Opthof T, Coronel R, Trimlett R, Pugsley W et al (2000) Inhomogeneous transmural conduction during early ischaemia in patients with coronary artery disease. J Mol Cell Cardiol 32(4):621–630
34. Quan W, Rudy Y (1990) Unidirectional block and reentry of cardiac excitation: a model study. Circ Res 66(2):367–382
35. Zhang H, Garrat CJ, Holden AV (2003) Onset and termination of reentrant excitation in homogeneous human virtual atrial tissue. Int J Bifurcat Chaos Appl Sci Eng 13(12):3631–3643
36. Seemann G, Keller DUJ, Weiss DL, Dössel O (2006) Modeling human ventricular geometry and fiber orientation based on diffusion tensor MRI. Computers in Cardiology [Internet]. 2006 [cited 2011 Jul 20]. pp 801–804. http://www.scopus.com/inward/record.url?eid=2-s2.0-38049006338&partnerID=40&md5=d7c99be0309654b17513e9b39ee96029
37. Keller DUJ, Kalayciyan R, Dössel O, Seemann G (2011) Fast creation of endocardial stimulation profiles for the realistic simulation of body surface ECGs. IFMBE Proceedings [Internet]. 2009 [cited 2011 Jul 20]. page 145–148. http://www.scopus.com/inward/record.url?eid=2-s2.0-77950134835&partnerID=40&md5=2db2b89cc19de5e28ec01ebbf0dffff0342
38. Durrer D, van Dam RT, Freud GE, Janse MJ, Meijler FL, Arzbaecher RC (1970) Total excitation of the isolated human heart. Circulation 41(6):899–912
39. Bangerth W, Hartmann R, Kanschat G (2007) Deal. II–A general-purpose object-oriented finite element library. ACM Trans Math Software [Internet]. 2007 [cited 2011 Jul 20];33(4). http://www.scopus.com/inward/record.url?eid=2-s2.0-34548277425&partnerID=40&md5=82ee0838c986804d48da9b3b93698365
40. Hackbusch W (1994) Iterative solution of large sparse systems of equations. Springer, New York
41. Hoberock J, Bell N (2010) Thrust: a parallel template library [Internet]. NVIDIA; 2010 [cited 2011 Nov 21]. http://www.meganewtons.com/

Chapter 6
Increased Vulnerability of the Human Ventricle to Re-entrant Excitation in hERG Linked SQT1

6.1 Introduction

The SQTS was first reported as a clinical entity in 2000 [1]. It is characterised by a markedly abbreviated QT interval, poor rate adaptation of the QT interval, shortened atrial and ventricular refractory periods, tall and peaked T-waves on the ECG, by atrial and ventricular arrhythmias and an increased incidence of sudden death [2–4]. Genetic analysis of affected patients revealed three distinct mutations to three distinct potassium channels: *KCNH2* (*hERG*), *KCNQ1* (*KvLQT1*) and *KCNJ2* encoded-potassium channel subunits [5–9].

As introduced in Chap. 3, the first variant of the SQTS (SQT1) is caused by an amino acid substitution of asparagine to lysine in position 588 (N588K) in the external S5-pore linker of the hERG potassium channel [5, 6]. SQT1 causes a marked rightward shift in voltage-dependent inactivation of this channel [10, 11]. In AP and voltage clamp experiments, this is reflected in the marked increase of I_{hERG} during ventricular and atrial AP repolarisation phases [5, 10–12]. Given that hERG encodes channels responsible for the rapid delayed rectifier potassium channel current (I_{Kr}) [13], the N588K gain-of-function mutation would be expected to amplify the contribution of I_{Kr} to cardiac repolarisation, and consequently shorten the QT interval [5, 10–12]. The ventricular effective refractory period (ERP) would in turn be anticipated to shorten, leading to increased susceptibility to re-entrant arrhythmia.

At present, no phenotypically accurate experimental model of the SQT1 exists to allow exploration of its functional consequences. In order to produce abbreviated repolarisation experimentally, investigators have performed experiments on a perfused canine left ventricular wedge treated with the adenosine triphosphate (ATP) potassium channel (K_{ATP}) opener pinacidil or the I_{Kr} activator PD-118057 [14, 15]. In these experiments, heterogeneous abbreviation of APs across the ventricular wall has been observed (and, thereby, amplified dispersion of repolarization), ERP abbreviation, QT interval shortening and ventricular tachycardia [14, 15]. Whilst the data from these studies are valuable in understanding a link between accelerated repolarization and arrhythmogenesis, the pharmacological

I. Adeniran, *Modelling the Short QT Syndrome Gene Mutations*,
Springer Theses, DOI: 10.1007/978-3-319-07200-5_6,

interventions used did not mimic precisely the changes induced by the N588K SQT1 mutation. In silico reconstruction offers an alternative approach to determining the arrhythmogenic substrates in the SQT1 [8, 16–19]. Existing SQT1 simulation data though are either incomplete or based on data obtained at ambient rather than physiological temperature [8, 16–18]. Moreover, no viable tissue substrate for ventricular arrhythmia in the SQT1 has hitherto been demonstrated in any simulation study.

Accordingly, the aims of the present study were:

i. To reproduce the kinetic changes to I_{Kr} caused by SQT1 based on available experimental data obtained at physiological temperature, in simulations constructed with both Hodgkin-Huxley (HH) and Markov chain (MC) formulations.
ii. To incorporate control and SQT1 I_{Kr} in human ventricular cell-based models in order to determine the functional consequences of the SQT1 mutation on AP repolarisation and the QT interval, and to compare the functional differences between the HH and MC variant models;
iii. To explore the arrhythmogenic substrate in SQT1 involving the N588K hERG mutation through the use of multicellular tissue and organ simulations.

As will be shown, the results obtained through addressing these aims provide a clear link between the kinetic changes to I_{hERG}/I_{Kr} in SQT1 and the altered ventricular tissue electrophysiology, favouring re-entrant arrhythmia in the SQT1.

6.2 Simulation of Single Cell I_{Kr} Under Control and SQT1 Conditions

Two SQT1 Markov models were developed: a full Markov model (f-MC) and a reduced Markov model (r-MC). A detailed discussion of the development of the SQT1 Markov models and the Hodgkin-Huxley models is given in Sect. 4.2. For the reader's convenience, the state transition diagrams for the f-MC and r-MC models are reproduced in Fig. 6.1. In the f-MC model, inactivation can occur from both the closed (C3) and the open (O) state whereas it occurs only from the (O) state in the r-MC model. This is the only structural difference between the two Markov models.

As a first step in model validation, the ability of the Markov models to reproduce published experimental data [10, 12] on the voltage-dependence of activation of WT and the N588K mutant hERG current at physiological temperature was tested. The same voltage clamp protocol used experimentally [20] was employed (Fig. 6.2aii, bii). Figure 6.2a shows representative $I_{Kr/hERG}$ current traces for WT (Fig. 6.2ai) and N588K (Fig. 6.2bi) elicited by the voltage clamp protocol. Current-voltage (I–V) relationships were constructed from these.

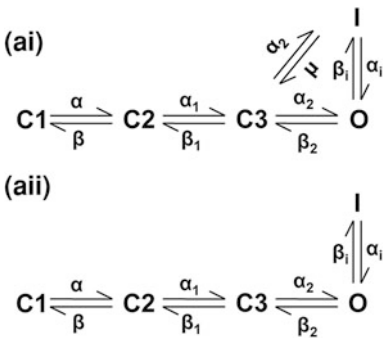

Fig. 6.1 State transition diagrams of the Markov models. **ai** Full Markov Chain (f-MC) state transition diagram. **aii** Reduced Markov Chain (r-MC) state transition diagram

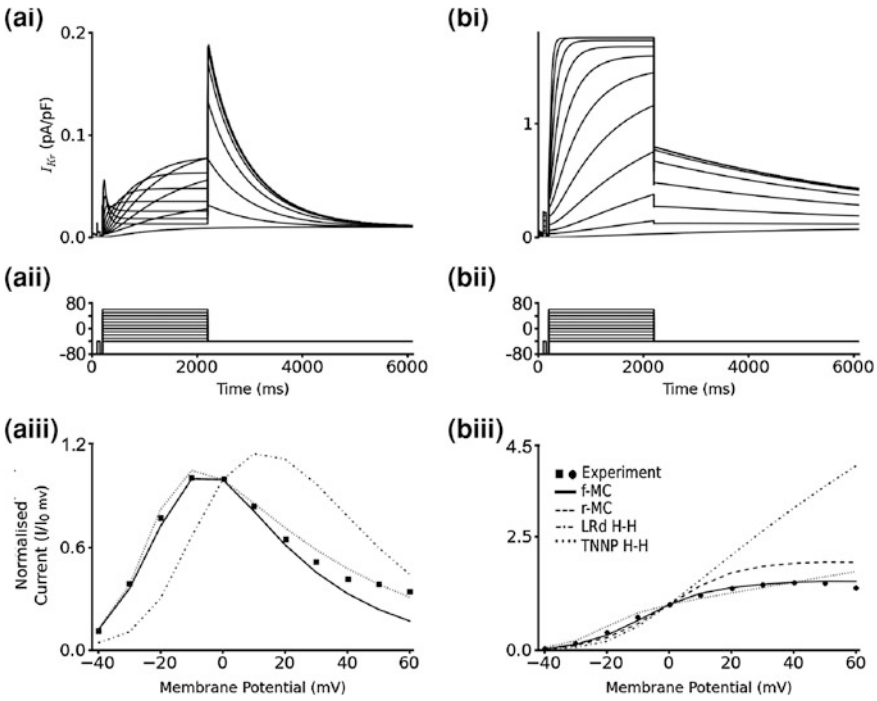

Fig. 6.2 Simulated Current-Voltage Relationships for I_{hERG}. **ai**, **bi** Current traces for WT (**a**) and N588K I_{hERG}/I_{Kr} (**b**) elicited by the voltage protocol shown in (**aii**, **bii**). **aiii**, **biii** I–V relations for end pulse currents for WT (**a**) and N588K I_{hERG}/I_{Kr} (**b**). End pulse currents were normalised to the current observed at 0 mV and then plotted against membrane potential

The full Markov model (f-MC) and the reduced Markov model (r-MC) were found to reproduce the experimental data quite closely in both the WT and N588K mutation conditions (Fig. 6.2aiii, Biii). The experimentally observed mutation-induced defect

in inactivation of the channel, which leads to the excessive generation of I_{Kr} was replicated by both Markov models. In comparative simulations, two Hodgkin Huxley models—Luo Rudy (LRd) and ten Tusscher-Noble-Noble-Panfilov (TNNP) models—failed to capture the kinetics of either the WT condition or N588K mutation. In the WT condition, all the models captured the rectification of the channel but it was rightward-shifted in the LRd model compared to the data (Fig. 6.2aiii). For the N588K mutation, the marked augmentation in I_{Kr} current in the mutation was seen in all the models (Fig. 6.2biii). However, only the f-MC and r-MC models accurately reproduce the data whereas there is no rectification of the I–V relation in the LRd model (Fig. 6.2biii).

The ability of the models to reproduce the dynamic properties of WT and N588K I_{Kr} under AP voltage-clamp ("AP clamp") and with paired AP commands (to mimic premature electrical stimulation) [12] was then examined (Fig. 6.3). Figure 6.3ai, aii show the time course of experimentally measured WT and N588K $I_{Kr/hERG}$ during the overlaid AP clamp [12], while Fig. 6.3aiii shows the paired AP command protocol. The simulated normalised 'instantaneous' I–V relationships for the WT and N588K mutant during the time course of the AP clamp are shown in Fig. 6.3bi–ei, bii–eii respectively for the Markov and Hodgkin-Huxley models. The equivalent experimental data [12] are superimposed on each plot for comparison with the model results.

The middle panels in Figs. 6.4 and 6.5 show representative WT and N588K $I_{Kr/hERG}$ obtained during ventricular AP voltage command (Figs. 6.4ai, aii and 6.5ai, aii). WT $I_{Kr/hERG}$ shows a small and gradual increase in current, which peaked during the repolarisation phase of the AP before declining in amplitude. In contrast, N588K $I_{Kr/hERG}$ shows a pronounced rise in outward current earlier than WT (due to the attenuation of inactivation by the mutation), leading to a dome-shaped current. Figures 6.4ci, cii and 6.5ci, cii show the simulation results from the f-MC and TNNP models respectively. The f-MC and r-MC models reproduced quite closely the experimental instantaneous I–V data for WT (Fig. 6.3bi, ci; Fig. 6.4ai–ci) and N588K mutation (Fig. 6.3bii, cii; Fig. 6.4aii–cii), including the positive shift in the peak repolarising current [12] caused by the N588K mutation. The TNNP and LRd models failed to reproduce accurately these experimental data for either the WT (Fig. 6.3di, ei; Fig. 6.5ai–ci) or mutant (Fig. 6.3dii, eii; Fig. 6.5aii–cii) conditions including the positive shift in peak repolarising current.

Figure 6.3biii–eiii shows the responses of hERG/I_{Kr} to the protocol comprised of paired-AP stimuli shown in Fig. 6.3aiii (see also [12]). The time-course profile of currents elicited by this protocol reflects the interaction between recovery from inactivation and deactivation of I_{hERG}/I_{Kr} channels [12, 21]. The f-MC, r-MC and TNNP models reproduced closely the experimental response of the hERG/I_{Kr} channel to a premature stimulus [12] while the LRd model failed to do so. Under the WT condition, the I_{Kr} amplitude increased with increasing inter-pulse interval reaching a peak at 30 ms after which it decreased with increasing inter-pulse intervals. Under the N588K condition, I_{Kr} amplitude began at significantly higher amplitude than WT and increased with increasing inter-pulse intervals. It peaked 10 ms earlier than for WT before it declined at greater intervals. During its

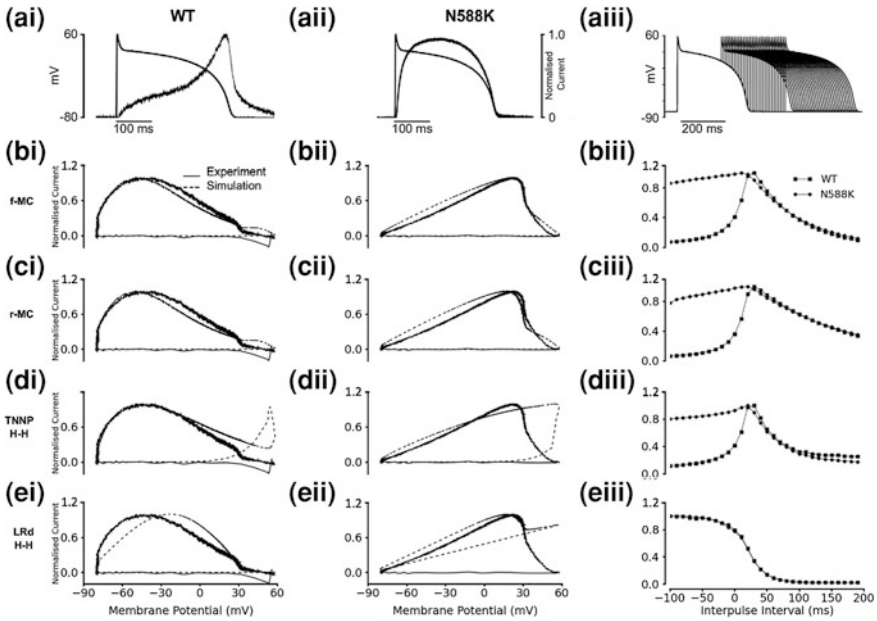

Fig. 6.3 I_{hERG}/I_{Kr} Current-Voltage (I–V) relations during action potential clamp and effect of premature stimuli. **a** Experimental recordings of current profiles of WT (**ai**) and N588K I_{hERG} (**aii**) elicited by the ventricular AP command waveform overlaid [12]. In each case, instantaneous current during AP repolarisation was normalised to maximal current elicited by the waveform. **aiii** Paired ventricular AP command waveform protocol used to elicit the I_{hERG}/I_{Kr} currents from which the normalised data in **biii**, **ciii**, **diii** and **eiii** were derived [12]. **b** Full Markov chain model: Instantaneous I–V relationships for WT (**bi**) and N588K I_{hERG}/I_{Kr} (**bii**). *Thick lines* show experimental recordings while the *dashed lines* show simulation results. **biii** Plots of I_{hERG}/I_{Kr} current during paired AP command waveforms (**aiii**) for WT (*squares*) and N588K condition (*circles*) respectively. **c** Reduced Markov chain model: Instantaneous I–V relationships for WT (**ci**) and N588K I_{hERG}/I_{Kr} (**cii**). *Thick lines* show experimental recordings while the *dashed lines* show simulation results. (**ciii**) Plots of I_{hERG}/I_{Kr} current during paired ventricular AP command waveforms (**aiii**) for WT (*squares*) and N588K condition (*circles*) respectively. **d** TNNP model: Instantaneous I–V relationships for WT (**di**) and N588K I_{hERG}/I_{Kr} (**dii**). *Thick lines* show experimental recordings while the *dashed lines* show simulation results. **diii** Plots of I_{hERG}/I_{Kr} current during paired ventricular AP command waveforms (**aiii**) for WT (*squares*) and N588K condition (*circles*) respectively. **e** Luo-Rudy model: Instantaneous I–V relationships for WT (**ei**) and N588K I_{hERG}/I_{Kr} (**eii**). *Thick lines* show experimental recordings while the *dashed lines* show simulation results. **eiii** Plots of I_{hERG}/I_{Kr} current during paired ventricular AP command waveforms (**aii**) for WT (*squares*) and N588K condition (*circles*) respectively

decline, it was smaller than WT in amplitude between 30 and 70 ms of the interpulse interval. However, the response of the LRd H–H model to paired-AP stimuli (Fig. 6.3eiii) failed to reproduce published experimental data [12]. Considered collectively, the AP clamp simulation data suggested that the f-MC and the r-MC models recapitulated better the dynamic properties of WT and N588K I_{hERG}/I_{Kr} at 37 °C than did the TNNP and Luo-Rudy H–H formulations.

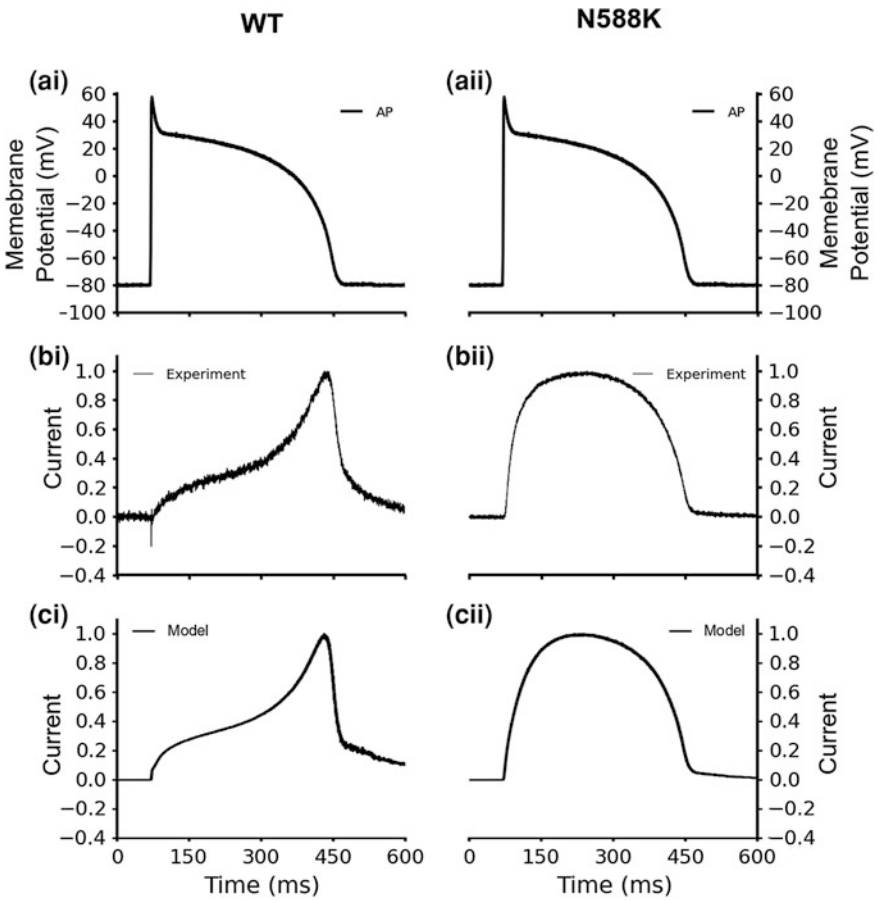

Fig. 6.4 Profile of I_{hERG} during ventricular AP voltage command under WT and N588K conditions obtained with the full Markov Chain model (f-MC). **a** Ventricular AP command waveform used to elicit the WT and N588K currents in (**b**) and (**c**). **b** Example current profiles of WT (**bi**) and N588K-hERG (**bii**) elicited by ventricular AP voltage clamp command. **c** Simulated current profiles of WT (**ci**) and N588K-hERG (**cii**) elicited by ventricular AP voltage clamp command

In order to characterise the functional effects of the N588K mutation on ventricular APs, the Markov models (f-MC and r-MC) and the HH models (Luo-Rudy and TNNP) for WT and N588K I_{Kr} were incorporated into the TNNP human ventricular single cell AP model. Figure 6.6a shows for the f-MC model in an EPI cell: simulated APs (6.6ai), I_{Kr} profile (6.6aii) and instantaneous I_{Kr} I–V relationship (6.6aiii). The MCELL and ENDO equivalents are shown in Fig. 6.6b, c respectively. In all three cell types, the N588K mutation abbreviated the action potential. Under the WT condition, following the upstroke of the AP, I_{Kr} increased in amplitude gradually, reaching a peak during the plateau phase just before

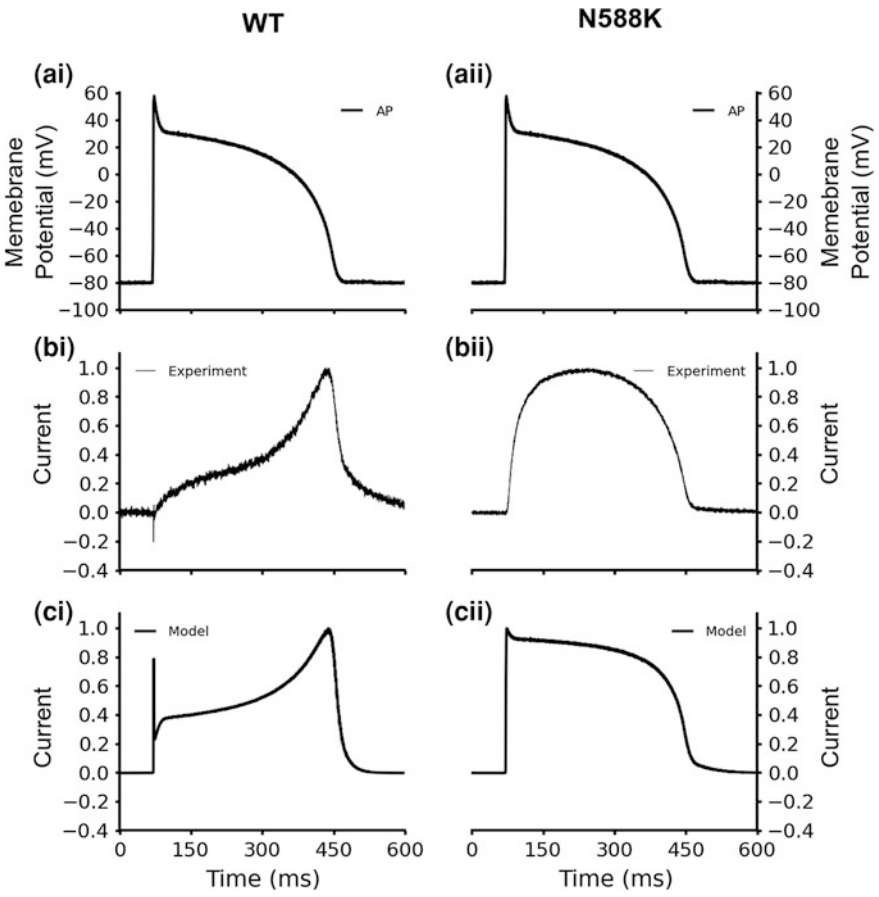

Fig. 6.5 Profile of I_{hERG} during ventricular AP voltage command under WT and N588K conditions obtained with the original TNNP I_{Kr} formulation model. **a** Ventricular AP command waveform used to elicit the WT and N588K currents in (**b**) and (**c**). **b** Example current profiles of WT (**bi**) and N588K-hERG (**bii**) elicited by ventricular AP voltage clamp command. **c** Simulated current profiles of WT (**ci**) and N588K-hERG (**cii**) elicited by ventricular AP voltage clamp command

terminal repolarisation. It then declined during the final repolarization phase of the AP [12, 15, 16, 18, 22]. With the N588K mutation, I_{Kr} activated earlier following the upstroke of the AP, increased considerably more rapidly and achieved significantly higher maximal amplitude earlier during the plateau phase than in the WT condition. Collectively, these changes in current profile led to a marked shortening of the APD. The APD_{90} for the WT and N588K mutant conditions plus the differences in APD_{90} are shown in Table 6.1.

Greater I_{Kr} earlier during the AP (in phase 2 rather than phase 3) caused the APD shortening in the N588K mutant condition, which resulted in accelerated repolarisation of the AP (Fig. 6.6ai, aii). The MIDDLE and ENDO cell models

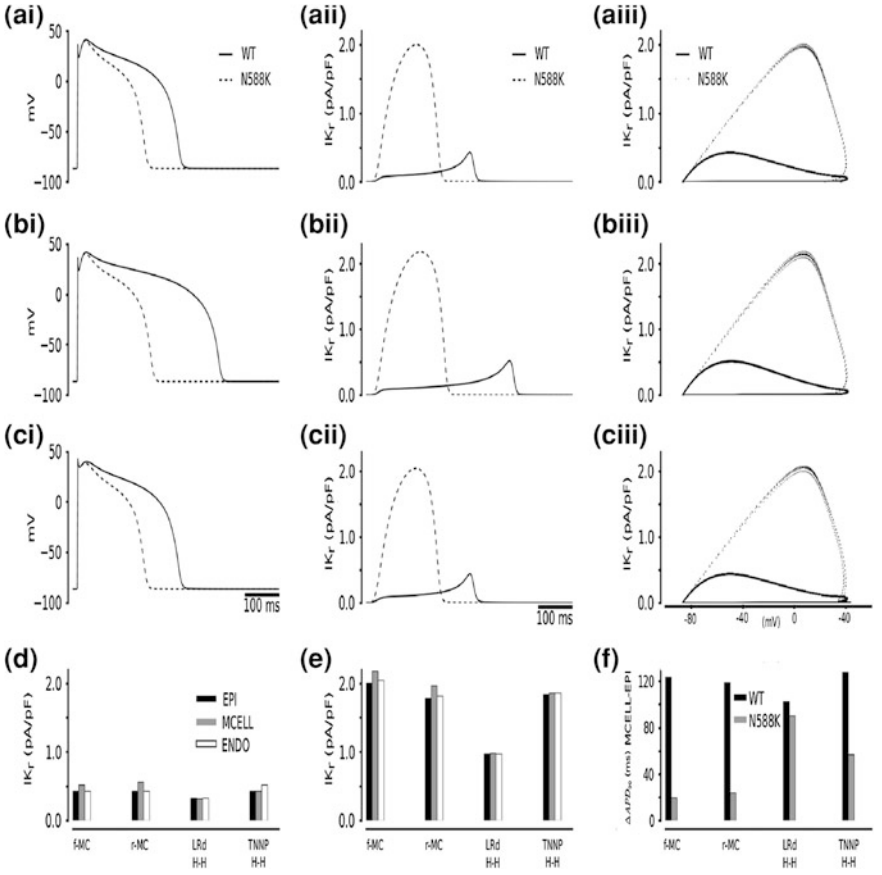

Fig. 6.6 Simulation of ventricular action potential and I_{Kr} time courses. *i* Steady state (1 Hz) action potentials for EPI (**ai**), MIDDLE (**bi**) and ENDO **ci** cells using the full Markov chain I_{hERG}/I_{Kr} model. *Thick lines* represent the WT and *dashed lines* represent the N588K condition. *ii* Corresponding I_{Kr} current profiles for EPI (**aii**), MIDDLE (**bii**) and ENDO (**cii**) cells. *Thick lines* represent the WT and *dashed lines* represent the N588K condition. *iii* Corresponding I–V relationships for EPI (**aiii**), MIDDLE (**biii**) and ENDO (**ciii**) cells. *Thick lines* represent the WT and *dotted lines* represent the N588K condition. **d**, **e** I_{Kr} current amplitude for EPI (*black bars*), MIDDLE (*grey bars*) and ENDO (*white bars*) cells for all four I_{hERG}/I_{Kr} formulations for WT (**d**) and N588K (**e**) conditions. **f** Computed APD difference between EPI and MIDDLE cells

similarly also showed APD reduction as illustrated in Fig. 6.6b, c. Figure 6.6d–f summarise the results for each of the f-MC, r-MC and the two HH I_{Kr} formulations in the EPI, MIDDLE and ENDO cell types. The marked APD shortening seen in these simulations due to augmented I_{Kr} in SQT1 agrees with results seen in previous studies, in which increased I_{Kr} due to the N588K mutation produced AP shortening in the Luo- Rudy and the Priebe-Beuckelmann AP models [16–18, 23].

One notable finding in respect of AP shortening is that the N588K mutation abbreviated APD_{90} to different degrees in the different cell types (i.e., non-

Table 6.1 Computed APD_{90} (ms) and ΔAPD_{90} (ms) under WT and N588K condition for the ENDO, MIDDLE and EPI cell models

Model	Cell type	WT APD_{90} (ms)	N588K APD_{90} (ms)	ΔAPD_{90} (ms)
f-MC	EPI	317	212	105
	MCELL	441	232	209
	ENDO	317	211	106
r-MC	EPI	317	225	92
	MCELL	436	249	187
	ENDO	317	224	93
TNNP	EPI	315	245	70
	MCELL	443	302	141
	ENDO	315	246	69
Luo-Rudy	EPI	316	295	21
	MCELL	419	386	33
	ENDO	316	296	20

ΔAPD_{90} was computed as the difference of APD_{90} between that of control condition and that of N588K condition

uniformly), with the greatest attenuation occurring in the MIDDLE cell. This situation has been seen in previous studies [16, 17]. Consequently, the mutation decreased the transmural dispersion of APD_{90} across the different cell types from the ventricular wall: EPI, MIDDLE and ENDO. Simulation results with the use of the f-MC, r-MC and H–H formulations all gave consistent results of decreased dispersion of APD_{90} by the N588K mutation when the models were compared (Fig. 6.6f).

Figure 6.7 shows the effect of the N588K mutation on APD restitution (APD-R). The four different I_{Kr} formulations were adjusted so that all the models showed similar APD restitution curves in the WT condition for EPI, MIDDLE and ENDO cells (Fig. 6.7ai–ci). Incorporation of the N588K mutation led to flattening of the APD restitution curves and to a reduction in APD_{90} in all three cell types. The mutation also shifted the APD restitution curves leftward and decreased the maximal slopes in the f-MC, r-MC and TNNP cell models (Fig. 6.7d). SQTS patients tend to exhibit poor rate-adaptation of their QT intervals [22, 24–28] and my results are consistent with this phenomenon as they suggested an attenuation of rate-adaptation of ventricular APD. To investigate this further, simulations of the steady state rate-dependence of the APD were performed (Fig. 6.8) using the f-MC model. Again, the N588K mutation flattened the curve and caused a leftwards shift. The f-MC and r-MC I_{Kr} mutant models showed greater APD abbreviation than the HH models, with the LRd I_{Kr} mutant model showing the least APD attenuation.

Figure 6.9 shows the effect of the N588K mutation on ERP restitution. As with the APD-R curves, the N588K mutation led to flattening of the ERP restitution (ERP-R) curves and to abbreviation of ventricular ERP in EPI, MIDDLE and ENDO cells (Fig. 6.9a–c). The mutation also shifted the ERP restitution curves leftward and decreased the maximal slopes in all the cell models (Fig. 6.9d).

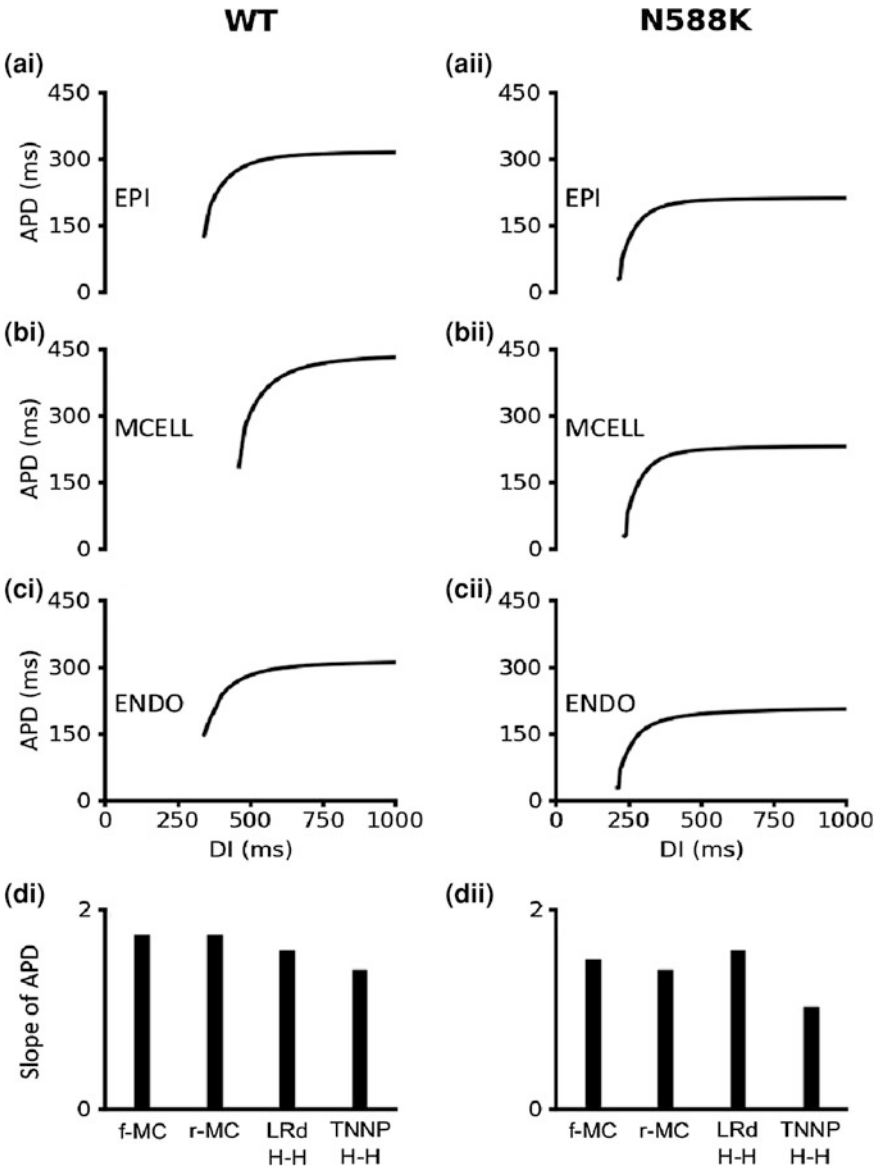

Fig. 6.7 Rate-dependent APD restitution. **ai–ci** WT APD restitution curves for EPI, MIDDLE and ENDO cells respectively for the full Markov chain I_{hERG}/I_{Kr} model formulation. **aii–cii** N588K APD restitution curves for EPI, MIDDLE and ENDO cells respectively for the full Markov chain I_{hERG}/I_{Kr} model formulation. **d**, **dii** Slopes of WT and N588K APD restitution curves for full Markov chain, reduced Markov chain, Luo-Rudy and TNNP hERG/I_{Kr} model formulations

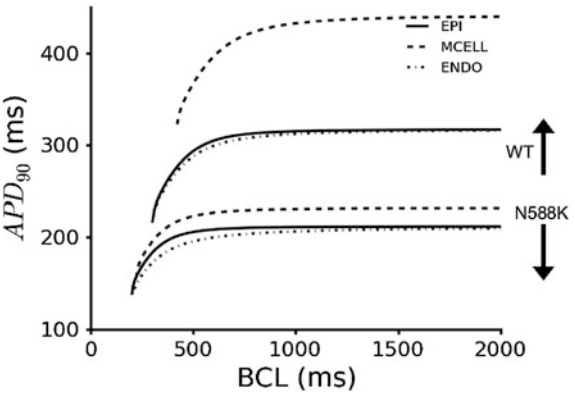

Fig. 6.8 Steady state APD rate dependence for the Full Markov Chain model (f-MC) incorporated into the TNNP ventricular action potential cell model

Similar to the APD-R results, these results also suggested a loss of rate-adaptation of ventricular ERP. In the WT condition, the four different I_{Kr} formulations produced similar ERP restitution curves, and as with the APD-R, the f-MC and r-MC I_{Kr} mutant models showed greater ERP reduction than the HH models, with the LRd I_{Kr} mutant model showing the least ERP attenuation.

6.3 Simulation of the ECG with WT and N588K Mutant I_{Kr}

A pseudo-ECG was computed (as described in Chap. 5, Sect. 5.3.1) using a 1D strand of cells across the ventricular wall for the WT and N588K conditions at a stimulation rate of 1 Hz (Fig. 6.10). Due to the limitations of the HH formulations in recapitulating the channel properties of I_{Kr} as shown in Figs. 6.2, 6.3, 6.4, 6.5, 6.6, 6.7, 6.8 and 6.9, these and all subsequent simulations were carried out with the f-MC model. A propagating excitation wave was initiated at the ENDO end of the strand by delivering a series of supra-threshold stimuli Sect. (5.2.3). The wave propagated from the ENDO through the MIDDLE and towards the EPI end of the strand. Figure 6.10a, b show space-time plots for WT and N588K conditions respectively, with space running vertically from ENDO at the bottom to EPI at top and time running horizontally from left to right. The N588K mutant shortened the QT interval to 240 ms from 378 ms for the WT condition (Fig. 6.10c (WT) and D (N588K)). Although the simulation of the N588K mutation reproduced the QT interval shortening seen in SQT1 patients, it failed to reproduce another key feature of SQT1 ECGs: a significant increase in the T-wave amplitude.

To rectify this deficiency, it was necessary to consider a heterogeneous distribution of I_{Kr} density in the 1D strand model. Available experimental data show that that hERG protein expression is approximately 1.5 times greater in the EPI region than in the MIDDLE region of human ventricle [29], providing a rational basis for the incorporation of heterogeneous I_{Kr} distribution in the strand. The I_{Kr}

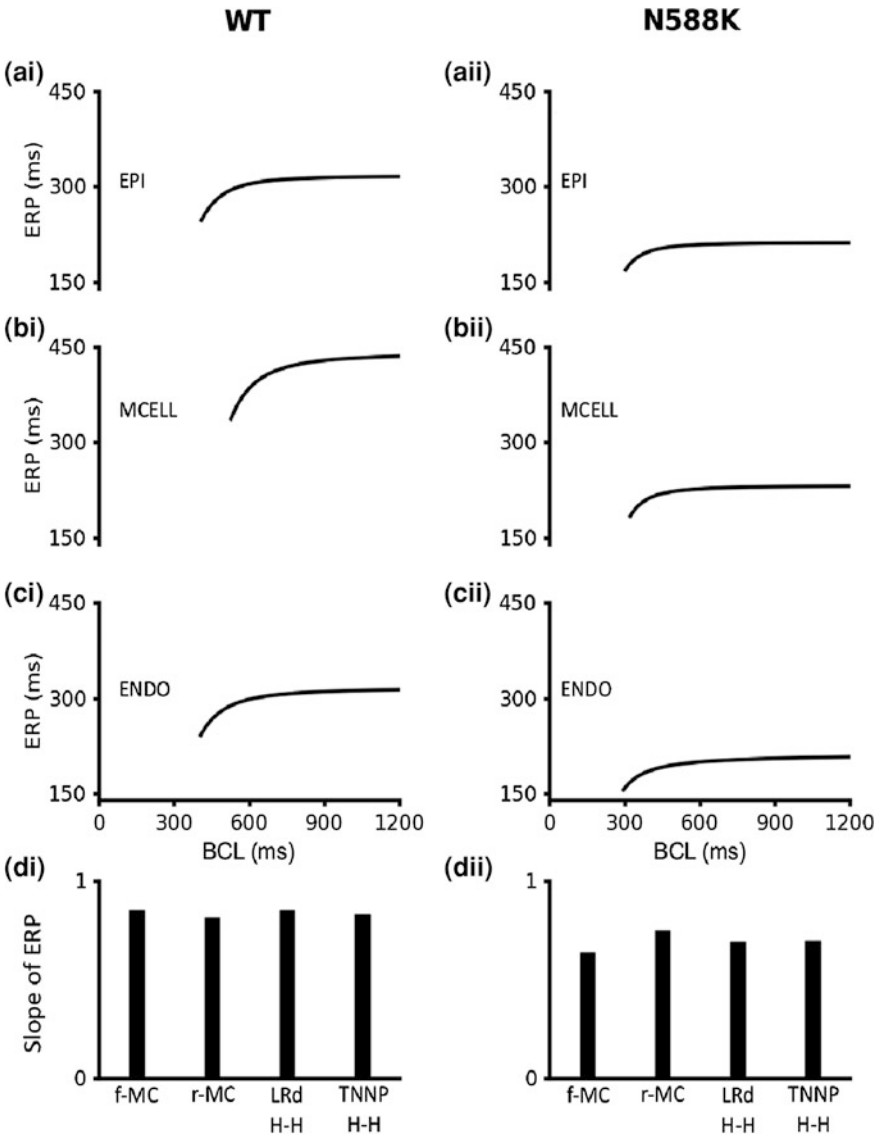

Fig. 6.9 ERP restitution curves of four models of ventricular myocytes. **ai–ci** WT ERP restitution curves for EPI, MIDDLE and ENDO cells respectively for the full Markov chain I_{hERG}/I_{Kr} model formulation. **aii–cii** N588K ERP restitution curves for EPI, MIDDLE and ENDO cells respectively for the full Markov chain I_{hERG}/I_{Kr} model formulation. **di**, **dii** Slopes of WT and N588K ERP restitution curves respectively for the full Markov chain, reduced Markov chain, Luo-Rudy and TNNP I_{hERG}/I_{Kr} model formulations

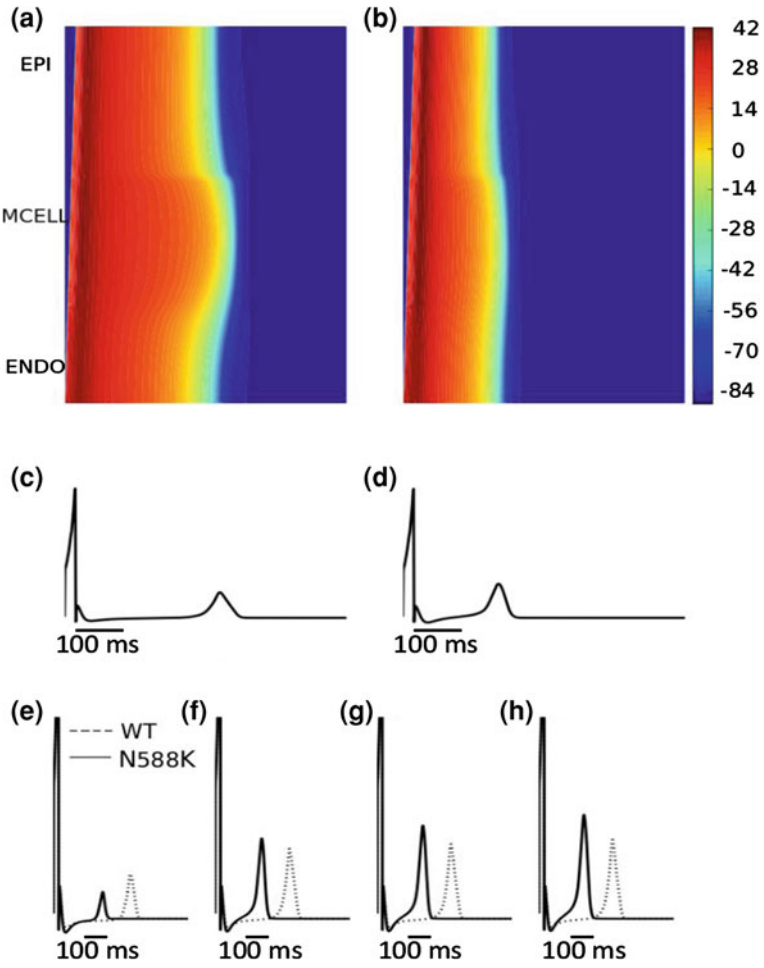

Fig. 6.10 Space-time plot of AP propagation along a 1D transmural ventricular tissue strand and computed pseudo-ECGs. **a**, **b** Colour mapping of membrane potential of cells along the 1D strand from *blue* (−86 mV) to *red* (−42 mV) (see colour key). Space runs vertically from the ENDO end to the EPI end at the *top*. Time runs horizontally. **a** Control (WT) condition. **b** SQT1 (N588K) condition. **c**, **d** Pseudo-ECGs corresponding to the WT and SQT1 (N588K) conditions respectively. **e–h** WT and N588K pseudo-ECGs for the different EPI: MIDDLE:ENDO I_{Kr} density ratios of 1.0:1:1, 1.5:1:1, 1.6:1:1 and 1.7:1:1 respectively

density was adjusted to be between 1.5-1.7 times greater in the EPI region than in the MIDDLE region. Following this adjustment, the model reproduced both key features of the SQT1 ECG under the mutation condition: QT interval abbreviation and increased T-wave amplitude. The results are shown in Fig. 6.10e–h.

6.4 Simulation of the Spatial Gradient of the Membrane Potential

Gima and Rudy [30] previously suggested that an increased spatial gradient of the membrane potential (δV) could be responsible for the tall T-wave height seen in hyperkalemia. It was also found to be relevant to the SQTS in a prior simulation study of SQT2 from our laboratories [23]. Therefore, to find out if the tall T-wave seen in the SQT1 ECGs shown in Fig. 6.10 could also be a consequence of this increased spatial gradient of δV, the effects were investigated of the N588K mutation on membrane potential heterogeneity (δV) during ventricular APs between the three cell types. The results are shown in Fig. 6.11, incorporating differing ratios of EPI I_{Kr} to MIDDLE and ENDO I_{Kr} in the WT (solid lines) and the N588K (dotted lines) mutation conditions. It shows the time course of the pair-wise differences of δV between the cell types for both the WT and N588K conditions.

With a ratio of 1:1:1 (Fig. 6.11a) of EPI I_{Kr} to MIDDLE and ENDO I_{Kr}, the N588K mutation decreased the (δV) in each pair-wise comparison. However, with ratios of 1.5:1:1 (Fig. 6.11b), 1.6:1:1 (Fig. 6.11c) and 1.7:1:1 (Fig. 6.11d) of the EPI I_{Kr} to MIDDLE and ENDO I_{Kr}, the N588K mutation increased the δV between ENDO and EPI cells (Fig. 6.11e), which is likely to have contributed to the increased T-wave amplitude in these simulation conditions [23, 30].

Figure 6.12a shows the spatial dispersion of APD_{90} across the intact transmural strand for both WT and N588K conditions with differing ratios of I_{Kr} density in the EPI, MIDDLE and ENDO regions. In the intact 1D strand, the electrotonic interactions between cells smoothed out the APD distribution (Fig. 6.12a) for both the WT and N588K mutation conditions. With a 1:1:1 ratio of EPI I_{Kr} to MIDDLE and ENDO I_{Kr}, the SQT1 mutant attenuated the spatial dispersion of APD_{90} relative to the WT condition. This is also illustrated by the plot of the spatial gradient of APD in Fig. 6.12b and its absolute value (Fig. 6.12c). However, with a ratio of 1.5:1:1 or above for the EPI I_{Kr} to MIDDLE and ENDO I_{Kr}, the N588K mutation augmented APD dispersion at localised regions of the MIDDLE region and at the junction region between the MIDDLE and EPI regions, which also contributed to an increased T-wave amplitude. A very sharp transition in APD_{90} can be seen between the MCELL and EPI regions in both Fig. 6.12b, c. This is due to a discontinuity in the electrical coupling at this border between MIDDLE and EPI cells, and is consistent with experimental observations made by Yan et al. [31] in an arterially perfused left ventricular wedge preparation and Drouin et al. [32] in their study (see Sect. 5.2.3).

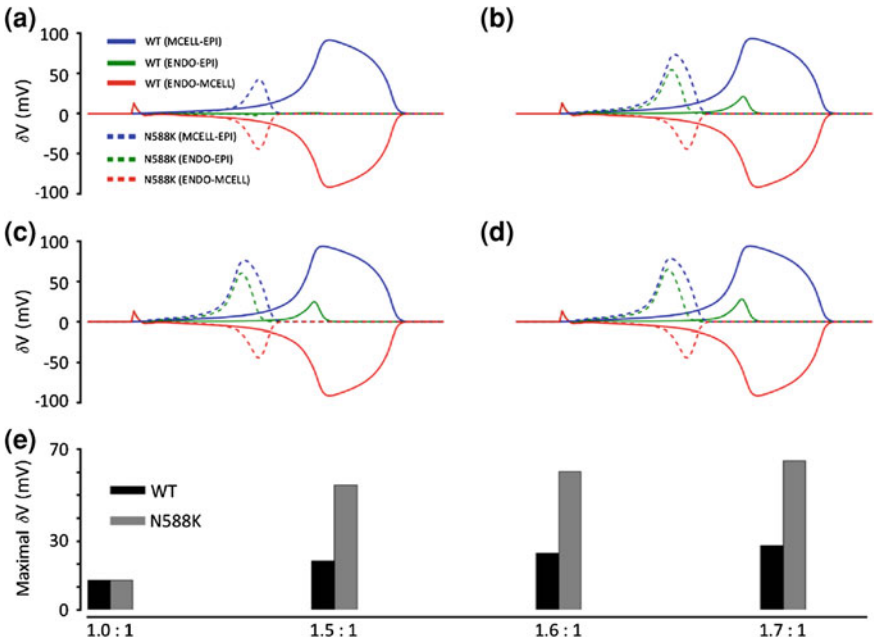

Fig. 6.11 Membrane potential heterogeneity (δV). **a–d** Plots of δV against time for WT (*continuous lines*) and N588K (*dotted lines*) conditions for different EPI:MIDDLE:ENDO I_{Kr} density ratios; **a** 1.0:1:1. **b**. 1.5:1:1. **c** 1.6:1:1. **d** 1.7:1:1. **e** Maximum δV during repolarization between ENDO-EPI cells in WT and N588K

6.5 Investigating the Arrhythmogenic Substrate in SQT1—1D Simulations

In order to investigate the susceptibility of the N588K mutant tissue to ventricular arrhythmias, simulations were carried out that quantified the vulnerability of the tissue to unidirectional conduction block in response to a premature stimulus: the susceptibility of the tissue to a premature stimulus provides a means of quantifying the risk of generating re-entrant excitation (that could lead to fibrillatory activity [33–36]). The premature stimulus was applied at the refractory tail of a previous excitation wave. Section 5.2.3.2 provides a detailed explanation of the procedure used to determine this vulnerable period of the tissue.

The results are shown in Fig. 6.13. The mutation decreased the vulnerable window throughout most of the strand except in the MIDDLE region marked by the superimposed vertical lines where the width of the vulnerable window was increased by the mutation. These results show that under the N588K mutation, the vulnerability of the tissue to arrhythmia is augmented in *localised* regions.

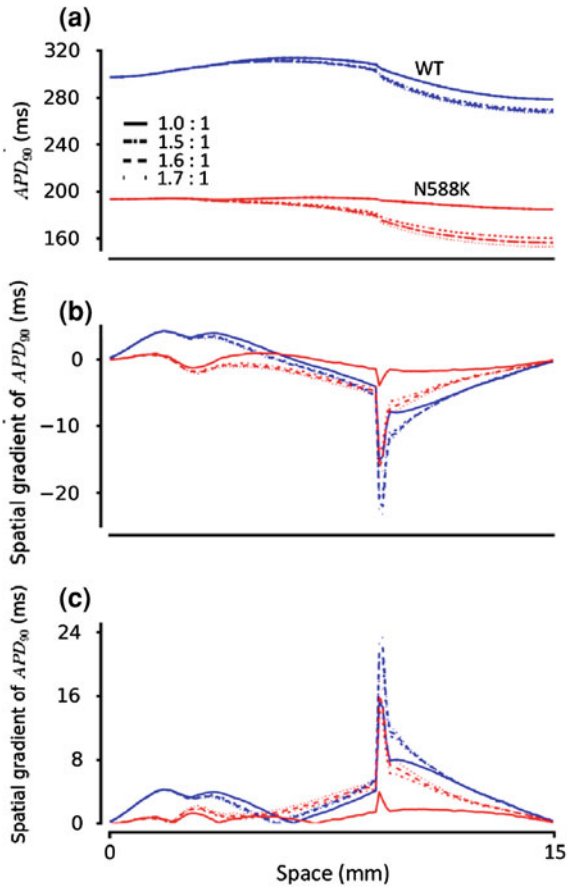

Fig. 6.12 Transmural APD_{90} distribution and its spatial gradient along a 1D tissue strand. **a** Spatial distribution of APD_{90} in the 1D transmural strand for WT (*blue*) and N588K (*red*) for different EPI:MIDDLE:ENDO I_{Kr} density ratios. *Continuous lines* (1.0:1:1), *dash-dot lines* (1.5:1:1), *dash-dash lines* (1.6:1:1), *dotted lines* (1.7:1:1). **b**, **c** Spatial gradient (**b**) and absolute spatial gradient (**c**) of APD_{90} in the 1D transmural strand for WT (*blue*) and N588K (*red*) for different EPI:MIDDLE:ENDO I_{Kr} density ratios. *Continuous lines* (1.0:1:1), *dash-dot lines* (1.5:1:1), *dash-dash lines* (1.6:1:1), *dotted lines* (1.7:1:1)

6.6 Investigating the Arrhythmogenic Substrate in SQT1: Idealised 2D Geometry Simulations

An idealised 2D tissue model was used to measure the minimal spatial size of a premature test stimulus necessary to produce re-entry under both WT and N588K conditions with a 1.6:1:1 ratio of the EPI I_{Kr} to MIDDLE I_{Kr} to ENDO I_{Kr}. The tissue had three distinct regions (ENDO, MCELL and EPI) similar to the

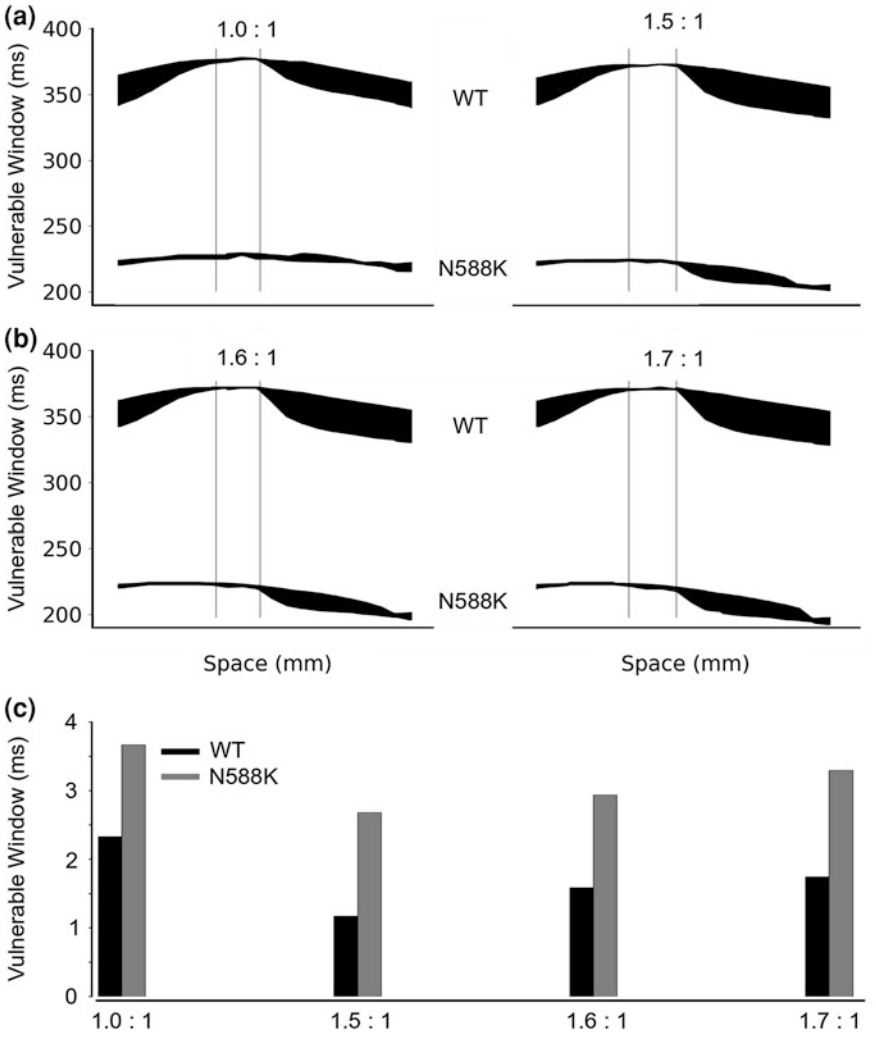

Fig. 6.13 Measured width of the vulnerable window along the 1D tissue strand. **a**–**d** Vulnerable window for WT and N588K along the 1D strand for different EPI:MIDDLE:ENDO I_{Kr} density ratios; **a** 1.0:1:1. **b** 1.5:1:1. **c** 1.6:1:1. **d** 1.7:1:1. **e** Comparison of the width of the vulnerable window between WT and N588K in the MIDDLE region of the 1D strand marked by *double lines*

transmural 1D strand; it was essentially the 1D strand swept out along the y-axis assuming the 1D strand is along the x-axis (Fig. 6.14a).

A planar excitation wave propagating from the ENDO towards the EPI region of the 2D sheet was evoked at the ENDO end via a conditioning stimulus for WT (Fig. 6.14ci) and N588K (Fig. 6.14di) conditions. After a time delay, a premature stimulus was applied to a local region in the EPI region during its VW (WT;

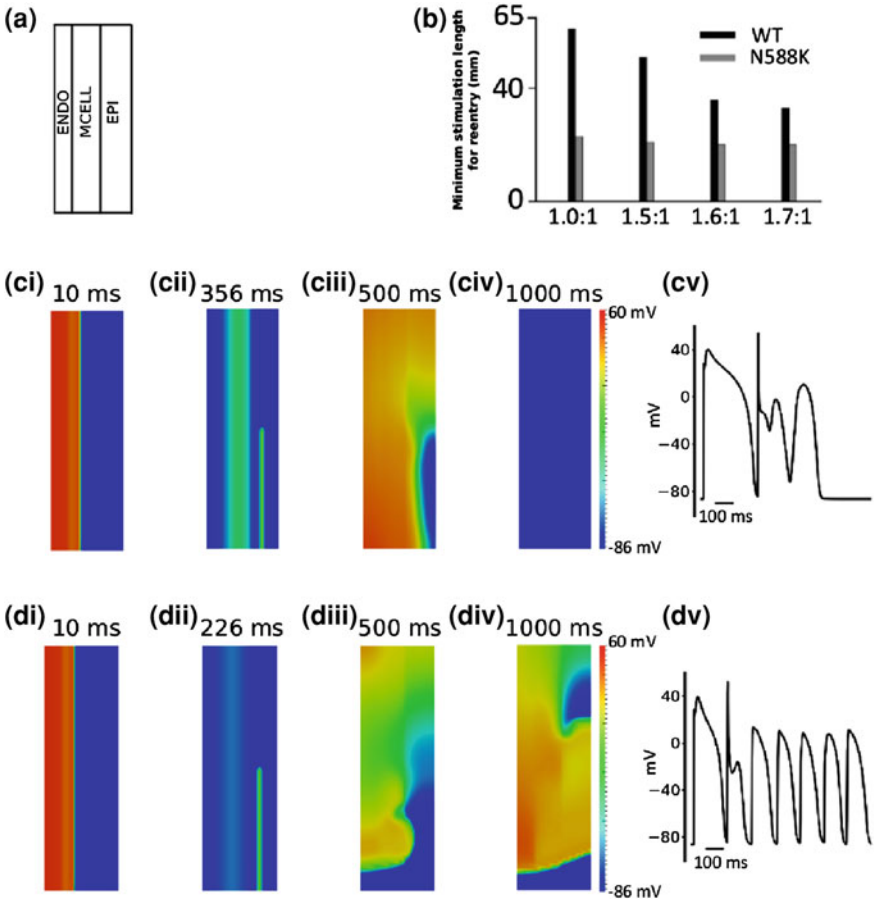

Fig. 6.14 Snapshots of initiation and conduction of re-entry in a 2D idealised model of transmural ventricle. **a** Schematic representation of the 2D model. **b** Minimal spatial length of a premature S2 stimulus that provides a sufficient substrate for the re-entrant circuit formation in WT and N588K for different EPI: MIDDLE:ENDO I_{Kr} density ratios; 1.0:1:1, 1.5:1:1, 1.6:1:1 and 1.7:1:1. **c**, **d, ci** and **di** A planar conditioning wave generated by S1 stimulus at the ENDO end. Snapshots at 10 ms. **cii** and **dii** S2 stimulus applied to the EPI part during the vulnerable window of the local tissue. **ciii** and **diii** Developed spiral wave from the S2 stimulus. Snapshots at 500 ms. **civ** and **div** Snapshot of spiral wave at 1,000 ms. Spiral wave self-terminated under the control condition before this recording point, but persisted under the SQT1 condition. **cv** and **dv** Evolution of the action potential of a cell in the epicardial region for WT and N588K conditions

Fig. 6.14cii and N588K; Fig. 6.14dii), thereby producing unidirectional conduction, towards the EPI end (as the MCELL region was still refractory). This resulted in the formation of spiral re-entrant excitation waves in both WT (Fig. 6.14ciii) and N588K (Fig. 6.14diii) conditions, which self-terminated under the WT condition (Fig. 6.14civ) but were sustained for the N588K condition (Fig. 6.14div).

As the formation of the re-entrant excitation waves is dependent on the size of the premature test stimulus, the minimal tissue substrate size that could evoke re-entry was measured. This is proportional to the wavelength of excitation (the product of conduction velocity and APD_{90}) and gives the minimal size of the substrate length necessary to sustain reentry in ventricular tissue. The measured size was 51 mm in the WT condition and 23 mm in the N588K condition (Fig. 6.14b), showing that with the N588K mutation, it was easier to induce re-entry and hence, ventricular arrhythmias. Once initiated, reentry terminated within 284 ms in WT but was sustained in the N588K mutant condition. Thus these simulations suggest that in the N588K mutation SQT1 condition there is a greater susceptibility to ventricular arrhythmia.

6.7 Investigating the Arrhythmogenic Substrate in SQT1: 2D and 3D Simulations with Realistic Geometry

Realistic ventricular geometry is considerably more complex structurally than an idealised 2D sheet. It also has anisotropic conduction due to the presence of fibre orientations. Therefore, it may be erroneous to assume that the results in the idealised 2D geometry necessarily translate into similar activity with realistic tissue geometry. Consequently, simulations were performed in a 2D cross-section of human ventricle tissue (Fig. 5.3) and in human 3D anatomical ventricle geometry (Fig. 5.5). The regions in the 2D and 3D ventricular geometries were divided into the same proportions of EPI, MCELL and ENDO as in the 1D strand and the idealised 2D geometry.

6.7.1 Simulations in Realistic 2D Geometry

Figure 6.15 shows the simulation results in the 2D human ventricle slice with a 1.6:1:1 ratio of the EPI I_{Kr} to MIDDLE I_{Kr} to ENDO I_{Kr}. Figure 6.15a, b show the application of a premature stimulus (WT: 400 ms and N588K: 241 ms) during the vulnerable window of a local region in the left ventricle in both WT and N588K conditions. This led to the development of re-entrant excitation waves in both conditions (Fig. 6.15b, g). These re-entrant spiral waves self-terminated within 755 ms in WT (Fig. 6.15d, k) but persisted in the N588K mutant (Fig. 6.15i, k). The spiral waves persisted for the entire duration (5 s) of the simulation in the N588K condition (Fig. 6.15k).

Figure 6.15e, j show the evolution of the AP in a local cell in the left ventricle under both WT and N588K conditions. Power spectrum analysis carried out on the APs showed a higher dominant frequency under the N588K condition compared to the WT condition (Fig. 6.15l). These results together are consistent with those from the idealised 2D tissue.

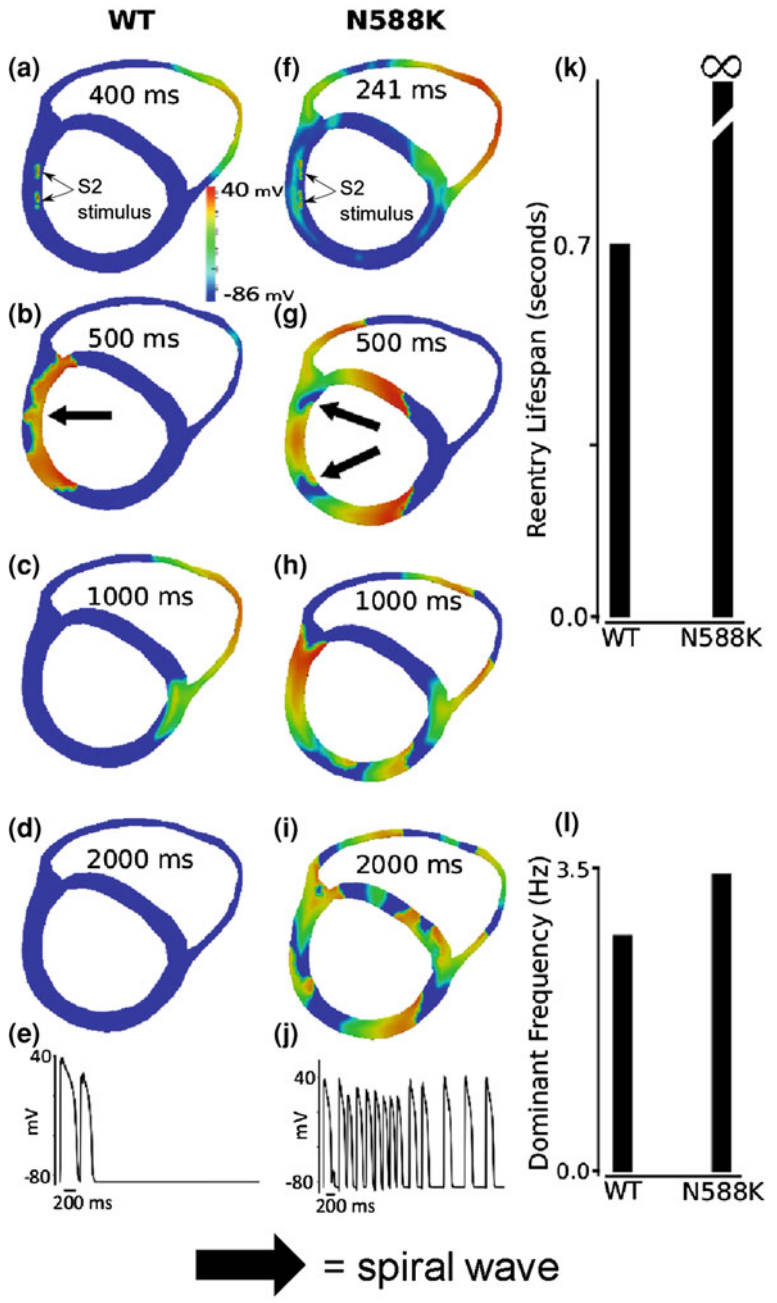
WT
N588K
(a)
400 ms
S2
stimulus
40 mV
-86 mV
(f)
241 ms
S2
stimulus
(b)
500 ms
(g)
500 ms
(c)
1000 ms
(h)
1000 ms
(d)
2000 ms
(i)
2000 ms
(e)
40
mV
-80
200 ms
(j)
40
mV
-80
200 ms
(k)
∞
Reentry Lifespan (seconds)
0.7
0.0
WT
N588K
(l)
3.5
Dominant Frequency (Hz)
0.0
WT
N588K
= spiral wave

◀ **Fig. 6.15** Snapshots of initiation and conduction of re-entry in realistic 2D model cross-section of ventricles. **a**, **f** Application of a premature S2 stimulus into the refractory and partially recovered region of an excitation wave after a delay of 400 ms for WT and 241 ms for N588K condition from the initial wave stimulus. **b**, **g** Developed spiral wave from the S2 stimulus. Snapshot at time = 500 ms. **c**, **h** Snapshot of spiral wave at time = 1,000 ms. The induced spiral wave transited from transmural re-entry with tip rotating within the ventricle wall to anatomical re-entry with tip rotating around the ventricle boundary in WT. However, transmural re-entry persisted in N588K condition and broke-up forming regenerative multiple re-entrant wavelets. **d** and **i** Snapshot of spiral wave at time = 2,000 ms. Spiral wave self-terminated in WT before this recording point, but persisted in N588K condition. **e** and **j** Evolution of the action potential of a cell in the *left* ventricle for WT and N588K conditions. **k** Measured lifespan of the re-entry circuits in WT and N588K condition. **l** Computed dominant frequency of electrical activity recorded from the tissue in WT and N588K conditions (about 2.7 Hz for WT and 3.4 Hz for N588K condition)

6.7.2 Simulations in Realistic 3D Geometry

Figure 6.16 shows the results of the simulations performed using the anatomical human 3D ventricle geometry, with a 1.6:1:1 ratio of the EPI I_{Kr} to MIDDLE I_{Kr} to ENDO I_{Kr}. The premature stimulus (with an amplitude of -104 pA/pF) was applied from the base of the ventricle up to halfway towards its apex, covering a region of approximately 90 × 63 mm in both WT (380 ms) and N588K (245 ms) conditions (Fig. 6.16a, b). This region included the left ventricle and the surrounding area of the right ventricular outflow tract. The premature stimulus was applied during the vulnerable window following the refractory tail of a previous excitation wave. It evoked an excitation wave that propagated uni-directionally in the retrograde direction of the control excitation wave, leading to the generation of re-entrant scroll waves within the ventricular wall (Fig. 6.16b, g).

The re-entrant scroll waves terminated within 600 ms in the WT condition (Fig. 6.16d) but broke up into sustained multiple wavelets under the N588K condition (Fig. 6.16i). Figure 6.16k shows the lifespan of re-entry under both conditions while Fig. 6.16e, j show the evolution of the AP in a local cell in the left ventricle under both WT and N588K conditions respectively. Power spectrum analysis on the APs showed a higher dominant frequency under the N588K condition (5.3 Hz) compared to the WT condition (2.7 Hz) (Fig. 6.16l). This further supports the pro-arrhythmic nature of the N588K mutation, which was shown in the 1D and 2D simulations.

6.8 Discussion and Conclusions

6.8.1 Summary of Major Findings

A phenotypically accurate mammalian experimental model of SQT1 does not yet exist. Therefore, the use of in silico models and methods provides an alternative

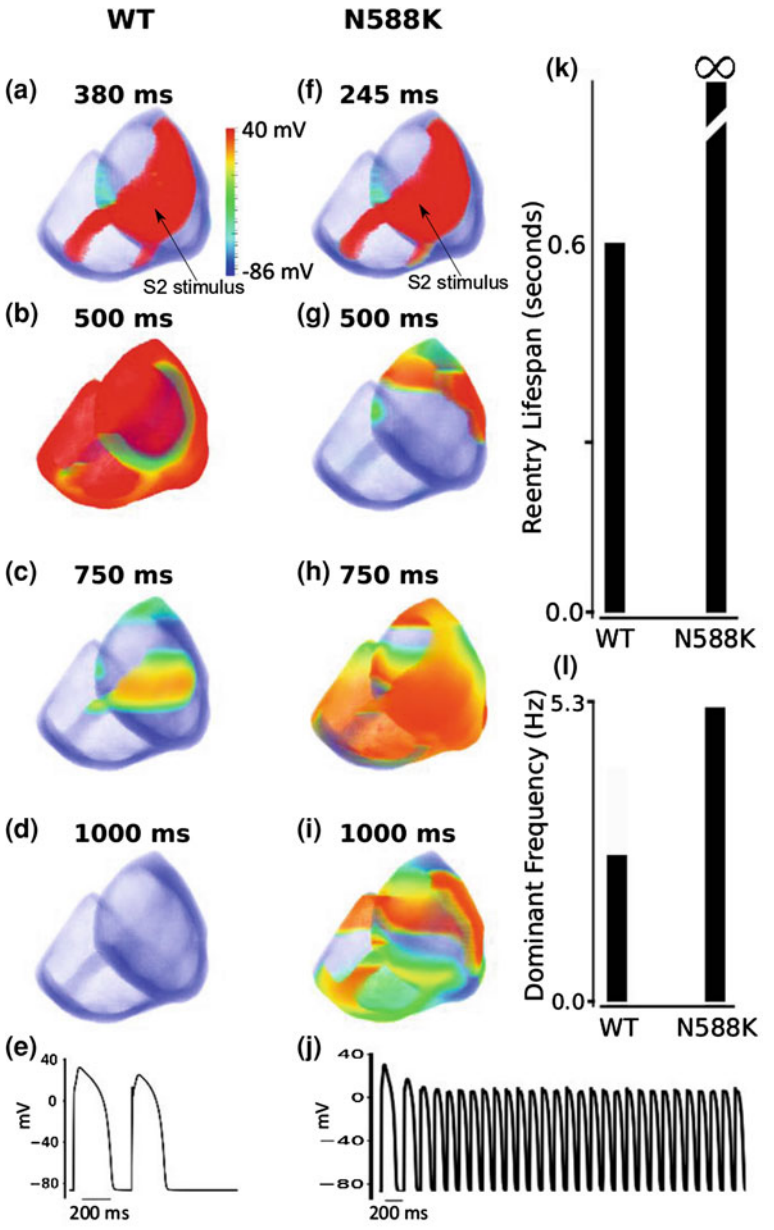
WT
N588K
(a) 380 ms
(f) 245 ms
40 mV
-86 mV
S2 stimulus
S2 stimulus
(b) 500 ms
(g) 500 ms
(c) 750 ms
(h) 750 ms
(d) 1000 ms
(i) 1000 ms
(e)
40
0
-40
-80
mV
200 ms
(j)
40
0
-40
-80
mV
200 ms
(k)
∞
0.6
0.0
Reentry Lifespan (seconds)
WT
N588K
(l)
5.3
0.0
Dominant Frequency (Hz)
WT
N588K

◀ **Fig. 6.16** Snapshots of initiation and conduction of re-entry in a 3D anatomical model of human ventricles. **a**, **f** Application of a S2 premature stimulus (*red*) in a local region during the refractory period of a previous conditioning excitation wave after a time delay of 380 ms for WT and 245 ms for N588K condition from the initial conditioning wave stimulus. **b**, **g** Developed scroll wave from the S2 stimulus. Snapshot at time = 500 ms. **c**, **h** Snapshot of scroll wave at time = 750 ms. The scroll wave self-terminated in the WT condition, but persisted and broke up forming regenerative wavelets in the N588K condition, **d** and **i** Snapshot of scroll wave at time = 1,000 ms. The scroll wave self-terminated in WT before this recording point, but still persisted in N588K condition. **e** and **j** Evolution of the action potential of a cell in the *left* ventricle for WT and N588K conditions. **k** Measured lifespan of re-entry scroll wave in WT and in N588K condition. **l** Computed dominant frequency of electrical activity recorded from ventricle in WT and N588K conditions (2.7 Hz for WT and 6.3 Hz for N588K condition)

and valuable means of investigating the functional consequences of SQT mutations on genesis and maintenance of ventricular arrhythmias. The major findings of the present study are:

(i) The Markov chain I_{Kr} formulations tested reproduced better the dynamic properties of hERG/I_{Kr} under both WT and N588K hERG SQT1 conditions than did the Luo-Rudy and TNNP H–H formulations;
(ii) The N588K hERG mutation is causally linked to QT interval shortening, whether or not I_{Kr} is presumed to be homogeneously distributed across the ventricular wall; however, a heterogeneous I_{Kr} density across the ventricular strand model was found to be necessary to reproduce a taller T-wave amplitude as has been seen clinically in SQT1;
(iii) With a heterogeneous I_{Kr} density across the strand, the N588K mutation led to augmented membrane potential differences (δV) between ENDO and EPI cells compared pair-wise and transmural APD dispersion in localised regions of the transmural strand that contributed to the increased T-wave amplitude;
(iv) The N588K mutation increased at some localised regions the tissue's temporal vulnerability to the genesis of uni-directional conduction by a premature excitation;
(v) The N588K mutation decreased the minimal tissue substrate size that facilitates the maintenance of re-entry as shown in both idealised and realistic tissue models of the human ventricle. These findings substantiate the causal link between the N588K mutation and QT interval shortening and, moreover, provide a comprehensive explanation for increased susceptibility to re-entry and perpetuation of re-entrant arrhythmia in the setting of SQT1.

6.8.2 Significance of the Study

In silico characterisation of the functional consequences of the N588K hERG, KvLQT1 V307L (SQT2) and KCNJ2 (SQT3) mutations on ventricular cell AP shortening and characteristics of simulated ECGs have been the subject of some

prior studies [8, 16, 23]. However, whilst for the V307L-KCNQ1 SQT2 mutation, investigation (using 1D and 2D idealised geometries) of its pro-arrhythmic effects has been conducted [23], simulations addressing the effects of the N588K mutation on perpetuating and facilitating re-entrant excitation waves in ventricular tissue have not been performed until now. Furthermore, the present study is the first to determine the arrhythmogenic consequences of the N588K mutation using multi-scale models of the human ventricles.

In an earlier study, Kogan et al. [37] used a simple model to demonstrate similar re-entrant propensity when the AP is shortened. They found that slowing the deactivation rate of delayed outward K^+ current had a profound effect on wave-front propagation. Although the Kogan et al. study is important in that it provides a causal link between augmented K^+ conductance (via deactivation alteration of deactivation characteristics) and arrhythmogenesis, the SQT1 N588K-hERG mutation is characterised by impaired inactivation not deactivation, and therefore requires targeted simulations that specifically reproduce kinetic changes to I_{Kr} by the SQT1 N588K-hERG mutation.

Prior studies [16, 17] have reported inhomogeneous shortening of ventricular APD with loss of I_{Kr} inactivation, which appears paradoxical in light of increased arrhythmia susceptibility in the syndrome. The present study resolves this apparent contradiction: whilst it has been demonstrated that the AP shortening as a result of N588K mutation is inhomogeneous, (resulting in a decreased APD_{90} and ERP dispersion, as the greatest shortening of APD_{90} occurred in MIDDLE cell APs), with heterogeneous I_{Kr} in the ventricle the mutation augmented both membrane potential difference between paired ENDO and EPI cells and the APD dispersion in some localised regions of the transmural strand. The present study is the first to incorporate heterogeneous I_{Kr} density in the ventricle [29] for the study of SQT1. These changes lead to an increased T-wave amplitude, which is different to previous simulation results but is consistent with clinical observations [5, 27, 38, 39]. Another consequence of these changes is greater susceptibility of the tissue to unidirectional conduction block in response to a premature excitation stimulus.

The present study also shows that the N588K mutation reduces the minimal tissue size of the substrate required to facilitate and sustain re-entry in both idealised 2D and realistic 2D and 3D geometries. This occurs with either a homogeneous or heterogeneous distribution of I_{Kr} across the ventricular wall. In all tissue models, a single reentrant excitation wave can break up into multiple re-entrant circuits, leading to a transition from tachycardia-like to fibrillation-like electrical excitation waves.

6.8.3 Relevance to Previous Studies

Extramiana and Antzelevitch [15] used the $I_{K,ATP}$ channel activator pinacidil on a perfused canine ventricular wedge to study arrhythmogenesis under an abbreviated repolarisation setting. This intervention resulted in preferential abbreviation of the

mid-myocardial AP, increased transmural dispersion of repolarisation and easily induced ventricular tachycardia via programmed electrical stimulation [15]. The I_{Kr} agonist, PD-118057, was also subsequently found to produce similar results [4], although the mechanism through which this compound increases I_{Kr} is mechanistically distinct from that of the hERG N588K mutation. Unlike N588K-hERG, PD-118057 does not affect the gating or kinetic properties of the hERG/I_{Kr} channel [40]; it has been postulated that this compound is able to bind directly to the channel and increase its open probability [40]. The simulations in this chapter show for the first time that with biophysically accurate I_{Kr} models of N588K-hERG, a similar pro-arrhythmic substrate does actually occur for SQT1.

A prior simulation study by Zhang et al. [23] has shown that the effects of the adult SQT2 variant also involve an augmentation of transmural APD heterogeneity, refractory dispersion and increased tissue vulnerability to arrhythmogenesis in the ventricle [23], although geometrically accurate 2D and 3D simulations were not investigated. Results of the present simulations suggest that there is however a difference in the extent and nature of transmural APD dispersion produced by SQT2 and SQT1 variants. Whilst SQT2 augments the APD dispersion across the whole transmural strand [23], SQT1 increases the APD dispersion in some localised regions (Fig. 6.12). The likely underlying mechanism is probably due to the difference in the augmentation of the spatial gradient of the membrane potential (δV). Compared to the WT condition, SQT1 augments δV pairwise only between ENDO and EPI cell types (Fig. 6.11) whereas the SQT2 variant augments δV pairwise between all cell types (Fig. 7.7a).

Thus, in the present study, it was discovered that, with a heterogeneous distribution of I_{Kr} density across the ventricular wall, the N588K hERG mutation may lead to augmented APD dispersion in localised regions of tissue and augmented membrane potential difference. These changes account for an increased T-wave amplitude on the ECG as observed clinically. In addition, they can also enhance the vulnerability of tissue to unidirectional conduction block in localised regions of the ventricular wall, thus facilitating reentry. Nevertheless, a similarity between SQT1 and SQT2 [25] from the simulations is that both the N588K mutation (this study) and the V307L-KCNQ1 mutation [23] reduce the minimal size of ventricular tissue to sustain reentry.

Since commencing this study, a new mutation to the *KCNH2* gene, which encodes the hERG channel has been discovered in a Chinese family [41]. It involves a single base pair C → T substitution at nucleotide 1853 (C1853T) of the *KCNH2* gene, which resulted in an amino-acid substitution (threonine to isoleucine exchange) at position 618 (T618I) in the hERG channel protein [41]. The T618I mutation alters hERG gating kinetics by attenuating inactivation and increasing the rate of recovery from inactivation [41]. The major benefit of the in silico approach adopted in the present study is that the models that have been developed can be used to investigate the pro-arrhythmic effects of the T168I mutation (and indeed any further new hERG mutations identified in the future in patients with variant 1 SQTS). The same approach also has utility in investigating the efficacy of

and consequently, the design of drugs to counter the pro-arrhythmic effects of the hERG mutations.

The study that constitutes the basis for this thesis chapter has been published in full paper form [42].

References

1. Gussak I, Brugada P, Brugada J, Wright RS, Kopecky SL, Chaitman BR et al (2000) Idiopathic short QT interval: a new clinical syndrome? Cardiology 94(2):99–102
2. Schimpf R, Wolpert C, Gaita F, Giustetto C, Borggrefe M (2005) Short QT syndrome. Cardiovasc Res 67(3):357–366
3. Maury P, Extramiana F, Sbragia P, Giustetto C, Schimpf R, Duparc A et al (2008) Short QT syndrome. Update on a recent entity. Arch Cardiovasc Dis 101(11–12):779–786
4. Patel C, Antzelevitch C (2008) Cellular basis for arrhythmogenesis in an experimental model of the SQT1 form of the short QT syndrome. Heart Rhythm 5(4):585–590
5. Brugada R, Hong K, Dumaine R, Cordeiro J, Gaita F, Borggrefe M et al (2004) Sudden death associated with short-QT syndrome linked to mutations in HERG. Circulation 109(1):30–35
6. Hong K, Bjerregaard P, Gussak I, Brugada R (2005) Short QT syndrome and atrial fibrillation caused by mutation in KCNH2. J Cardiovasc Electrophysiol 16(4):394–396
7. Bellocq C, van Ginneken ACG, Bezzina CR, Alders M, Escande D, Mannens MMAM et al (2004) Mutation in the KCNQ1 gene leading to the short QT-interval syndrome. Circulation 109(20):2394–2397
8. Priori SG, Pandit SV, Rivolta I, Berenfeld O, Ronchetti E, Dhamoon A et al (2005) A novel form of short QT syndrome (SQT3) is caused by a mutation in the KCNJ2 gene. Circ Res 96(7):800–807
9. Hong K, Piper DR, Diaz-Valdecantos A, Brugada J, Oliva A, Burashnikov E et al (2005) De novo KCNQ1 mutation responsible for atrial fibrillation and short QT syndrome in utero. Cardiovasc Res 68(3):433–440
10. McPate MJ, Duncan RS, Milnes JT, Witchel HJ, Hancox JC (2005) The N588K-HERG K+ channel mutation in the "short QT syndrome": mechanism of gain-in-function determined at 37 degrees C. Biochem Biophys Res Commun 334(2):441–449
11. Cordeiro JM, Brugada R, Wu YS, Hong K, Dumaine R (2005) Modulation of I(Kr) inactivation by mutation N588K in KCNH2: a link to arrhythmogenesis in short QT syndrome. Cardiovasc Res 67(3):498–509
12. McPate MJ, Zhang H, Adeniran I, Cordeiro JM, Witchel HJ, Hancox JC (2009) Comparative effects of the short QT N588K mutation at 37 degrees C on hERG K + channel current during ventricular, Purkinje fibre and atrial action potentials: an action potential clamp study. J Physiol Pharmacol 60(1):23–41
13. Mitcheson JS, Sanguinetti MC (1999) Biophysical properties and molecular basis of cardiac rapid and slow delayed rectifier potassium channels. Cell Physiol Biochem 9(4–5):201–216
14. Antzelevitch C, Sicouri S (1994) Clinical relevance of cardiac arrhythmias generated by afterdepolarizations. Role of M cells in the generation of U waves, triggered activity and torsade de pointes. J Am Coll Cardiol 23(1):259–277
15. Extramiana F, Antzelevitch C (2004) Amplified transmural dispersion of repolarization as the basis for arrhythmogenesis in a canine ventricular-wedge model of short-QT syndrome. Circulation 110(24):3661–3666
16. Weiss DL, Seemann G, Sachse FB, Dössel O (2005) Modelling of short QT syndrome in a heterogeneous model of the human ventricular wall. Europace 7(Suppl 2):105–117

17. Zhang H, Hancox JC (2004) In silico study of action potential and QT interval shortening due to loss of inactivation of the cardiac rapid delayed rectifier potassium current. Biochem Biophys Res Commun 322(2):693–699
18. Itoh H, Horie M, Ito M, Imoto K (2006) Arrhythmogenesis in the short-QT syndrome associated with combined HERG channel gating defects: a simulation study. Circ J 70(4):502–508
19. Kharche S, Garratt CJ, Boyett MR, Inada S, Holden AV, Hancox JC et al (2008) Atrial proarrhythmia due to increased inward rectifier current (I(K1)) arising from KCNJ2 mutation—a simulation study. Prog Biophys Mol Biol 98(2–3):186–197
20. El Harchi A, McPate MJ, Zhang YH, Zhang H, Hancox JC (2010) Action potential clamp and mefloquine sensitivity of recombinant "I KS" channels incorporating the V307L KCNQ1 mutation. J Physiol Pharmacol 61(2):123–131
21. Lu Y, Mahaut-Smith MP, Varghese A, Huang CL, Kemp PR, Vandenberg JI (2001) Effects of premature stimulation on HERG K(+) channels. J Physiol (Lond) 537(Pt 3):843–851
22. Brugada R, Hong K, Cordeiro JM, Dumaine R (2005) Short QT syndrome. CMAJ 173(11):1349–1354
23. Zhang H, Kharche S, Holden AV, Hancox JC (2008) Repolarisation and vulnerability to re-entry in the human heart with short QT syndrome arising from KCNQ1 mutation–a simulation study. Prog Biophys Mol Biol 96(1–3):112–131
24. Gussak I, Brugada P, Brugada J, Antzelevitch C, Osbakken M, Bjerregaard P (2002) ECG phenomenon of idiopathic and paradoxical short QT intervals. Card Electrophysiol Rev 6(1–2):49–53
25. Couderc J-P, Lopes CM (2010) Short and long QT syndromes: does QT length really matter? J Electrocardiol 43(5):396–399
26. Patel U, Pavri BB (2009) Short QT syndrome: a review. Cardiol Rev 17(6):300–303
27. Giustetto C, Di Monte F, Wolpert C, Borggrefe M, Schimpf R, Sbragia P et al (2006) Short QT syndrome: clinical findings and diagnostic-therapeutic implications. Eur Heart J 27(20):2440–2447
28. Gaita F, Giustetto C, Bianchi F, Schimpf R, Haissaguerre M, Calò L et al (2004) Short QT syndrome: pharmacological treatment. J Am Coll Cardiol 43(8):1494–1499
29. Szabó G, Szentandrássy N, Bíró T, Tóth BI, Czifra G, Magyar J et al (2005) Asymmetrical distribution of ion channels in canine and human left-ventricular wall: epicardium versus midmyocardium. Pflugers Arch 450(5):307–316
30. Gima K, Rudy Y (2002) Ionic current basis of electrocardiographic waveforms: a model study. Circ Res 90(8):889–896
31. Yan GX, Shimizu W, Antzelevitch C (1998) Characteristics and distribution of M cells in arterially perfused canine left ventricular wedge preparations. Circulation 98(18):1921–1927
32. Drouin E, Charpentier F, Gauthier C, Laurent K, Le Marec H (1995) Electrophysiologic characteristics of cells spanning the left ventricular wall of human heart: evidence for presence of M cells. J Am Coll Cardiol 26(1):185–192
33. Zhang H, Wang J, Yang L, Wu R-J, Mei X, Zhao W (2011) Vulnerability in simulated ischemic ventricular transmural tissues. Chin J Physiol 54(6):427–434
34. Chen XZ, Zhang H, Jin YB, Yang L (2009) Vulnerability to unidirectional conduction block and reentry in rabbit left ventricular wedge preparation: effects of stimulation sequence and location. Chin J Physiol 52(1):16–22
35. Trénor B, Romero L, Ferrero JM Jr, Sáiz J, Moltó G, Alonso JM (2007) Vulnerability to reentry in a regionally ischemic tissue: a simulation study. Ann Biomed Eng 35(10):1756–1770
36. Qu Z, Garfinkel A, Weiss JN (2006) Vulnerable window for conduction block in a one-dimensional cable of cardiac cells, 1: single extrasystoles. Biophys J 91(3):793–804
37. Kogan BY, Karplus WJ, Billett BS, Pang AT, Khan SS, Mandel WJ et al (1991) The role of diastolic outward current deactivation kinetics on the induction of spiral waves. Pacing Clin Electrophysiol 14(11 Pt 2):1688–1693

38. Gollob MH, Redpath CJ, Roberts JD (2011) The short QT syndrome: proposed diagnostic criteria. J Am Coll Cardiol 57(7):802–812
39. Watanabe H, Makiyama T, Koyama T, Kannankeril PJ, Seto S, Okamura K et al (2010) High prevalence of early repolarization in short QT syndrome. Heart Rhythm 7(5):647–652
40. Zhou J, Augelli-Szafran CE, Bradley JA, Chen X, Koci BJ, Volberg WA et al (2005) Novel potent human ether-a-go-go-related gene (hERG) potassium channel enhancers and their in vitro antiarrhythmic activity. Mol Pharmacol 68(3):876–884
41. Sun Y, Quan X-Q, Fromme S, Cox RH, Zhang P, Zhang L et al (2011) A novel mutation in the KCNH2 gene associated with short QT syndrome. J Mol Cell Cardiol 50(3):433–441
42. Adeniran I, McPate MJW, Witchel HJ, Hancox JC, Zhang H (2011) Increased vulnerability of human ventricle to re-entrant excitation in herg-linked variant 1 short QT syndrome. Plos Comput Biol 7(12):e1002313

Chapter 7
Mathematically Modelling the Functional Consequences of the SQT2 Mutation

7.1 Introduction

Variant 2 of the SQTS (SQT2) is associated with gain-of-function mutations to the KCNQ1 protein [1, 2], which when co-expressed with KCNE1 (mink; β-subunit) recapitulates the I_{Ks} channel [3, 4] that is partly responsible for repolarization of the action potential. As introduced in Chap. 3, adult SQT2 was the second variant to be identified in an SQT patient [1]. A valine to leucine substitution at position 307 (V307L) on the P-loop of the KCNQ1 protein was found in a 70-year-old man successfully resuscitated from ventricular fibrillation. He was observed to have a shortened rate-corrected QT (QT_c) interval of ~300 ms [1]. In vitro electrophysiological studies have revealed that the V307L mutation shifts the voltage-dependence of activation towards more negative voltages and accelerates the time-course of current activation, resulting in increased repolarizing I_{Ks} which has been assumed to shorten the action potential duration leading to an abbreviated QT interval [1]. However, due to lack of experimental animal models, the causal link between the V307L mutation and a shortened QT interval, especially the exact mechanism(s) by which it increases the risk of arrhythmogenesis has not been elucidated.

As discussed in previous chapters, in silico studies constitute an alternative approach that can be used to identify arrhythmogenic substrates and mechanisms in the SQTS. In reporting the SQT2 variant, Bellocq et al. [1] also conducted limited in silico investigation; while they observed the characteristic action potential shortening, they did not investigate the mutation's impact on the QT interval or its pro-arrhythmic effects. Subsequently, using Hodgkin–Huxley style formulations [5, 6] for I_{Ks}, Zhang et al. [7] conducted the first detailed in silico study of adult SQT2:

$$I_{Ks} = g_{Ks} \times x_s^2 \times (V - E_{Ks}) \tag{1}$$

$$\frac{dx_s}{dt} = \frac{(x_{s,\infty} - x_s)}{\tau_{x_s}} \tag{2}$$

I. Adeniran, *Modelling the Short QT Syndrome Gene Mutations*, Springer Theses, DOI: 10.1007/978-3-319-07200-5_7,

$$x_{s,\infty} = \frac{1}{1 + e^{(V_{0.5} - V_m)/S}} \tag{3}$$

where g_{ks} is the maximal conductance (μS/pF), x_s is the activation variable, $x_{s,\infty}$ is the steady state activation variable, E_{Ks} is the equilibrium potential of the channel, τ_{xs} is the voltage-dependent time constant of activation, s is the slope factor, V_m is the membrane potential and $V_{0.5}$ is the half-activation voltage. This study [7] modified parameters in Eqs. (1–3) to reproduce the data of Bellocq et al. [1]. However, a subsequent in vitro study reported an additional kinetic change to KCNQ1 + KCNE1 channel current: slowed current deactivation in the SQT2 [8]. This finding was not available at the time of the study of Zhang et al. [7], nor does the study by Zhang et al. [7] consider the functional consequences of the mutation in anatomically realistic geometries in two and three dimensions.

The present study was conducted to address these issues, and has gone further by developing a Markov chain model for the effects on I_{Ks} of the SQT2 V307L KCNQ1 mutation (Sect. 4.3). Markov chain models have several advantages over HH-style models including the ability to reproduce more accurately the kinetics of ion channels (see Sect. 4.1 for a detailed discussion of their advantages over HH models).

The specific aims of the present study were:

i. To reproduce the kinetic changes to I_{Ks} in SQT2 based on available experimental data at physiological temperature by using a novel Markov chain model formulation.
ii. To use human ventricular cell-based models to determine the functional consequences of incorporating the SQT2 mutation on AP repolarization and the QT interval.
iii. To explore the arrhythmogenic substrate in SQT2 by using "realistic" 2D tissue and 3D organ simulations.

As will be shown, the results provide a clear link between the kinetic changes to $I_{KCNQ1\text{-}KCNE1}/I_{Ks}$ in SQT2 and the altered ventricular tissue electrophysiology, which produces re-entrant arrhythmia in the SQT2.

7.2 Homozygote and Heterozygote Formulations

Section 4.3 gives a detailed discussion of the development of the SQT2 (homozygote—i.e. 'pure' SQT2 mutation). The Markov chain model developed for V307L KCNQ1 containing I_{Ks} was validated against experimental data [8] and was then used to investigate the functional consequences of SQT2 in single cell and realistic multicellular (1D, 2D and 3D) tissue. Figure 4.4 shows the state transition diagram for the SQT2 Markov chain model. The developed Markov chain models in Sect. 4.3 represent the WT and pure homozygote (V307L)

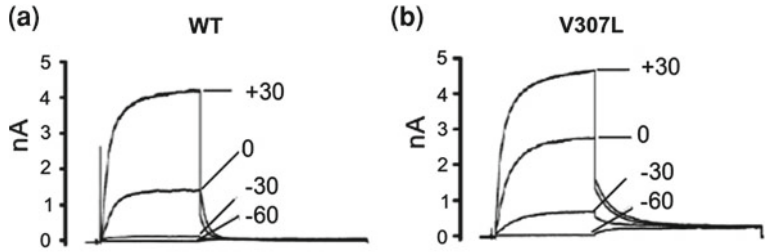

Fig. 7.1 WT and V307L $I_{KCNQ1\text{-}KCNE1}$ experimental current traces under voltage clamp. **a** WT experimental traces and **b** V307L experimental current traces elicited by voltage clamp commands shown in Fig. 7.2**aii** and **bii**. Figure modified from [8]

conditions only. However, the proband in whom the SQT2 mutation was discovered was heterozygotic for the mutation [1]. Therefore, to mimic the heterozygous state of the proband, a heterozygous formulation (WT-V307L) consisting of 50 % WT and 50 % V307L was constructed and used to investigate the effects of the KCNQ1 V307L mutation in this heterozygous condition.

7.3 Simulation of Single Cell I_{Ks} Under Control and SQT2 Conditions

As the first step, the ability of the Markov chain model to reproduce published experimental data [8] on the voltage-dependence of activation of WT and the V307L mutant at physiological temperature was tested. The same voltage clamp protocol used experimentally [8] was employed. Figure 7.1a shows representative experimental current traces for WT (Fig. 7.1a) and V307L (Fig. 7.1b) $I_{KCNQ1\text{-}KCNE1}$ elicited by the voltage clamp protocol in Fig. 7.2aii and bii. The simulated current traces are shown in Fig. 7.2ai and bi for WT and V307L respectively. The I–V relationships for WT (Fig. 7.2aiii) and V307L (Fig. 7.2biii) were reconstructed from the current traces. Of significance is that the simulated current traces (Fig. 7.2ai, bi) match experimental recordings (Fig. 7.1a, b) and showed the slower deactivation rate of the I_{Ks} channel under the V307L condition [1, 8], compared to the WT, which is reproduced almost faultlessly (Fig. 7.2ai, bi).

The developed Markov chain model of I_{Ks} was validated by its ability to reproduce the dynamic properties of WT and V307L I_{Ks} under AP clamp. Figure 7.2aiv and biv show the results of the simulated I_{Ks} time traces during AP clamps, which are compared to those obtained experimentally [8]. As shown in the figure, the Markov chain model reproduced the experimental data of I_{Ks} during the time course of AP, including the augmented I_{Ks} current in the KCNQ1 V307L mutation condition.

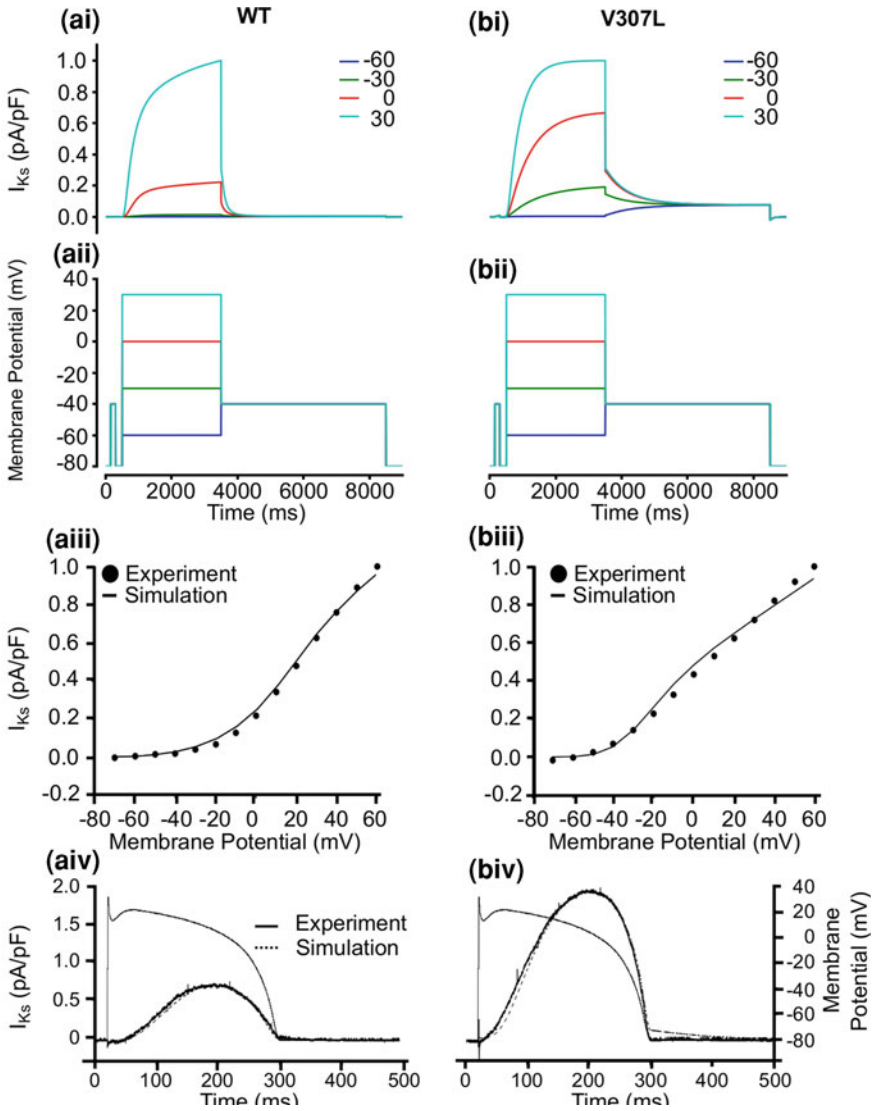

Fig. 7.2 Simulated Current-Voltage Relationships for I_{Ks}. Current traces for WT (**ai**) and V307L I_{Ks} (**bi**) elicited by the voltage protocol shown in (**aii**, **bii**). I–V relation for I_{Ks} for WT (**aiii**) and V307L I_{Ks} (**biii**). Profile of I_{Ks} during ventricular AP voltage command under WT (**aiv**) and V307L (**biv**) conditions

In order to characterise the functional effects of the V307L mutation on ventricular APs, the Markov chain model formulation was then incorporated into the 2006 TNNP ventricular single cell model [9] for WT, V307L mutation and heterozygous mutation (WT-V307L) conditions (Sect. 7.2). Figure 7.3 shows the

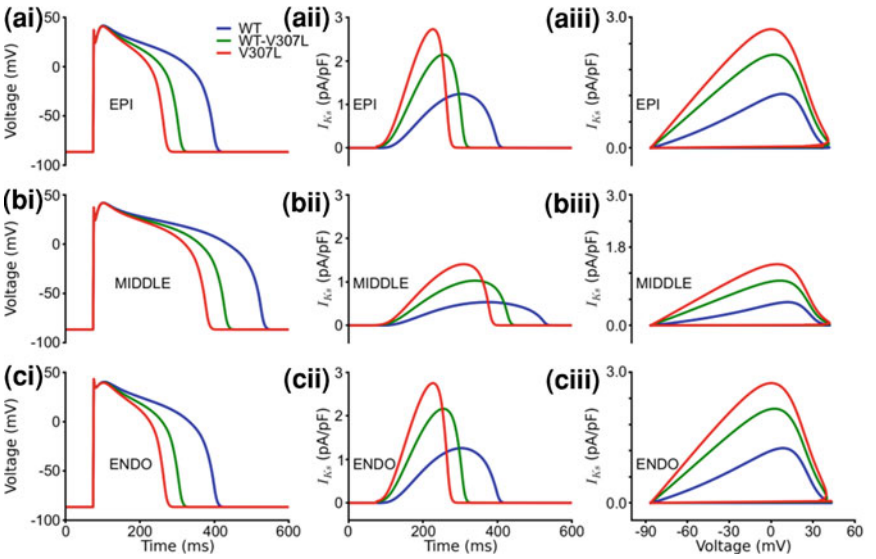

Fig. 7.3 Simulation of action potential and sI_{Ks} time courses. (i) Steady state (1 Hz) action potentials for EPI (**ai**), MIDDLE (**bi**) and ENDO (**ci**) cells. *Blue lines* represent WT, *green lines* represent WT-V307L and *red lines* represent the V307L condition. (ii) Corresponding I_{Ks} current profiles for EPI (**aii**), MIDDLE (**bii**) and ENDO (**cii**) cells. *Blue lines* represent WT, *green lines* represent WT-V307L and *red lines* represent the V307L condition. (iii) Corresponding I–V relationships for EPI (**aiii**), MIDDLE (**biii**) and ENDO (**ciii**) cells. *Blue lines* represent WT, *green lines* represent WT-V307L and *red lines* represent the V307L condition

simulated APs (ai), the I_{Ks} profile (aii) and I_{Ks} instantaneous I–V relationship for an EPI cell model. The MIDDLE and ENDO counterparts are shown in Fig. 7.3bi and ci respectively. In the WT condition, during the time course of the AP, I_{Ks} increased progressively following the upstroke of the AP and reached maximal amplitude very late during the plateau phase before declining rapidly during terminal repolarization. WT-V307L I_{Ks} activated earlier than WT and increased in amplitude more rapidly. Unlike in the WT condition, it reached significantly higher maximal amplitude early during the plateau leading to the abbreviation of the APD. V307L I_{Ks} activated the earliest of the three conditions, increased the most rapidly and attained the greatest maximal amplitude. Consequently, it abbreviated the APD to the greatest extent.

Under the WT condition, the computed APD_{90} was 326, 454 and 327 ms for EPI, MIDDLE and ENDO cells respectively. These were shortened respectively to 233, 355 and 234 ms under the WT-V307L condition and to 194, 306 and 194 ms under the V307L mutation condition. The APD_{90} values for all the conditions are summarised in Table 7.1. The APD shortening resulted from the augmented I_{Ks} early during the plateau phase of the AP as shown by time course of I_{Ks} (Fig. 7.3aii–cii) and the I–V phase plots in Fig. 7.3aiii–ciii. These results agree

Table 7.1 Computed APD_{90} (ms) for EPI, MCELL and ENDO cell types under WT, WT-V307L and V307L conditions

	WT (ms)	WT-V307L (ms)	V307L (ms)
EPI	325.56	232.98	193.60
MCELL	453.62	355.38	305.94
ENDO	327.36	233.76	194.04

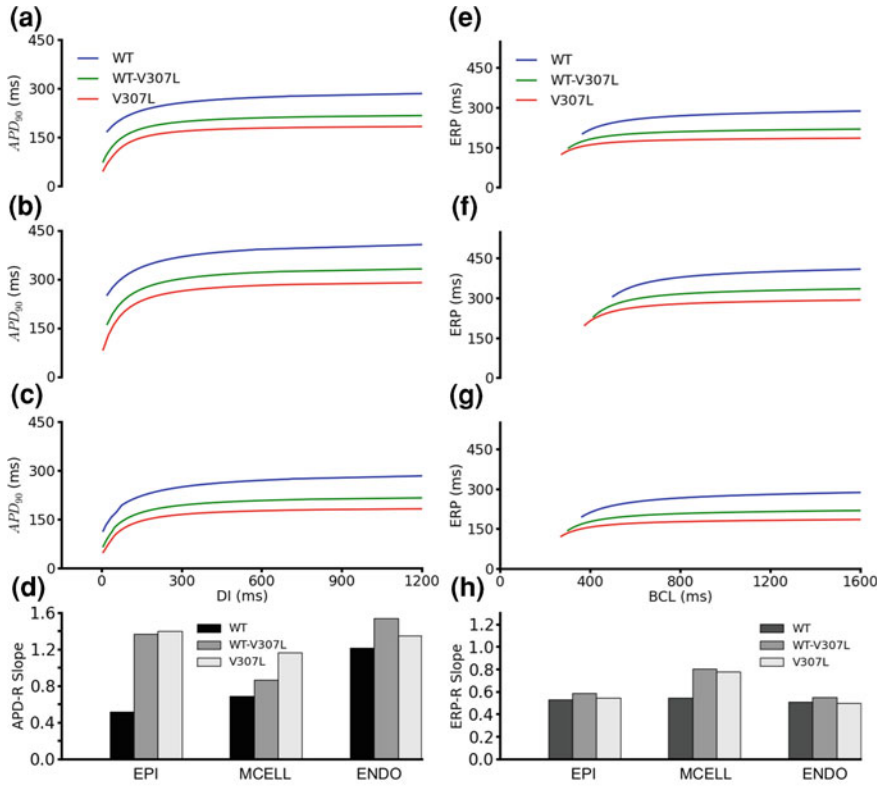

Fig. 7.4 APD and ERP restitution curves. **a**, **b**, **c**: APD restitution curves for EPI (**a**), MIDDLE (**b**) and ENDO (**c**) cells respectively for the WT, WT-V307L and V307L conditions. **d** Measured slopes of APD restitution curves for EPI, MIDDLE and ENDO cells in WT, WT-V307L and V307L conditions. **e**, **f**, **g** ERP restitution curves for EPI (**e**), MIDDLE (**f**) and ENDO (**g**) cells respectively for the WT, WT-V307L and V307L conditions. **h** Measured slopes of ERP restitution curves for EPI, MIDDLE and ENDO cells for WT, WT-V307L and V307L conditions

with the findings of Bellocq et al. [1] who observed an increase in I_{Ks} and APD shortening under V307L condition using the Priebe-Beuckelmann AP model [10].

The APD abbreviation was rate-dependent as shown by the APD-Restitution (APD-R) curves in Fig. 7.4a–c for the EPI, MIDDLE and ENDO cell types respectively. Over the range of diastolic intervals (DI) studied, the APD was

smaller in the WT-V307L and V307L mutants than in the WT condition. The mutations also steepened the APD-R curves in each cell type as shown by the computed maximal slopes for each APD-R curve in Fig. 7.4d. In the EPI cell, the maximal slopes of the WT-V307L and V307L mutations were similar, while there was a progressive increase in steepness of the slopes in the MIDDLE cell type. In the ENDO cell, while the slopes under the WT-V307L and V307L conditions were steeper than WT, the slope of the WT-V307L mutant was steeper than that of the V307L mutant.

The ERP reduction was also rate-dependent. It was reduced under the WT-V307L and V307L mutation conditions compared to the WT condition across the range of basic stimulus cycle lengths (BCL) as shown in ERP-R curve in Fig. 7.4e–g for the EPI, MIDDLE and ENDO cell types respectively. In the EPI and ENDO cells, there was little difference in the slopes of the ERP-R curves between the WT, WT-V307L and V307L conditions (Fig. 7.4h). The slope was steeper for the mutation conditions in the MIDDLE cell compared to WT cell but the slope for the WT-V307L condition was slightly steeper than that for the V307L mutant. The mutations also shifted the ERP-R curve leftwards implying that the KCNQ1 V307L mutation enabled ventricular cells to support electrical activity at higher rates (as normally seen during VT and VF).

Figure 7.5 shows the state occupancy of the WT, WT-V307L and V307L I_{Ks} channels during the AP in zone 1 (blue), zone 2 (green) and the open states; O_1 and O_2 (red) Fig. 4.4. Zone 2 is occupied by channels where the voltage sensors still need to make the slow transition to zone 1 before transitioning to the open state while channels in zone 1 have already made this transition and only need to undertake a fast transition to the open states (see Sect. 4.3.1). Under the WT condition (Fig. 7.5ai, bi), approximately all channels accumulate in zone 2 at AP initiation and thus need to make the slow transition to zone 1 before full activation, which accounts for the delay in activation seen in I_{Ks} channels [11–14].

Under the WT-V307L condition (Fig. 7.5aii, bii), at the initiation of the AP, approximately 2 % of the channels occupy zone 1 (compared with 0 % in WT) while the rest occupy zone 2. Therefore, the delay in activation is shorter under the WT-V307L condition and channels transition to the open states faster. Nevertheless, one would assume a similar activation rate and progression as the WT condition, but due to the slower deactivation under the WT-V307L condition, channels accumulate in the open state resulting in excess current during the plateau phase of the AP and hence AP shortening. Under the V307L condition (Fig. 7.5aiii, biii), on AP initiation, $\sim$3.5 % of the channels occupy zone 1 with the remainder occupying zone 2. Therefore, just as with the WT-V307L condition, as the AP progresses, there is faster open state transition and more open state accumulation (due to slower channel deactivation) compared to both WT and WT-V307L conditions leading to the even greater AP shortening.

These results imply that under both the WT-V307L and V307L conditions, the primary mechanism for excessive current that causes AP shortening is the greater channel occupancy of zone 1 with a fast transition to the open state coupled with

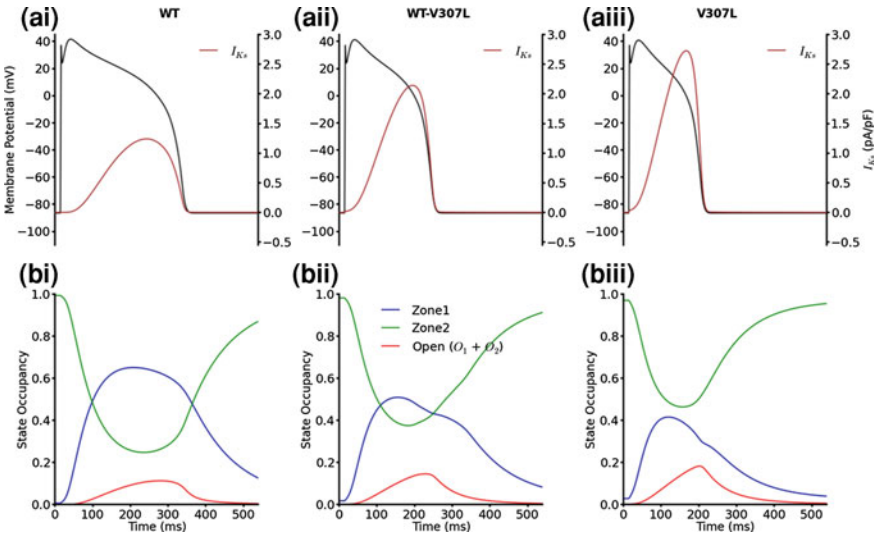

Fig. 7.5 WT, WT-V307L and V307L state occupancy during the AP. **ai**, **aii**, **aiii**: Action potential and I_{Ks} under the WT (**ai**), WT-V307L (**aii**), V307L (**aiii**). **bi**, **bii**, **biii**: State occupancy during the APs. *Green* shows zone 2 occupancy, *blue* shows zone 1 occupancy and *red* shows open state occupancy. Accumulation in zone 2 leads to a slow transition to zone 1 and hence a delay in activation under WT (**bi**). Accumulation in zone 1 and open-state accumulation due to slow channel deactivation accelerates channel opening and larger I_{Ks} during the AP under WT-V307L condition (**bii**) leading to APD abbreviation (**aii**). Slow channel deactivation results in open-state accumulation under the V307L condition coupled with greater accumulation in zone 1 (**biii**) leading to AP shortening (**aiii**)

accumulation in the open state due to slower channel deactivation. Under the V307L condition, this open state accumulation is greater than under the V307L condition.

7.4 Simulation of the ECG with WT and SQT2 Mutant I_{Ks}

Using a 1D strand model of the ventricular wall, pseudo-ECGs were computed under the WT, WT-V307L and V307L conditions (Fig. 7.6d–f). These were extracted from a propagating wave from the ENDO end of the strand towards the EPI end (Fig. 7.6a–c). Time runs horizontally from left to right in Fig. 7.6a–c while space runs vertically from the ENDO end at the bottom to the EPI end at the top. The QT interval was shortened from 351 ms in the WT condition to 292 ms in the WT-V307L condition and to 262 ms in the V307L condition (Fig. 7.6g). T-wave width (measured as the time interval between T_{peak} and T_{end}) also changed from 49 (WT) to 60 ms (WT-V307L) and 64 ms (V307L). These simulations thus reproduce the key features observed in the ECGs of SQTS patients; abbreviated QT interval, tall and peaked T-waves and wider T_{peak} to T_{end} [15–20]. As the only

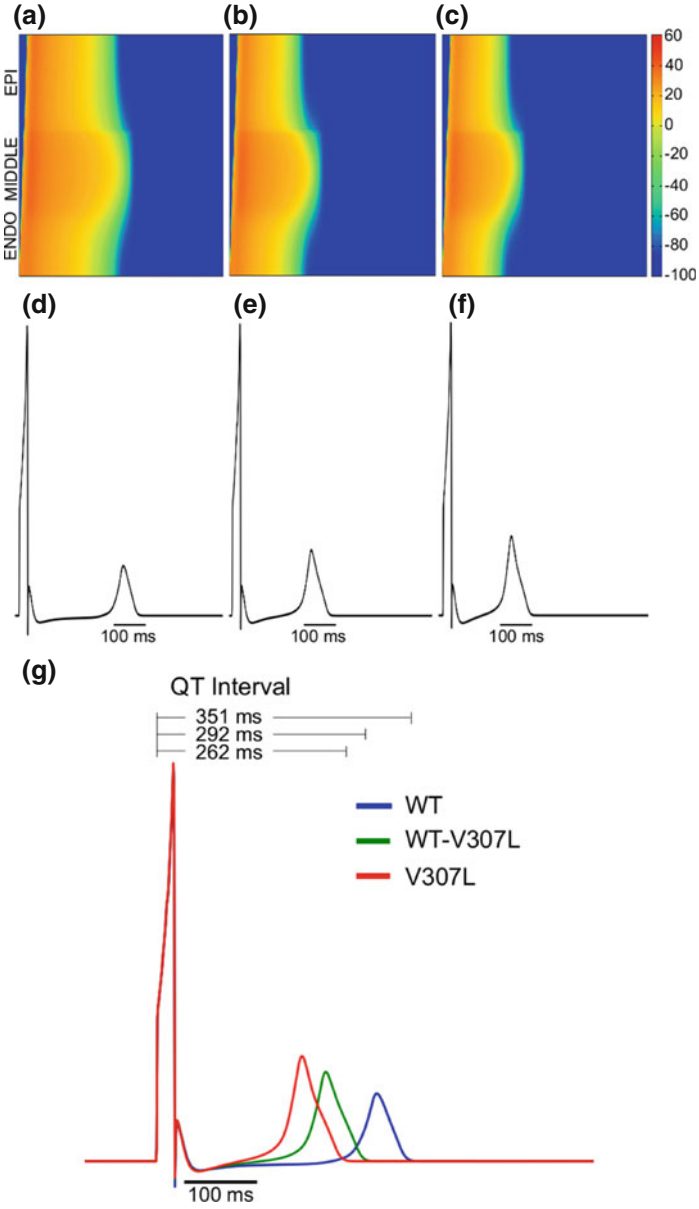

Fig. 7.6 Pseudo ECGs under the WT, WT-V307L and V307L conditions **a**, **b**, **c** *Colour* mapping of membrane potential of cells along the 1D strand from *blue* (−86 mV) to *red* (−42 mV) (see *colour* key, in mV). Space runs vertically from the ENDO end to the EPI end at the *top*. Time runs *horizontally*. **a** WT condition. **b** WT-V307L condition. **c** V307L condition. **d**, **e**, **f** Pseudo-ECGs corresponding to the WT, WT-V307L and V307L conditions respectively. **g** Superimposed pseudo-ECGs for the WT, WT-V307L, V307L conditions respectively and their associated QT intervals

difference between these simulations is the altered kinetics of the I_{Ks} channel by the mutations, the observed changes in the QT interval, T-wave height and width can confidently be attributed to the parameters corresponding to the V307L mutation.

Gima and Rudy [21] suggested that an increased spatial gradient of the membrane potential (δV) could be responsible for the increase in T-wave height seen in hyperkalemia. Therefore, in order to determine if the same effect was responsible for the taller T-wave amplitudes in the WT-V307L and V307L ECGs (Fig. 7.6d–g), the effects of the V307L mutation on membrane potential (δV) heterogeneity during ventricular APs between the three cell types were investigated. The results are shown in Fig. 7.8. Figure 7.7a shows the pairwise differences between EPI, MIDDLE and ENDO cells during an AP. Under the KCNQ1 WT-V307L and V307L mutation conditions, the maximal δV between EPI-MIDDLE (Fig. 7.7b) and ENDO-MIDDLE cells were greater than under the WT condition, which contributed to the augmented T-wave amplitude [21–23].

The dispersion of APD_{90} across the intact 1D strand under the WT, WT-V307L and V307L conditions was also measured. Figure 7.7c–e show the measured spatial distribution of APD_{90} (Fig. 7.7c), the spatial gradient of APD_{90} (Fig. 7.7d) and the absolute value of the spatial gradient of APD_{90} (Fig. 7.7e). The spatial gradient of APD_{90} was augmented across the strand and markedly so in the ENDO region. The sharp transition of APD_{90} and spike in the spatial gradient between the EPI-MIDDLE border is due to the discontinuity in the electrical coupling at this border and is consistent with experimental observations made by Yan et al. [24] in an arterially perfused left ventricular wedge preparation and Drouin et al. in a normal human heart [25].

7.5 Investigating the Arrhythmogenic Substrate in SQT2—1D Simulations

Using the 1D strand, the vulnerability of WT, WT-V307L and V307L tissue to unidirectional block in response to a premature stimulus applied during the refractory tail of a previous excitation wave was investigated. Figure 7.8 shows the width of the vulnerability window across the strand during which the tissue is predisposed to a premature stimulus that can lead to ventricular fibrillation. Under the WT-V307L condition, the tissue's vulnerability was increased across the whole strand compared to WT except for a very small region in the middle of the strand (Fig. 7.8a). For the V307L condition, the tissue's vulnerability was greater than WT and WT-V307L in the region marked by the arrow in Fig. 7.8a, b shows the temporal vulnerability window width for the marked region (arrow) under WT, WT-V307L and V307L conditions. On either side of the middle of the strand, within the region marked with the arrow, the vulnerability window of the tissue increased from 15.8 ms in the WT condition to 21.7 and 28.8 ms under the WT-V307L and V307L conditions respectively.

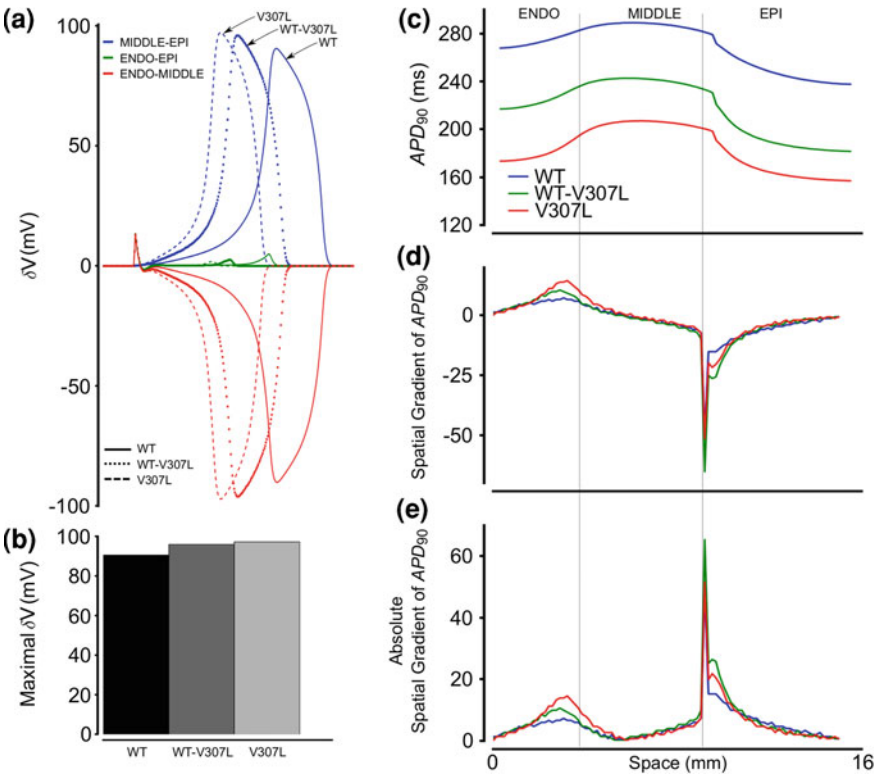

Fig. 7.7 Membrane potential heterogeneity (δV), transmural distribution and spatial gradient of APD_{90}. **a** Plots of δV against time for WT (*continuous lines*), WT-V307L (*dotted lines*) and V307L (*dashed lines*) conditions. **b** Maximum δV during repolarization between MIDDLE-EPI cells in WT, WT-V307L and V307L. **c** Spatial distribution of APD_{90} in the 1D transmural strand for WT (*blue*), WT-V307L (*green*) and V307L (*red*). **d**, **e** Absolute spatial gradient (**e**) and actual spatial gradient (**d**) of APD_{90} in the 1D transmural strand for WT (*blue*), WT-V307L (*green*) and V307L (*red*)

7.6 Investigating the Arrhythmogenic Substrate in SQT2—2D and 3D Simulations with Realistic Geometry

7.6.1 Simulations in 2D Realistic Geometry

In a realistic human ventricle cross-sectional slice (Fig. 7.9), the response of WT, WT-V307L and V307L tissue to a local premature stimulus applied within the left ventricular wall during the tissue's vulnerable window was investigated (WT: 370 ms after the arrival of conditional wavefront; WT-V307L: 310 ms after the arrival of conditional wavefront; V307L: 230 ms after the arrival of conditional wavefront). The results of the 2D simulations are shown in Fig. 7.9.

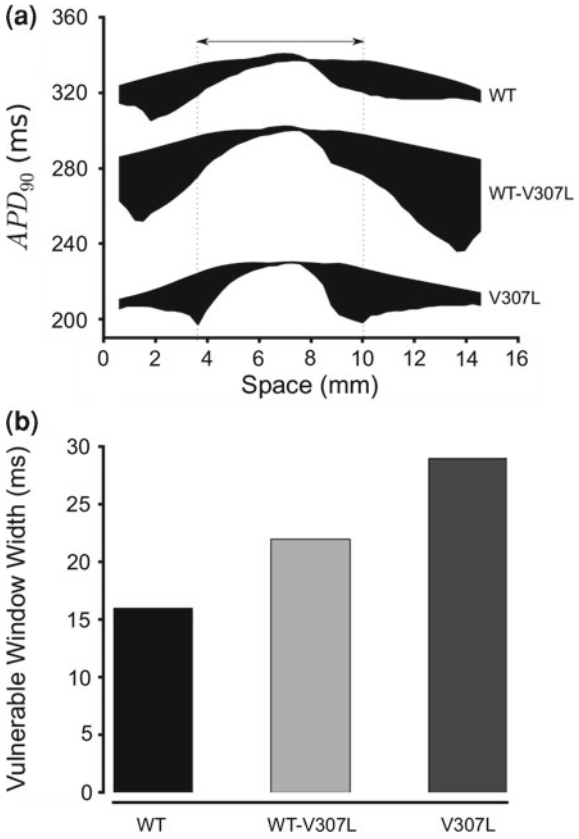

Fig. 7.8 Vulnerable window across the transmural 1D strand. **a** Measured vulnerable window for WT, WT-D172 N and D172 N along the 1D strand. **b** Measured vulnerable window width in the region depicted by the *arrow* in (**a**)

Following the premature stimulus, a re-entrant excitation wave was initiated within the left ventricular wall as shown in Fig. 7.9ai–di for WT, Fig. 7.9aii–dii for WT-V307L and Fig. 7.9aiii–diii for the V307L condition. The snap-shots shown in Fig. 7.9a–d show subsequent conduction of the induced re-entrant excitation waves from the applied premature stimulus for the WT (Fig. 7.9bi–di), WT-V307L (Fig. 7.9bii–dii) and V307L (Fig. 7.9biii–diii) conditions. Under the WT condition, the initiated re-entry self-terminated after 1.1 s (Fig. 7.9di, f) but it persisted under the mutation conditions throughout the 5 s simulation period (WT-V307L: Fig. 7.9bii–dii; V307L: Fig. 7.9biii–diii) and (Fig. 7.9f). The time course of an AP in the left ventricle is shown for the WT, WT-V307L and V307L conditions in Fig. 7.9ei–eiii respectively.

Power spectrum analysis of the recorded whole-field averaged electrical activity from the tissue revealed a higher dominant frequency in the mutation conditions (3.32 Hz for WT-V307L and 4.30 Hz for V307L compared to the WT condition (1.96 Hz) (Fig. 7.9g). These 2D simulation results illustrate that the KCNQ1 V307L mutation increases tissue susceptibility to arrhythmogenesis and maintenance of re-entrant excitation waves.

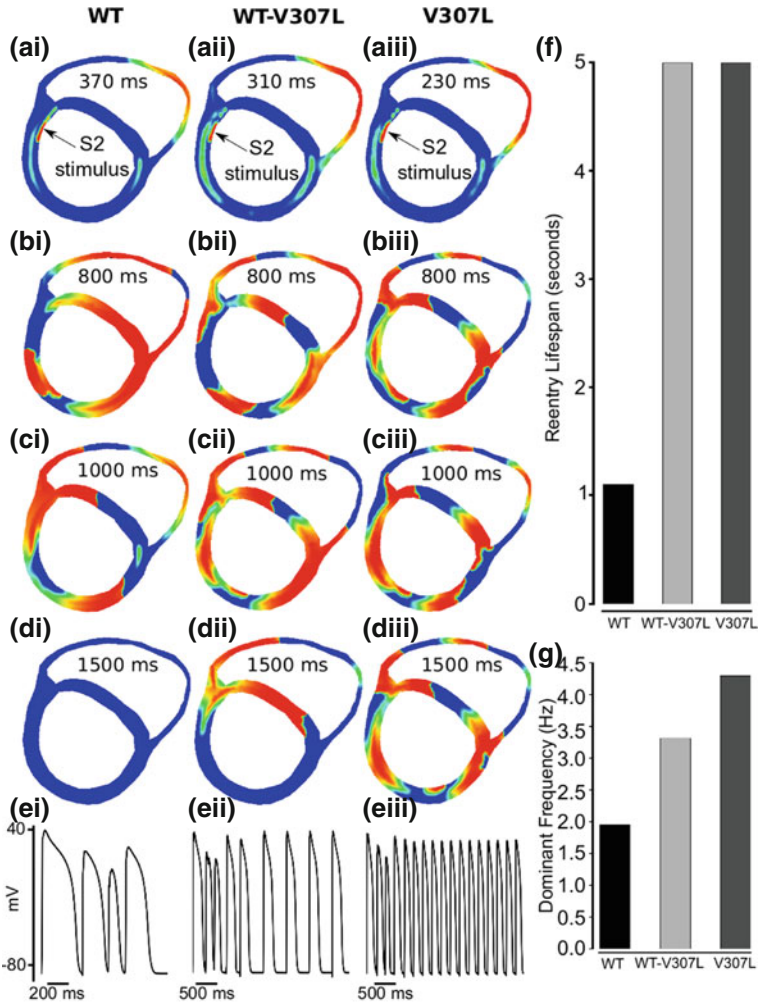

Fig. 7.9 Snapshots of initiation and conduction of re-entry in realistic 2D model cross-section of ventricles **ai**, **aii**, **aiii** Application of a premature S2 stimulus into the refractory and partially recovered region of an excitation wave after a delay of 370 ms for WT, 310 ms for WT-V307L and 230 ms for V307L condition from the initial wave stimulus. **bi**, **bii**, **biii** Developed spiral wave from the S2 stimulus. Snapshot at time = 800 ms. **ci**, **cii**, **ciii** Snapshot of spiral wave at time = 1000 ms. The induced spiral wave transited from transmural re-entry with tip rotating within the ventricle wall to anatomical re-entry with tip rotating around the ventricle boundary in WT and WT-V307L conditions. However, transmural re-entry persisted in the V307L condition and broke-up forming regenerative multiple re-entrant wavelets. **di**, **dii**, **diii** Snapshot of spiral wave at time = 1500 ms. Spiral wave self-terminated in WT before this recording point, but persisted in WT-V307L and V307L conditions. **ei**, **eii**, **eiii** Recorded time series of the action potential of a cell in the *left* ventricle for the WT, WT-V307L and V307L conditions. **f** Measured lifespan of re-entry scroll wave in WT, WT-V307L and V307L conditions. **g** Computed dominant frequency of electrical activity recorded from ventricle in WT, WT-V307L and V307L conditions. (1.96 Hz for WT, 3.32 Hz for WT-V307L and 4.30 Hz for V307L condition)

7.6.2 Simulations in 3D Realistic Geometry

Realistically, the ventricles are three-dimensional and have a much more complex anisotropic geometry compared to the 2D ventricular slice. Therefore, it would be erroneous to assume that sustained reentry in the 2D tissue model necessarily translates to similar activity in 3D tissue. Consequently, further simulations were performed using a 3D anatomical human ventricle geometry. The results are shown in Fig. 7.10, which shows snapshots of the evolution of re-entrant scroll waves (WT: Fig. 7.10ai–di; WT-V307L: Fig. 7.10aii–dii; V307L: Fig. 7.10aiii–diii) developing as a response to a premature stimulus. For the WT condition, the scroll wave self-terminated with a lifespan of 0.5 s (Fig. 7.10f). However, under WT-V307L and V307L mutation conditions, the scroll wave broke up forming multiple re-entrant wavelets that self-terminated within 2.5 s in WT-V307L tissue but were sustained throughout the 5 s simulation period in V307L tissue (Fig. 7.10f).

Power spectrum analysis of the recorded whole-field averaged electrical activity shows the dominant frequency of ventricle excitation to be 2.34 Hz for the WT condition, 3.13 Hz for the WT-V307L mutation condition and 7.42 Hz for the V307L mutation condition (Fig. 7.10g). Figure 7.10ei–eiii show a recording of the evolution of the AP of a cell in the left ventricle for the WT, WT-V307L and V307L conditions. Although, in the WT-V307L mutation condition, the re-entrant wavelets self-terminated as opposed to being sustained as in the 2D ventricular slice (Fig. 7.9f), these 3D results further illustrate the pro-arrhythmic effects of the KCNQ1 V307L mutation.

7.7 Investigating Blockade of I_{Ks} as a Potential Therapeutic Target in the SQT2

As a theoretical "pseudo-pharmacological" approach to treating patients with the adult SQT2 variant, blockade of the I_{Ks} channel by drugs was mimicked in order to determine the extent of blockade required to normalise the QT interval. First, I_{Ks} was blocked in the EPI, MIDDLE and ENDO single cell types. Figure 7.11a–e show the results for an EPI cell under the WT-V07L (Fig. 7.11a, b) and V307L (Fig. 7.11d, e) conditions (results for MIDDLE and ENDO cells are similar). In all three cell types, approximately 60 % I_{Ks} blockade was required to make the APD comparable to that of WT under the WT-V307L mutation condition while approximately 76 % I_{Ks} blockade was necessary under the V307L mutation condition.

Using the intact 1D tissue strand, a similar investigation on the normalisation of the QT interval was carried out. In tissue, due to the electrical coupling between cells via gap junctions, the APD between the different cell types are smoothed out. Thus, for the WT-V307L mutation condition (Fig. 7.11c), 59 % I_{Ks} blockade was

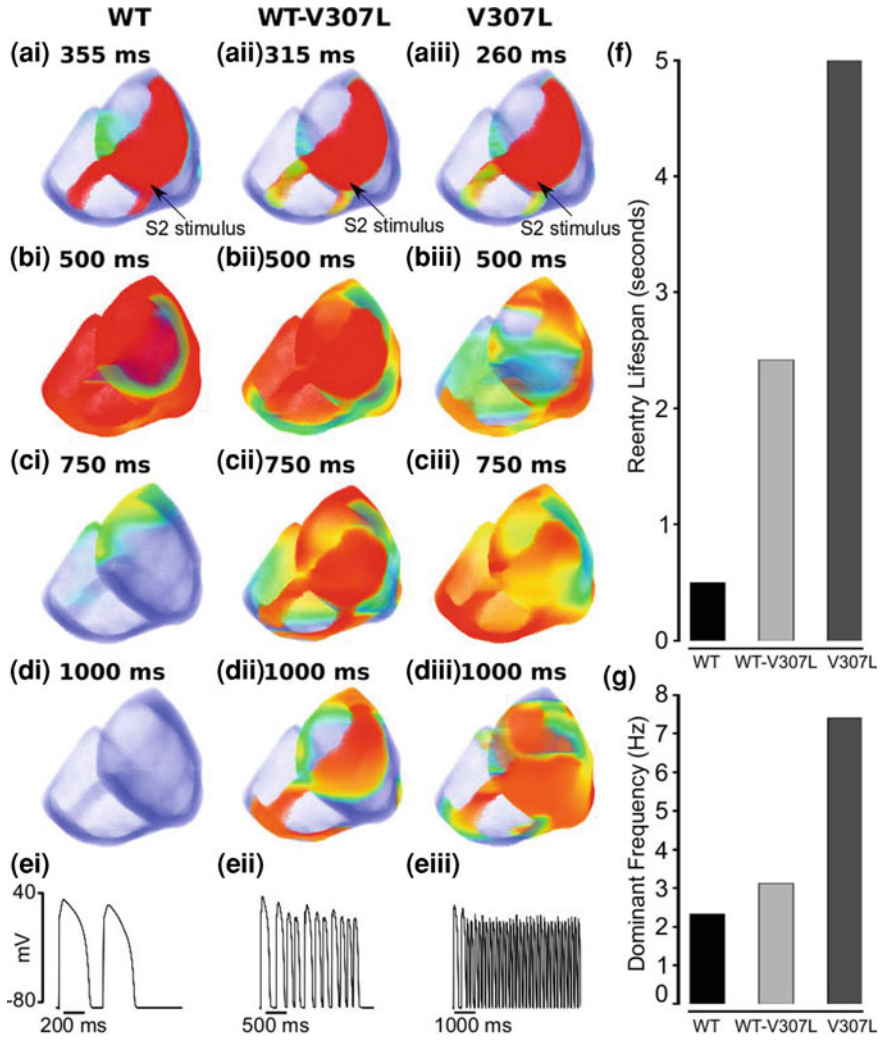

Fig. 7.10 Snapshots of initiation and conduction of re-entry in a 3D anatomical model of human ventricles. **ai**, **aii**, **aiii** Application of a S2 premature stimulus in a local region at refractory period of a previous conditioning excitation wave after a time delay of 355 ms for WT, 315 ms for WT-V307L and 260 ms for V307L conditions from the initial conditioning wave stimulus. **bi**, **bii**, **biii** Developed scroll wave from the S2 stimulus for the WT, WT-V307L and V307L conditions. Snapshot at time = 500 ms. **ci** ,**cii**, **ciii** Snapshot of scroll wave at time = 750 ms for the WT, WT-V307L and V307L conditions. **di**, **dii**, **diii** Snapshot of scroll wave at time = 1000 ms. The scroll wave self-terminated in WT, but persisted and broke up forming regenerative wavelets in WT-V307L and V307L conditions. **ei**, **eii**, **eiii** Recorded time series of the action potential of a cell in the *left* ventricle for WT, WT-V307L and V307L conditions. **f** Measured lifespan of re-entry scroll wave in WT, WT-V307L and V307L conditions. **g** Computed dominant frequency of electrical activity recorded from ventricle in WT, WT-V307L and V307L conditions (2.34 Hz for WT, 3.13 Hz for WT-V307L and 7.42 Hz for V307L condition)

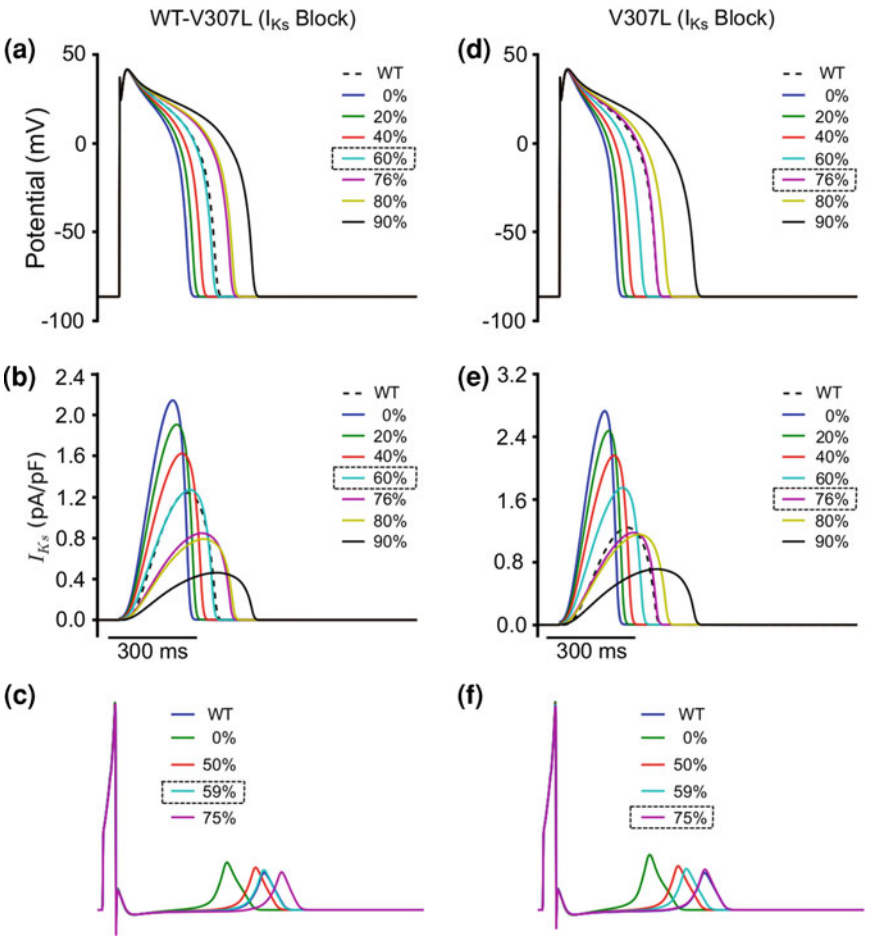

Fig. 7.11 Blockade of I_{Ks} in the single cell under the WT-V307L and V307L conditions **a**, **d** EPI action potentials of WT-V307L (**a**) and V307L (**d**) resulting from varying percentage block of I_{Ks}. *Dashed line* represents WT and boxed percentage represents the I_{Ks} blockade required to normalise the AP under the mutation conditions. **b**, **e** Corresponding I_{Ks} current profile to APs in (**a**) and (**d**) for the WT-V307L (**b**) and V307L (**e**) conditions. **c**, **f** Resulting ECGs from blockade of I_{Ks} in the 1D transmural strand under the WT (**c**) and (WT-V307L (**f**) conditions. *Blue line* represents WT and boxed percentage represents the I_{Ks} blockade required to normalise the QT interval under the mutation conditions

needed to normalise the QT interval to that of WT while under the V307L mutation condition, approximately 75 % I_{Ks} blockade was necessary (Fig. 7.11f). These results are similar to the single cell simulations.

Finally, simulations to determine if I_{Ks} blockade could terminate re-entrant activity under the mutation conditions in the 3D anatomical human ventricle (Fig. 7.12) were performed. Figure 7.12a shows the WT condition with a

premature stimulus applied during the tissue's vulnerable window at 355 ms. If I_{Ks} blockade under the mutation conditions normalises the QT interval, then the application of a premature stimulus at this same time (355 ms) should produce somewhat similar activity to WT. Figure 7.11b and c show WT-V307L and V307L mutated tissue with no I_{Ks} blockade, i.e., the pure heterozygote and homozygote mutants respectively with a premature stimulus applied at 315 ms for WT-V307L and 260 ms for V307L leading to re-entrant activity that persists beyond the WT reentry lifespan. It transpired that 58 % I_{Ks} blockade was sufficient to make the WT-V307L reentry lifespan (Fig. 7.12bii) comparable to that of WT while 65 % I_{Ks} blockade was adequate under the V307L mutation condition (Fig. 7.12cii). These simulations illustrate the possibility of I_{Ks} as a relevant drug target to treat tachyarrhythmia in the SQT2 setting.

7.8 Discussion and Conclusions

7.8.1 Summary of Major Findings

The proband in whom the KCNQ1 V307L mutation was discovered was heterozygotic for the SQT2 mutation (WT-V307L) [1]. He was successfully resuscitated following a VF episode. It is of significance that with the WT-V307L expression model, mimicking the heterozygous state of the proband, the 3D simulations (Fig. 7.10) showed that re-entrant activity in the heterozygote condition (WT-V307L) (Fig. 7.10aii–dii) self-terminated within 2.5 s (Fig. 7.10f) with a dominant frequency of 3.13 Hz (Fig. 7.10g). However, in the homozygote condition (V307L) (Fig. 7.10aiii–diii), re-entrant activity was sustained (Fig. 7.10f) with a dominant frequency of 7.42 Hz (Fig. 7.10g).

The major findings are:

1. The development of a novel Markov chain model of the SQT2 mutation which reproduces better the kinetic changes of I_{Ks} under both the WT and V307L conditions compared to previous studies [1, 7]. It also reproduces the slowed deactivation of the I_{Ks} channel due to the V307L mutation.
2. The KCNQ1 V307L mutation abbreviates the AP duration and steepens the APD-R curve.
3. The KCNQ1 V307L mutation shortens the QT interval, increases T wave amplitude and T_{peak}—T_{end} duration, all of which are concordant with clinical observations regarding the SQTS.
4. The KCNQ1 V307L mutation leads to augmented membrane potential differences (δV) between paired cells and transmural APD dispersion in localised regions of the transmural strand that contributes to the increased T-wave amplitude.

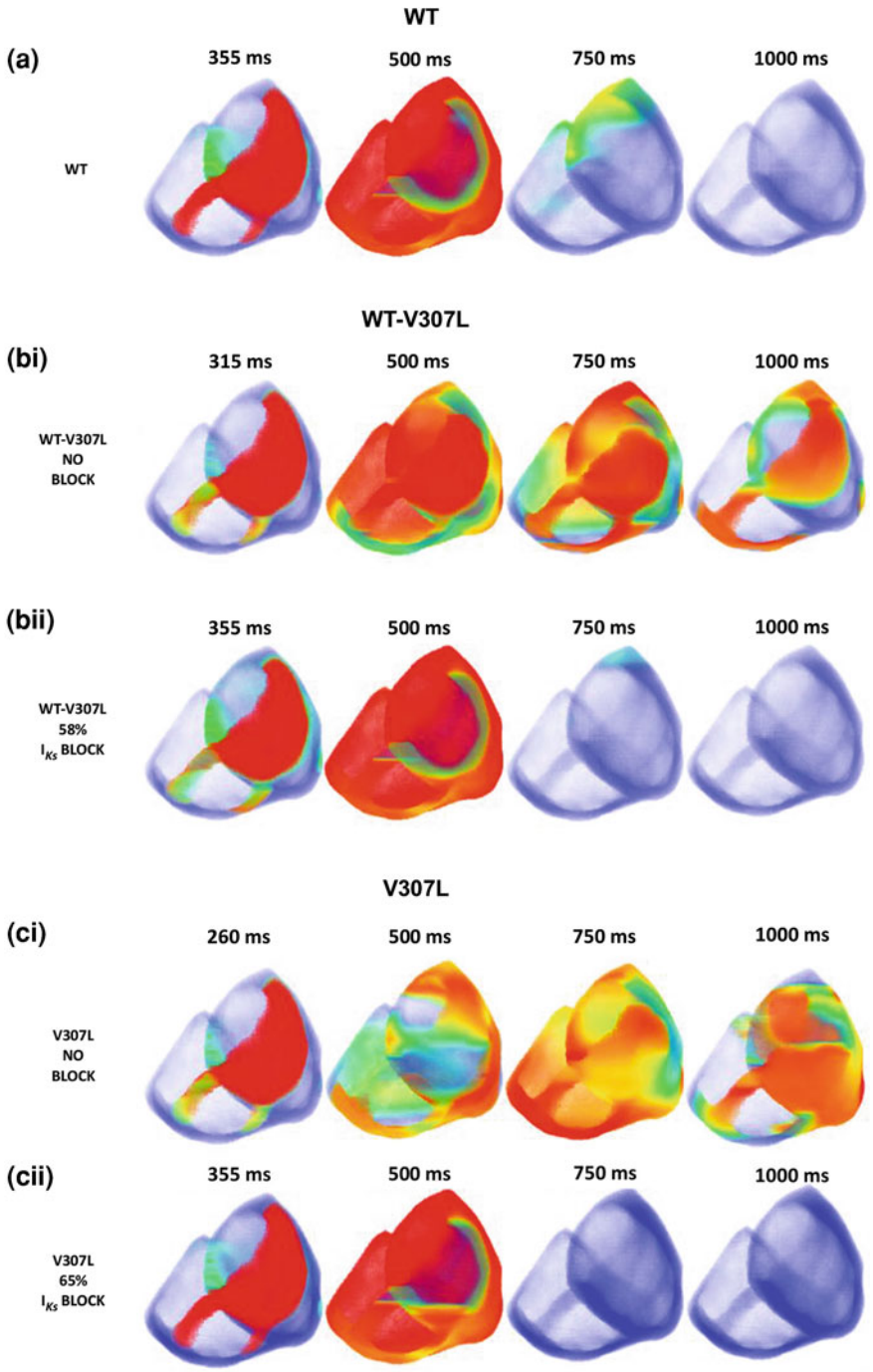
WT
(a)
355 ms
500 ms
750 ms
1000 ms
WT
WT-V307L
(bi)
315 ms
500 ms
750 ms
1000 ms
WT-V307L
NO
BLOCK
(bii)
355 ms
500 ms
750 ms
1000 ms
WT-V307L
58%
I_{Ks} BLOCK
V307L
(ci)
260 ms
500 ms
750 ms
1000 ms
V307L
NO
BLOCK
(cii)
355 ms
500 ms
750 ms
1000 ms
V307L
65%
I_{Ks} BLOCK

◀ **Fig. 7.12** Termination of reentry by I_{Ks} blockade **a** Application of a premature stimulus during the vulnerable window of a local region of WT tissue (355 ms) leads to the development of a spiral wave (500 ms) that terminates before 1000 ms. **bi** WT-V307L mutated tissue with no blockade of I_{Ks}. Application of a premature stimulus during the vulnerable window of a local region of the tissue (315 ms) leads to the development of a spiral wave (500 ms) that is sustained beyond 1000 ms. **bii** WT-V307L mutated tissue with 58 % blockade of I_{Ks}. Application of a premature stimulus during the vulnerable window of a local region of the tissue (355 ms) leads to the development of a spiral wave (500 ms) that terminates before 1000 ms. **bi** V307L mutated tissue with no blockade of I_{Ks}. Application of a premature stimulus during the vulnerable window of a local region of the tissue (260 ms) leads to the development of a spiral wave (500 ms) that is sustained beyond 1000 ms. **bii** V307L mutated tissue with 65 % blockade of I_{Ks}. Application of a premature stimulus during the vulnerable window of a local region of the tissue (355 ms) leads to the development of a spiral wave (500 ms) that terminates before 750 ms

5. The KCNQ1 V307L mutation increases the tissue's temporal vulnerability to the genesis of uni-directional conduction by a premature excitation at some localised regions;
6. The KCNQ1 V307L mutation reduces the minimal tissue substrate size that facilitates the maintenance of re-entry and accelerates reentrant excitation waves.
7. I_{Ks} blockade is a potential therapeutic target in normalizing the QT interval and terminating re-entrant activity in the SQT2 setting.

These findings provide a causal link between the KCNQ1 V307L mutation, QT interval shortening and tachyarrhythmias. Moreover, they provide a comprehensive explanation for the increased susceptibility to re-entry and perpetuation of re-entrant arrhythmia in the SQT2 setting.

7.8.2 Significance of the Study and Relevance to Previous Studies

In first reporting the existence of the KCNQ1 V307L mutation in a patient with the SQTS, Bellocq et al. [1] used a Priebe-Beuckelmann ventricular cell AP model [10] to demonstrate AP shortening. In the initial report of the KCNJ2-linked SQT3 [26], a simulated pseudo-ECG for the KCNQ1 V307L mutation showing QT interval shortening was presented in comparison to that of the KCNH2-linked SQT1 and the KCNJ2-linked SQT3 mutants. Zhang et al. [7], in a previous study, used the 2004 TNNP human ventricular AP cell model [6] with modified Hodgkin–Huxley I_{Ks} formulations reproducing the KCNQ1 V307L kinetics to also demonstrate AP abbreviation, QT interval shortening, T wave morphology changes, reduced minimal substrate size for re-entry and reentrant activity in idealised 2D geometry. However, the current study is the first to develop a Markov Model of the KCNQ1 V307L mutation, which reproduces the kinetics of the mutation including the faster deactivation of the I_{Ks} channel under the KCNQ1 V307L

mutation and to examine the mutation's functional consequences in realistic 2D and 3D anatomical geometries. This current study is also the first to investigate the blockade of I_{Ks} as a potential pharmacological intervention for treating SQT2 patients.

The advantage of and the greater insight into arrhythmogenic mechanisms provided by the Markov chain model can be seen in Fig. 7.5, which shows the channel state occupancy under WT, WT-V307L and V307L conditions. Under the WT condition (Fig. 7.5ai, bi), at AP initiation, the channels reside in zone 2 (Fig. 7.5bi), where the voltage sensors need to complete a slow transition to zone 1 and then a fast transition to the open state. This leads to a delay in activation (Fig. 7.5ai). This delay is a kinetic property of the WT I_{Ks} channel [11–14]. However, under the WT-V307L condition (Fig. 7.5aii, bii), 2 % of the channels reside in zone 1 on AP initiation (Fig. 7.5bii), which facilitates channel opening and larger I_{Ks} during the AP resulting in AP abbreviation (Fig. 7.5aii). Open-state accumulation is also greater than in WT due to slower deactivation. Thus, the primary mechanism for larger I_{Ks} in the WT-V307L mutation is greater zone 1 occupancy coupled with slower deactivation. In the V307L condition, compared to WT, 3.5 % of channels occupy zone 1 and because the V307L mutation slows channel deactivation considerably, open-state accumulation is greater than under the WT or WT-V307L conditions. Consequently, this leads to larger I_{Ks} during the AP. This kind of insight is not possible with simple Hodgkin–Huxley models, as channel state occupancy is not accounted for in such formulations in the way that is possible with a Markov-based approach.

7.8.3 Arrhythmogenic Mechanisms of the KCNQ1 V307L Mutation

The SQTS is associated with malignant tachycardias [1, 27–29] and some patients present with ventricular fibrillation episodes [1, 30] including the SQT2 proband [1] who was successfully resuscitated. Bellocq et al. [1] hypothesized that heterogeneous APD abbreviation would be anticipated to provide a substrate for increased risk of re-entrant arrhythmia.

The simulations in the present study support this hypothesis that the transmural dispersion of APD_{90} due to differential APD abbreviation among EPI, MIDDLE and ENDO cells is pro-arrhythmic. It resulted in an augmented APD dispersion in some regions of the transmural strand, which increased the tissue's vulnerable time window in which uni-directional conduction block could occur as shown in Fig. 7.8. The KCNQ1 V307L mutation also increased the membrane potential heterogeneity (δV) between paired cell type APs: MIDDLE-ENDO and MIDDLE-EPI (Fig. 7.7a, b). This augmented the APD of cells in the intact tissue model via electrical gap junction coupling between cells and contributed to the heterogeneous transmural APD_{90} dispersion. The augmented δV also accounted for the

increased T-wave amplitude in the pseudo-ECGs (Fig. 7.6). Maintenance of re-entrant activity is also aided by the ERP reduction under the KCNQ1 V307L mutation as it decreases the wavelength of ventricular excitation waves, allowing higher activation frequencies of re-entrant excitation waves (Fig. 7.10). Under the heterozygote (WT-V307L) mutation condition, re-entrant activity self-terminated in the 3D simulation (Fig. 7.10aii–dii and Fig. 7.10f). This is the relevant clinical condition with which the proband is associated [1]). Given that there's only one known case of SQT2 with this mutation [1] and that the patient reached the age of 70 without any complaints including VF [1], this can be considered a strength of the present study. In addition, during electrophysiological study, no arrhythmias could be induced [1]. The 3D data are also suggestive of perhaps other factors being required to make ventricular tachycardia (VT) persist into VF in the heterozygote condition.

7.8.4 SQT2 Treatment

The use of Implantable Cardioverter Defibrillators (ICD) is the current treatment for the SQTS [27, 28, 31–33]. However, as the SQTS is characterised by tall and peaked T-waves, there is the risk of inappropriate shocks to the patient due to T-wave oversensing [27, 28, 31, 32, 34]. Additionally, ICDs do not restore the QT interval to its normal duration and are not suitable for all patients, e.g., infants. Therefore, pharmacological alternatives that can restore the normal duration of the QT interval and offer protection from arrhythmias are being actively pursued [27, 28, 35, 36]. Pharmacologically, there is very little information available on SQT2 (likely due to a complete lack of clinically used pure I_{Ks} blockers). Although I_{Ks} is selectively blocked by chromanol compounds such as chromanol 293B [31, 37, 38], its blocking potency was reduced by the KCNQ1 V307L mutation [31, 37]. However, a recent study by El Harchi et al. [8] found that recombinant I_{Ks} channels incorporating the KCNQ1 V307L mutation were effectively inhibited by mefloquine.

The simulations in the present study show in silico simulation of the effects of a drug that selectively blocks the I_{Ks} channel. In the SQT2 setting, under the WT-V307L heterozygote condition, a blockade of I_{Ks} by $\sim$58 % was sufficient to restore the QT interval to its original WT duration and make the tissue behave like WT tissue while under the V307L homozygote condition, a blockade of I_{Ks} by $\sim$65 % was sufficient to achieve the same result. These QT interval restorations terminate re-entrant activity in the tissue. Of course, as there is a potential risk with I_{Ks} blockade of torsade de pointes [38–40], caution must be exercised in designing and using a drug that blocks I_{Ks}; however, in the setting of accelerated repolarization such a drug might have utility. It should also be noted that the precise quantitative information on amount of I_{Ks} block required to normalise the QT interval may be model dependent. Therefore, for this reason, it would be informative in the future to conduct similar pseudo-pharmacological simulations with other human ventricular myocyte models.

References

1. Bellocq C, van Ginneken ACG, Bezzina CR, Alders M, Escande D, Mannens MMAM et al (2004) Mutation in the KCNQ1 gene leading to the short QT-interval syndrome. Circulation 109(20):2394–2397
2. Hong K, Piper DR, Diaz-Valdecantos A, Brugada J, Oliva A, Burashnikov E et al (2005) De novo KCNQ1 mutation responsible for atrial fibrillation and short QT syndrome in utero. Cardiovasc Res 68(3):433–440
3. Barhanin J, Lesage F, Guillemare E, Fink M, Lazdunski M, Romey G (1996) K(V)LQT1 and lsK (minK) proteins associate to form the I(Ks) cardiac potassium current. Nature 384(6604):78–80
4. Sanguinetti MC, Curran ME, Zou A, Shen J, Spector PS, Atkinson DL et al (1996) Coassembly of K(V)LQT1 and minK (IsK) proteins to form cardiac I(Ks) potassium channel. Nature 384(6604):80–83
5. Courtemanche M, Ramirez RJ, Nattel S (1998) Ionic mechanisms underlying human atrial action potential properties: insights from a mathematical model. Am J Physiol 275(1 Pt 2):H301–H321
6. ten Tusscher KHWJ, Noble D, Noble PJ, Panfilov AV (2004) A model for human ventricular tissue. Am J Physiol Heart Circ Physiol 286(4):H1573–H1589
7. Zhang H, Kharche S, Holden AV, Hancox JC (2008) Repolarization and vulnerability to re-entry in the human heart with short QT syndrome arising from KCNQ1 mutation–a simulation study. Prog Biophys Mol Biol 96(1–3):112–131
8. El Harchi A, McPate MJ, Zhang YH, Zhang H, Hancox JC (2010) Action potential clamp and mefloquine sensitivity of recombinant IKS channels incorporating the V307L KCNQ1 mutation. J Physiol Pharmacol 61(2):123–131
9. ten Tusscher KHWJ, Panfilov AV (2006) Alternans and spiral breakup in a human ventricular tissue model. Am J Physiol Heart Circ Physiol 291(3):H1088–H1100
10. Priebe L, Beuckelmann DJ (1998) Simulation study of cellular electric properties in heart failure. Circ Res 82(11):1206–1223
11. Silva J, Rudy Y (2005) Subunit interaction determines IKs participation in cardiac repolarization and repolarization reserve. Circulation 112(10):1384–1391
12. Rudy Y, Silva JR (2006) Computational biology in the study of cardiac ion channels and cell electrophysiology. Q Rev Biophys 39(1):57–116
13. Osteen JD, Sampson KJ, Kass RS (2010) The cardiac IKs channel, complex indeed. Proc Natl Acad Sci USA 107(44):18751–18752
14. Jespersen T, Grunnet M, Olesen S-P (2005) The KCNQ1 potassium channel: from gene to physiological function. Physiology (Bethesda) 20:408–416
15. Cross B, Homoud M, Link M, Foote C, Garlitski A, Weinstock J et al (2011) The short QT syndrome. J Intervent Card Electrophysiol 31(1):25–31
16. Gussak I, Brugada P, Brugada J, Wright RS, Kopecky SL, Chaitman BR et al (2000) Idiopathic short QT interval: a new clinical syndrome? Cardiology 94(2):99–102
17. Couderc J-P, Lopes CM (2010) Short and long QT syndromes: does QT length really matter? J Electrocardiol 43(5):396–399
18. Patel U, Pavri BB (2009) Short QT syndrome: a review. Cardiol Rev 17(6):300–303
19. Giustetto C, Di Monte F, Wolpert C, Borggrefe M, Schimpf R, Sbragia P et al (2006) Short QT syndrome: clinical findings and diagnostic-therapeutic implications. Eur Heart J 27(20):2440–2447
20. Brugada R, Hong K, Cordeiro JM, Dumaine R (2005) Short QT syndrome. CMAJ 173(11):1349–1354
21. Gima K, Rudy Y (2002) Ionic current basis of electrocardiographic waveforms: a model study. Circ Res 90(8):889–896

22. Adeniran I, McPate MJW, Witchel HJ, Hancox JC, Zhang H (2011) Increased vulnerability of human ventricle to re-entrant excitation in hERG-linked variant 1 Short QT Syndrome. Plos Comput Biol 7(12):e1002313
23. Adeniran I, El Harchi A, Hancox JC, Zhang H (2012) Proarrhythmia in KCNJ2-linked short QT syndrome—insights from modelling. Cardiovasc Res 94(1):66–76
24. Yan GX, Shimizu W, Antzelevitch C (1998) Characteristics and distribution of M cells in arterially perfused canine left ventricular wedge preparations. Circulation 98(18):1921–1927
25. Drouin E, Charpentier F, Gauthier C, Laurent K, Le Marec H (1995) Electrophysiologic characteristics of cells spanning the left ventricular wall of human heart: evidence for presence of M cells. J Am Coll Cardiol 26(1):185–192
26. Priori SG, Pandit SV, Rivolta I, Berenfeld O, Ronchetti E, Dhamoon A et al (2005) A novel form of short QT syndrome (SQT3) is caused by a mutation in the KCNJ2 gene. Circ Res 96(7):800–807
27. Schimpf R, Wolpert C, Gaita F, Giustetto C, Borggrefe M (2005) Short QT syndrome. Cardiovasc Res 67(3):357–366
28. Maury P, Extramiana F, Sbragia P, Giustetto C, Schimpf R, Duparc A et al (2008) Short QT syndrome, update on a recent entity. Arch Cardiovasc Dis 101(11–12):779–786
29. Schimpf R, Borggrefe M, Wolpert C (2008) Clinical and molecular genetics of the short QT syndrome. Curr Opin Cardiol 23(3):192–198
30. Watanabe H, Makiyama T, Koyama T, Kannankeril PJ, Seto S, Okamura K et al (2010) High prevalence of early repolarization in short QT syndrome. Heart Rhythm 7(5):647–652
31. Hancox JC, McPate MJ, Harchi A, Duncan RS, Dempsey CE, Witchel HJ et al (2011) The Short QT syndrome. In: Tripathi ON, Ravens U, Sanguinetti MC (eds) Heart rate and rhythm (Internet). Springer, Heidelberg, pp 4–49 Available via DIALOG. http://www.springerlink.com/content/m8l86l8n3h81w43m/. Accessed 10 Jul 2011
32. Schimpf R, Wolpert C, Bianchi F, Giustetto C, Gaita F, Bauersfeld U et al (2003) Congenital short QT syndrome and implantable cardioverter defibrillator treatment: inherent risk for inappropriate shock delivery. J Cardiovasc Electrophysiol 14(12):1273–1277
33. Schimpf R, Bauersfeld U, Gaita F, Wolpert C (2005) Short QT syndrome: successful prevention of sudden cardiac death in an adolescent by implantable cardioverter-defibrillator treatment for primary prophylaxis. Heart Rhythm 2(4):416–417
34. Anttonen O, Junttila J, Giustetto C, Gaita F, Linna E, Karsikas M et al (2009) T-Wave morphology in short QT syndrome. Ann Noninvasive Electrocardiol 14(3):262–267
35. Bjerregaard P, Jahangir A, Gussak I (2006) Targeted therapy for short QT syndrome. Expert Opin Ther Targets 10(3):393–400
36. Duncan RS, McPate MJ, Ridley JM, Gao Z, James AF, Leishman DJ et al (2007) Inhibition of the HERG potassium channel by the tricyclic antidepressant doxepin. Biochem Pharmacol 74(3):425–437
37. Lerche C, Bruhova I, Lerche H, Steinmeyer K, Wei AD, Strutz-Seebohm N et al (2007) Chromanol 293B binding in KCNQ1 (Kv7.1) channels involves electrostatic interactions with a potassium ion in the selectivity filter. Mol Pharmacol 71(6):1503–1511
38. Billman GE (2010) Novel therapeutic targets for antiarrhythmic drugs, 1st edn. Wiley, New York
39. Towart R, Linders JTM, Hermans AN, Rohrbacher J, van der Linde HJ, Ercken M et al (2009) Blockade of the I(Ks) potassium channel: an overlooked cardiovascular liability in drug safety screening? J Pharmacol Toxicol Methods 60(1):1–10
40. Curtis MJ (2004) Is cardiac IKs a relevant drug target? Cardiovasc Res 61(4):651–652

Chapter 8
Proarrhythmia in KCNJ2-Linked Short QT Syndrome: Insights from Modelling

8.1 Introduction

As discussed in Chaps. 1 and 2, a number of K^+ channels contribute to ventricular AP repolarisation. Due to its voltage dependence, I_{K1} plays little or no role during phases 0 or 1 of the AP, it contributes slightly during phase 2 (the plateau phase) but its major effect is seen during phase 3, particularly during terminal repolarisation [1–3] (also see Sect. 2.4 and Fig. 2.10). At this stage of the AP, I_{Kr} declines and I_{K1} increases. I_{K1} also plays a significant role in maintaining a stable resting potential in atrial and ventricular cells [4, 5].

Mutations to channels responsible for I_{K1} can be arrhythmogenic [4]. For example, loss-of-function mutations to the Kir2.1 protein result in the Andersen-Tawil syndrome. This syndrome delays ventricular repolarisation and facilitates ventricular arrhythmia [6, 7]. On the other hand, Kir2.1 over-expressing mice exhibit up-regulation of I_{K1}, which enhances the risk of ventricular arrhythmia via the production of a substrate that stabilises and facilitates high frequency rotor development [8]. Similarly, a gain-in-function (V93I) Kir2.1 mutation has been implicated in a familial form of atrial fibrillation [9].

The SQT3 variant of the SQTS is due to a gain-of-function mutation in the *KCNJ2* gene [10] that encodes Kir2.1. SQT3 was first identified in a 5-year-old child and her father, both of whom had abbreviated QTc of 315 and 320 ms respectively. Their ECGs showed abnormally narrow and peaked T-waves [10]. Genetic analysis showed an amino acid substitution of aspartate to asparagine (D → N) substitution at position 172 in the Kir2.1 protein. At both ambient and physiological temperatures, whole cell patch clamp recordings showed that the D172N mutation preferentially increased the outward over the inward current through recombinant Kir2.1 channels [10, 11].

In vitro ventricular AP clamp experiments have provided a direct demonstration of the D172N mutation on Kir2.1 current during physiological waveforms [11]. The results of these experiments have shown increased outward Kir2.1 current during terminal repolarisation [11].

I. Adeniran, *Modelling the Short QT Syndrome Gene Mutations*,
Springer Theses, DOI: 10.1007/978-3-319-07200-5_8,

As for the SQT1 and SQT2 variants, at present there is no phenotypically accurate experimental model of the SQT3 mutation for the investigation of the arrhythmia substrate in this variant of the SQTS. There are limited simulation data available; an example being one for which the kinetic changes to Kir2.1 current induced by the D172N Kir2.1 mutation were incorporated into a Priebe-Beucklemann model [12]. Simulations incorporating D172N Kir2.1 exhibited a shortened AP duration and steepened the AP restitution [10]. Simulations using a 1D tissue model reproduced the T-wave morphology seen clinically [10]. However detailed simulations to investigate the arrhythmogenic substrate in SQT3 were not performed.

The aim of this study was to investigate the arrhythmogenic substrate in the SQT3 syndrome. This aim was pursued by using physiologically accurate ventricular cell and tissue models (1–3D) with transmural and structural heterogeneity, incorporating kinetic changes to Kir2.1 current seen during voltage and AP clamp.

8.2 Simulation of Single Cell I_{K1} Under Control and SQT3 Conditions

A detailed discussion of the development of the SQT3 model formulations for the WT condition, the WT-D172N (heterozygote) and D172N (homozygote) conditions is given in Sect. 4.4. Figure 8.1ai shows the simulated I–V relationship for the WT, WT-D172N and D172N mutations compared to the experimental data [11]. The WT conductance was adjusted to show the same peak current density as the original ten Tusscher et al. [13–15] I_{K1} formulation current density during the I–V relation (Fig. 8.1aii), thus maintaining the overall current densities, APD_{90} and dynamic properties of the ten Tusscher et al. human ventricular model [13–15]. Relative current proportions for WT, WT-D172N and D172N conditions were then scaled using relative proportions of peak $I_{Kir2.1}$ obtained previously from AP clamp experiments [11] (V_{hold} of −80 mV and E_{rev} of ∼−88 to −89 mV). The SQT3 model reproduced quite closely the experimental data (Fig. 8.1ci–ciii) in all the three conditions (Fig. 8.1bi–biii).

In order to characterise the functional effects of the WT-D172N and D172N mutation on ventricular APs, the SQT3 model formulations for the WT, WT-D172N and D172N mutant conditions were incorporated into the 2006 TNNP single cell model for human ventricular cell action potentials [13]. Figure 8.2 shows simulated APs (8.2ai), I_{K1} profile (8.2aii) and instantaneous I_{K1} I–V relationship (8.2aiii) of an EPI ventricular cell. The MCELL and ENDO counterparts are shown in Fig. 8.2b–c respectively. In all three cell types, the WT-D172N and D172N mutations abbreviated the AP. Under the WT condition, I_{K1} was inactive during practically all of the plateau phase but its outward component began to increase in amplitude gradually during phase 3 (repolarisation phase) of the AP

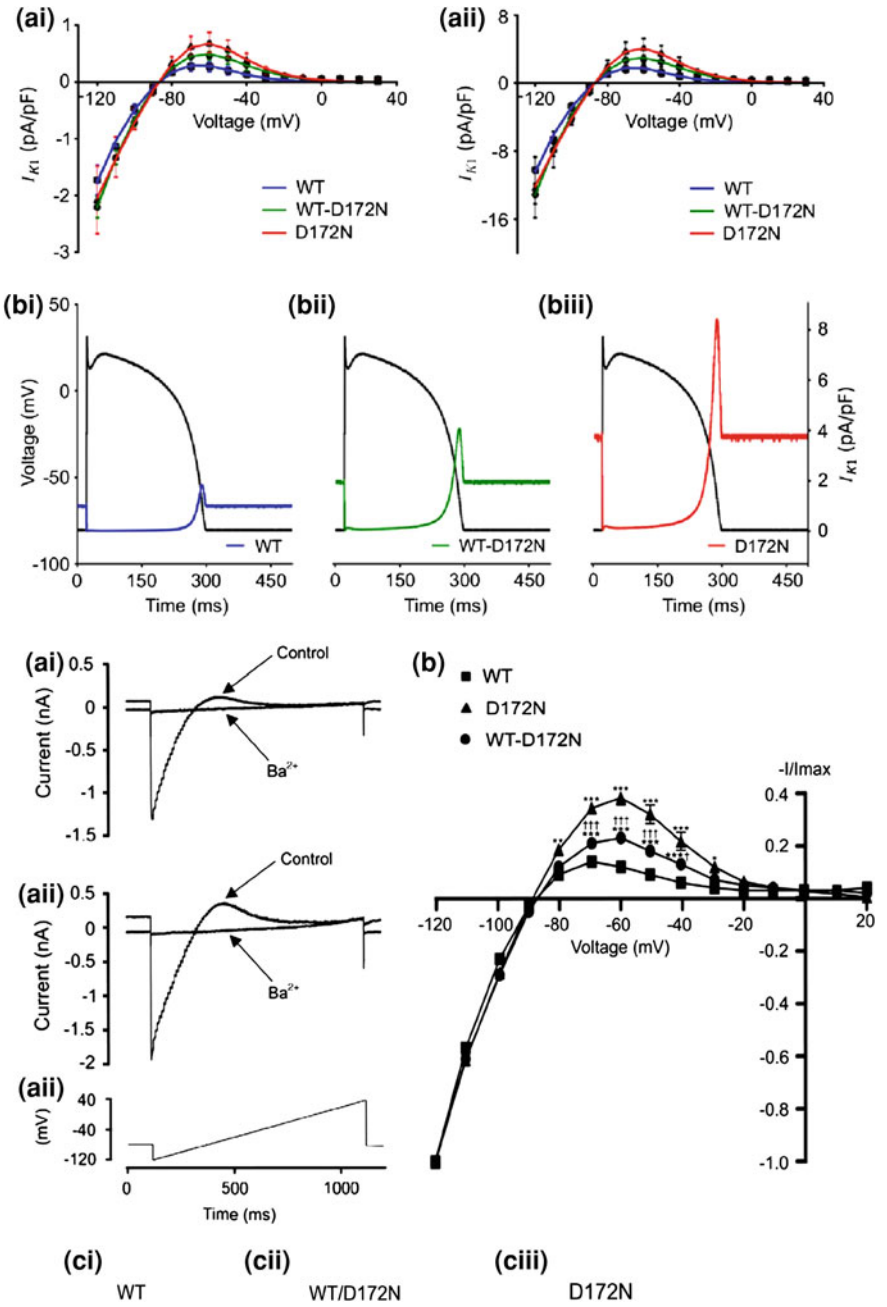

Fig. 8.1 SQT3 model fit to experimental data. **ai**, **aii** Model fit to normalised experimental current-voltage (I–V) relations (**ai**) for WT (*blue*), WT-D172N (*green*) and D172N (*red*) conditions and model-derived I_{K1} current densities (**aii**) based on the original TNNP I_{K1} channel current density. **bi**, **bii**, **biii** Simulated profile of I_{K1} for WT (**bi**), WT-D172N (**bii**) and D172N (**biii**) during an epicardial ventricular AP command. **ci**, **cii**, **ciii** Experimental profile of I_{K1} for WT (**ci**), WT-D172N (**cii**) and D172N (**ciii**) during an epicardial ventricular AP command. Modified from [11]

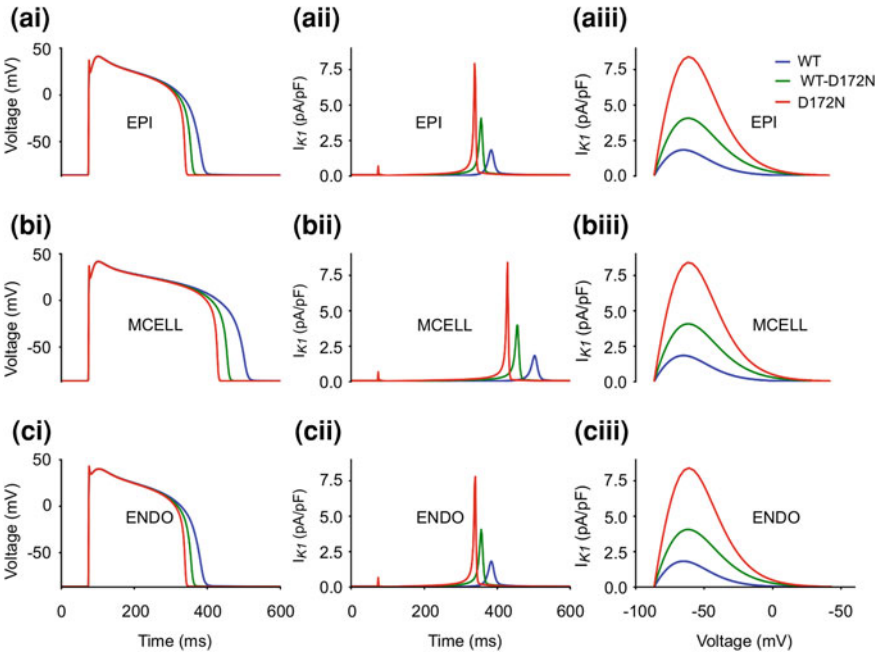

Fig. 8.2 Simulations of ventricular action potentials for WT, WT-D172N and D172N conditions. **ai**, **aii**, **aiii** Epicardial simulation of action potentials (**ai**), time course and amplitude of I_{K1} (**aii**) and instantaneous I–V relations (**aiii**) under WT, WT-D172N and D172N conditions. **bi**, **bii**, **biii** Mid-myocardial simulation of action potentials (**bi**), time course and amplitude of I_{K1} (**bii**) and instantaneous I–V relations (**biii**) under WT, WT-D172N and D172N conditions. **ci**, **cii**, **ciii** Endocardial simulation of action potentials (**ci**), time course and amplitude of I_{K1} (**cii**) and instantaneous I–V relations (**ciii**) under WT, WT-D172N and D172N conditions

and reached a peak during terminal repolarisation after which it declined. The same pattern was observed for the WT-D172N mutation except that the rise of the outward component of I_{K1} began slightly earlier during phase 3 of the AP and it reached a higher amplitude than in the WT condition. With the D172N mutation, I_{K1} was activated earlier than the WT-D172N condition, increased more rapidly and achieved significantly higher maximal amplitude during terminal repolarisation than WT and WT-D172N. This led to the marked shortening of the APD in both the WT-D172N and D172N conditions.

The measured WT APD_{90} was 312 ms, 431 and 312 ms, respectively, for the EPI, MIDDLE and ENDO cells. These values were decreased respectively to 283, 382 and 284 ms for the WT-D172N condition and to 265, 354 and 265 ms for the D172N condition (Table 8.1). The shortening in APD was due to the increased I_{K1} during the AP repolarisation phase as shown by the time-course of I_{K1} (Fig. 8.2aii–cii) and the instantaneous I–V plot during AP repolarisation (Fig. 8.2aiii–ciii). The observed resting potential values were −86.2, −86.4 and −86.5 mV for the WT, WT-D172N and D172N conditions respectively.

Table 8.1 Computed APD_{90} (ms) for EPI, MCELL and ENDO cell types under WT, WT-D172N and D172N conditions

	EPI	MCELL	ENDO
WT (ms)	311.84	430.76	312.00
WT-D172N (ms)	283.20	382.40	283.50
D172N (ms)	264.86	353.98	265.20

The abbreviation of APD_{90} by the WT-D172N and D172N conditions was rate-dependent. The APD restitution (APD-R) curve is shown in Fig. 8.3a–c. The APD_{90} was smaller in the WT-D172N and D172N conditions than in the WT condition across the range of diastolic intervals (DIs) investigated. The mutant conditions also steepened the APD-R curve as shown by the computed maximal slopes in Fig. 8.3d. WT-D172N and D172N conditions increased the slope of the APD-R curves in the EPI and ENDO cells. However, in the MCELL, there was a reduction in the slope in the WT-D172N condition, but a significant increase in slope by the D172N condition.

The WT-D172N and D172N mutations also shortened the effective refractory period (ERP) for all three cell types and resulted in a leftward shift of the ERP restitution (ERP-R) curve (Fig. 8.3e–g). This shortening was also rate-dependent and was smaller in the mutation conditions than in WT across the range of basic stimulus cycle lengths (BCL) studied. As with the APD-R curves, the mutation conditions also steepened the ERP-R curves as shown by the computed maximal ERP slopes (Fig. 8.3h). Steepening of the APD-R and ERP-R curves is associated with increased instability of re-entrant excitation waves [16], which predisposes towards their breakup and consequently leads to the formulation of multiple re-entrant excitation wavelets [16–18]. The leftward shift of the ERP-R curves by the mutation conditions also implies an ability of the mutation conditions to sustain electrical activity at higher rates (as seen under VT and VF conditions). These results therefore provide evidence for the pro-arrhythmic nature of the KCNJ2 Kir2.1 WT-D172N and D172N mutations.

8.3 Simulation of the ECG with WT, WT-D172N and D172N Mutant I_{K1}

A pseudo-ECG was computed using a 1D strand of cells across the ventricular wall for the WT, WT-D172N and D172N conditions at a stimulation rate of 1 Hz (Fig. 8.4d–f). Details of the method used to simulate the pseudo-ECG can be found in Sect. 5.3.1. A propagating excitation wave was initiated at the ENDO end of the strand by delivering a series of supra-threshold stimuli (Sect. 5.2.3). The wave propagated from the ENDO through the MIDDLE and towards the EPI direction.

Figure 8.4a–c show a space-time plot with space running vertically from ENDO at the bottom to EPI at top and time running horizontally from left to right.

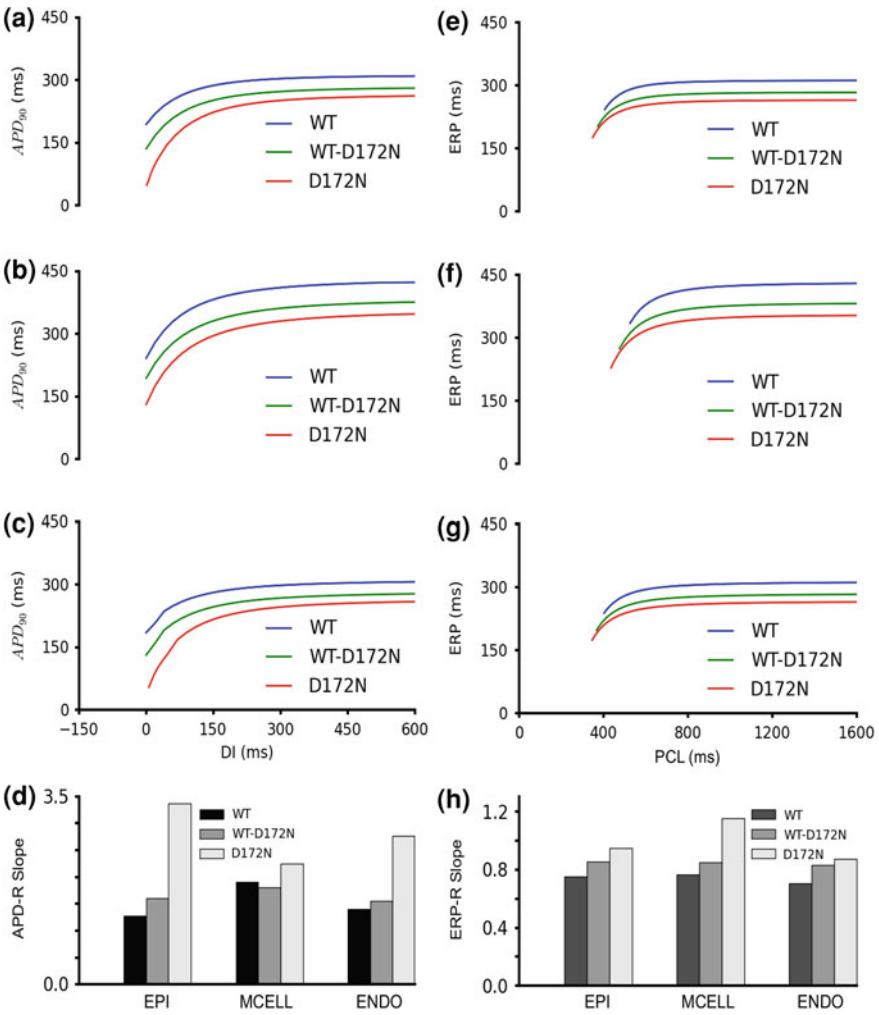

Fig. 8.3 Rate-dependent APD and ERP restitution curves. **a**, **b**, **c**: APD restitution curves for EPI (**a**), MIDDLE (**b**) and ENDO (**c**) cells respectively for the WT, WT-D172N and D172N conditions. **d** Measured slopes of APD restitution curves for EPI, MIDDLE and ENDO cells in WT, WT-D172N and D172N conditions. **e**, **f**, **g** ERP restitution curves for EPI (**e**), MIDDLE (**f**) and ENDO (**g**) cells respectively for the WT, WT-D172N and D172N conditions. **h** Measured slopes of ERP restitution curves for EPI, MIDDLE and ENDO cells for WT, WT-D172N and D172N conditions. DI-Diastolic interval; PCL—Pacing cycle length

The WT-D172N and D172N mutants shortened the QT interval from 363 ms for WT to 319 and 295 ms respectively (Fig. 8.4g). The T-waves for the mutant conditions were also taller and peaked, and the T-wave width (measured as the difference between T_{peak}—T_{end}) decreased from 51 ms (WT) to 39 ms (WT-D172N) and 33 ms (D172N). Given that only the channel kinetics of I_{K1} were

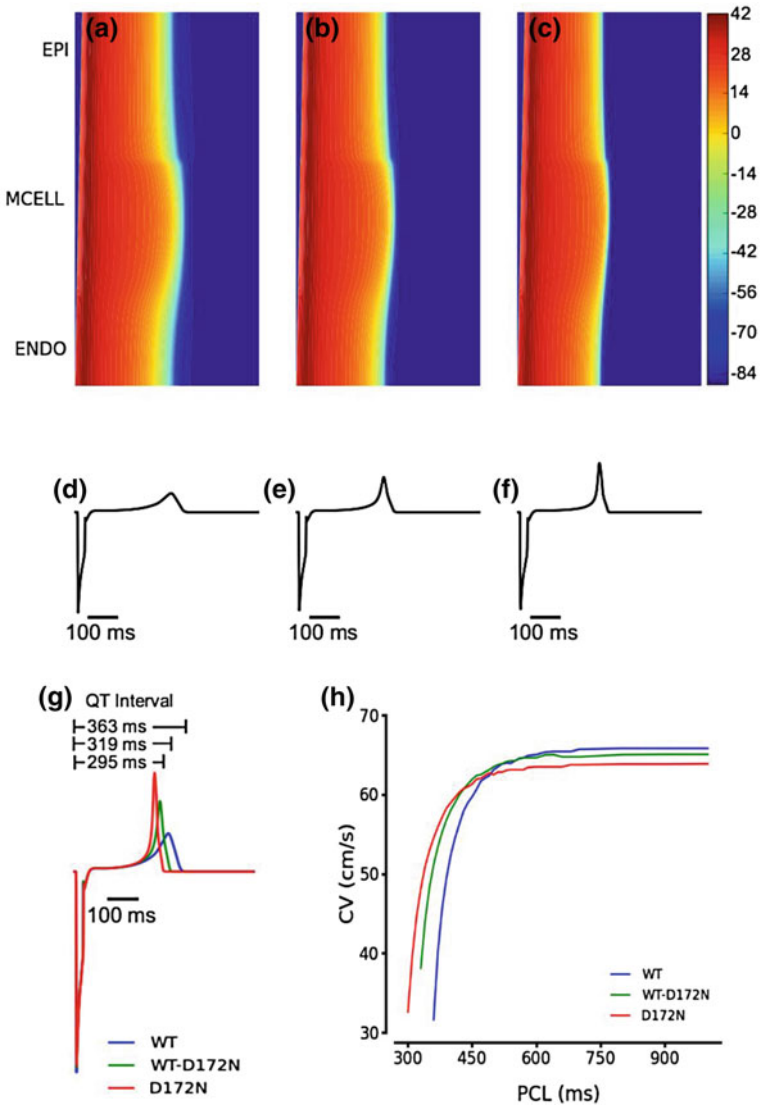

Fig. 8.4 Space-time plot of AP propagation along a 1D transmural ventricular strand, computed pseudo-ECGs and CV. **a**, **b**, **c** Colour mapping of membrane potential of cells along the 1D strand from *blue* (−86 mV) to *red* (−42 mV) (see *colour key*). Space runs vertically from the ENDO end to the EPI end at the top. Time runs horizontally. **a** WT condition. **b** WT-D172N condition. **c** D172N condition. **d**, **e**, **f** Pseudo-ECGs corresponding to the WT, WT-D172N and D172N conditions respectively. **g** Superimposed pseudo-ECGs for the WT, WT-D172N, D172N conditions respectively and their associated QT intervals. **h** CV restitution under WT (*blue*), WT-D172N (*green*) and D172N (*red*) conditions. PCL—pacing cycle length

different in the three simulation conditions, the observed shortening of the QT interval, the changes in T-wave height and width can be attributed with confidence to the effect on the simulations of the altered WT-D172N and D172N parameters.

8.4 Simulation of Transmural APD Dispersion and Temporal Vulnerability

Figure 8.5a shows the spatial dispersion of APD_{90} across the transmural strand for WT, WT-D172N and D172N conditions. The mutants reduced the APD_{90} across the strand but did not significantly alter the spatial dispersion of APD_{90} relative to WT. Figure 8.5b shows the spatial gradient of the transmural dispersion of the APD_{90} across the strand and its absolute value is shown in Fig. 8.5c. The spatial gradient of APD_{90} dispersion was increased in the mutant conditions in the EPI region and in localised parts of the MCELL and ENDO regions, which also contributed to the increased T-wave amplitude. A very sharp transition in APD_{90} can be seen between the MCELL and EPI region in Fig. 8.5a–c. This is due to the discontinuity in the electrical coupling at this border and is consistent with experimental observations made by Yan et al. [19] in an arterially perfused left ventricular wedge preparation and by Drouin et al. [20] in a normal heart.

8.5 Investigating the Conduction Velocity in SQT3

The conduction velocity (CV) across the ventricular transmural strand was computed under the WT, WT-D172N and D172N conditions (Fig. 8.4h). The mutants decreased CV at low rates (PCL >560 ms; rate <107 beats/min) but enhanced it at higher rates. The decreased CV at low rates was due to reduced tissue excitability (Fig. 8.6) as no change in the inter-cellular electrical coupling was considered. At a rate of 60 beats/min (BCL = 1000 ms), the measured CV was 66 cm s^{-1} for the WT, 64 cm s^{-1} for the WT-D172N and 62 cm s^{-1} for the D172N conditions. However, at higher rates between 158 and 196 beats/min (305 ms < PCL < 380 ms), the measured CV was much higher in the WT-D172N and D172N conditions than in the WT condition.

The increased CV at high rates under the mutant conditions is due to shorter ERP under these conditions compared to the WT condition. At a stimulus rate above 167 beats/min (SI < 360 ms), conduction failed in the WT condition, as a large part of the tissue was still refractory but conduction was sustained in the WT-D172N and D172N conditions. The highest rate for ventricular tissue to support conduction was 183 beats/min (SI = 327 ms) under the WT-D172N condition and 201 beats/min (SI = 298 ms) for the D172N condition. Thus the increased I_{K1} facilitated ventricular conduction at high rates close to those observed in clinical ventricular tachycardia [21].

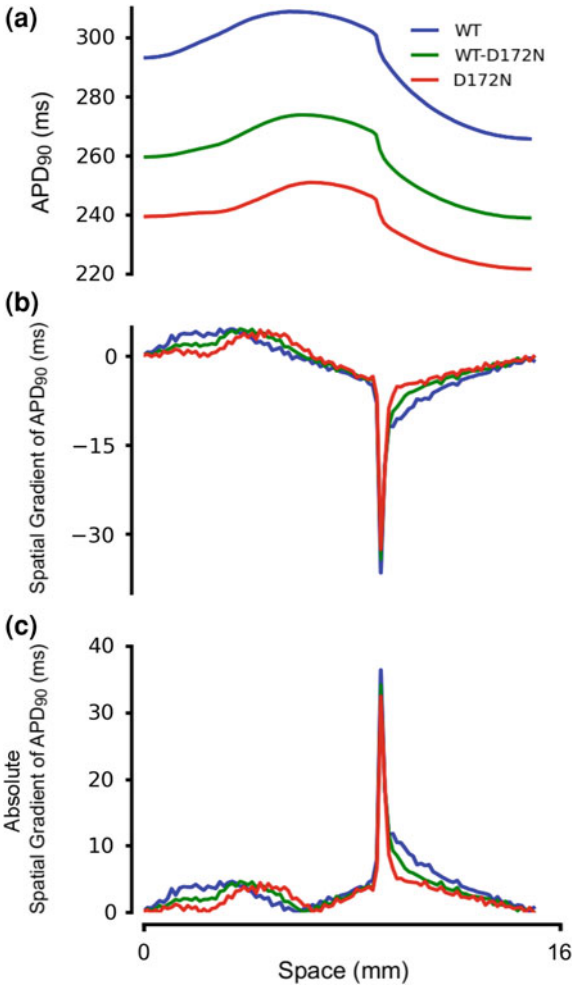

Fig. 8.5 Transmural APD_{90} distribution and its spatial gradient along a 1D transmural strand. **a** Spatial distribution of APD_{90} in the 1D transmural strand for WT (*blue*), WT-D172N (*green*) and D172N (*red*). **b** Actual spatial gradient of APD_{90} in the 1D transmural strand for WT (*blue*), WT-D172N (*green*) and D172N (*red*). **c** Absolute spatial gradient of APD_{90} in the 1D transmural strand for WT (*blue*), WT-D172N (*green*) and D172N (*red*)

8.6 Investigating the Arrhythmogenic Substrate in SQT3: 1D Simulations

The vulnerable window of the mutant tissue to a premature stimulus, i.e., its temporal vulnerability to unidirectional conduction in response to premature stimuli was then investigated. The period of vulnerability occurs during the refractory period of a previous excitation wave and represents the period during which a premature stimulus can elicit unidirectional conduction, which can act as a substrate for arrhythmogenesis [22–25]. Figure 8.7a–c show the width of the vulnerable window across the tissue in the WT, WT-D172N and D172N conditions respectively. The window at any point in the strand—from the ENDO (0 mm

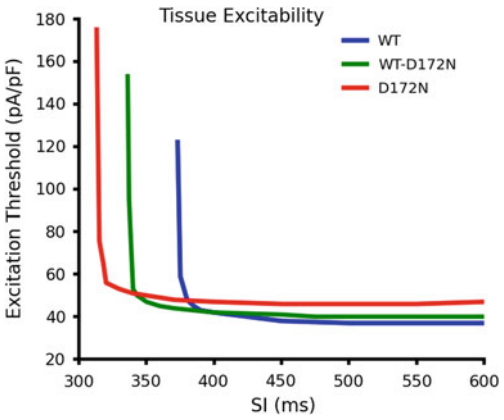

Fig. 8.6 Excitation threshold plotted against stimulus intervals (*SIs*) for the WT, WT-D172N and D172N mutation conditions

on the x-axis) to the EPI (15 mm on the x-axis) end—is the difference between the upper envelope T1 on the y-axis and the lower envelope T2. It can be seen that in the D172N mutation condition, the tissue's temporal vulnerability was increased across the whole strand, but only at most of the MIDDLE region in the WT-D172N mutation condition.

8.7 Investigating the Arrhythmogenic Substrate in SQT3: Idealised 2D Geometry Simulations

An idealised 2D tissue model was used to measure the minimal spatial size of a premature test stimulus necessary to produce re-entry under WT, WT-D172N and D172N conditions. Similar to the 1D transmural strand, the 2D tissue had three distinct regions (ENDO, MCELL and EPI) and can be considered to be equivalent to the 1D strand, but swept out in the y-direction (assuming the 1D strand is in the x-direction). A planar excitation wave propagating from the ENDO towards the EPI region of the 2D sheet was evoked at the ENDO via a conditioning stimulus. After a time delay, a premature stimulus was applied to a localized portion of the EPI region and during its VW, thereby producing unidirectional conduction (towards the EPI end, as the MCELL region was still refractory). This resulted in the formation of spiral re-entrant excitation waves, which self-terminated for the WT condition but were sustained for the WT-D172N and D172N conditions.

As the formation of the re-entrant excitation waves is dependent on the size of the premature test stimulus, the minimal stimulus size that could evoke re-entry was measured. The measured size was 49 mm in the WT condition, 21 mm in the WT-D172N condition and 18 mm in the D172N condition, showing that under conditions with the D172N mutation present, it was easier to induce reentry and hence, ventricular fibrillation. The reduction in the critical size of the substrate

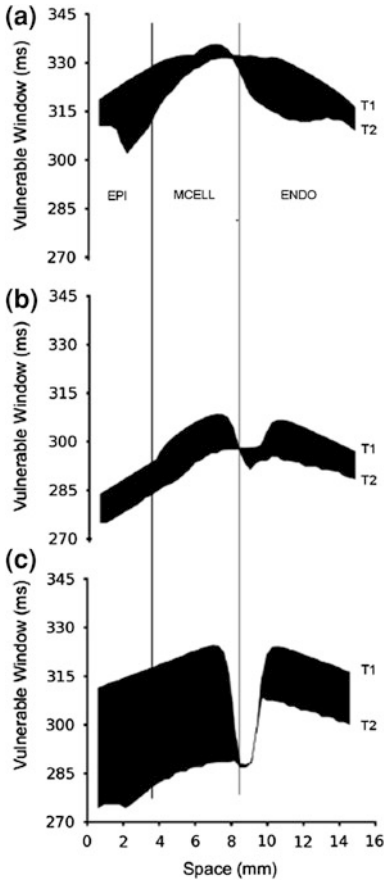

Fig. 8.7 The measured width of the temporal vulnerable window along the 1D strand for WT (**a**), WT-D172N (**b**) and D172N (**c**) conditions

required to support the formation and maintenance of re-entrant spiral waves was significant; it was reduced by 57 % in the WT-D172N condition and 63 % in the D172N condition. Thus, under the WT-D172N and D172N mutation conditions, there was a greater susceptibility of idealised 2D tissue to ventricular arrhythmia.

8.8 Investigating the Arrhythmogenic Substrate in SQT3: 2D and 3D Simulations with Realistic Geometry

8.8.1 Simulations with Realistic 2D Geometry

Realistic ventricular geometry is considerably more complex than an idealised 2D sheet and in addition, involves anisotropic conduction due to the presence of differing fibre orientations. Consequently, similar to SQT1 (Chap. 6) and SQT2

(Chap. 7), simulations were performed in a 2D cross-section of human ventricle tissue and in an anatomical, human 3D ventricle geometry (see Sect. 5.2.4.2). Transmural heterogeneity (EPI, MCELL and ENDO regions) in the ventricle was also considered.

Figure 8.8 shows simulation results obtained for the 2D human ventricle slice. Figure 8.8a–b show the application of a premature stimulus (WT: 335 ms, WT-D172N: 301 ms and D172N: 285 ms) during the vulnerable window of a local region in the left ventricle in WT (Fig. 8.8ai–di), WT-D172N (Fig. 8.8aii–dii) and D172N (Fig. 8.8aiii–diii) conditions. This led to the generation of re-entrant excitation waves in WT (Fig. 8.8bi–di), WT-D172N (Fig. 8.8bii–dii) and D172N (Fig. 8.8biii–diii) conditions. The re-entrant spiral waves self-terminated within 0.7 s in WT (Fig. 8.8di and Fig. 8.9a) but not in the WT-D172N (Fig. 8.8dii) or D172N (Fig. 8.8diii) conditions, where they persisted for the entire duration (5 s) of the simulation conditions (Fig. 8.9a).

Figure 8.8ei–eiii show the evolution of the AP in a local cell in the ventricle under the WT (Fig. 8.8ei), WT-D172N (Fig. 8.8eii) and D172N (Fig. 8.8eiii) conditions. Power spectrum analysis of the recorded whole-field averaged electrical activity from the tissue carried out on the APs showed a higher dominant frequency (Fig. 8.9b) under the mutant conditions (WT-D172N: 3.1 Hz and D172N: 3.6 Hz) compared to the WT (2.8 Hz) condition (Fig. 8.9b). Taken together, these results show that the D172N mutation is able to increase the susceptibility of the ventricular tissue to genesis and maintenance of re-entrant excitation waves leading to ventricular arrhythmia.

8.8.2 Simulations with 3D Realistic Geometry

Due to the complex geometry and anisotropic properties of ventricular tissue, it cannot be assumed that sustained re-entry in a 2D tissue model under the mutation conditions studied above necessarily translates into similar activity in a 3D tissue model. Therefore, similar to SQT1 (Chap. 6) and SQT2 (Chap. 7), further simulations were performed using three-dimensional anatomical human ventricle geometry (Fig. 8.10).

Figure 8.10 shows the results of the simulations obtained using anatomical human 3D ventricle geometry. The premature stimulus was applied from the base of the ventricle up to half-way towards its apex, covering a region of approximately 90 × 63 mm in the WT, WT-D172N and D172N conditions (Fig. 8.10ai–aiii). This region included the left ventricle and the surrounding area of the right ventricular outflow tract. The premature stimulus was applied during the vulnerable window of the aforementioned region following the refractory tail of a previous excitation wave.

This generated re-entrant scroll waves in all conditions, which terminated under the WT condition within 0.7 s but were sustained in the WT-D172N and D172N

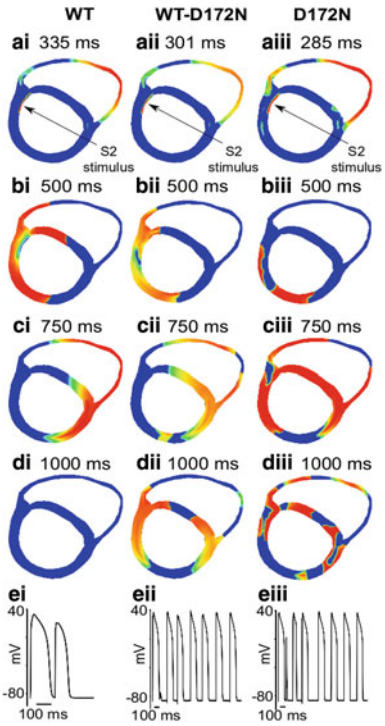

Fig. 8.8 Snapshots of initiation and conduction of re-entry in realistic 2D model cross-section of ventricles. **ai**, **aii**, **aiii** Application of a premature S2 stimulus into the refractory and partially recovered region of an excitation wave after a delay of 335 ms for WT, 301 ms for WT-D172N and 285 ms for D172N condition from the initial wave stimulus. **bi**, **bii**, **biii** Developed spiral wave from the S2 stimulus. Snapshot at time = 500 ms. **ci**, **cii**, **ciii** Snapshot of spiral wave at time = 750 ms. The induced spiral wave transited from transmural re-entry with tip rotating within the ventricle wall to anatomical re-entry with tip rotating around the ventricle boundary in WT and WT-D172N conditions. However, transmural re-entry persisted in the D172N condition and broke-up forming regenerative multiple re-entrant wavelets. **di**, **dii**, **diii** Snapshot of spiral wave at time = 1000 ms. Spiral wave self-terminated in WT before this recording point, but persisted in WT-D172N and D172N conditions. **ei**, **eii**, **eiii** Recorded time series of the action potential of a cell in the left ventricle for the WT, WT-D172N and D172N conditions

conditions (Figs. 8.10 and 8.11a) throughout the entire simulation period of 10 s. Figure 8.10ei–eiii show the evolution of the AP in a local cell in the ventricles and Fig. 8.11a shows the lifespan of re-entry under all conditions. Power spectrum analysis on the APs showed a higher dominant frequency under the WT-D172N and D172N conditions compared to the WT condition (Fig. 8.11b). This further supports the pro-arrhythmic nature of the D172N mutation, as shown in the 1D and 2D simulations.

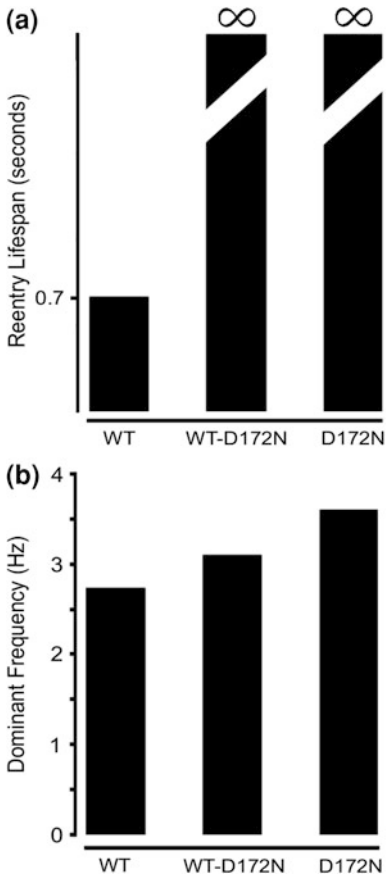

Fig. 8.9 Reentry lifespan and dominant frequency in realistic 2D model cross-section of ventricles. **a** Measured lifespan of re-entry spiral waves in WT, WT-D172N and D172N conditions. **b** Computed dominant frequency of electrical activity recorded from ventricle in WT, WT-D172N and D172N conditions (WT: 2.8 Hz; WT-D172N: 3.1 Hz; D172N: 3.6 Hz)

8.9 Discussion

The results from these simulations constitute novel evidence regarding the pro-arrhythmic effects of the augmented outward current component of the KCNJ2 D172N mutations. The WT-D172N and D172N expression conditions increased the susceptibility of the tissue to the initiation, stabilization and acceleration of re-entry. Priori et al. [10] in their first report of the mutation used the Priebe-Beuckelmann ventricular AP model [12] to demonstrate AP shortening, steeper APD and ERP restitution curves, QT interval shortening and alterations to T-wave morphology. The present study not only reproduces those findings but has also for the first time examined the functional consequences of the mutation at the 2D tissue and 3D organ levels. In addition to QT interval shortening, my simulations show increased susceptibility to the initiation and stabilisation of re-entry under both WT-D172N and D172N expression conditions. It is significant that under the WT-D172N condition (which mimics the heterozygote state of the proband), the

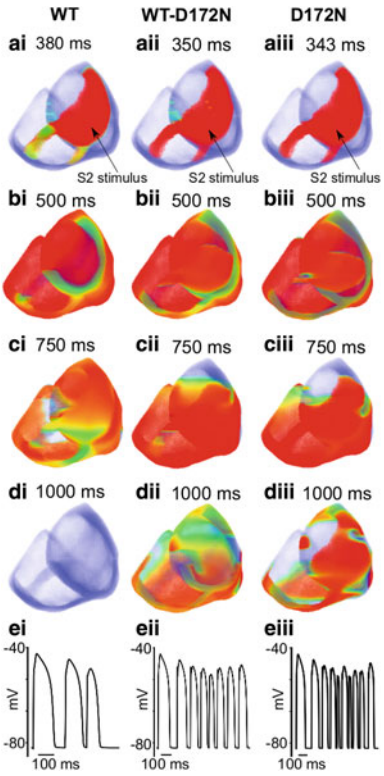

Fig. 8.10 Snapshots of initiation and conduction of re-entry in a 3D anatomical model of human ventricles. **ai**, **aii**, **aiii** Application of an S2 premature stimulus in a local region at refractory period of a previous conditioning excitation wave after a time delay of 380 ms for WT, 350 ms for WT-D172N and 343 ms for D172N conditions from the initial conditioning wave stimulus. **bi**, **bii**, **biii** Developed scroll wave from the S2 stimulus for the WT, WT-D172N and D172N conditions. Snapshot at time = 500 ms. **ci**, **cii**, **ciii** Snapshot of scroll wave at time = 750 ms for the WT, WT-D172N and D172N conditions. **di**, **dii**, **diii** Snapshot of scroll wave at time = 1000 ms. The scroll wave self-terminated in WT, but persisted and broke up forming regenerative wavelets in WT-D172N and D172N conditions. **ei**, **eii**, **eiii** Recorded time series of the action potential of a cell in the left ventricle for WT, WT-D172N and D172N conditions. restitution curves, QT interval shortening and alterations to T-wave morphology. The present study not only reproduces those findings but has also for the first time examined the functional consequences of the mutation at the 2D tissue and 3D organ levels. In addition to QT interval shortening, my simulations show increased susceptibility to the initiation and stabilisation of re-entry under both WT-D172N and D172N expression conditions. It is significant that under the WT-D172N condition (which mimics the heterozygote state of the proband), the QT interval shortened by $\sim$12 % and was practically equivalent to that of the proband. Tissue vulnerability and re-entry lifespan, which are factors of augmented arrhythmogenic susceptibility, were also increased

QT interval shortened by $\sim$12 % and was practically equivalent to that of the proband. Tissue vulnerability and re-entry lifespan, which are factors of augmented arrhythmogenic susceptibility, were also increased.

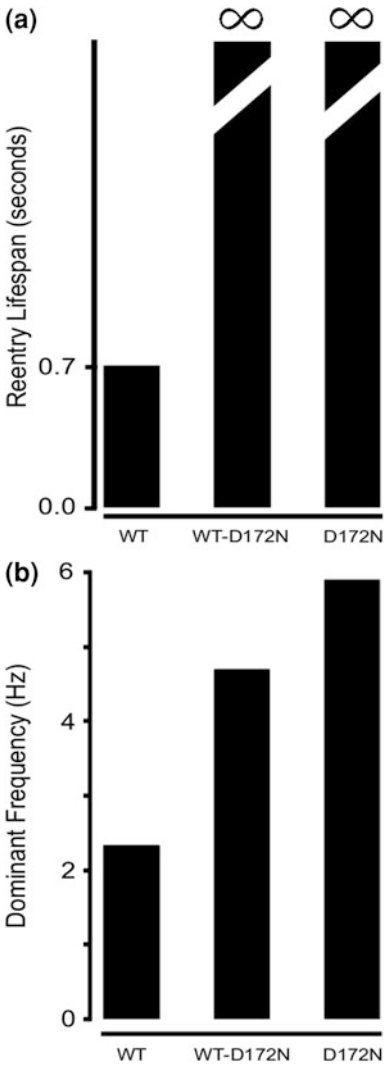

Fig. 8.11 Reentry lifespan and dominant frequency in realistic 3D anatomical model of human ventricles. **a** Measured lifespan of re-entry scroll wave in WT, WT-D172N and D172N conditions. **b** Computed dominant frequency of electrical activity recorded from ventricle in WT, WT-D172N and D172N conditions (2.3 Hz for WT, 4.8 Hz for WT-D172N and 6.0 Hz for D172N condition)

8.9.1 Pro-Fibrillatory Mechanisms of the Kir2.1 D172N Mutation

Clinically, SQTS patients present with ventricular tachycardias [26–28] and some have been known to have ventricular fibrillation [29]. Ventricular fibrillation was elicited via programmed electrical stimulation in the SQT3 setting. The proband in whom the SQT3 mutation was discovered had no prior history of cardiac arrhythmias but her father had prior incidents of presyncopal events and palpitations [10].

Priori et al. conjectured that the steeper APD and ERP restitution curves in the D172N mutation condition would provide a substrate for increased risk of stable reentry in tissue [10]. The simulation results in this chapter provide evidence that these steepening of the APD and ERP restitution curves plus the APD and ERP shortening by the D172N mutation are pro-arrhythmic. They reduce the minimal size of the substrate required to initiate and maintain reentry. In the WT-D172N and D172N conditions, the measured minimal substrate size was reduced by 57 and 63 % respectively compared to the WT condition. Reentry self-terminated in the WT condition but was perpetuated under the WT-D172N and D172N conditions. It self-terminated in the WT condition because the ERP and consequently the wavelength of the reentrant circuit(s) was too large to be sustained in such a limited mass of tissue. However, in the mutation conditions, the reduced ERP and consequently the reduced wavelength of the reentrant circuit(s) allowed its accommodation within the tissue mass. The SQT2 mutation also shortened APD and ERP, steepened the APD-R curve but did so less differentially across the ventricular wall for the ERP-R curve and was also able to support and facilitate re-entry (Chap. 7). Similarly, the SQT1 mutation also shortened APD and ERP but reduced the slopes of the APD-R and ERP-R curves. It was also able to support and facilitate re-entry via mechanisms described in Chap. 6.

The KCNJ2 D172N mutation differentially abbreviated the APD and ERP in the EPI, MIDDLE and ENDO cells (i.e., it augmented transmural heterogeneity). This led to augmentation of the transmural dispersion of APD/ERP in different regions of the transmural strand (Figs. 8.5 and 8.7). The effect of this was increased susceptibility of the tissue to arrhythmogenic stimuli, as the tissue's vulnerable window to premature stimuli was increased (Fig. 8.7).

The D172N mutation also stabilised and accelerated reentry in 2D and 3D tissue further reflecting its pro-arrhythmic nature. This is consistent with findings in previous studies of the role of I_{K1} in arrhythmogenesis [4, 8, 30]. There are however, some differences between those studies and that of the present chapter. In the previous studies, both the outward and inward components of I_{K1} were increased or scaled proportionally, which had the effect of steepening the slope of the I–V curve. Consequently, any membrane potential change close to the potassium equilibrium potential (E_K) would act in such a way as to shift the resting potential towards E_K. Therefore, during high excitation rates, sodium current (I_{Na}) recovery from inactivation is increased, thereby helping to stabilise reentry. In my study, only the outward component of the I_{K1} current is enhanced (the inward component is unaffected). There is thus less effect on the slope of the I–V curve and the resting potential was found to be little altered by the D172N mutation. Consequently, the stabilisation of reentry under these conditions was not through increased I_{Na} recovery but via increased tissue excitability at high excitation rates (Fig. 8.6) and the shorter ERP of the WT-D172N and D172N mutations (Fig. 8.3). The reduced ERP of the mutations also reduced the wavelength of the reentrant excitation waves thus allowing their activation at higher frequencies (Figs. 8.8 and 8.10) and once formed, the waves were stable and persistent.

8.9.2 Relevance to Previous I_{K1} Studies

Channelopathies related to I_{K1} are known to lead to cardiac arrhythmias, e.g., Anderson's syndrome [31, 32], long QT syndrome [33–35] and short QT syndrome [33–35]. In experimental animal models, a few studies have also implicated I_{K1} in the genesis and maintenance of ventricular fibrillation [36–38]. In transgenic mouse heart with overexpression of Kir2.1, the initiation and stabilisation of ventricular fibrillation was the consequence of increased I_{K1} [8]. In a guinea pig heart model, it was found that I_{K1} played a significant part in rotor dynamics and its blockade terminated ventricular fibrillation [36, 37]. These studies have resulted in greater awareness of the role played by I_{K1} in cardiac arrhythmias.

In summary, the results of this chapter support this accumulating evidence of the prominent role played by I_{K1} in the initiation and maintenance of cardiac arrhythmias [4, 36, 37, 39]. The Kir2.1 D172N mutation stabilised and accelerated reentry, which is consistent with the experimental study of mice with Kir2.1 overexpression [8]. The D172N Kir2.1 mutation also increased human ventricular tissue susceptibility to the initiation of reentry. Thus, in some settings I_{K1} may offer a potential therapeutic target for the treatment of cardiac arrhythmias.

The study that constitutes the basis for this thesis chapter has been published in full paper form [40].

References

1. Tamargo J, Caballero R, Gómez R, Valenzuela C, Delpón E (2004) Pharmacology of cardiac potassium channels. Cardiovasc Res 62(1):9–33
2. Shimoni Y, Clark RB, Giles WR (1992) Role of an inwardly rectifying potassium current in rabbit ventricular action potential. J Physiol (Lond) 448:709–727
3. Mitcheson JS, Hancox JC (1999) An investigation of the role played by the E-4031-sensitive (rapid delayed rectifier) potassium current in isolated rabbit atrioventricular nodal and ventricular myocytes. Pflugers Arch 438(6):843–850
4. Dhamoon AS, Jalife J (2005) The inward rectifier current (IK1) controls cardiac excitability and is involved in arrhythmogenesis. Heart Rhythm 2(3):316–324
5. Gaborit N, Le Bouter S, Szuts V, Varro A, Escande D, Nattel S et al (2007) Regional and tissue specific transcript signatures of ion channel genes in the non-diseased human heart. J Physiol (Lond) 582(Pt 2):675–693
6. Plaster NM, Tawil R, Tristani-Firouzi M, Canún S, Bendahhou S, Tsunoda A et al (2001) Mutations in Kir2.1 cause the developmental and episodic electrical phenotypes of Andersen's syndrome. Cell 105(4):511–519
7. Tristani-Firouzi M, Jensen JL, Donaldson MR, Sansone V, Meola G, Hahn A et al (2002) Functional and clinical characterization of KCNJ2 mutations associated with LQT7 (Andersen syndrome). J Clin Invest 110(3):381–388
8. Noujaim SF, Pandit SV, Berenfeld O, Vikstrom K, Cerrone M, Mironov S et al (2007) Up-regulation of the inward rectifier K + current (I K1) in the mouse heart accelerates and stabilizes rotors. J Physiol (Lond) 578(Pt 1):315–326

9. Xia M, Jin Q, Bendahhou S, He Y, Larroque M-M, Chen Y et al (2005) A Kir2.1 gain-of-function mutation underlies familial atrial fibrillation. Biochem Biophys Res Commun 332(4):1012–1019
10. Priori SG, Pandit SV, Rivolta I, Berenfeld O, Ronchetti E, Dhamoon A et al (2005) A novel form of short QT syndrome (SQT3) is caused by a mutation in the KCNJ2 gene. Circ Res 96(7):800–807
11. El Harchi A, McPate MJ, Zhang Y hong, Zhang H, Hancox JC (2009) Action potential clamp and chloroquine sensitivity of mutant Kir21 channels responsible for variant 3 short QT syndrome. J Mol Cell Cardiol 47(5):743–747
12. Priebe L, Beuckelmann DJ (1998) Simulation study of cellular electric properties in heart failure. Circ Res 82(11):1206–1223
13. ten Tusscher KHWJ, Panfilov AV (2006) Alternans and spiral breakup in a human ventricular tissue model. Am J Physiol Heart Circ Physiol 291(3):1088–1100
14. ten Tusscher KHWJ, Noble D, Noble PJ, Panfilov AV (2004) A model for human ventricular tissue. Am J Physiol Heart Circ Physiol 286(4):1573–1589
15. ten Tusscher KHWJ, Panfilov AV (2006) Cell model for efficient simulation of wave propagation in human ventricular tissue under normal and pathological conditions. Phys Med Biol 51(23):6141–6156
16. Xie F, Qu Z, Garfinkel A, Weiss JN (2002) Electrical refractory period restitution and spiral wave reentry in simulated cardiac tissue. Am J Physiol Heart Circ Physiol 283(1):448–460
17. Keldermann RH, ten Tusscher KHWJ, Nash MP, Bradley CP, Hren R, Taggart P et al (2009) A computational study of mother rotor VF in the human ventricles. Am J Physiol Heart Circ Physiol 296(2):370–379
18. ten Tusscher KHWJ, Mourad A, Nash MP, Clayton RH, Bradley CP, Paterson DJ et al (2009) Organization of ventricular fibrillation in the human heart: experiments and models. Exp Physiol 94(5):553–562
19. Yan GX, Shimizu W, Antzelevitch C (1998) Characteristics and distribution of M cells in arterially perfused canine left ventricular wedge preparations. Circulation 98(18):1921–1927
20. Drouin E, Charpentier F, Gauthier C, Laurent K, Le Marec H (1995) Electrophysiologic characteristics of cells spanning the left ventricular wall of human heart: evidence for presence of M cells. J Am Coll Cardiol 26(1):185–192
21. Tung R, Josephson ME, Reddy V, Reynolds MR (2010) Influence of clinical and procedural predictors on ventricular tachycardia ablation outcomes: an analysis from the substrate mapping and ablation in sinus rhythm to halt ventricular tachycardia Trial (SMASH-VT). J Cardiovasc Electrophysiol 21(7):799–803
22. Zhang H, Wang J, Yang L, Wu R-J, Mei X, Zhao W (2011) Vulnerability in simulated ischemic ventricular transmural tissues. Chin J Physiol 54(6):427–434
23. Chen XZ, Zhang H, Jin YB, Yang L (2009) Vulnerability to unidirectional conduction block and reentry in rabbit left ventricular wedge preparation: effects of stimulation sequence and location. Chin J Physiol 52(1):16–22
24. Trénor B, Romero L, Ferrero JM Jr, Sáiz J, Moltó G, Alonso JM (2007) Vulnerability to reentry in a regionally ischemic tissue: a simulation study. Ann Biomed Eng 35(10):1756–1770
25. Qu Z, Garfinkel A, Weiss JN (2006) Vulnerable window for conduction block in a one-dimensional cable of cardiac cells, 1: single extrasystoles. Biophys J 91(3):793–804
26. Maury P, Extramiana F, Sbragia P, Giustetto C, Schimpf R, Duparc A et al (2008) Short QT syndrome. Update on a recent entity. Arch Cardiovasc Dis 101(11–12):779–786
27. Bellocq C, van Ginneken ACG, Bezzina CR, Alders M, Escande D, Mannens MMAM et al (2004) Mutation in the KCNQ1 gene leading to the short QT-interval syndrome. Circulation 109(20):2394–2397
28. Schimpf R, Borggrefe M, Wolpert C (2008) Clinical and molecular genetics of the short QT syndrome. Curr Opin Cardiol 23(3):192–198
29. Watanabe H, Makiyama T, Koyama T, Kannankeril PJ, Seto S, Okamura K et al (2010) High prevalence of early repolarization in short QT syndrome. Heart Rhythm 7(5):647–652

30. Pandit SV, Berenfeld O, Anumonwo JMB, Zaritski RM, Kneller J, Nattel S et al (2005) Ionic determinants of functional reentry in a 2-D model of human atrial cells during simulated chronic atrial fibrillation. Biophys J 88(6):3806–3821
31. Sung RJ, Wu S-N, Wu J-S, Chang H-D, Luo C-H (2006) Electrophysiological mechanisms of ventricular arrhythmias in relation to Andersen-Tawil syndrome under conditions of reduced IK1: a simulation study. Am J Physiol Heart Circ Physiol 291(6):2597–2605
32. Zhang L, Benson DW, Tristani-Firouzi M, Ptacek LJ, Tawil R, Schwartz PJ et al (2005) Electrocardiographic features in Andersen-Tawil syndrome patients with KCNJ2 mutations: characteristic T-U-wave patterns predict the KCNJ2 genotype. Circulation 111(21):2720–2726
33. Xu Y, Zhang Q, Chiamvimonvat N (2007) IK1 and cardiac hypoxia: after the long and short QT syndromes, what else can go wrong with the inward rectifier K + currents? J Mol Cell Cardiol 43(1):15–17
34. Domenighetti AA, Boixel C, Cefai D, Abriel H, Pedrazzini T (2007) Chronic angiotensin II stimulation in the heart produces an acquired long QT syndrome associated with IK1 potassium current downregulation. J Mol Cell Cardiol 42(1):63–70
35. Gross GJ (2006) IK1: the long and the short QT of it. Heart Rhythm 3(3):336–338
36. Jalife J (2009) Inward rectifier potassium channels control rotor frequency in ventricular fibrillation. Heart Rhythm 6(11 Suppl):44–48
37. Warren M, Guha PK, Berenfeld O, Zaitsev A, Anumonwo JMB, Dhamoon AS et al (2003) Blockade of the inward rectifying potassium current terminates ventricular fibrillation in the guinea pig heart. J Cardiovasc Electrophysiol 14(6):621–631
38. Sekar RB, Kizana E, Cho HC, Molitoris JM, Hesketh GG, Eaton BP et al (2009) IK1 heterogeneity affects genesis and stability of spiral waves in cardiac myocyte monolayers. Circ Res 104(3):355–364
39. Jalife J, Berenfeld O, Mansour M (2002) Mother rotors and fibrillatory conduction: a mechanism of atrial fibrillation. Cardiovasc Res 54(2):204–216
40. Adeniran I, El Harchi A, Hancox JC, Zhang H (2012) Proarrhythmia in KCNJ2-linked short QT syndrome—insights from modelling. Cardiovasc Res 94(1):66–76

Chapter 9
Relationship Between Electrical and Mechanical Systole in the Short QT Syndrome: Insights from Modelling

9.1 Electromechanical Cardiac Myocyte Model

In Chaps. 6–8, a pure electrophysiology model—the ten Tusscher et al. human ventricular cell model (TNNP) [1]—representing the electrical activity of the human ventricle was used to investigate the functional consequences of the SQTS on cardiac electrical excitation wave conduction. It is feasible that changes to repolarisation time might influence electromechanical coupling in the SQTS setting. In order to investigate the effects of the SQTS on cardiac mechanical dynamics, a contracting or force-generating human ventricular myocyte, an electromechanically coupled model of cardiac cell and tissue is required.

9.2 Myofilament Model

To describe the mechanics of the cardiac myocyte, the Rice et al. [2] myocyte contraction model (RMM) was adopted. It is based on the cross-bridge cycling model of mechanical contraction as explained in Sect. 1.9.2.3. It is able to replicate a wide range of experimental data [2] including:

- steady state force-sarcomere length relations (F-SL relations).
- steady state force-calcium relations (F–Ca relations) including SL effects.
- steady state sarcomere length-calcium relations (SL-Ca relations) for unloaded cells.
- steady state force-velocity relations (F–V relations).

The biophysical processes of cell contraction are represented by systems of ordinary differential equations (ODE) [2].

I. Adeniran, *Modelling the Short QT Syndrome Gene Mutations*,
Springer Theses, DOI: 10.1007/978-3-319-07200-5_9,

9.3 Coupling the Electrophysiology Model with the Myofilament Mechanics Model

The essential link between the electrophysiology model and the myofilament mechanics model (MM) is the intracellular calcium concentration $[Ca^{2+}]_i$ and associated Ca^{2+}-handling dynamics. $[Ca^{2+}]_i$ is produced as dynamic output from the electrophysiology model and used as an input to the mechanics model from where the amount that is buffered to troponin is calculated. In the TNNP electrophysiology model, the myoplasmic calcium concentration is calculated via [1]:

$$\frac{dCa_i}{dt} = Ca_{ibufc}\left(\frac{V_{sr}}{V_c}(I_{leak} - I_{up}) + I_{xfer}\right) - C_m\frac{I_{bca} + I_{pca} - 2I_{Naca}}{2V_cF} \tag{9.1}$$

where Ca_{ibufc} is the total cytoplasmic buffer concentration, V_{sr} is the volume of the sarcoplasmic reticulum (SR), V_c is the cytoplasmic volume, I_{leak} is the sarcoplasmic reticulum (SR) Ca^{2+} leak current, I_{up} is the SR Ca^{2+} pump current, I_{xfer} is diffusive Ca^{2+} current between diadic Ca^{2+} subspace and bulk cytoplasm, C_m is the membrane cell capacitance per unit surface area, I_{bCa} is the background Ca^{2+} current, I_{pCa} is the plateau Ca^{2+} current, I_{NaCa} is the Na^+/Ca^{2+} exchanger current and F is the Faraday constant.

The flux of the binding of calcium to troponin from the myofilament mechanics model is added to the calcium concentration calculation in Eq. (9.1), which then becomes:

$$\frac{dCa_i}{dt} = Ca_{ibufc}\left(\frac{V_{sr}}{V_c}(I_{leak} - I_{up}) + I_{xfer}\right) - C_m\frac{I_{bca} + I_{pca} - 2I_{Naca}}{2V_cF} - \frac{dTrop_{Ca}}{1000} \tag{9.2}$$

where $dTrop_{Ca}$ represents the concentration of calcium bound to troponin. With all the state variables describing the myofilament mechanics model included in the TNNP electromechanical model, and with Eq. (9.2) substituted for Eq. (9.1), the two models become effectively coupled, yielding an electromechanical cell model of a human ventricular myocyte. Consequently, the electromechanical model is formulated as a system of differential-algebraic equations (DAE) of the form [1, 2]:

$$\frac{dy}{dt} = f(y, z) \tag{9.3}$$

$$g(y, z) = 0 \tag{9.4}$$

Figure 9.1 shows the APs from the EPI, MIDDLE and ENDO cells for the TNNP model and the newly coupled electromechanical model at 1 Hz under the WT, SQT1, SQT2 and SQT3 conditions. The changing transmembrane potential of the electromechanics model during each AP waveform is identical to and visually indistinguishable from that of the TNNP model.

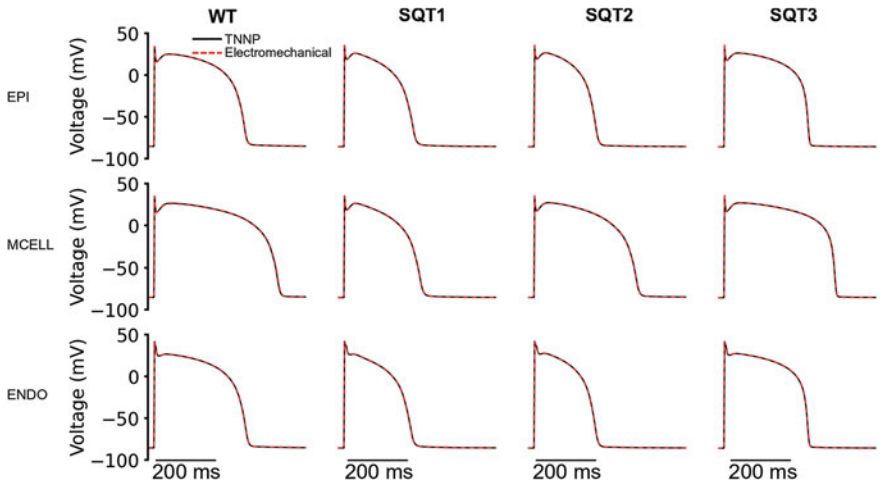

Fig. 9.1 Action potentials from the epicardial, mid-myocardial and endocardial cell types of the original ten Tusscher et al. [1] model (the pure electrophysiology model) and the newly coupled electromechanics model

9.3.1 Stretch-Activated Channel

In cardiac tissue, a number of ionic channels that are activated by cell stretch have been identified [3–7]. These are known as stretch-activated channels (SACs) and can have significant effects on cardiac electrophysiological properties [3–7] (see Sect. 1.8). They respond to mechanical stimuli by an increase in open probability rather than conductance [8, 9].

A stretch-activated current (I_{sac}) was incorporated into the electromechanics model following the work of Panfilov et al. [10], Lunze et al. [11], Kuijpers [12], Youm et al. [13] and Kohl and Sachs [8]. I_{sac} is formulated as:

$$I_{sac} = G_{sac} \cdot P_m \cdot (V_m - E_{sac}) \tag{9.5}$$

where V_m is the membrane potential, G_{sac} and E_{sac} are the maximum membrane conductance and reversal potential of the stretch-activated channels respectively. P_m is the open channel probability and is modelled as:

$$P_m = \frac{1.0}{1 + e^{-\left(\frac{\varepsilon - \varepsilon_{1/2}}{k_\varepsilon}\right)}} \tag{9.6}$$

where $\varepsilon_{1/2}$ is the half-activation strain, ε is the strain, which has an explicit dependence on the sarcomere length and $k_\varepsilon = 0.02$ [11, 13, 14] is the activation slope. E_{sac} in the electromechanics model was typically 1 and describes the experimentally observed depolarising effect of the channel [15, 16].

Additionally, in the electromechanics model, the channel is permeable to Na^+, K^+ and Ca^{2+} with I_{sac} defined by:

$$I_{sac} = I_{sac,Na} + I_{sac,K} + I_{sac,Ca} \tag{9.7}$$

where $I_{sac,Na}$, $I_{sac,K}$ and $I_{sac,Ca}$ represent the contributions of Na^+, K^+ and Ca^{2+} to I_{sac} respectively. In order to investigate the effects of the channel's permeability to Na^+, K^+ and Ca^{2+}, two cases were considered in the single cell simulations: $P_{Na}:P_K:P_{Ca} = 1:1:1$ and $P_{Na}:P_K:P_{Ca} = 1:1:0$ with P_{Na}, P_K and P_{Ca} being the relative permeabilities to Na^+, K^+ and Ca^{2+} respectively.

9.4 Tissue Mechanics Model

The cardiac tissue is modelled within the theoretical framework of nonlinear finite elasticity. Within this framework, any boundary value problem is comprised of three basic relations: kinematics relations, equations of motion and constitutive relations [17–19].

The kinematics relations govern the motion and deformation of the body under investigation; they define the relationship between the displacement of the body and the strain field. The equations of motion or the equilibrium relations are balance principles that describe the fundamental laws of physics governing the motion of a continuum. The constitutive relations describe the behaviour of a particular material, i.e., its response to an applied load [19–25].

Similar to other studies, cardiac tissue is modelled as an inhomogeneous, anisotropic, incompressible, nonlinear material [26–34]. The undeformed tissue occupies the region Ω_0 with coordinates $\mathbf{X} = (X_1, X_2, X_3)$ while the deformed tissue occupies the region Ω with coordinates $\mathbf{x} = (x_1, x_2, x_3)$. The deformation gradient ($\boldsymbol{F}$), an important quantity in nonlinear continuum mechanics, is a tensor that maps or transforms elements from the undeformed configuration to the deformed configuration [19–25]. It is given by:

$$F = \frac{\partial x}{\partial X} \tag{9.8}$$

where:

$$F_{ij} = \frac{\partial x_i}{\partial X_j} \tag{9.9}$$

which provides a means of computing the components of the tensor $\boldsymbol{F}$ given a referential description of the motion relative to a Cartesian coordinate system [19–25].

The Right Cauchy-Green stress tensor, $\boldsymbol{C}$ is defined as:

$$C = F^T F \tag{9.10}$$

It quantifies the squared length of infinitesimal fibres in the deformed configuration.

The Green-Lagrange strain tensor, $\boldsymbol{E}$, quantifies the length changes in a material fibre and angles between pairs of fibres in a deformed solid. It is defined as:

$$E = \frac{1}{2}(C - I) \tag{9.11}$$

where I is the second-order identity tensor. In the absence of body forces, and assuming that the body is always in instantaneous equilibrium and no inertial effects, the coordinates of the deformed body then satisfy the steady-state equilibrium equation with incompressibility enforced, i.e., the volume of the material is preserved:

$$\frac{\partial}{\partial X_M}(T_{MN} F_{iN}) = 0 \tag{9.12}$$

$$\det(F) = 1 \tag{9.13}$$

where i = 1, 2, 3. $T = (T_{MN})$ is the second Piola-Kirchhoff stress tensor; it relates a stress measure (in this case, $\boldsymbol{C}$) to a strain measure (in this case, $\boldsymbol{E}$) and refers to the deformed body. The incompressibility constraint is enforced via Eq. (9.13), which simply states that the volume of the body is preserved with deformation.

T is composed of two parts; an elastic force component (the passive stress due to deformation) and a biochemically-generated force component [26]. Therefore, it can be written as:

$$T = T^{elastic} + T^{biochem} \tag{9.14}$$

To calculate T, a strain energy function (W) is required, which defines the constitutive behaviour of the material. For cardiac tissue, many strain energy functions have been proposed [27, 30, 32, 35–37]. In this work, the Pole-Zero strain energy function was used (see Sect. 9.5). Written in terms of the strain energy function, W, the entries of $T^{elastic}$ are:

$$T_{MN}^{elastic} = \frac{1}{2}\left(\frac{\partial W}{\partial E_{MN}} + \frac{\partial W}{\partial E_{NM}}\right) \tag{9.15}$$

In this work, it assumed that the fibre direction is parallel to the X1-axis and similar to previous studies [26, 30, 32–34], it is assumed that the direction of the biochemically-generated force/tension acts only in the fibre direction. For example, for a 2D rectangular sheet with width (base) parallel to the x-axis, the fibre

direction is chosen as the x-axis and this would also be the direction of the biochemically-generated force/tension. Following the work of Pathmanathan and Whiteley [26], $T_{biochem}$ is calculated as:

$$T_{biochem} = \frac{Ta}{C_{11}} \delta_{M1} \delta_{N1} \tag{9.16}$$

where Ta is the active force/tension obtained from the electromechanics cell model, C_{11} is the indexed component of the Right Cauchy-Green stress tensor, $\boldsymbol{C}$, and $\delta_{M1}\delta_{N1}$ ensure that Ta acts only in the fibre direction. Equation (9.14) can then be written as:

$$T_{MN} = \frac{1}{2}\left(\frac{\partial W}{\partial E_{MN}} + \frac{\partial W}{\partial E_{NM}}\right) + \frac{Ta}{C_{11}} \delta_{M1} \delta_{N1} \tag{9.17}$$

9.5 The Pole-Zero Strain Energy Function

For cardiac tissue, Nash and Hunter [30] used the pole-zero strain energy function, which is also employed in the current study. It encapsulates microstructural observations and bi-axial test results for myocardium [30]. It is given as:

$$W = \sum_{M.N=1}^{3} k_{MN} \frac{E_{MN}^2}{\left(a_{MN} - E_{MN}\right)^{b_{MN}}} \tag{9.18}$$

where a_{MN} are physical properties of the tissue that are measured directly from microstructural observations. They are referred to as limiting strains or poles. b_{MN} are related to the curvature of the uniaxial stress-strain relationships and were estimated by biaxial tension test results [38, 39]. k_{MN} are weighting factors that determine the contribution of the deformation to the strain energy of the material. E is the Green Lagrange strain tensor (see Sect. 9.4). Greater detail on the estimation of these parameter and coefficients can be found in [39].

9.6 Mechanical Feedback in the Electrophysiology Tissue Model

As with the electrical simulations in Chaps. 6–8, the monodomain representation of cardiac tissue is employed [40–42]. However, the equation is modified to take into account the effect of the deforming tissue by incorporating a feedback in the diffusion term:

$$C_m \frac{dV}{dt} = -(I_{ion} + I_{stim}) + \nabla \cdot (DC^{-1}\nabla V) \tag{9.19}$$

Here, the only difference from Eq. (81) is the C^{-1} term, which is the inverse of the Right Cauchy-Green deformation tensor. This is in common with previous studies [26, 34, 43]. Physiologically, this term reflects the fact that the gap junctions between the cells distort with a deforming body. Hence, the electrical propagation across these gap junctions and throughout the tissue in deformed tissue is different to that in undeformed tissue.

9.7 Numerical Methods

9.7.1 Meshes

The electromechanical investigations were carried out on idealised, anisotropic, 2D tissue measuring 15 mm by 50 mm (see Sect. 5.2.4.1). The mesh used had a spatial resolution of 0.15 mm in both the x and y directions and 100 by 333 P1 finite elements [44–46]. The spatial and temporal resolution for cardiac electrophysiological simulations is well understood (in terms of the granularity necessary to sufficiently capture the essential features of electrical wave propagation in cardiac tissue) [47–49] and the mesh resolution is similar to the lengths of ventricular myocytes (80–150 μm) as suggested by Feigenbaum [50]. The mesh also consisted of three transmural regions; EPI, MCELL and ENDO as described in Sects. 5.2.3, 5.2.4.1 and Fig. 5.2.

9.7.2 Electrophysiology Problem

Obtaining a solution to the electromechanics problem in tissue involves solving two distinct sub-problems: an electrophysiology problem and a mechanics problem. The electrophysiological problem is solved with a Strang splitting method [51]. It is discretised in time using the Crank-Nicholson method [52] and in space using the Finite Element Method [44, 45, 52, 53] (see Sect. 5.2.2.2). I_{ion} in Eq. (9.19) represents the coupled electromechanics single cells discussed in Sect. 9.3. It is solved as described in Sect. 5.2.1 using the forward Euler method with a time step of 0.02 ms. In addition to obtaining the membrane potential as a solution from I_{ion}, it also produces the active tension/force, which is passed as input to the Tissue Mechanics model to calculate tissue deformation.

9.7.3 The Mechanics Problem

The active tension/force (Ta) output from the electrophysiology solution is projected onto the mechanics mesh via an optimisation calculation that involves the solution of the Laplace equation. The active tension produces a state of stress in the tissue that causes it to deform. *Ta* is incorporated into the mechanics problem as discussed in Eqs. (9.14)–(9.17).

The mechanics problem consists of only an elliptic component, which is also discretised using the Finite Element Method [44, 45, 52, 53]. In the finite element analysis of systems which are subject to constraint conditions such as incompressibility (in this particular case, the incompressibility constraint in Eq. 9.13), numerical difficulties, often termed *locking phenomena* arise [53–56]. This is an excessive stiffness of the system where the finite element is unable to distort while simultaneously satisfying the incompressibility constraint at every point in the body [19, 23, 53–56].

In order to avoid locking phenomena, a mixed formulation based on a three-field Hu-Washizu variational principle [19, 23, 57–60] was employed to solve Eq. (9.12). It incorporated three independent variables: the deformation (**u**), Green-Lagrange strain tensor (***E*** from Eq. 9.11) and the second Piola-Kirchhoff stress tensor (***T*** from Eq. 9.14). The functional on the three-field Hu-Washizu principle in the absence of body forces (see Eq. 9.12) is defined as:

$$\Pi(u, E, T) = \int_{\Omega} [W(E) + T \cdot (E(u) - E)] d\Omega \tag{9.20}$$

where W(E) is the stored strain energy function given in Eq. (9.18). The stationary condition on this functional with respect to *u, E* and *T* yields three independent equations:

$$D\Pi(u, E, T)[\delta u] = \int_{\Omega} T \cdot E(\delta u) d\Omega \tag{9.21}$$

$$D\Pi(u, E, T)[\delta E] = \int_{\Omega} \delta E . \left(\frac{\partial W}{\partial E} - T \right) d\Omega \tag{9.22}$$

$$D\Pi(u, E, T)[\delta T] = \int_{\Omega} [\delta T \cdot (E(u) - E)] d\Omega \tag{9.23}$$

where δu, δE and δT are variations in the displacement, strain and stresses respectively. Equations (9.21)–(9.23) represent the weak forms of the momentum balance equation (Eq. 9.12), the displacement-strain equation and a hyperelastic constitutive equation for *T* respectively. Equations (9.22)–(9.23) represent constraint terms enforcing incompressibility of the cardiac tissue (Eq. 9.13), which have to be fulfilled together with Eq. (9.21). Thus, δE and δT can be interpreted as Lagrange multipliers.

Over a typical finite element domain, P1 elements [44–46] are used to discretize the displacement variable, u, while the Green-Lagrange strain, E and second Piola-Kirchhoff, T variables are discretized with discontinuous (constant) functions. The nonlinear system in Eq. (9.21)–(9.23) is linearized and solved iteratively using the Newton-Raphson method [18, 23, 24, 59] to determine the system's equilibrium configuration. At mechanical equilibrium, a state of deformation is attained, which is represented by the Right Cauchy-Green stress tensor C. This is used to update the conductivity tensor of the electrophysiology problem in Eq. (9.19).

9.7.4 Combining the Electrophysiology and Mechanics Problems

In common with similar studies [26, 43, 61–63], the electrophysiology problem was solved with time step Δt for N steps. Then, the mechanics problem was solved with time step $N\Delta t$ to update the deformation of the tissue as it is more computationally intensive. The implementation and solution of both the electrophysiology and mechanics problems were developed using FEniCS, the automated finite element computing software suite [64, 65].

9.8 Single Cell Electromechanical Simulations Without I_{sac}

9.8.1 SQT1

Figure 9.2 shows the effects of the SQT1 mutation on the intracellular Ca^{2+} concentration, the sarcomere length and the active force development in an electromechanically coupled single cell without the stretch-activated current (I_{sac}). The abbreviation of the AP by SQT1 is shown for the different cell types: EPI (Fig. 9.2ai), MCELL (Fig. 9.2bi) and ENDO (Fig. 9.2ci). The difference in shortening between the pure electrophysiology model and the coupled electromechanics model was insignificant in all the cell types (less than 0.01 %, Fig. 9.1).

Compared to WT, the SQT1 mutation reduced the intracellular calcium concentration by $\sim$36 % in EPI (Fig. 9.2aii) and ENDO (Fig. 9.2cii) and by $\sim$47 % in MCELL (Fig. 9.2bii). The initial sarcomere length for all cell types in both WT and SQT1 was 2.17 μm (Fig. 9.2aiii–ciii). The minimum contracted sarcomere length (SL) in the WT condition was $\sim$1.92 μm (EPI), $\sim$1.80 μm (MCELL) and $\sim$1.89 μm (ENDO). This was reduced with the SQT1 mutation to $\sim$2.10 μm (EPI), $\sim$2.01 μm (MCELL) and $\sim$2.06 μm (ENDO). This is shown in Fig. 9.2-aiii–ciii for EPI, MCELL and ENDO respectively. The reduction in the intracellular calcium concentration was accompanied by a consequent reduction in the contractile force compared to WT by $\sim$70 % in EPI (Fig. 9.2aiv), $\sim$56 % in MCELL

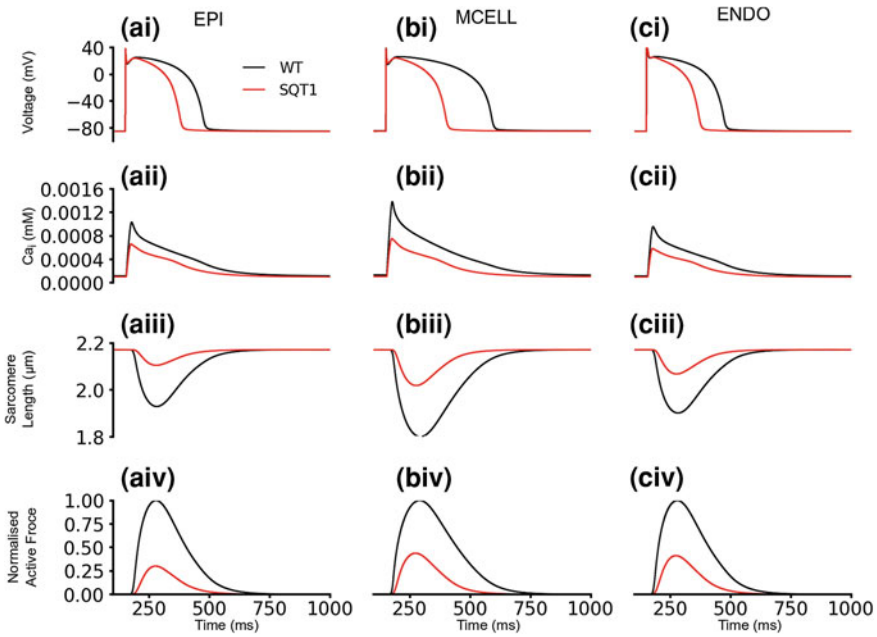

Fig. 9.2 Single cell electromechanical effects of the SQT1 mutation without I_{sac}. (**ai, bi, ci**) WT (*black*) and SQT1 (*red*) action potentials in the EPI (**ai**), MCELL (**bi**) and ENDO (**ci**) cells. (**aii, bii, cii**) WT (*black*) and SQT1 (*red*) calcium concentration in the EPI (**aii**), MCELL (**bii**) and ENDO (**cii**) cells. (**aiii, biii, ciii**) WT (*black*) and SQT1 (*red*) sarcomere length in the EPI (**aiii**), MCELL (**biii**) and ENDO (**ciii**) cells. (**aiv**, **biv**, **civ**) WT (*black*) and SQT1 (*red*) normalised active force in the EPI (**aiv**), MCELL (**biv**) and ENDO (**civ**) cells

Table 9.1 Without I_{sac}—Minimal length of contracted sarcomere with the SQT1 mutation and the consequent active force of contraction relative to WT

	Sarcomere length (μM)			Force of contraction (%)		
	EPI	MCELL	ENDO	EPI	MCELL	ENDO
WT	1.92	1.80	1.89	100	100	100
SQT1	2.10	2.01	2.06	30	44	41

Initial sarcomere length is 2.17 μM. The smaller the sarcomere length, the greater is the force of contraction

(Fig. 9.2biv) and ∼59 % in ENDO (Fig. 9.2civ). A summary of these results is shown in Table 9.1.

9.8.2 SQT2

Figure 9.3 shows the effects of the SQT2 mutation on the intracellular Ca^{2+} concentration, the sarcomere length and the active force development in an

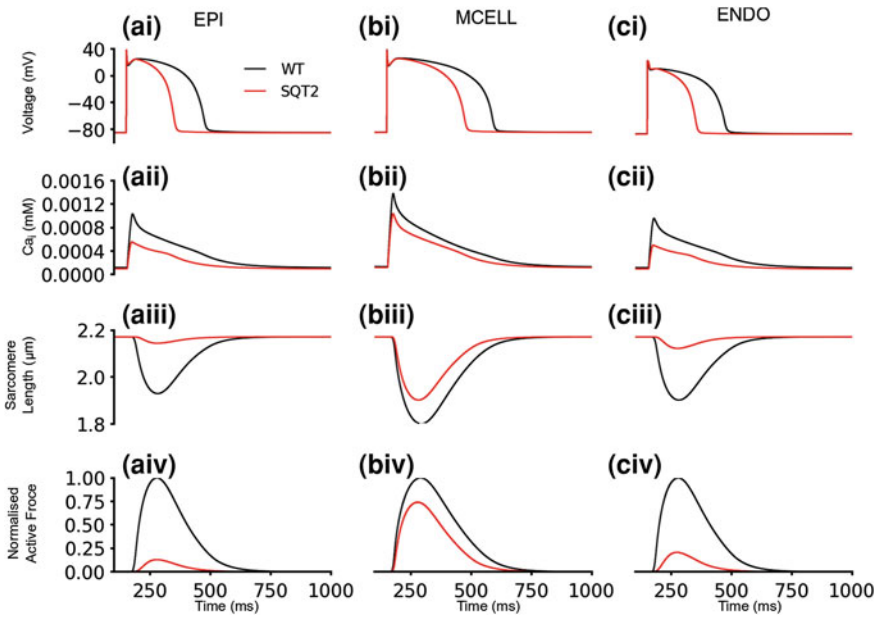

Fig. 9.3 Single cell electromechanical effects of the SQT2 mutation without I_{sac}. (**ai, bi, ci**) WT (*black*) and SQT2 (*red*) action potentials in the EPI (**ai**), MCELL (**bi**) and ENDO (**ci**) cells. (**aii, bii, cii**) WT (*black*) and SQT2 (*red*) calcium concentration in the EPI (**aii**), MCELL (**bii**) and ENDO (**cii**) cells. (**aiii, biii, ciii**) WT (*black*) and SQT2 (*red*) sarcomere length in the EPI (**aiii**), MCELL (**biii**) and ENDO (**ciii**) cells. (**aiv, biv, civ**) WT (*black*) and SQT2 (*red*) normalised active force in the EPI (**aiv**), MCELL (**biv**) and ENDO (**civ**) cells

electromechanically coupled single cell without the stretch-activated current (I_{sac}). The abbreviation of the AP by SQT2 is shown for the different cell types: EPI (Fig. 9.3ai), MCELL (Fig. 9.3bi) and ENDO (Fig. 9.3ci). The difference in shortening between the pure electrophysiology model and the coupled electromechanics model was insignificant in all the cell types (less than 0.01 %, Fig. 9.1).

Compared to WT, the SQT2 mutation reduced the calcium concentration by ∼47 % in EPI (Fig. 9.3aii) and ENDO (Fig. 9.3cii) and by ∼26 % in MCELL (Fig. 9.3bii). The initial sarcomere length for all cell types in both WT and SQT2 was 2.17 μm (Fig. 9.3aiii–ciii). The minimum contracted sarcomere length (SL) in the WT condition was ∼1.92 μm (EPI), ∼1.80 μm (MCELL) and ∼1.89 μm (ENDO). This was reduced with the SQT2 mutation to ∼2.14 μm (EPI), ∼1.89 μm (MCELL) and ∼2.12 μm (ENDO) and is shown in Fig. 9.3aiii–ciii for EPI, MCELL and ENDO respectively. The reduction in the intracellular calcium concentration was accompanied by a consequent reduction in the contractile force compared to WT by ∼87 % in EPI (Fig. 9.3aiv) and ∼79 % in ENDO (Fig. 9.3civ) but was only reduced by ∼26 % in MCELL (Fig. 9.3biv). A summary of these results is shown in Table 9.2.

Table 9.2 Without I_{sac}—Minimal length of contracted sarcomere with the SQT2 mutation and the consequent active force of contraction relative to WT

	Sarcomere length (μM)			Force of contraction (%)		
	EPI	MCELL	ENDO	EPI	MCELL	ENDO
WT	1.92	1.80	1.89	100	100	100
SQT2	2.14	1.89	2.12	13	74	21

Initial sarcomere length is 2.17 μM. The smaller the sarcomere length, the greater is the force of contraction

9.8.3 SQT3

Figure 9.4 shows the effects of the SQT3 mutation on the intracellular Ca^{2+} concentration, the sarcomere length, and the active force development in an electromechanically coupled single cell without the stretch-activated current (I_{sac}). The abbreviation of the AP by SQT3 is shown for the different cell types: EPI (Fig. 9.4ai), MCELL (Fig. 9.4bi) and ENDO (Fig. 9.4ci). The difference in shortening between the pure electrophysiology model and the coupled electromechanics model was insignificant in all the cell types (less than 0.01 %, Fig. 9.1).

Compared to WT, the SQT3 mutation reduced the intracellular calcium concentration by ∼17 % in EPI (Fig. 9.4aii) and ENDO (Fig. 9.4Cii) and by ∼18 % in MCELL (Fig. 9.4bii). The initial sarcomere length for all cell types in both WT and SQT3 was 2.17 μm (Fig. 9.4aiii–ciii). The minimum contracted sarcomere length (SL) in the WT condition was ∼1.92 μm (EPI), ∼1.80 μm (MCELL) and ∼1.89 μm (ENDO). This was reduced with SQT3 mutation to ∼1.99 μm (EPI), ∼1.86 μm (MCELL) and ∼1.96 μm (ENDO) and is shown in Fig. 9.4aiii–ciii for EPI, MCELL and ENDO respectively. The reduction in the intracellular calcium concentration was accompanied by a consequent reduction in the contractile force compared to WT by ∼25 % in EPI (Fig. 9.4aiv), and ∼22 % in ENDO (Fig. 9.4civ) but was only reduced by ∼17 % in MCELL (Fig. 9.4biv). A summary of these results is shown in Table 9.3.

9.8.4 Simulated AP Clamp

The effects of the mutations on contractile force (particularly SQT1 and SQT2) are quite profound (Figs. 9.2, 9.3). A patient with such a severe reduction in contractility would be expected to suffer heart failure and die. In order to gain a mechanistic insight into these large effects on the contractile force, a simulated AP clamp was performed on the WT electromechanics model only (Fig. 9.5). This model (with no changes) was subjected to two different AP waveforms of differing durations—a normal waveform and a shortened waveform (Fig. 9.5a)—in order to observe how these waveforms influence the amplitude of the intracellular Ca^{2+} concentration, the sarcomere length and force of contraction in the WT

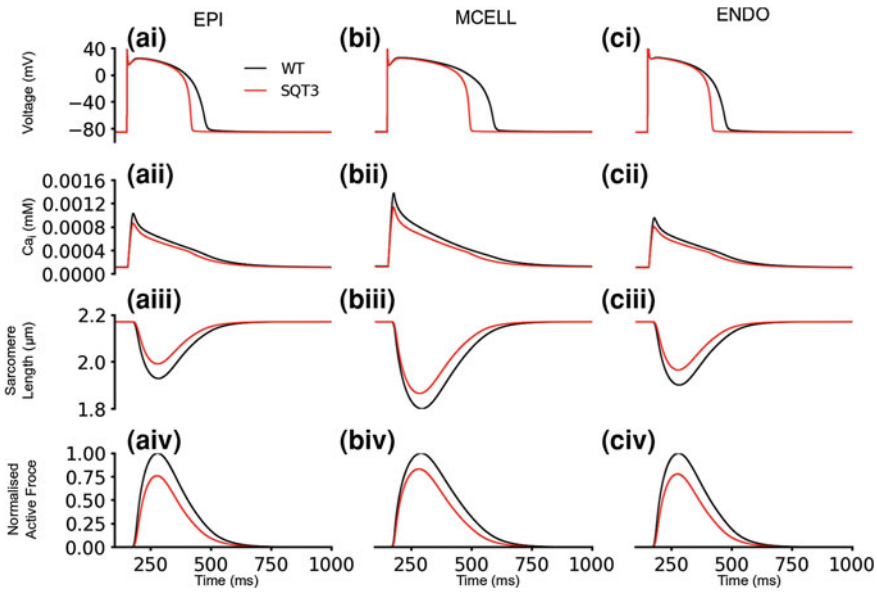

Fig. 9.4 Single cell electromechanical effects of the SQT3 mutation without I_{sac}. (**ai, bi, ci**) WT (*black*) and SQT3 (*red*) action potentials in the EPI (**ai**), MCELL (**bi**) and ENDO (**ci**) cells. (**aii, bii, cii**) WT (*black*) and SQT3 (*red*) calcium concentration in the EPI (**aii**), MCELL (bii) and ENDO (**cii**) cells. (**aiii, biii, ciii**) WT (*black*) and SQT3 (*red*) sarcomere length in the EPI (**aiii**), MCELL (**biii**) and ENDO (**ciii**) cells. (**aiv, biv, civ**) WT (*black*) and SQT3 (*red*) normalised active force in the EPI (**aiv**), MCELL (**biv**) and ENDO (**civ**) cells

Table 9.3 Without I_{sac}—Minimal length of contracted sarcomere with the SQT3 mutation and the consequent active force of contraction relative to WT. Initial sarcomere length is 2.17 μM

	Sarcomere length (μM)			Force of contraction (%)		
	EPI	MCELL	ENDO	EPI	MCELL	ENDO
WT	1.92	1.80	1.89	100	100	100
SQT3	1.99	1.86	1.96	76	83	78

The smaller the sarcomere length, the greater is the force of contraction

electromechanics model. The reasoning was that if on application of the AP waveforms with different durations to the same model under AP clamp, the same profound differences seen in the SQT models are observed, this would imply that the key factor is the effect of AP shortening on Ca^{2+} handling (and on SR content in particular).

Figure 9.5 shows the results of the simulated AP clamp, which shows the same pronounced effects as the SQT models on the intracellular calcium concentration amplitude (Fig. 9.5c), the sarcomere length shortening (Fig. 9.5d) and contractility

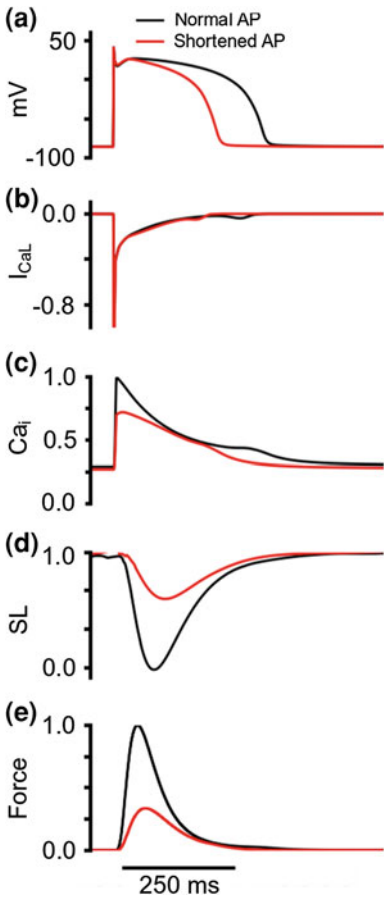

Fig. 9.5 Simulated AP clamp using the WT electromechanics model without I_{sac}. **a** The normal (*black*) and shortened (*red*) AP waveforms applied to the WT electromechanics model. **b** I_{CaL} elicited by the two AP waveforms in (**a**). **c** $[Ca]_i$ elicited by the two AP waveforms in (**a**). **d** SL shortening elicited by the two AP waveforms in (**a**). **e** Contractile force elicited by the two AP waveforms in **a** All units are normalised to the maximum value

(Fig. 9.5e). The peak I_{CaL} is the same with both normal and shortened waveforms (Fig. 9.5b) but with a slight increase in amplitude during terminal repolarisation in the shortened waveform (Fig. 9.5b).

9.9 Single Cell Electromechanical Simulations with I_{sac}

Figure 9.6 shows the effects of incorporating a stretch-activated current into the electromechanics model. It shows three cases; the effects on the WT electromechanics model:

1. without I_{sac}.
2. with I_{sac} and the SACs having relative permeabilities to Na^+, K^+ and Ca^{2+} in the ratio 1:1:1 (P_{Na}:P_K:P_{Ca} = 1:1:1) and
3. with I_{sac} and the SACs having relative permeabilities to Na^+, K^+ and Ca^{2+} in the ratio 1:1:0 (P_{Na}:P_K:P_{Ca} = 1:1:0).

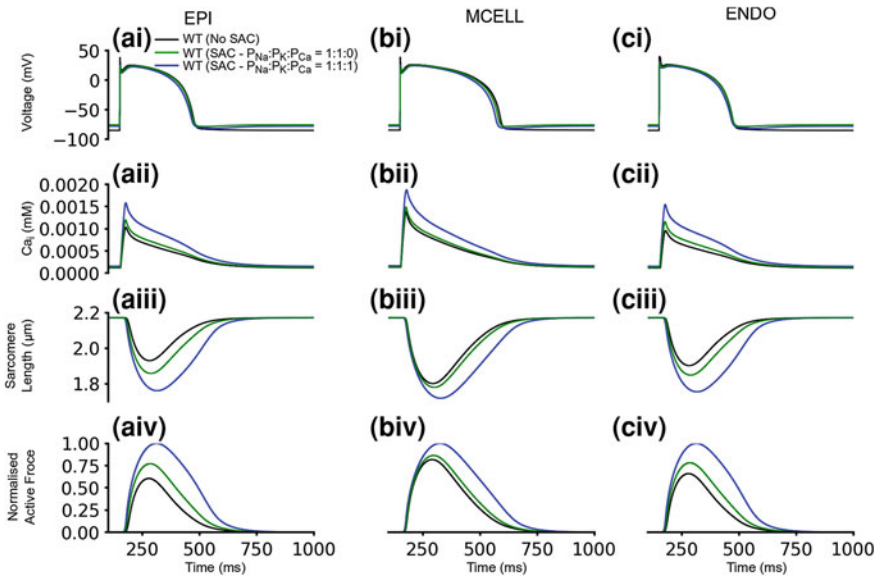

Fig. 9.6 Effects of stretch-activated current (I_{sac}) on the WT electromechanics model. (**ai, bi, ci**) Action potentials in the EPI (**ai**), MCELL (bi) and ENDO (**ci**) cells of WT with no I_{sac} (*black*), WT with I_{sac} (P_{Na}:P_K:P_{Ca} = 1:1:0, *green*) and WT with I_{sac} (P_{Na}:P_K:P_{Ca} = 1:1:1, *blue*). (**aii, bii, cii**) Calcium concentration in the EPI (**aii**), MCELL (**bii**) and ENDO (**cii**) cells of WT with no I_{sac} (*black*), WT with I_{sac} (P_{Na}:P_K:P_{Ca} = 1:1:0, *green*) and WT with I_{sac} (P_{Na}:P_K:P_{Ca} = 1:1:1, *blue*). (**aiii, biii, ciii**) Sarcomere length in the EPI (**aiii**), MCELL (**biii**) and ENDO (**ciii**) cells of WT with no I_{sac} (*black*), WT with I_{sac} (P_{Na}:P_K:P_{Ca} = 1:1:0, *green*) and WT with I_{sac} (P_{Na}:P_K:P_{Ca} = 1:1:1, *blue*). (**aiv, biv, civ**) Normalised active force in the EPI (**aiv**), MCELL (**biv**) and ENDO (**civ**) cells of WT with no I_{sac} (black), WT with I_{sac} (P_{Na}:P_K:P_{Ca} = 1:1:0, *green*) and WT with I_{sac} (P_{Na}:P_K:P_{Ca} = 1:1:1, *blue*)

Across the ventricular wall, the resting potential of EPI (Fig. 9.6ai), MCELL (Fig. 9.6bi) and ENDO (Fig. 9.6ci) increased from −86 mV (WT without I_{sac}) to −76 mV (WT with I_{sac} -P_{Na}:P_K:P_{Ca} = 1:1:0) and to −79 mV (WT with I_{sac} -P_{Na}:P_K:P_{Ca} = 1:1:1). This is an experimentally observed effect of SACs [66, 67].

I_{sac} with both permeability ratios shortened the action potential in EPI (Fig. 9.6ai), MCELL (Fig. 9.6bi) and ENDO (Fig. 9.6ci) with the greater shortening occurring with P_{Na}:P_K:P_{Ca} = 1:1:1. AP shortening is one of the effects that has been observed experimentally with SACs [68–71] (also see Sect. 1.8). AP lengthening has also been observed [72–74]. These changes are thought to be related to the inward Ca^{2+} current and to changes in the Na^+/Ca^{2+} exchanger [13, 75]. I_{sac} with both permeability ratios also increased the amplitude of the intracellular Ca^{2+} concentration (Fig. 9.6aii–cii), the Sarcomere length shortening (Fig. 9.6aiii–cii) and the active force of contraction (Fig. 9.6aiv–civ) [73, 75–81] with the greater lengthening occurring with P_{Na}:P_K:P_{Ca} = 1:1:1. Tables 9.4, 9.5, 9.6 and 9.7 give quantitative comparison of the degree of AP shortening, intracellular

Table 9.4 WT Changes in APD due to I_{sac} at P_{Na}:P_K:P_{Ca} = 1:1:0 and P_{Na}:P_K:P_{Ca} = 1:1:1

	APD (ms)		
	EPI	MCELL	ENDO
WT	317	441	317
WT (I_{sac} P_{Na}:P_K:P_{Ca} = 1:1:0)	310	433	314
WT (I_{sac} P_{Na}:P_K:P_{Ca} = 1:1:1)	306	420	310

Table 9.5 WT changes in Ca_i due to I_{sac} at P_{Na}:P_K:P_{Ca} = 1:1:0 and P_{Na}:P_K:P_{Ca} = 1:1:1

	Ca_i (% WT)		
	EPI	MCELL	ENDO
WT	100	100	100
WT (I_{sac} P_{Na}:P_K:P_{Ca} = 1:1:0)	118	108	122
WT (I_{sac} P_{Na}:P_K:P_{Ca} = 1:1:1)	154	136	164

Table 9.6 WT changes in minimal length of contracted sarcomere due to I_{sac} at P_{Na}:P_K:P_{Ca} = 1:1:0 and P_{Na}:P_K:P_{Ca} = 1:1:1. Initial sarcomere length is 2.17 μM

	SL (μm)		
	EPI	MCELL	ENDO
WT	1.92	1.80	1.89
WT (I_{sac} P_{Na}:P_K:P_{Ca} = 1:1:0)	1.85	1.77	1.84
WT (I_{sac} P_{Na}:P_K:P_{Ca} = 1:1:1)	1.75	1.71	1.75

The smaller the sarcomere length, the greater is the force of contraction

Table 9.7 WT changes in contractile force due to I_{sac} at P_{Na}:P_K:P_{Ca} = 1:1:0 and P_{Na}:P_K:P_{Ca} = 1:1:1

	Force of contraction (%WT)		
	EPI	MCELL	ENDO
WT	100	100	100
WT (I_{sac} P_{Na}:P_K:P_{Ca} = 1:1:0)	126	107	120
WT (I_{sac} P_{Na}:P_K:P_{Ca} = 1:1:1)	167	123	153

calcium concentration amplitude augmentation, greater SL shortening and increased active force respectively. Table 9.8 shows the effects of I_{sac} on the APDs of the SQT1-SQT3 variants with P_{Na}:P_K:P_{Ca} = 1:1:0 and P_{Na}:P_K:P_{Ca} = 1:1:1.

Table 9.8 SQT1, SQT2 and SQT3 changes in APD due to I_{sac} at P_{Na}:P_K:P_{Ca} = 1:1:0 and P_{Na}:P_K:P_{Ca} = 1:1:1

		APD (ms)		
		Without I_{sac}	I_{sac} P_{Na}:P_K:P_{Ca} = 1:1:0	I_{sac} P_{Na}:P_K:P_{Ca} = 1:1:1
SQT1	EPI	212	214	218
	MCELL	232	230	237
	ENDO	211	218	218
SQT2	EPI	233	232	230
	MCELL	355	345	343
	ENDO	234	228	226
SQT3	EPI	283	269	253
	MCELL	382	355	336
	ENDO	284	270	257

9.9.1 SQT1

9.9.1.1 P_{Na}:P_K:P_{Ca} = 1:1:0

Figure 9.7 shows the effects of the SQT1 mutation on the intracellular Ca^{2+} concentration, the sarcomere length and the active force development in an electromechanically coupled single cell with the stretch-activated current (I_{sac}) at a relative permeability ratio to Na^+, K^+ and Ca^{2+} of 1:1:0. Both the WT and SQT1 electromechanics models used this permeability ratio. The abbreviation of the AP by SQT1 is shown for the different cell types: EPI (Fig. 9.7ai), MCELL (Fig. 9.7bi) and ENDO (Fig. 9.7ci).

Compared to WT, the SQT1 mutation reduced the intracellular calcium concentration by ~31 % in EPI (Fig. 9.7aii) and ENDO (Fig. 9.7cii) and by ~39 % in MCELL (Fig. 9.7bii). The initial sarcomere length for all cell types in both WT and SQT1 was 2.17 μm (Fig. 9.7aiii–ciii). The minimum contracted sarcomere length (SL) in the WT condition was ~1.85 μm (EPI), ~1.77 μm (MCELL) and ~1.84 μm (ENDO). This was reduced by the SQT1 mutation to ~1.97 μm (EPI), ~1.93 μm (MCELL) and ~1.97 μm (ENDO). This is shown in Fig. 9.7-aiii–ciii for EPI, MCELL and ENDO respectively. The reduction in the intracellular calcium concentration was accompanied by a consequent reduction in the contractile force compared to WT by ~40 % in EPI (Fig. 9.7aiv), ~39 % in MCELL (Fig. 9.7biv) and ~36 % in ENDO (Fig. 9.7civ). A summary of these results is shown in Table 9.9.

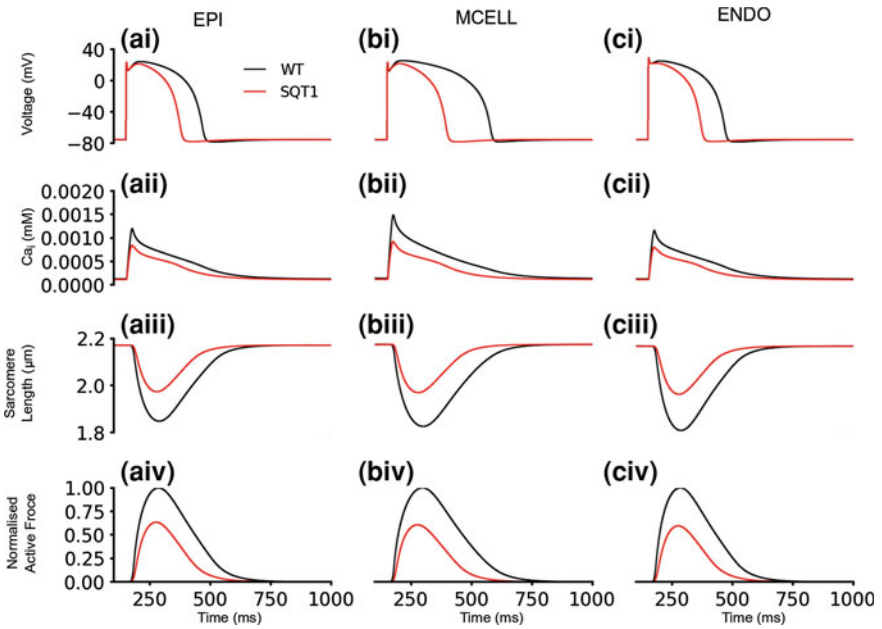

Fig. 9.7 Single cell electromechanical effects of the SQT1 mutation with I_{sac} at P_{Na}:P_K:P_{Ca} = 1:1:0. (**ai, bi, ci**) WT (*black*) and SQT1 (*red*) action potentials in the EPI (**ai**), MCELL (**bi**) and ENDO (**ci**) cells. (**aii, bii, cii**) WT (*black*) and SQT1 (**red**) calcium concentration in the EPI (**aii**), MCELL (**bii**) and ENDO (**cii**) cells. (**aiii, biii, ciii**) WT (*black*) and SQT1 (*red*) sarcomere length in the EPI (**aiii**), MCELL (**biii**) and ENDO (**ciii**) cells. (**aiv, biv, civ**) WT (*black*) and SQT1 (*red*) normalised active force in the EPI (**aiv**), MCELL (**biv**) and ENDO (**civ**) cells

Table 9.9 SQT1 (I_{sac} at P_{Na}:P_K:P_{Ca} = 1:1:0)—minimal length of contracted sarcomere with the SQT1 mutation and the consequent active force of contraction relative to WT

	SL (μm)		
	EPI	MCELL	ENDO
WT (I_{sac} P_{Na}:P_K:P_{Ca} = 1:1:0)	1.85	1.77	1.84
SQT1 (I_{sac} P_{Na}:P_K:P_{Ca} = 1:1:0)	1.97	1.93	1.97
	Force of Contraction (%WT)		
WT (I_{sac} P_{Na}:P_K:P_{Ca} = 1:1:0)	100	100	100
SQT1 (I_{sac} P_{Na}:P_K:P_{Ca} = 1:1:0)	60	61	64

Initial sarcomere length is 2.17 μM. The smaller the sarcomere length, the greater is the force of contraction

9.9.1.2 P_{Na}:P_K:P_{Ca} = 1:1:1

Figure 9.8 shows the effects of the SQT1 mutation on the intracellular Ca^{2+} concentration, the sarcomere length and the active force development in an

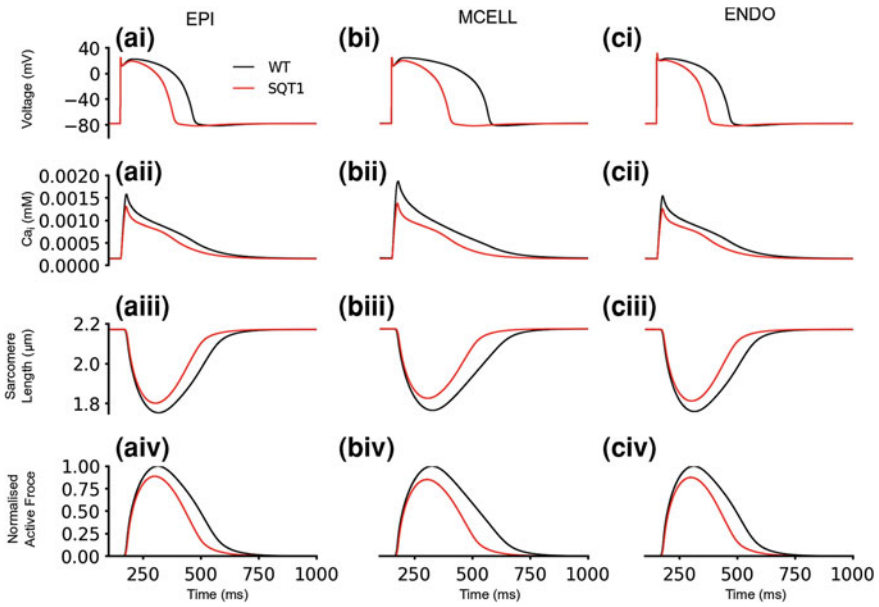

Fig. 9.8 Single cell electromechanical effects of the SQT1 mutation with I_{sac} at P_{Na}:P_K:P_{Ca} = 1:1:1. (**ai, bi, ci**) WT (*black*) and SQT1 (*red*) action potentials in the EPI (**ai**), MCELL (**bi**) and ENDO (**ci**) cells. (**aii, bii, cii**) WT (*black*) and SQT1 (*red*) calcium concentration in the EPI (**aii**), MCELL (**Bii**) and ENDO (**cii**) cells. (**aiii, biii, ciii**) WT (*black*) and SQT1 (*red*) sarcomere length in the EPI (**aiii**), MCELL (**biii**) and ENDO (**ciii**) cells. (**aiv, biv, civ**) WT (*black*) and SQT1 (*red*) normalised active force in the EPI (**aiv**), MCELL (**biv**) and ENDO (**civ**) cells

electromechanically coupled single cell with the stretch-activated current (I_{sac}) and relative permeability ratio to Na^+, K^+ and Ca^{2+} of 1:1:1. Both the WT and SQT1 electromechanics models used this permeability ratio. The abbreviation of the AP by SQT1 is shown for the different cell types: EPI (Fig. 9.8ai), MCELL (Fig. 9.8bi) and ENDO (Fig. 9.8ci).

Compared to WT, the SQT1 mutation reduced the intracellular calcium concentration by ∼16 % in EPI (Fig. 9.8aii) and ENDO (Fig. 9.8cii) and by ∼25 % in MCELL (Fig. 9.8bii). The initial sarcomere length for all cell types in both WT and SQT1 was 2.17 μm (Fig. 9.8aiii–ciii). The minimum contracted sarcomere length (SL) in the WT condition was ∼1.75 μm (EPI), ∼1.71 μm (MCELL) and ∼1.75 μm (ENDO). This was reduced by the SQT1 mutation to ∼1.81 μm (EPI), ∼1.78 μm (MCELL) and ∼1.80 μm (ENDO). This is shown in Fig. 9.8aiii–ciii for EPI, MCELL and ENDO respectively. The reduction in the intracellular calcium concentration was accompanied by a consequent reduction in the contractile force compared to WT by ∼13 % in EPI (Fig. 9.8aiv), ∼15% in MCELL (Fig. 9.8biv) and ∼11 % in ENDO (Fig. 9.8civ). A summary of these results is shown in Table 9.10.

Table 9.10 SQT1 (I_{sac} at P_{Na}:P_K:P_{Ca} = 1:1:1)—minimal length of contracted sarcomere with the SQT1 mutation and the consequent active force of contraction relative to WT

	SL (μm)		
	EPI	MCELL	ENDO
WT (I_{sac} P_{Na}:P_K:P_{Ca} = 1:1:1)	1.75	1.71	1.75
SQT1 ($I_{sac}P_{Na}$:P_K:P_{Ca} = 1:1:1)	1.81	1.78	1.80
	Force of Contraction (%WT)		
WT ($I_{sac}P_{Na}$:P_K:P_{Ca} = 1:1:1)	100	100	100
SQT1 ($I_{sac}P_{Na}$:P_K:P_{Ca} = 1:1:1)	87	85	89

Initial sarcomere length is 2.17 μM. The smaller the sarcomere length, the greater is the force of contraction

9.9.2 SQT2

9.9.2.1 P_{Na}:P_K:P_{Ca} = 1:1:0

Figure 9.9 shows the effects of the SQT2 mutation on the intracellular Ca^{2+} concentration, the sarcomere length and the active force development in an electromechanically coupled single cell with the stretch-activated current (I_{sac}) and relative permeability ratio to Na^+, K^+ and Ca^{2+} of 1:1:0. Both the WT and SQT2 electromechanics models used this permeability ratio. The abbreviation of the AP by SQT2 is shown for the different cell types: EPI (Fig. 9.9ai), MCELL (Fig. 9.9bi) and ENDO (Fig. 9.9ci).

Compared to WT, the SQT2 mutation reduced the intracellular calcium concentration by ~42 % in EPI (Fig. 9.9aii) and ENDO (Fig. 9.9cii) and by ~21 % in MCELL (Fig. 9.9bii). The initial sarcomere length for all cell types in both WT and SQT2 was 2.17 μm (Fig. 9.9aiii–ciii). The minimum contracted sarcomere length (SL) in the WT condition was ~1.85 μm (EPI), ~1.77 μm (MCELL) and ~1.84 μm (ENDO). This was reduced by the SQT2 mutation to ~2.04 μm (EPI), ~1.85 μm (MCELL) and ~2.05 μm (ENDO). This is shown in Fig. 9.9aiii–ciii for EPI, MCELL and ENDO respectively. The reduction in the intracellular calcium concentration was accompanied by a consequent reduction in the contractile force compared to WT by ~57 % in EPI (Fig. 9.9aiv), ~18 % in MCELL (Fig. 9.9biv) and ~60 % in ENDO (Fig. 9.9civ). A summary of these results is shown in Table 9.11.

9.9.2.2 P_{Na}:P_K:P_{Ca} = 1:1:1

Figure 9.10 shows the effects of the SQT2 mutation on the intracellular Ca^{2+} concentration, the sarcomere length and the active force development in an electromechanically coupled single cell with the stretch-activated current (I_{sac}) and relative permeability ratio to Na^+, K^+ and Ca^{2+} of 1:1:1. Both the WT and SQT2

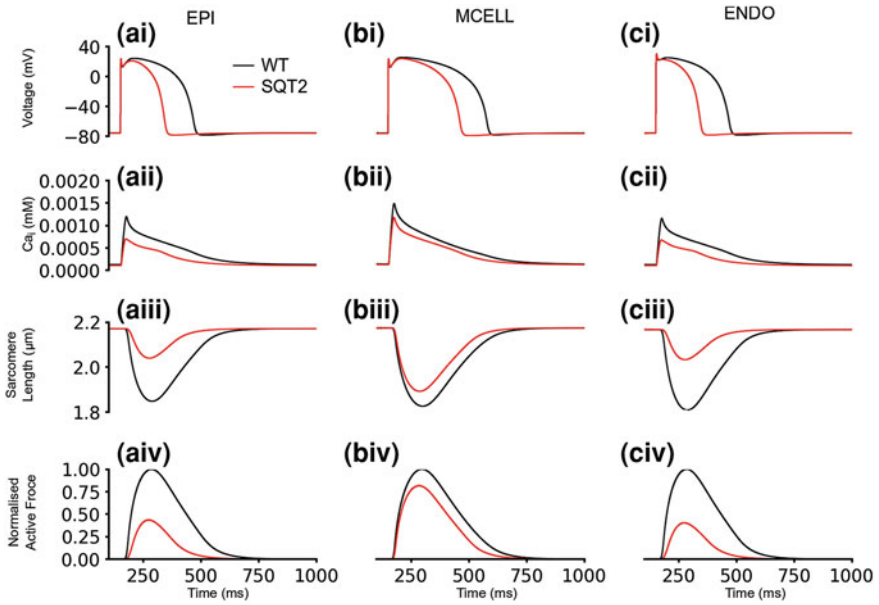

Fig. 9.9 Single cell electromechanical effects of the SQT2 mutation with I_{sac} at P_{Na}:P_K:P_{Ca} = 1:1:0. (**ai, bi, ci**) WT (*black*) and SQT2 (*red*) action potentials in the EPI (**ai**), MCELL (bi) and ENDO (**ci**) cells. (**aii, bii, cii**) WT (*black*) and SQT2 (*red*) calcium concentration in the EPI (**aii**), MCELL (**bii**) and ENDO (**cii**) cells. (**aiii, biii, ciii**) WT (*black*) and SQT2 (*red*) sarcomere length in the EPI (**aiii**), MCELL (**biii**) and ENDO (**ciii**) cells. (**aiv, biv, civ**) WT (*black*) and SQT2 (*red*) normalised active force in the EPI (**aiv**), MCELL (**biv**) and ENDO (**civ**) cells

Table 9.11 SQT2 (I_{sac} at P_{Na}:P_K:P_{Ca} = 1:1:0)—minimal length of contracted sarcomere with the SQT2 mutation and the consequent active force of contraction relative to WT

	SL (μm)		
	EPI	MCELL	ENDO
WT (I_{sac} P_{Na}:P_K:P_{Ca} = 1:1:0)	1.85	1.77	1.84
SQT2 (I_{sac} P_{Na}:P_K:P_{Ca} = 1:1:0)	2.04	1.85	2.05
	Force of contraction (%WT)		
WT (I_{sac} P_{Na}:P_K:P_{Ca} = 1:1:0)	100	100	100
SQT2 (I_{sac} P_{Na}:P_K:P_{Ca} = 1:1:0)	43	82	40

Initial sarcomere length is 2.17 μM. The smaller the sarcomere length, the greater is the force of contraction

electromechanics models used this permeability ratio. The abbreviation of the AP by SQT2 is shown for the different cell types: EPI (Fig. 9.10ai), MCELL (Fig. 9.10bi) and ENDO (Fig. 9.10ci).

Compared to WT, the SQT2 mutation reduced the intracellular calcium concentration by ∼25% in EPI (Fig. 9.10aii) and ENDO (Fig. 9.10cii) and

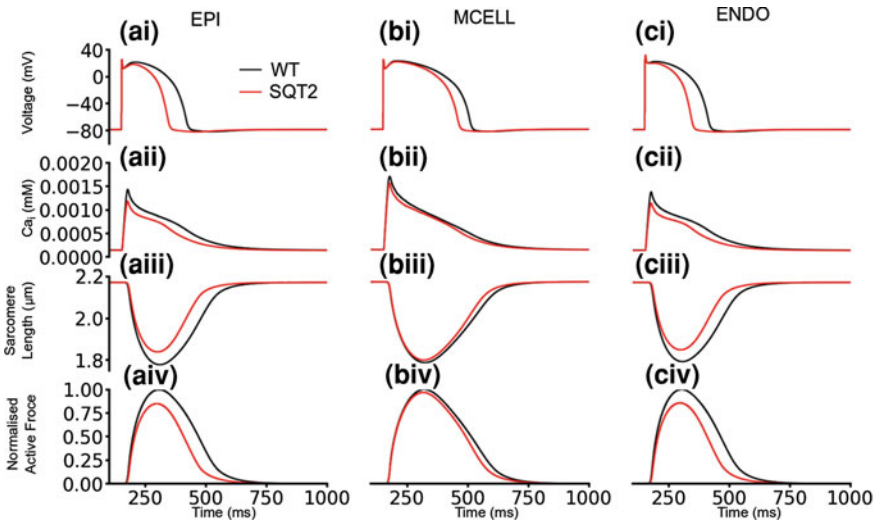

Fig. 9.10 Single cell electromechanical effects of the SQT2 mutation with I_{sac} at P_{Na}:P_K:P_{Ca} = 1:1:1. (**ai, bi, ci**) WT (*black*) and SQT2 (*red*) action potentials in the EPI (**ai**), MCELL (**bi**) and ENDO (**ci**) cells. (**aii, bii, Cii**) WT (*black*) and SQT2 (*red*) calcium concentration in the EPI (**aii**), MCELL (**bii**) and ENDO (**cii**) cells. (**aiii, biii, ciii**) WT (*black*) and SQT2 (*red*) sarcomere length in the EPI (**aiii**), MCELL (**biii**) and ENDO (**ciii**) cells. (**aiv,biv,civ**) WT (*black*) and SQT2 (*red*) normalised active force in the EPI (**aiv**), MCELL (**biv**) and ENDO (**civ**) cells

Table 9.12 SQT2 (I_{sac} at P_{Na}:P_K:P_{Ca} = 1:1:1)—minimal length of contracted sarcomere with the SQT2 mutation and the consequent active force of contraction relative to WT

	SL (μm)		
	EPI	MCELL	ENDO
WT (I_{sac} P_{Na}:P_K:P_{Ca} = 1:1:1)	1.75	1.71	1.75
SQT2 ($I_{sac}P_{Na}$:P_K:P_{Ca} = 1:1:1)	1.84	1.75	1.84
	Force of contraction (%WT)		
WT ($I_{sac}P_{Na}$:P_K:P_{Ca} = 1:1:1)	100	100	100
SQT2 ($I_{sac}P_{Na}$:P_K:P_{Ca} = 1:1:1)	79	91	80

Initial sarcomere length is 2.17 μM. The smaller the sarcomere length, the greater is the force of contraction

by ∼17 % in MCELL (Fig. 9.10bii). The initial sarcomere length for all cell types in both WT and SQT2 was 2.17 μm (Fig. 9.10aiii–ciii). The minimum contracted sarcomere length (SL) in the WT condition was ∼1.75 μm (EPI), ∼1.71 μm (MCELL) and ∼1.75 μm (ENDO). This was reduced by the SQT2 mutation to ∼1.84 μm (EPI), ∼1.75 μm (MCELL) and ∼1.84 μm (ENDO). This is shown in Fig. 9.10aiii–ciii for EPI, MCELL and ENDO respectively. The reduction in the intracellular calcium concentration was accompanied by a consequent

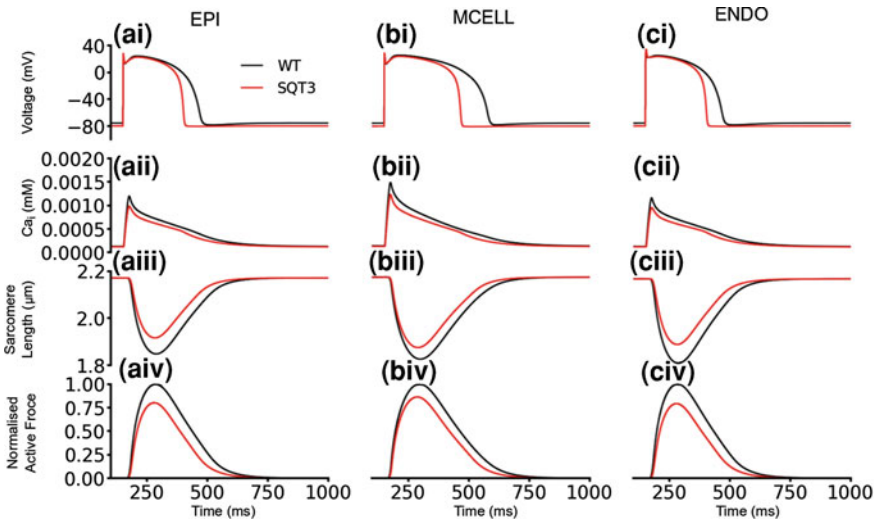

Fig. 9.11 Single cell electromechanical effects of the SQT3 mutation with I_{sac} at P_{Na}:P_K:P_{Ca} = 1:1:0. (**ai, bi, ci**) WT (*black*) and SQT3 (*red*) action potentials in the EPI (**ai**), MCELL (**bi**) and ENDO (**ci**) cells. (**aii, bii, cii**) WT (*black*) and SQT3 (red) calcium concentration in the EPI (**aii**), MCELL (**bii**) and ENDO (**cii**) cells. (**aiii, biii, ciii**) WT (*black*) and SQT3 (*red*) sarcomere length in the EPI (**aiii**), MCELL (**biii**) and ENDO (**ciii**) cells. (**aiv, biv, civ**) WT (*black*) and SQT3 (*red*) normalised active force in the EPI (**aiv**), MCELL (**biv**) and ENDO (**civ**) cells

reduction in the contractile force compared to WT by ∼21 % in EPI (Fig. 9.10aiv), ∼9 % in MCELL (Fig. 9.10biv) and ∼20 % in ENDO (Fig. 9.10civ). A summary of these results is shown in Table 9.12.

9.9.3 SQT3

9.9.3.1 P_{Na}:P_K:P_{Ca} = 1:1:0

Figure 9.11 shows the effects of the SQT3 mutation on the intracellular Ca^{2+} concentration, the sarcomere length and the active force development in an electromechanically coupled single cell with the stretch-activated current (I_{sac}) and relative permeability ratio to Na^+, K^+ and Ca^{2+} of 1:1:0. Both the WT and SQT3 electromechanics models used this permeability ratio. The abbreviation of the AP by SQT3 is shown for the different cell types: EPI (Fig. 9.11ai), MCELL (Fig. 9.11bi) and ENDO (Fig. 9.11ci).

Compared to WT, the SQT3 mutation reduced the intracellular calcium concentration by ∼19 % in EPI (Fig. 9.11aii), ENDO (Fig. 9.11cii) and MCELL (Fig. 9.11bii). The initial sarcomere length for all cell types in both WT and SQT3 was 2.17 μm (Fig. 9.11aiii–ciii). The minimum contracted sarcomere length (SL)

Table 9.13 SQT3 (I_{sac} at P_{Na}:P_K:P_{Ca} = 1:1:0)—minimal length of contracted sarcomere with the SQT3 mutation and the consequent active force of contraction relative to WT

	SL (μm)		
	EPI	MCELL	ENDO
WT (I_{sac} P_{Na}:P_K:P_{Ca} = 1:1:0)	1.85	1.77	1.84
SQT3 (I_{sac} P_{Na}:P_K:P_{Ca} = 1:1:0)	1.91	1.83	1.92
	Force of contraction (%WT)		
WT (I_{sac} P_{Na}:P_K:P_{Ca} = 1:1:0)	100	100	100
SQT3 (I_{sac} P_{Na}:P_K:P_{Ca} = 1:1:0)	80	86	79

Initial sarcomere length is 2.17 μM. The smaller the sarcomere length, the greater is the force of contraction

in the WT condition was ~ 1.85 μm (EPI), ~ 1.77 μm (MCELL) and ~ 1.84 μm (ENDO). This was reduced by the SQT3 mutation to ~ 1.91 μm (EPI), ~ 1.83 μm (MCELL) and ~ 1.92 μm (ENDO). This is shown in Fig. 9.11aiii–ciii for EPI, MCELL and ENDO respectively. The reduction in the intracellular calcium concentration was accompanied by a consequent reduction in the contractile force compared to WT by ~ 20 % in EPI

(Figure 9.11aiv), ~14 % in MCELL (Fig. 9.11biv) and ~21 % in ENDO (Fig. 9.11civ). A summary of these results is shown in Table 9.13.

9.9.3.2 P_{Na}:P_K:P_{Ca} = 1:1:1

Figure 9.12 shows the effects of the SQT3 mutation on the intracellular Ca^{2+} concentration, the sarcomere length and the active force development in an electromechanically coupled single cell with the stretch-activated current (I_{sac}) and relative permeability ratio to Na^+, K^+ and Ca^{2+} of 1:1:1. Both the WT and SQT3 electromechanics models used this permeability ratio. The abbreviation of the AP by SQT3 is shown for the different cell types: EPI (Fig. 9.12ai), MCELL (Fig. 9.12bi) and ENDO (Fig. 9.12ci).

Compared to WT, the SQT3 mutation reduced the intracellular calcium concentration by ~13 % in EPI (Fig. 9.12aii) and ENDO (Fig. 9.12cii) and by ~17 % in MCELL (Fig. 9.12bii). The initial sarcomere length for all cell types in both WT and SQT3 was 2.17 μm (Fig. 9.12aiii–ciii). The minimum contracted sarcomere length (SL) in the WT condition was ~1.75 μm (EPI), ~1.71 μm (MCELL) and ~1.75 μm (ENDO). This was reduced by the SQT3 mutation to ~1.78 μm (EPI), ~1.75 μm (MCELL) and ~1.79 μm (ENDO). This is shown in Fig. 9.12aiii–ciii for EPI, MCELL and ENDO respectively. The reduction in the intracellular calcium concentration was accompanied by a consequent reduction in the contractile force compared to WT by ~8 % in EPI (Fig. 9.12aiv), MCELL (Fig. 9.12biv) and ENDO (Fig. 9.12civ). A summary of these results is shown in Table 9.14.

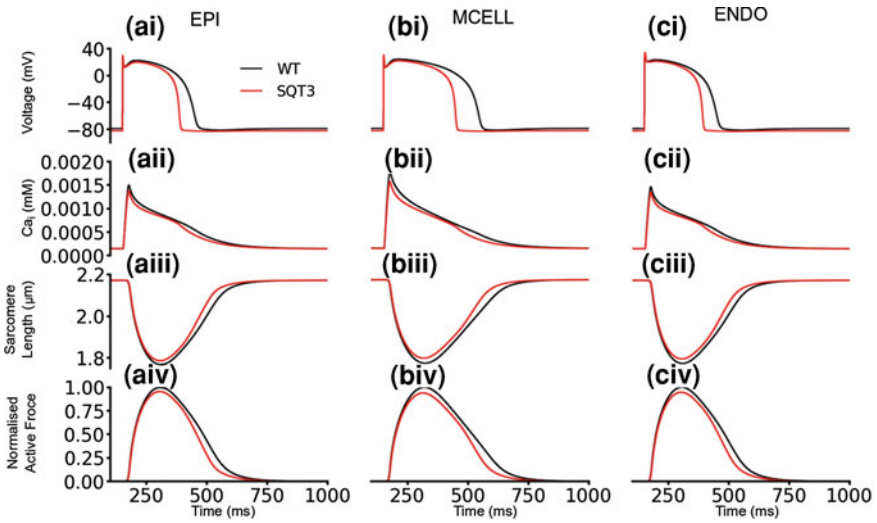

Fig. 9.12 Single cell electromechanical effects of the SQT3 mutation with I_{sac} at P_{Na}:P_K:P_{Ca} = 1:1:1. (**ai, bi, ci**) WT (*black*) and SQT3 (*red*) action potentials in the EPI (**ai**), MCELL (**bi**) and ENDO (**ci**) cells. (**aii, bii, cii**) WT (*black*) and SQT3 (*red*) calcium concentration in the EPI (**aii**), MCELL (**bii**) and ENDO (**cii**) cells. (**aiii, biii, ciii**) WT (*black*) and SQT3 (*red*) sarcomere length in the EPI (**aiii**), MCELL (**biii**) and ENDO (**ciii**) cells. (**aiv, biv, civ**) WT (*black*) and SQT3 (*red*) normalised active force in the EPI (**aiv**), MCELL (**biv**) and ENDO (**civ**) cells

Table 9.14 SQT3 (I_{sac} at P_{Na}:P_K:P_{Ca} = 1:1:1)—minimal length of contracted sarcomere with the SQT3 mutation and the consequent active force of contraction relative to WT

	SL (μm)		
	EPI	MCELL	ENDO
WT (I_{sac} P_{Na}:P_K:P_{Ca} = 1:1:1)	1.75	1.71	1.75
SQT3 ($I_{sac}P_{Na}$:P_K:P_{Ca} = 1:1:1)	1.78	1.75	1.79
	Force of contraction (%WT)		
WT ($I_{sac}P_{Na}$:P_K:P_{Ca} = 1:1:1)	100	100	100
SQT3 ($I_{sac}P_{Na}$:P_K:P_{Ca} = 1:1:1)	92	92	92

Initial sarcomere length is 2.17 μM. The smaller the sarcomere length, the greater is the force of contraction

9.10 Tissue Simulations

Figure 9.13 shows the results of the electromechanical simulations in an idealised, transmural 2D sheet of the left ventricle for the WT, SQT1, SQT2 and SQT3 conditions without I_{sac} while Fig. 9.14 shows simulations with I_{sac} present. The 2D

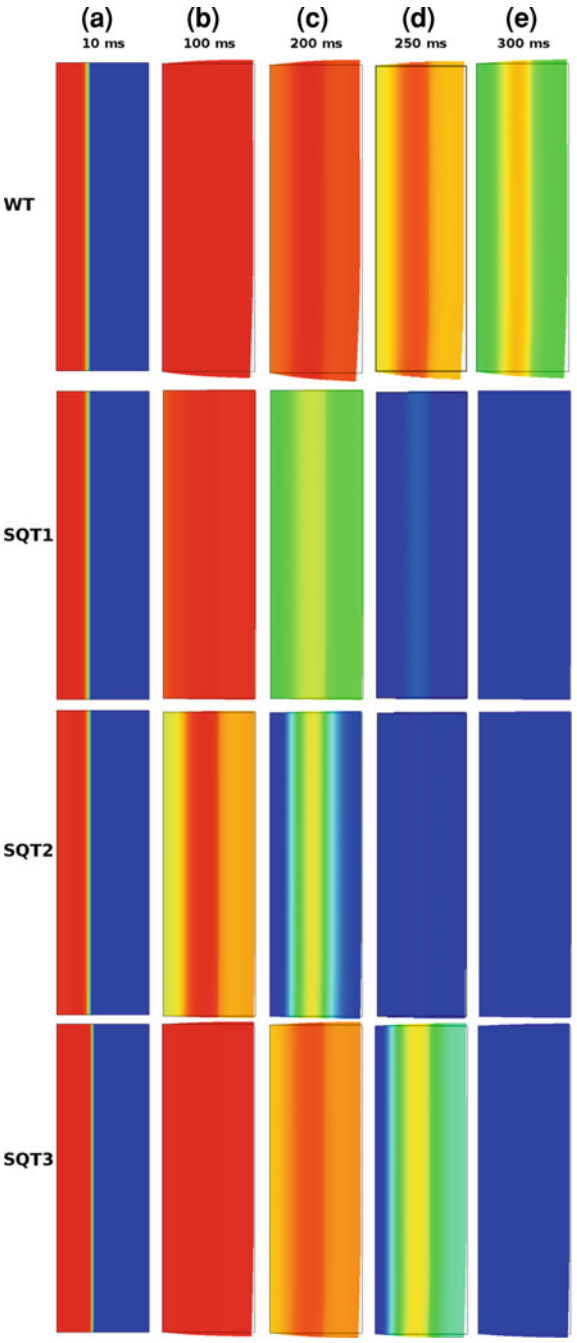

Fig. 9.13 Electromechanical coupling in 2D ventricular tissue under the SQTS mutations (Results without stretch-activated current, I_{sac}). Snapshots of tissue deformation induced by the superimposed electrical wave propagation in *WT*, *SQT1*, *SQT2* and *SQT3* at 10 ms (**a**), 100 ms (**b**), 200 ms (**c**), 250 ms (**d**) and 300 ms (**e**)

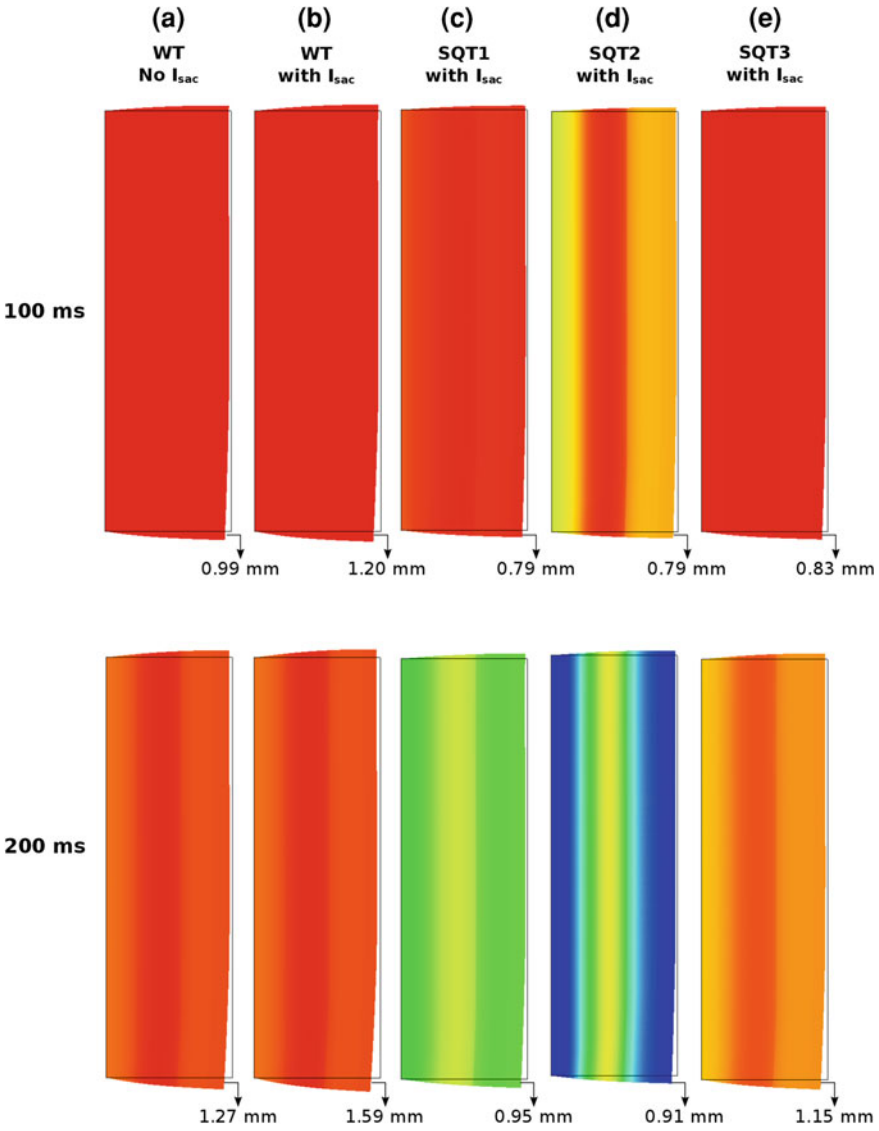

Fig. 9.14 Electromechanical coupling in 2D ventricular tissue under the SQTS mutations with stretch-activated current, I_{sac}. Snapshots of tissue deformation induced by the superimposed electrical wave propagation at 100 and 200 ms in WT without I_{sac} (**a**), WT with I_{sac} (**b**), SQT1 with I_{sac} (**c**), SQT2 with I_{sac} (**d**) and SQT3 with I_{sac} (**e**). The vertical displacement of the node in the *bottom right-hand corner* of the undeformed sheet is depicted with *arrows*

mesh is fixed along the left edge (X = 0) in order to avoid rigid body rotation while the unrestricted edges are free to move and have no externally applied force. In a realistic setting, the fixed edge would move in tandem with the ventricular wall.

The 2D simulations show the electrical wave propagation in the electrophysiology mesh on which is superimposed the mechanics mesh showing deformations induced by the active tension calculated from the electrical wave propagation at 10 ms (Fig. 9.13a), 100 ms (Fig. 9.13b), 200 ms (Fig. 9.13c), 250 ms (Fig. 9.13d) and 300 ms (Fig. 9.13e). The 2D simulations without I_{sac} (Fig. 9.13) reflect the results in the single cell simulations without I_{sac} (Figs. 9.2, 9.3 and 9.4). The stimulus (applied along the left edge of the sheet, X = 0) initiated electrical propagation from the ENDO end towards the EPI end of the sheet (Fig. 9.13a), and induced deformation of the sheet (Fig. 9.13b–e). The induced deformation was strongest for the WT condition (Fig. 9.13b–e, top row) but there was extremely weak deformation in SQT1 (Fig. 9.13, second row) and SQT2 (Fig. 9.13, third row) and some degree of deformation in SQT3 (Fig. 9.13, bottom row). In addition, by 300 ms, repolarisation was complete in SQT1 and SQT2 (Fig. 9.13e) but was still in progress in WT and SQT3 (Fig. 9.13e) due to their longer APDs compared to SQT1 and SQT2.

As the contractile function in SQT patients does not significantly differ from that of control patients [82, 83], the 2D simulations with I_{sac} incorporated were performed with the relative permeability ratio P_{Na}:P_K:P_{Ca} = 1:1:1 as it had the greater contractile force in the single cell compared to P_{Na}:P_K:P_{Ca} = 1:1:0 (Figs. 9.7, 9.8, 9.9, 9.10, 9.11, 9.12 and Tables 9.9, 9.10, 9.11, 9.12, 9.13 and 9.14).

Figure 9.14 shows the effects on tissue deformation with the addition of I_{sac} to the electromechanics models. There is deformation in all the conditions (Fig. 9.14a–e). The vertical displacement of the node at the bottom right-hand corner of the undeformed sheet under all the conditions is indicated with an arrow. At 100 ms, under the WT condition without I_{sac}, this node was displaced by 0.99 mm but was displaced by 1.20 mm with the incorporation of I_{sac}. In the SQT electromechanics models with the incorporation of I_{sac}, the node was displaced by 0.79 mm (SQT1), 0.79 mm (SQT2) and 0.83 mm (SQT3) at 100 ms. At 200 ms, under the WT condition without I_{sac}, the node was displaced by 1.27 mm but was displaced by 1.59 mm with the incorporation of I_{sac}. In the SQT electromechanics models with the incorporation of I_{sac}, the node was displaced by 0.95 mm (SQT1), 0.91 mm (SQT2) and 1.15 mm (SQT3) at 200 ms. This results also reflect the single cell electromechanics simulations with I_{sac} incorporated at a relative permeability ratio P_{Na}:P_K:P_{Ca} = 1:1:1 (Figs. 9.8, 9.10 and 9.12).

9.11 Discussion

9.11.1 Simulations without $\mathbf{I_{sac}}$

Associated with the contraction of the sarcomere is the generated (active) force of contraction. In the single cell simulations without consideration of I_{sac}, this was

severely impaired in the SQT1 and SQT2 mutations. The force generated was only 30 % in EPI, 44 % in MCELL and 41 % in ENDO in the SQT1 condition. It was only 13 % in EPI, 74 % in MCELL and 21 % in ENDO in the SQT2 condition. The greater force in the MCELL under both conditions is due to its longer APD compared to EPI and ENDO cells. This profound reduction in contractile force is very severe and in a real heart would probably lead to heart failure, instant collapse and death of the patient. The situation was more favourable with the SQT3 mutation. The force of contraction was 76 % in EPI, 83 % in MCELL and 78 % in ENDO. This is because SQT3 acts during terminal repolarisation and thus has longer APDs across the ventricular wall compared to SQT1 and SQT2. A key question that arises is how these modelled changes relate to the real situation in SQTS patients?

At present, there are few experimental data on the effects of the SQTS on ventricular mechanical contraction with which to validate and compare the above findings. Gaita et al. [84] performed echocardiography, cardiac MRI and stress tests on the two families in which the SQTS was first reported [84] and found no structural abnormalities. In a 70 year male patient with the SQT2 mutation, Bellocq et al. [85] also found no structural abnormalities. Tests performed on this patient, including echocardiography, exercise testing, coronary angiography, left and right ventricular angiography, scintigraphy, and ergonovine coronary spasm test showed no abnormalities. In addition, ejection fraction from the left ventricle was 49 % [85].

Of particular significance is the finding by Schimpf et al. [83], who in their study to determine whether abbreviation of cardiac repolarisation altered mechanical function in the SQTS found that both SQTS patients and control subjects had no significant differences in end systolic, end diastolic volume and ejection fraction. This particularly calls into question, the severe reduction in contractility in the SQT1 and SQT2 electromechanical simulation results without the incorporation of I_{sac} (Fig. 9.2aiv–civ, Fig. 9.3aiv–civ and Fig. 9.13). Nevertheless, the SQTS is characterised by an increased risk of sudden death [84, 86–89].

Simulated AP clamp experiments in which the WT electromechanics model (without I_{sac}) was subjected to AP waveforms of different durations (normal and shortened) provided a mechanistic insight into the reason for the profound reduction and effects on contractility. It showed AP shortening to be intrinsically linked to contractile force and hence calcium binding to troponin (which seems to be impaired). Therefore, a possible explanation is that under the SQTS, the severely reduced contractility is most likely due to reduced SR Ca^{2+} loading. AP shortening alters currents and dynamics and provides less time for SR Ca^{2+} loading and therefore SR Ca^{2+} content may be compromised. There would then be reduced SR Ca^{2+} for release and consequently reduced contraction. Thus, calcium binding to the troponin-tropomyosin complex becomes defective, insufficient active ADP sites are uncovered, which in turn affects cross-bridge binding by the myosin filaments to the actin filaments. Consequently, the power stroke required to generate the contraction of the sarcomere becomes weakened.

9.11.2 Simulations with $\mathbf{I_{sac}}$

The coupling of electrical and mechanical activity in the heart is an active area of research and an important mechanism of electromechanical coupling is the presence of cardiac ion channels activated by mechanical stimuli such as changes in cell volume or cell stretch [3–7]. Consequently, a non-selective cationic stretch-activated current (I_{sac}) was incorporated into the electromechanics models. The stretch-activated channel was assumed to be permeable to Na^+, K^+ and Ca^{2+}. Two relative permeability cases were considered: P_{Na}:P_K:P_{Ca} = 1:1:0 and P_{Na}:P_K:P_{Ca} = 1:1:1.

Incorporation of I_{sac} with both permeability ratios resulted in increased amplitude of the intracellular Ca^{2+}, increased shortening of the sarcomere length and consequently greater contractile force under all the conditions; WT, SQT1, SQT2, SQT3 (Tables 9.6, 9.7, 9.9, 9.10, 9.11, 9.12, 9.13 and 9.14). These effects are similar to those reported experimentally [75, 82–85]. Permeability ratio P_{Na}:P_K:P_{Ca} = 1:1:1 had the greater effect on these features. With I_{sac} in the electromechanics models, the contractile force under the SQT variants increased considerably particularly with permeability ratio P_{Na}:P_K:P_{Ca} = 1:1:1; SQT1 (87 % in EPI (from 30 % without I_{sac}), 85 % in MCELL (from 44 % without I_{sac}) and 89 % in ENDO (from 41 % without I_{sac})—Table 9.10). Under the SQT2 condition, the contractile force was 79 % in EPI (from 13 % without I_{sac}), 91 % in MCELL (from 74 % without I_{sac}) and 80 % in ENDO (from 21 % without I_{sac})—Table 9.12). Under the SQT3 condition, the contractile force was 92 % in EPI (from 76 % without I_{sac}), 92 % in MCELL (from 83 % without I_{sac}) and 92 % in ENDO (from 78 % without I_{sac})—Table 9.14). Hence, it seems that a compensatory mechanism for the profound reduction in contractile force is the presence of stretch-activated channels in cardiac tissue.

Without I_{sac}, there was very little deformation in 2D tissue under the SQT1 and SQT2 conditions (Fig. 9.13). However, there was some degree of deformation under the SQT3 mutation because across the ventricular wall, its APD is greater than the SQT1 and SQT2 mutations as it acts during terminal repolarisation. With the incorporation of I_{sac} at a permeability ratio of P_{Na}:P_K:P_{Ca} = 1:1:1, there was greater deformation (contraction) in the SQT1-3 conditions (Fig. 9.14). With foreknowledge that contractile function in SQT patients is not significantly altered from that of control patients [82–85], I_{sac} was incorporated in the tissue simulation at the permeability ratio of P_{Na}:P_K:P_{Ca} = 1:1:1 as it generates the greater contractile force compared to P_{Na}:P_K:P_{Ca} = 1:1:0.

The simulations in this chapter constitute a first attempt to link electrical and mechanical systems in the setting of the SQTS. The dissonance between the magnitude of effects predicted from the simulations and the information available on SQTS patients indicates that further work is required. Example areas that need to be investigated are the link between APD and SR loading and myofilament sensitivity to released Ca^{2+}. It is hoped that these simulations form a basis for

further investigation and dissemination of relevant experimental data by clinicians, experimentalists and mathematical modellers, out of which, over the next few years, a clearer picture will emerge.

References

1. ten Tusscher KHWJ, Panfilov AV (2006) Alternans and spiral breakup in a human ventricular tissue model. Am J Physiol Heart Circ Physiol 291(3):H1088–H1100
2. Rice JJ, Wang F, Bers DM, de Tombe PP (2008) Approximate model of cooperative activation and cross bridge cycling in cardiac muscle using ordinary differential equations. Biophys J 95(5):2368–2390
3. Morris CE (1990) Mechanosensitive ion channels. J Membr Biol 113(2):93–107
4. Van Wagoner DR (1993) Mechanosensitive gating of atrial ATP-sensitive potassium channels. Circ Res 72(5):973–983
5. Suleymanian MA, Clemo HF, Cohen NM, Baumgarten CM (1995) Stretch-activated channel blockers modulate cell volume in cardiac ventricular myocytes. J Mol Cell Cardiol 27(1):721–728
6. Bustamante JO, Ruknudin A, Sachs F (1991) Stretch-activated channels in heart cells: relevance to cardiac hypertrophy. J Cardiovasc Pharmacol 17(Suppl 2):S110–S113
7. Hagiwara N, Masuda H, Shoda M, Irisawa H (1992) Stretch-activated anion currents of rabbit cardiac myocytes. J Physiol (Lond) 456:285–302
8. Kohl P, Sachs F (2001) Mechanoelectric feedback in cardiac cells. Phil Trans R Soc Lond A 359(1783):1173–1185
9. Sachs F (1997) Mechanical transduction by ion channels: how forces reach the channel. Soc Gen Physiol Ser 52:209–218
10. Panfilov AV, Keldermann RH, Nash MP (2005) Self-organized pacemakers in a coupled reaction-diffusion-mechanics system. Phys Rev Lett 95(25):258104
11. Lunze K, Stålhand J, Leonhardt S (2010) Modeling of stretch-activated sarcolemmal channels in smooth muscle cells. In: Dössel O, Schlegel WC (eds) World congress on medical physics and biomedical engineering, September 7 - 12, 2009, Munich, Germany [Internet]. Springer Berlin Heidelberg; 2010 [cited 2012 Sep 20]. Accessed 20 Sep 2012 http://www.springerlink.com/content/k3052r8670832k70/abstract/
12. Kuijpers NHL (2008) Cardiac Electrophysiology and Mechanoelectric Feedback. Eindhoven University of Technology, Eindhoven
13. Youm JB, Han J, Kim N, Zhang Y-H, Kim E, Leem CH et al (2012) Role of stretch-activated channels in the heart: action potential and Ca2 + transients—mechanosensitivity in cells and tissues—NCBI bookshelf. In: Kamkin A, Kiseleva I (eds) Academia, Moscow 2005. Accessed 15 Sep 2012. http://www.ncbi.nlm.nih.gov/books/NBK7490/
14. Zabel M, Koller BS, Sachs F, Franz MR (1996) Stretch-induced voltage changes in the isolated beating heart: importance of the timing of stretch and implications for stretch-activated ion channels. Cardiovasc Res 32(1):120–130
15. Trayanova N, Li W, Eason J, Kohl P (2004) Effect of stretch-activated channels on defibrillation efficacy. Heart Rhythm 1(1):67–77
16. Kohl P, Hunter P, Noble D (1999) Stretch-induced changes in heart rate and rhythm: clinical observations, experiments and mathematical models. Prog Biophys Mol Biol 71(1):91–138
17. Marsden JE, Hughes TJR (1994) Mathematical foundations of elasticity. Dover Publications, New York
18. Ibrahimbegovic A (2009) Nonlinear solid mechanics: theoretical formulations and finite element solution methods, 1st edn. Springer, Berlin

19. Holzapfel GA (2000) Nonlinear solid mechanics: a continuum approach for engineering. 1st edn. Wiley, New York
20. Green AE, Adkins JE (1970) Large Elastic Deformations. 2nd edn. Oxford University Press, Oxford
21. Gurtin ME (1981) An introduction to continuum mechanics. 1st edn. Academic Press, Burlington
22. Malvern LE (1977) Introduction to the mechanics of a continuous medium. 1st edn. Prentice Hall, New York
23. Bonet J, Wood RD (2008) Nonlinear Continuum Mechanics for Finite Element Analysis. 2nd edn. Cambridge University Press, Cambridge
24. Belytschko T, Liu WK, Moran B (2000) Nonlinear finite elements for continua and structures. 1st edn. Wiley, NewYork
25. Bower AF (2009) Applied mechanics of solids. 1st edn. CRC Press, Boca Raton
26. Pathmanathan P, Whiteley JP (2009) A numerical method for cardiac mechanoelectric simulations. Ann Biomed Eng 37(5):860–873
27. Costa KD, Holmes JW, Mcculloch AD (2001) Modelling cardiac mechanical properties in three dimensions. Phil Trans R Soc Lond A 359(1783):1233–1250
28. Hunter PJ, Nash MP, Sands GB (1997) Computational mechanics of the heart. In: Panfilov AV, Holden AV (eds).Computational biology of the heart. west sussex, Wiley, UK. pp 345–407
29. Hunter PJ, McCulloch AD, ter Keurs HE (1998) Modelling the mechanical properties of cardiac muscle. Prog Biophys Mol Biol 69(2–3):289–331
30. Nash MP, Hunter PJ (2012) Computational mechanics of the heart. In: Cowin SC, Humphrey JD (eds) Cardiovascular soft tissue mechanics [Internet]. Kluwer Academic Publishers, Dordrecht, pp 113–141. Accessed 29 Feb 2012 http://www.springerlink.com/content/r0331nr728202762/
31. Niederer SA, Smith NP (2008) An improved numerical method for strong coupling of excitation and contraction models in the heart. Prog Biophys Mol Biol 96(1–3):90–111
32. Remme EW, Nash MP, Hunter PJ (2005) Distributions of myocyte stretch, stress and work in models of normal and infarcted ventricles. In: Kohl P, Sachs F, Franz MR (eds) Cardiac mechano–electric feedback and arrhythmias: from pipette to patient, edited by P. Kohl, F. Sachs, and M.R. Franz. Saunders–Elsevier, UK pp 381–391
33. Smith NP, Nickerson DP, Crampin EJ, Hunter PJ (2004) Multiscale computational modelling of the heart. Acta Numerica 13:371–431
34. Whiteley JP, Bishop MJ, Gavaghan DJ (2007) Soft tissue modelling of cardiac fibres for use in coupled mechano-electric simulations. Bull Math Biol 69(7):2199–2225
35. Guccione JM, Costa KD, McCulloch AD (1995) Finite element stress analysis of left ventricular mechanics in the beating dog heart. J Biomech 28(10):1167–1177
36. Schmid H, Nash MP, Young AA, Hunter PJ (2006) Myocardial material parameter estimation-a comparative study for simple shear. J Biomech Eng 128(5):742–750
37. Usyk T, Mazhari R, Mcculloch A (2000) Effect of laminar orthotropic myofiber architecture on regional stress and strain in the canine left ventricle. J Elast 61:143–164
38. Smaill BH, Hunter PJ (1991) Structure and function of the diastolic heart: material properties of passive myocardium. In: Glass L, Hunter PJ, McCulloch AD (eds) Theory of heart: biomechanics, biophysics, and nonlinear dynamics of cardiac function. Springer, New York, pp 1–29
39. Nash M (1998) Mechanics and material properties of the heart using an anatomically accurate mathematical model. University of Auckland, New Zealand
40. Clements JC, Nenonen J, Li PKJ, Horácek BM (2004) Activation dynamics in anisotropic cardiac tissue via decoupling. Ann Biomed Eng 32(7):984–990
41. Colli Franzone P, Pavarino LF, Taccardi B (2005) Simulating patterns of excitation, repolarization and action potential duration with cardiac bidomain and monodomain models. Math Biosci 197(1):35–66

42. Keener J, Sneyd J (2008) Mathematical physiology: II: systems physiology. 2nd edn. Springer, Berlin
43. Nash MP, Panfilov AV (2004) Electromechanical model of excitable tissue to study reentrant cardiac arrhythmias. Prog Biophys Mol Biol 85(2–3):501–522
44. Braess D (2007) Finite elements: theory, fast solvers, and applications in solid mechanics. 3rd edn. Cambridge University Press, Cambridge
45. Brenner SC, Scott R (2010) The mathematical theory of finite element methods. Softcover reprint of hardcover. 3rd edn. Springer, Berlin
46. Ciarlet PG (2002) The finite element method for elliptic problems, 2nd edn. SIAM: Society for Industrial and Applied Mathematics, Philadelphia
47. ten Tusscher KHWJ, Noble D, Noble PJ, Panfilov AV (2004) A model for human ventricular tissue. Am J Physiol Heart Circ Physiol 286(4):H1573–H1589
48. Potse M, Dubé B, Richer J, Vinet A, Gulrajani RM (2006) A comparison of monodomain and bidomain reaction-diffusion models for action potential propagation in the human heart. IEEE Trans Biomed Eng 53(12 Pt 1):2425–2435
49. Whiteley JP (2007) Physiology driven adaptivity for the numerical solution of the bidomain equations. Ann Biomed Eng 35(9):1510–1520
50. Feigenbaum H (1994) Echocardiolography. Fifth. Lee and Febiger, Philadelphia
51. Sundnes J, Lines GT, Tveito A (2005) An operator splitting method for solving the bidomain equations coupled to a volume conductor model for the torso. Math Biosci 194(2):233–248
52. Burnett DS (1987) Finite element analysis: from concepts to applications, 1st edn. Addison Wesley, Reading
53. Hughes TJR (2000) The finite element method: linear static and dynamic finite element analysis. Dover Publications, New York
54. Zienkiewicz OC, Taylor RL, Zhu JZ (2005) The finite element method: its basis and fundamentals, 6th edn. Butterworth-Heinemann, Oxford
55. Zienkiewicz OC, Taylor RL (2005) The finite element method for solid and structural mechanics, 6th ed. Butterworth-Heinemann, New York
56. Hughes TJR, Cohen M, Haroun M (1978) Reduced and selective integration techniques in the finite element analysis of plates. Nucl Eng Des 46(1):203–222
57. Hu H-C (1955) On some variational principles in the theory of elasticity and the theory of plasticity. Sci Sinica 4(8):33–54
58. Washizu K (1955) On the variational principles of elasticity and plasticity. M.I.T. Aeroelastic and Structures Research Laboratory, Cambridge
59. Wriggers P (2010) Nonlinear finite element methods. Softcover reprint of hardcover 1st ed. 2008. Springer; 2010
60. Wriggers P, Carstensen C (eds) (2010) Mixed finite element technologies. softcover reprint of hardcover. 1st edn. 2009. Springer, Berlin
61. Nickerson D, Smith N, Hunter P (2005) New developments in a strongly coupled cardiac electromechanical model. Europace 7(Suppl 2):118–127
62. Smith NP, Buist ML, Pullan AJ (2003) Altered T wave dynamics in a contracting cardiac model. J Cardiovasc Electrophysiol 14(10 Suppl):S203–S209
63. Keldermann RH, Nash MP, Panfilov AV (2009) Modeling cardiac mechano-electrical feedback using reaction-diffusion-mechanics systems. Physica D 238(11–12):1000–1007
64. Logg A, Mardal K-A, Wells G (eds) Automated solution of differential equations by the finite element method: the FEniCS book. 2012th edn. Springer, Berlin
65. Logg A, Wells GN (2010) DOLFIN: automated finite element computing. ACM Transactions on Mathematical Software 37(2):1–28
66. Boland J, Troquet J (1980) Intracellular action potential changes induced in both ventricles of the rat by an acute right ventricular pressure overload. Cardiovasc Res 14(12):735–740
67. Franz MR, Cima R, Wang D, Profitt D, Kurz R (1992) Electrophysiological effects of myocardial stretch and mechanical determinants of stretch-activated arrhythmias. Circulation 86(3):968–978

68. Calkins H, el-Atassi R, Kalbfleisch S, Langberg J, Morady F (1992) Effects of an acute increase in atrial pressure on atrial refractoriness in humans. Pacing Clin Electrophysiol 15(11 Pt 1):1674–1680
69. Dean JW, Lab MJ (1989) Effect of changes in load on monophasic action potential and segment length of pig heart in situ. Cardiovasc Res 23(10):887–896
70. Franz MR, Burkhoff D, Yue DT, Sagawa K (1989) Mechanically induced action potential changes and arrhythmia in isolated and in situ canine hearts. Cardiovasc Res 23(3):213–223
71. Taggart P (1996) Mechano-electric feedback in the human heart. Cardiovasc Res 32(1):38–43
72. Belus A, White E (2003) Streptomycin and intracellular calcium modulate the response of single guinea-pig ventricular myocytes to axial stretch. J Physiol (Lond) 546(Pt 2):501–509
73. Tavi P, Han C, Weckström M (1998) Mechanisms of stretch-induced changes in [Ca2 +]i in rat atrial myocytes: role of increased troponin C affinity and stretch-activated ion channels. Circ Res 83(11):1165–1177
74. Zeng T, Bett GC, Sachs F (2000) Stretch-activated whole cell currents in adult rat cardiac myocytes. Am J Physiol Heart Circ Physiol 278(2):H548–H557
75. Crozatier B (1996) Stretch-induced modifications of myocardial performance: from ventricular function to cellular and molecular mechanisms. Cardiovasc Res 32(1):25–37
76. Alvarez BV, Pérez NG, Ennis IL, Camilión de Hurtado MC, Cingolani HE (1999) Mechanisms underlying the increase in force and Ca(2 +) transient that follow stretch of cardiac muscle: a possible explanation of the Anrep effect. Circ Res 85(8):716–722
77. Gannier F, White E, Lacampagne A, Garnier D, Le Guennec JY (1994) Streptomycin reverses a large stretch induced increases in [Ca2 +]i in isolated guinea pig ventricular myocytes. Cardiovasc Res 28(8):1193–1198
78. Gannier F, White E, Garnier, Le Guennec JY (1996) A possible mechanism for large stretch-induced increase in [Ca2 +]i in isolated guinea-pig ventricular myocytes. Cardiovasc Res 32(1):158–167
79. Kentish JC, Wrzosek A (1998) Changes in force and cytosolic Ca2 + concentration after length changes in isolated rat ventricular trabeculae. J Physiol (Lond) 506(Pt 2):431–444
80. Le Guennec JY, White E, Gannier F, Argibay JA, Garnier D (1991) Stretch-induced increase of resting intracellular calcium concentration in single guinea-pig ventricular myocytes. Exp Physiol 76(6):975–978
81. White E, Le Guennec JY, Nigretto JM, Gannier F, Argibay JA, Garnier D (1993) The effects of increasing cell length on auxotonic contractions; membrane potential and intracellular calcium transients in single guinea-pig ventricular myocytes. Exp Physiol 78(1):65–78
82. Matsuda H, Saigusa A, Irisawa H (1987) Ohmic conductance through the inwardly rectifying K channel and blocking by internal Mg2+. Nature 325(7000):156–159
83. Schimpf R, Antzelevitch C, Haghi D, Giustetto C, Pizzuti A, Gaita F et al (2008) Electromechanical coupling in patients with the short QT syndrome: further insights into the mechanoelectrical hypothesis of the U wave. Heart Rhythm 5(2):241–245
84. Gaita F, Giustetto C, Bianchi F, Wolpert C, Schimpf R, Riccardi R et al (2003) Short QT Syndrome: a familial cause of sudden death. Circulation 108(8):965–970
85. Bellocq C, van Ginneken ACG, Bezzina CR, Alders M, Escande D, Mannens MMAM et al (2004) Mutation in the KCNQ1 gene leading to the short QT-interval syndrome. Circulation 109(20):2394–2397
86. Anttonen O, Junttila J, Giustetto C, Gaita F, Linna E, Karsikas M et al (2009) T-Wave morphology in short QT syndrome. Ann Noninvasive Electrocardiol 14(3):262–267
87. Schimpf R, Wolpert C, Gaita F, Giustetto C, Borggrefe M (2005) Short QT syndrome. Cardiovasc Res 67(3):357–366
88. McPate MJ, Witchel HJ, Hancox JC (2006) Short QT syndrome. Future Cardiol 2(3):293–301
89. Giustetto C, Di Monte F, Wolpert C, Borggrefe M, Schimpf R, Sbragia P et al (2006) Short QT syndrome: clinical findings and diagnostic-therapeutic implications. Eur Heart J 27(20):2440–2447

Chapter 10
Discussion and Conclusion

The work presented in this thesis centres on the in silico investigation of arrhythmia substrates in the inherited cardiac condition: the short QT syndrome (SQTS). It has focused on the functional consequences of the gene mutations associated with the first three variants of the SQTS; SQT1, SQT2 and SQT3. SQT1 affects the hERG channel, which is responsible for the rapid-delayed outward rectifier potassium current (I_{Kr}) [1–3], SQT2 affects the KCNQ1 gene, which encodes the α subunit of channels mediating slow-delayed outward rectifier potassium channel (I_{Ks}) [4]. SQT3 affects KCNJ2, which encodes the Kir2.1 protein that contributes to inwardly-rectifying potassium channel current (I_{K1}) [5].

In the absence of phenotypically accurate models of the SQTS variants (SQT1–SQT3), in silico models offer the best complementary method to investigating the functional consequences of these and other gene mutations. Consequently, Markov models that reproduced the kinetic properties of the SQT1 and SQT2 mutations were developed while a Hodgkin–Huxley style model was developed for the SQT3 mutation with the same objective. These models were incorporated into the TNNP single cell human ventricular AP model, which was in turn extended into multi-cellular models. Investigations were carried out at the single cell, 1D, 2D and 3D organ levels with anatomically realistic geometries.

On the basis of these in silico investigations, insights into the arrhythmogenic mechanisms of the SQT1–SQT3 mutations were attained, which elucidated the commonalities and differences between these SQTS variants.

10.1 Summary of the Functional Consequences of the SQT1, SQT2 and SQT3 Variants

10.1.1 SQT1

1. The SQT1 mutation abbreviated AP duration. AP shortening occurred regardless of I_{Kr} density distribution across the ventricular wall, i.e., homogeneous or heterogeneous I_{Kr} density distribution. However, in the ventricular

I. Adeniran, *Modelling the Short QT Syndrome Gene Mutations*,
Springer Theses, DOI: 10.1007/978-3-319-07200-5_10,

TNNP strand model, a heterogeneous distribution of I_{Kr} density across the ventricular wall was found to be necessary to reproduce a tall and peaked T-wave as seen clinically in SQT1. Szabo et al. [6] reported a greater abundance in the expression of hERG/I_{Kr} in the epicardium compared to the midmyocardium in the human left-ventricular wall.

2. With the heterogeneously distributed I_{Kr} density, the SQT1 mutation augmented the membrane potential differences (δV) between paired ENDO-EPI cells across a left-ventricular strand. In addition, in localised regions of the strand, the SQT1 mutation augmented the transmural dispersion of APD. These augmentations of δV and APD served to help increase the T-wave amplitude on the ECG.
3. With the heterogeneously distributed I_{Kr} density, the SQT1 mutation increased the temporal vulnerability of the tissue to unidirectional condition by a premature excitation.
4. The SQT1 mutation substantially reduced the minimal substrate size of tissue required to initiate and facilitate the maintenance of re-entry.
5. In the absence of a stretch-activated current (I_{sac}) from the electromechanics model, the SQT1 mutation compromised the binding of calcium to troponin and as a consequence, the contractile force of the left ventricular myocyte was severely impaired. The contractile force was ∼38 % of WT across the ventricular wall. With the incorporation of I_{sac} at a relative permeability ratio $P_{Na}{:}P_K{:}P_{Ca} = 1{:}1{:}1$, the contractile force was increased to ∼87 % of WT across the ventricular wall.

These findings substantiate the causal link between the N588K mutation and QT interval shortening and, moreover, provide a comprehensive explanation for increased susceptibility to re-entry and perpetuation of re-entrant arrhythmia in the setting of SQT1. The present study is the first to determine the arrhythmogenic consequences of the N588K mutation using multi-scale models of the human ventricles.

In an earlier study, Kogan et al. [7] used a simple model to demonstrate re-entrant activity when the AP is shortened. They found that slowing the deactivation rate of delayed outward K^+ current had a profound effect on wave-front propagation. Although the Kogan et al. study is important in that it provides a causal link between augmented K^+ conductance (via deactivation alteration of deactivation characteristics) and arrhythmogenesis, the SQT1 N588K-hERG mutation is characterised by impaired inactivation not deactivation, and therefore requires targeted simulations that specifically reproduce kinetic changes to I_{Kr} by the SQT1 N588K-hERG mutation.

Prior studies [8, 9] have reported inhomogeneous shortening of ventricular APD with loss of I_{Kr} inactivation, which appears paradoxical in light of increased arrhythmia susceptibility in the syndrome. The present study resolves this apparent contradiction: whilst the present study has demonstrated that the AP shortening as a result of N588K mutation is inhomogeneous, (resulting in a decreased APD_{90} and ERP dispersion, as the greatest shortening of APD_{90} occurred in MIDDLE cell

APs), with heterogeneous I_{Kr} in the ventricle, the mutation augmented both membrane potential difference between paired ENDO-EPI cells and the APD dispersion in some localised regions of the transmural strand. The present study is the first to incorporate heterogeneous I_{Kr} density in the ventricle [6] for the study of SQT1. These changes lead to an increased T-wave amplitude, which is different to previous simulation results but is consistent with clinical observations [10–13]. Another consequence of these changes is greater susceptibility of the tissue to unidirectional conduction block in response to a premature excitation stimulus.

The present study also shows that the N588K mutation reduces the minimal tissue size of the substrate required to facilitate and sustain re-entry in both idealised 2D and realistic 2D and 3D geometries. This occurs with either a homogeneous or heterogeneous distribution of I_{Kr} across the ventricular wall. In all tissue models, a single reentrant excitation wave can break up into multiple re-entrant circuits, leading to a transition from tachycardia-like to fibrillation-like electrical excitation waves.

10.1.2 SQT2

1. The SQT2 mutation abbreviated AP duration and steepened the APD-R curve. It consequently shortened the QT interval, increased T wave amplitude and T_{peak}–T_{end} duration, all of which are concordant with clinical observations regarding the SQTS [4, 14, 15].
2. The SQT2 mutation augmented the δV between paired cells across a left-ventricular strand. In addition, in localised regions of the strand, the mutation augments the transmural dispersion of APD. These augmentations of δV and APD served to help increase the T-wave amplitude on the ECG.
3. The SQT2 mutation increased the temporal vulnerability of the tissue to the genesis of unidirectional conduction by a premature excitation at some localised regions of transmural strand.
4. The SQT2 mutation reduced the minimal tissue substrate size required to initiate and facilitate the maintenance of re-entry and accelerate reentrant excitation waves.
5. In the absence of a stretch-activated current (I_{sac}) from the electromechanics model, the SQT2 mutation compromised the binding of calcium to troponin and as a consequence, impaired the contractile force of the left ventricular myocyte. The contractile force was ∼36 % of WT across the ventricle wall. With the incorporation of I_{sac} at a relative permeability ratio P_{Na}:P_K:P_{Ca} = 1:1:1, the contractile force was increased to ∼83 % of WT across the ventricular wall.

Just as with SQT1, these findings also provide a causal link between the KCNQ1 SQT2 mutation, QT interval shortening and tachyarrhythmias. They also provide a comprehensive explanation for the increased susceptibility to re-entry and the perpetuation of re-entrant arrhythmia in the SQT2 setting.

The novel SQT2 Markov model developed in this thesis provides greater utility and insight into the arrhythmogenic mechanisms of the mutation. With the Markov model, the state occupancy of the channels during the AP could be monitored. On AP initiation, 2 % of the I_{Ks} channels reside in zone 1, which is a fast transition zone to the open state. The remaining 98 % reside in zone 2 (a slow transition zone to zone 1), i.e., the channels need to make a slow transition from zone 2 to zone 1 before transitioning to the open state. In contrast, WT has 100 % of its channels residing in zone 2, leading to a delay in WT activation.

The greater occupancy of zone 1 by the SQT2 mutant channels facilitates channel opening and larger I_{Ks} during the AP resulting in AP abbreviation. Open-state accumulation is also greater than in WT due to slower deactivation of the mutant channel. Thus, the primary mechanism for larger I_{Ks} in the SQT2 mutation is greater zone 1 occupancy coupled with slower channel deactivation.

The use of Implantable Cardioverter Defibrillators (ICD) is the current treatment for the SQTS [16–20]. However, as the SQTS is characterised by tall and peaked T-waves, there is the risk of inappropriate shocks to the patient due to T-wave over-sensing [16–19, 21]. Additionally, ICDs do not restore the QT interval to its normal duration and are not suitable for all patients, e.g., infants. Therefore, pharmacological alternatives that can restore the normal duration of the QT interval and offer protection from arrhythmias are being actively pursued [17, 18, 22, 23]. Pharmacologically, there is very little available on SQT2 but a recent study by El Harchi et al. [24] found that recombinant I_{Ks} channels incorporating the KCNQ1 V307L mutation were effectively inhibited by mefloquine. Although I_{Ks} is selectively blocked by chromanol compounds such as chromanol 293B [16, 25, 26], its blocking potency was reduced by the KCNQ1 V307L mutation [16, 25].

The present study shows by mimicking drugs that selectively block the I_{Ks} channel in the SQT2 setting that under the WT-V307L heterozygote condition, a blockade of I_{Ks} by $\sim$58 % is sufficient to restore the QT interval to its original WT duration. Under the V307L homozygote condition, a blockade of I_{Ks} by $\sim$65 % is sufficient to achieve the same result. These QT interval restorations terminate re-entrant activity in the tissue.

10.1.3 SQT3

1. The SQT3 mutation abbreviated AP duration and steepened the APD and ERP restitution curves. It consequently shortened the QT interval and modified the T-wave characteristics on the ECG; the T-wave became peaked, tall and asymmetric with a slow rise and sharp decline as seen clinically in SQT3 patients [5].
2. The SQT3 mutation increased the transmural APD dispersion across the ventricular wall in different regions of the transmural strand, the effect of which was increased susceptibility of the tissue to premature stimuli.

3. The SQT3 mutation stabilised, accelerated and perpetuated reentry. It reduced the minimal substrate size of tissue required to initiate and facilitate the maintenance of re-entry and accelerated re-entrant excitation waves.
4. In the absence of a stretch-activated current (I_{sac}) from the electromechanics model, the SQT3 mutation compromised the binding of calcium to troponin and as a consequence, impaired the contractile force of the left ventricle. The contractile force was ~79 % of WT across the ventricle wall. With the incorporation of I_{sac} at a relative permeability ratio P_{Na}:P_K:P_{Ca} = 1:1:1, the contractile force was increased to ~92 % of WT across the ventricular wall.

As with the SQT1 and SQT2 mutations, these characteristics of the KCNJ2 D172N mutation reveal a causal link between the mutation and QT interval shortening, and offer a novel explanation for increased vulnerability of tissue to re-entry and maintenance of re-entrant arrhythmia in the SQT3 setting.

The SQT3 mutation stabilised and accelerated reentry in tissue reflecting its pro-arrhythmic nature. This is consistent with findings in previous studies of the role of I_{K1} in arrhythmogenesis [27–29]. There are however, some differences between those studies and mine. In the previous studies, both the outward and inward components of I_{K1} were increased or scaled proportionally, which had the effect of steepening the slope of the I–V curve. Consequently, any membrane potential change close to the potassium equilibrium potential (E_K) would act in such a way as to shift the resting potential towards E_K. Therefore, during high excitation rates, sodium current (I_{Na}) recovery from inactivation is increased, thereby helping to stabilise reentry.

In my study, only the outward component of the I_{K1} current is enhanced (the inward component is unaffected) There is thus less effect on the slope of the I–V curve and the resting potential was found to be little altered by the D172N mutation. Consequently, the stabilisation of reentry under these conditions was not through increased I_{Na} recovery but via increased tissue excitability at high excitation rates and the shorter ERP of the SQT3 mutation. The reduced ERP of the mutation also reduced the wavelength of the reentrant excitation waves thus allowing their activation at higher frequencies and once formed, the waves were stable and persistent.

10.2 Common Mechanisms Between the SQT1-3 Variants

The three short QT variants (SQT1, SQT2 and SQT3) considered in this thesis share common elements and arrhythmia mechanisms. These are depicted in Fig. 10.1. Each mutation is a gain-of-function mutation (SQT1: gain-of-function mutation of the I_{Kr} channel, SQT2: gain-of-function mutation of the I_{Ks} channel and SQT3: gain-of-function mutation of the I_{K1} channel). SQT1 generates excessive I_{Kr} earlier during the AP, SQT2 produces excessive I_{Ks} during repolarisation and SQT3 generates excessive outward I_{K1} during terminal repolarisation. The excessive current leads to a shortening of the APD and ERP in the three mutations with an

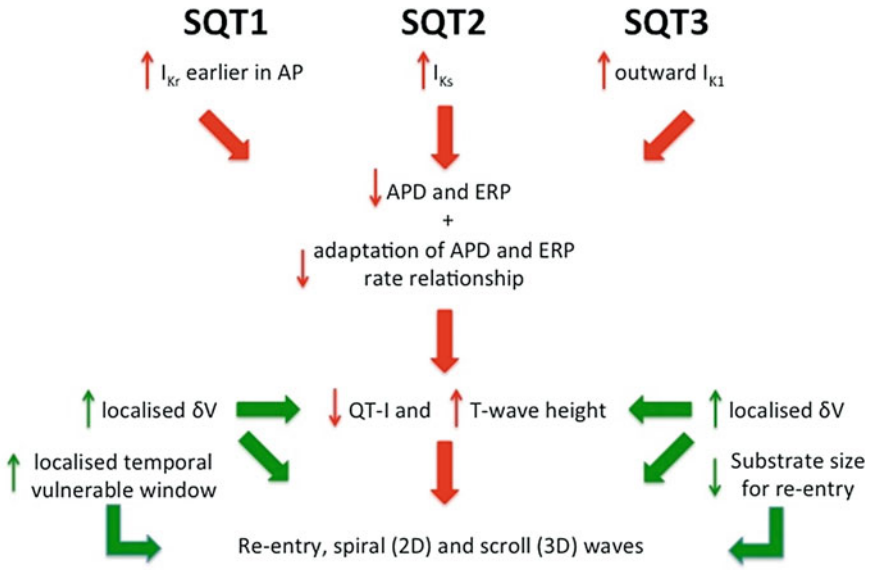

Fig. 10.1 Common mechanisms between SQT1-3 variants

associated reduction in APD and ERP rate adaptation. The SQT variants shorten the QT interval on the ECG and alter the morphology of the T-wave, which is increased in amplitude, and becomes tall and peaked. All these characteristics make the SQT mutations pro-arrhythmic thus enabling them to stabilise, accelerate and perpetuate reentry.

The increase in the T-wave height is due to the augmentation of the membrane potential differences (δV) between paired cells across the ventricular wall and amplification of the transmural dispersion of APD in localised regions. The mutations increased the temporal vulnerability of the tissue to the genesis of unidirectional conduction by a premature excitation at some localised regions and reduced the minimal tissue substrate size required to initiate and facilitate the maintenance of re-entry and accelerate re-entrant excitation waves. These augmentations of δV, transmural dispersion of APD, the increase in the temporal vulnerability window to premature stimulus and the reduction in the minimal substrate size required to initiate re-entry confer on the SQT1-3 mutations a pro-arrhythmic nature.

10.3 Potential Limitations of the Simulations

1. The TNNP human ventricular single cell model was used in the simulations and although it has been suggested to be well-suited to the study of re-entrant arrhythmia [30–32] and most of its constituent ion channel kinetic formulations have been derived from experimental data using human ventricular

myocytes [33], it still has its shortcomings. For example, because of incomplete experimental data sets on the transmural heterogeneity of human ion channel current densities, incongruities between the simulated transmural APD dispersion and experimentally observed data are known [34–37]; the ENDO and EPI APD_{90} from the model are very similar; the differences in APD between the MCELL and ENDO and EPI are smaller than those observed experimentally; the APD and APD restitution properties of the model were developed using a general knowledge of the influence of certain model parameters. These limitations are discussed extensively in [30, 31].

2. In the multicellular simulations, due to insufficient experimental data regarding the proportion of EPI, MIDDLE and ENDO cell types in the ventricular wall, a cell type proportion was chosen to produce a positive T-wave and also a conduction velocity across the ventricular wall similar to that observed experimentally [38]. Nonetheless, this proportion is similar to that used in other studies [8, 9, 39, 40].
3. The multicellular models assume the presence of M Cells in the human heart. This is a subject of disagreement and debate in the literature. Taggart et al. [33] reported no transmural difference in APD in the left ventricular wall while other studies have reported the presence of M Cells in the human heart [34–37]. The most recent of these studies is that of Glukhov et al. [37] who found M Cells clustered in islands in the deep subendocardium of the human heart.
4. All the multicellular simulations assume a monodomain representation of tissue structure as opposed to a bidomain representation. Previous studies found extremely small differences in the solutions between the monodomain and bidomain models [41–43]. Potse et al. [42] found that propagation of activation was only 2 % faster in the bidomain model [42] while they all found that the ECGs from both models were visually indistinguishable [41–43]. Bourgault and Pierre [44] carried out convergence analyses on both models and reported a relative error in activation time of order 1 %. The only situation where the bidomain has been deemed absolutely necessary is in the presence of applied currents, e.g., a defribrillation shock [42].
5. While the 3D human ventricle incorporates a realistic stimulation sequence (tailored to that of the owner of the heart), it does not possess a purkinje fibre network. This may play a role in the genesis of arrhythmia in the SQTS.
6. The models do not consider uncertainty in parameters for a specific human heart, for example, pacing frequency and variations of model parameters, which can play significant roles in ventricular fibrillation genesis.
7. The left-ventricular 2D sheet used for the mechanical simulations is fixed along the left edge in order to avoid rigid body rotation but in a realistic setting, this edge would move in tandem with the ventricular wall. It is also assumed that the active tension force generated by the ventricular cells acts in the x-direction only (which was considered the fibre direction for those simulations). Realistically, the force would act orthotropically in the fibre, sheet and cross-sheet directions.
8. There is no consideration of cardiac mechanics on realistic tissue geometries, which may have important consequences for the genesis and maintenance of

reentry. Since repolarisation occurs during tension development, the effect of cardiac mechanics on tissue geometry and stretch-activated channels could be significant. There is also evidence of altered electromechanical coupling in some SQT patients [45]. However, it is notable that electrophysiological changes due to the altered kinetics of I_{K1} by the D172N mutation appear to be sufficient to increase the risk of arrhythmogenesis.

Whilst it is important to enumerate the potential limitations of the models used in these simulations, they do not adversely affect the conclusions that can be drawn on the substrates and the likely mechanisms by which the SQT1, SQT2 and SQT3 mutations facilitate, stabilise and perpetuate arrhythmia.

10.4 Future Developments

10.4.1 Drug Actions

An important extension to the work carried out in this thesis is the investigation of the effects of channel-blocking drugs on the SQTS. Using the SQTS models developed in this thesis, it is possible to investigate or mimic the action of several drugs on the SQT-mutated channel. Three possible questions to investigate would be:

1. Does mimicking drugs that block hERG/I_{Kr}, I_{Ks} and I_{K1} terminate re-entrant activity in SQT1, SQT2 and SQT3 respectively?
2. Does blocking one of hERG/I_{Kr}, I_{Ks} and I_{K1} affect SQT variants involving the other channel types?
3. To what extent does the mutated channel need to be inhibited to normalise the QT interval?
4. In blocking the channel current, is there a cut-off point or limit at which re-entry is terminated and yet the QT interval is still not normalised? In other words, what is the lower limit of channel block required to terminate reentry?

This is all the more pertinent, given the growing interest in determining if acquired QT interval shortening via drugs (as for drug-induced forms of the LQTS) renders the patient more susceptible to arrhythmia [46, 47]. There are currently insufficient data on this issue and no regulatory guidelines regarding drug candidates that result in QT interval shortening.

10.4.2 Mechanical Function

The simulations in Chap. 9 suggest that abbreviated repolarisation alters mechanical function in the SQTS but that there could be compensatory mechanisms such as stretch-activated channels (SACs) which maintain the normal

amplitude of the contractile force in SQTS patients. Simulations without stretch-activated current (I_{sac}) profoundly impaired ventricular contraction whereas incorporation of I_{sac} maintained contractile force at an adequate level but still below that of WT. The results depend on the presence/absence of SACs in human ventricular myocytes and with SACs, it also likely depends (i) on the magnitude of the current incorporated and (ii) the extent to which Ca^{2+} permeability is incorporated into the SAC simulation equations.

However, at present, there are insufficient data (experimental and in silico) to reach a definite conclusion. The most notable work on mechanical function in the SQTS is by Schimpf et al. [45] in which no significant difference in end systolic volume, end diastolic volume and ejection fraction was seen between control subjects and SQTS patients. It is anticipated that the electromechanics simulation results of the present thesis form a basis for further research by clinicians, experimentalists and mathematical modellers, out of which, over the next few years, a clearer picture will emerge.

10.5 Closing Words

Three novel in silico models of the variants of the SQTS that affect potassium channels have been developed; Markov models for SQT1 and SQT2 and a Hodgkin–Huxley model of SQT3. These models have been use to investigate the functional consequences of SQT1-3 in the human ventricle at the single cell, 1D, 2D and 3D levels. The findings in this thesis provide a comprehensive explanation for clinical consequences of these forms of the SQTS in terms of abbreviation of repolarisation and susceptibility to arrhythmia. The multiscale ventricular models developed and employed also have further utility for probing the basis of arrhythmia in other forms of the SQTS and other repolarisation disorders and in the design and investigation of therapeutic interventions for the SQTS.

References

1. Brugada R, Hong K, Dumaine R, Cordeiro J, Gaita F, Borggrefe M et al (2004) Sudden death associated with short-QT syndrome linked to mutations in HERG. Circulation 109(1):30–35
2. Hong K, Bjerregaard P, Gussak I, Brugada R (2005) Short QT syndrome and atrial fibrillation caused by mutation in KCNH2. J Cardiovasc Electrophysiol 16(4):394–396
3. Sun Y, Quan X-Q, Fromme S, Cox RH, Zhang P, Zhang L et al (2011) A novel mutation in the KCNH2 gene associated with short QT syndrome. J Mol Cell Cardiol 50(3):433–441
4. Bellocq C, van Ginneken ACG, Bezzina CR, Alders M, Escande D, Mannens MMAM et al (2004) Mutation in the KCNQ1 gene leading to the short QT-interval syndrome. Circulation 109(20):2394–2397
5. Priori SG, Pandit SV, Rivolta I, Berenfeld O, Ronchetti E, Dhamoon A et al (2005) A novel form of short QT syndrome (SQT3) is caused by a mutation in the KCNJ2 gene. Circ Res 96(7):800–807

6. Szabó G, Szentandrássy N, Bíró T, Tóth BI, Czifra G, Magyar J et al (2005) Asymmetrical distribution of ion channels in canine and human left-ventricular wall: epicardium versus midmyocardium. Pflugers Arch 450(5):307–316
7. Kogan BY, Karplus WJ, Billett BS, Pang AT, Khan SS, Mandel WJ et al (1991) The role of diastolic outward current deactivation kinetics on the induction of spiral waves. Pacing Clin Electrophysiol 14(11 Pt 2):1688–1693
8. Weiss DL, Seemann G, Sachse FB, Dössel O (2005) Modelling of short QT syndrome in a heterogeneous model of the human ventricular wall. Europace 7(Suppl 2):105–117
9. Zhang H, Hancox JC (2004) In silico study of action potential and QT interval shortening due to loss of inactivation of the cardiac rapid delayed rectifier potassium current. Biochem Biophys Res Commun 322(2):693–699
10. Schimpf R, Wolpert C, Gaita F, Giustetto C, Borggrefe M (2005) Short QT syndrome. Cardiovasc Res 67(3):357–366
11. Bidoggia H, Maciel JP, Capalozza N, Mosca S, Blaksley EJ, Valverde E et al (2000) Sex differences on the electrocardiographic pattern of cardiac repolarization: possible role of testosterone. Am Heart J 140(4):678–683
12. Hancox JC, Choisy SC, James AF (2009) Short QT interval linked to androgen misuse: wider significance and possible basis. Ann Noninvasive Electrocardiol 14(3):311–312
13. Patel C, Antzelevitch C (2008) Cellular basis for arrhythmogenesis in an experimental model of the SQT1 form of the short QT syndrome. Heart Rhythm 5(4):585–590
14. Gollob MH, Redpath CJ, Roberts JD (2011) The short QT syndrome: proposed diagnostic criteria. J Am Coll Cardiol 57(7):802–812
15. Patel U, Pavri BB (2009) Short QT syndrome: a review. Cardiol Rev 17(6):300–303
16. Hancox JC, McPate MJ, Harchi A, Duncan RS, Dempsey CE, Witchel HJ, et al (2011) The short QT syndrome. In: Tripathi ON, Ravens U, Sanguinetti MC (eds). Heart rate and rhythm. Springer, Berlin, pp 431–449. http://www.springerlink.com/content/m8l86l8n3h81w43m/
17. Jiang M, Xu X, Wang Y, Toyoda F, Liu X-S, Zhang M et al (2009) Dynamic partnership between KCNQ1 and KCNE1 and influence on cardiac IKs current amplitude by KCNE2. J Biol Chem 284(24):16452–16462
18. Hancox JC, Levi AJ, Witchel HJ (1998) Time course and voltage dependence of expressed HERG current compared with native "rapid" delayed rectifier K current during the cardiac ventricular action potential. Pflugers Arch 436(6):843–853
19. Glowatzki E, Fakler G, Brändle U, Rexhausen U, Zenner HP, Ruppersberg JP et al (1995) Subunit-dependent assembly of inward-rectifier K + channels. Proc Biol Sci 261(1361):251–261
20. Yang J, Jan YN, Jan LY (1995) Determination of the subunit stoichiometry of an inwardly rectifying potassium channel. Neuron 15(6):1441–1447
21. Anttonen O, Junttila J, Giustetto C, Gaita F, Linna E, Karsikas M et al (2009) T-Wave morphology in short QT syndrome. Ann Noninvasive Electrocardiol 14(3):262–267
22. James AF, Choisy SCM, Hancox JC (2007) Recent advances in understanding sex differences in cardiac repolarization. Prog Biophys Mol Biol 94(3):265–319
23. Sanguinetti MC, Curran ME, Spector PS, Keating MT (1996) Spectrum of HERG K + -channel dysfunction in an inherited cardiac arrhythmia. Proc Natl Acad Sci USA 93(5):2208–2212
24. Levi AJ (1993) A role for sodium/calcium exchange in the action potential shortening caused by strophanthidin in guinea pig ventricular myocytes. Cardiovasc Res 27(3):471–481
25. Garberoglio L, Giustetto C, Wolpert C, Gaita F (2007) Is acquired short QT due to digitalis intoxication responsible for malignant ventricular arrhythmias? J Electrocardiol 40(1):43–46
26. Workman AJ, Kane KA, Rankin AC (2001) The contribution of ionic currents to changes in refractoriness of human atrial myocytes associated with chronic atrial fibrillation. Cardiovasc Res 52(2):226–235
27. Dhamoon AS, Jalife J (2005) The inward rectifier current (IK1) controls cardiac excitability and is involved in arrhythmogenesis. Heart Rhythm 2(3):316–324

28. Noujaim SF, Pandit SV, Berenfeld O, Vikstrom K, Cerrone M, Mironov S et al (2007) Up-regulation of the inward rectifier K + current (I K1) in the mouse heart accelerates and stabilizes rotors. J Physiol (Lond) 578(Pt 1):315–326
29. Pandit SV, Berenfeld O, Anumonwo JMB, Zaritski RM, Kneller J, Nattel S et al (2005) Ionic determinants of functional reentry in a 2-D model of human atrial cells during simulated chronic atrial fibrillation. Biophys J 88(6):3806–3821
30. ten Tusscher KHWJ, Panfilov AV (2006) Alternans and spiral breakup in a human ventricular tissue model. Am J Physiol Heart Circ Physiol 291(3):1088–1100
31. ten Tusscher KHWJ, Noble D, Noble PJ, Panfilov AV (2004) A model for human ventricular tissue. Am J Physiol Heart Circ Physiol 286(4):1573–1589
32. Ten Tusscher KHWJ, Panfilov AV (2006) Cell model for efficient simulation of wave propagation in human ventricular tissue under normal and pathological conditions. Phys Med Biol 51(23):6141–6156
33. Taggart P, Sutton PM, Opthof T, Coronel R, Trimlett R, Pugsley W et al (2001) Transmural repolarisation in the left ventricle in humans during normoxia and ischaemia. Cardiovasc Res 50(3):454–462
34. Antzelevitch C (2010) M cells in the human heart. Circ Res 106(5):815–817
35. Drouin E, Charpentier F, Gauthier C, Laurent K, Le Marec H (1995) Electrophysiologic characteristics of cells spanning the left ventricular wall of human heart: evidence for presence of M cells. J Am Coll Cardiol 26(1):185–192
36. Li GR, Feng J, Yue L, Carrier M (1998) Transmural heterogeneity of action potentials and Ito1 in myocytes isolated from the human right ventricle. Am J Physiol 275(2 Pt 2):369–377
37. Glukhov AV, Fedorov VV, Lou Q, Ravikumar VK, Kalish PW, Schuessler RB et al (2010) Transmural dispersion of repolarization in failing and nonfailing human ventricle. Circ Res 106(5):981–991
38. Taggart P, Sutton PM, Opthof T, Coronel R, Trimlett R, Pugsley W et al (2000) Inhomogeneous transmural conduction during early ischaemia in patients with coronary artery disease. J Mol Cell Cardiol 32(4):621–630
39. Zhang H, Kharche S, Holden AV, Hancox JC (2008) Repolarisation and vulnerability to re-entry in the human heart with short QT syndrome arising from KCNQ1 mutation–a simulation study. Prog Biophys Mol Biol 96(1–3):112–131
40. Gima K, Rudy Y (2002) Ionic current basis of electrocardiographic waveforms: a model study. Circ Res 90(8):889–896
41. Clements JC, Nenonen J, Li PKJ, Horácek BM (2004) Activation dynamics in anisotropic cardiac tissue via decoupling. Ann Biomed Eng 32(7):984–990
42. Potse M, Dubé B, Richer J, Vinet A, Gulrajani RM (2006) A comparison of monodomain and bidomain reaction-diffusion models for action potential propagation in the human heart. IEEE Trans Biomed Eng 53(12 Pt 1):2425–2435
43. Boulakia M, Cazeau S, Fernández MA, Gerbeau J-F, Zemzemi N (2010) Mathematical modeling of electrocardiograms: a numerical study. Ann Biomed Eng 38(3):1071–1097
44. Bourgault Y, Pierre C (2010) Comparing the bidomain and monodomain models in electrocardiology through convergence analysis. INSMI. hal–00545888
45. Schimpf R, Antzelevitch C, Haghi D, Giustetto C, Pizzuti A, Gaita F et al (2008) Electromechanical coupling in patients with the short QT syndrome: further insights into the mechanoelectrical hypothesis of the U wave. Heart Rhythm 5(2):241–245
46. Pugsley MK, Curtis MJ (2007) Safety pharmacology methods: anticipating the transition from long QT (LQTS) to short QT syndromes (SQTS)? J Pharmacol Toxicol Methods 56(2):87–90
47. Shah RR (2010) Drug-induced QT interval shortening: potential harbinger of proarrhythmia and regulatory perspectives. Br J Pharmacol 159(1):58–69